Online diagnostics of time-resolved electron beam properties with femtosecond resolution for X-ray FELs

Dissertation

zur Erlangung des Doktorgrades
an der Fakultät für Mathematik, Informatik und Naturwissenschaften
Fachbereich Physik
der Universität Hamburg

vorgelegt von

Dipl.-Phys. Minjie Yan
aus Shanghai

Hamburg
2015

Gutachter der Dissertation	Prof. Dr. Jörg Roßbach Prof. Dr. Anke-Susanne Müller
Mitglieder der Prüfungskommission	Prof. Dr. Jörg Roßbach Prof. Dr. Anke-Susanne Müller Prof. Dr. Daniela Pfannkuche PD Dr. Bernhard Schmidt Prof. Dr. Wilfried Wurth
Datum der Disputation	26. April 2016

Abstract

The European X-ray Free-electron Laser (XFEL) puts high demands on the quality of the high-brightness driving electron beam with bunch lengths in the femtosecond regime. Longitudinal diagnostics is requested to optimize and control the longitudinal profile, the longitudinal phase space, the slice energy spread and the slice emittance of the electron bunch, all of which are crucial to the generation of Self-Amplified Spontaneous Emission (SASE). The high bunch repetition rate of the super-conducting accelerator renders diagnostic method that is (quasi) non-destructive to the generation of SASE possible. In this thesis, three online diagnostic sections utilizing transverse deflecting structures (TDS) have been designed for the European XFEL, providing access to all parameters of interest with a longitudinal resolution down to below 10 fs. The requirement on the non-destructive capability has been realized by the implementation of fast kicker magnets and off-axis screens, which has been validated experimentally using an installation of the same concept at the Free-electron Laser in Hamburg. A special slicing procedure has been developed to significantly enhance the accuracy of slice energy spread measurements. Suppression of coherence effects, which impede the beam imaging in the TDS diagnostics, has been first demonstrated experimentally using the spatial separation method with scintillator screens. Comparison of the results of emittance measurements using the quadrupole scan method with those using the multi-screen method has proved the reliability of the latter method, which has been modelled intensively for the European XFEL.

Kurzbeschreibung

Der europäische Freie-Elektronen Röntgen-Laser (European XFEL) stellt hohe Anforderung an die Eigenschaften der verwendeten Elektronenpakete mit Paketlängen in Femtosekunden Bereich. Longitudinale Strahldiagnose ist gefragt für die Optimierung und Kontrolle des longitudinalen Profils, des longitudinalen Phasenraums, der Scheibenenergiespanne und der Scheibenemittanz, von denen alle entscheidend für die Erzeugung der Photonpulse sind. Die hohe Repetitionsrate des supraleitenden Beschleunigers ermöglicht zerstörungsfreie Diagnose der Elektronenpakete. In dieser Arbeit wurden drei online longitudinale Strahldiagnostiksektionen mittels transversal ablenkenden Strukturen (TDS) für den European XFEL entworfen, welche mit einer longitudinalen Auflösung von unter 10 fs den Zugang zu sämtlichen Parametern gewähren. Die Anforderung an die zerstörungsfreie Fähigkeit wurde erfüllt durch die Implementierung von schnell ablenkenden Magneten und der zur Strahlachse versetzten Schirmen. Technische Realisierung eines Monitors des longitudinalen Profils an dem Freie-Elektronen Laser in Hamburg hat die Umsetzbarkeit dieses Konzeptes bestätigt. Eine spezielle Methode zur Bestimmung der Scheibenteilung wurde entwickelt, welche die Genauigkeit der Messung der Scheibenenergiespanne wesentlich erhöht. Die Unterdrückung von kohärenten Effekten, die die Strahlbreitenmessung in Abbildungdiagnostik verhindern, wurden experimentell mit der Methode der räumlichen Trennung mit Einsatz von Szintillatorschirmen demonstriert. Vergleiche der Emittanz, gemessen mit der Multischirm-Methode, und gemessen mit der Quadrupolmagnet-Methode, hat die Zuverlässigkeit der Multischirm-Methode gezeigt, für welche detaillierte Studien für den European XFEL durchgeführt wurden.

Contents

List of figures

List of tables

Introduction

X-rays in the wavelength range from (sub-)Ångström to several nanometers have enabled scientific research on the structure of matter into the fundamental level of atoms, revolutionising understandings in a wide range of fields such a Physics, Chemistry, Medicine and Biology [B+08]. X-ray science has been further advanced by developments on accelerator-based synchrotron radiation sources (from the 1st. to the 3rd. generation light sources), which excel in their reliable operation stability and capability of providing X-ray pulses with high average brilliance as well as tunable wavelengths.

When the aforementioned advantages of high-brilliance X-ray beams are combined with the additional property of short pulse duration in the order of femtoseconds or below, exploration of ultra-fast phenomena on the natural time scales of the atoms with resolutions in their spatial scales becomes possible. Such X-ray sources are realized with the advance of free-electron lasers (FEL) driven by relativistic electron bunches from linear accelerators (the 4th. generation light sources), whose performance significantly exceeds that of synchrotron radiation sources in terms of higher peak brilliance, higher levels of coherence (high spatial and partial temporal coherence), and shorter pulse durations [BBC+10, Hua13]. Due to the outstanding properties of the photon pulses, FELs have gained in recent years increasing attention in the community of X-ray ultra-fast photon science [GC07, NWvdS+00] for research in a variety of subjects, such as dynamics in atoms and molecules (e.g., in Refs. [SSK+13, SSK+14, KMW+12]), condensed matter (e.g., in Ref. [HBS+10]), magnetisation processes (e.g., in Ref. [FMS+14]), and biological structure (e.g., in Ref. [C+11]).

The principle of FEL, first introduced by John Madey [Mad71] in 1971, is based on the interaction between the electrons and the electro-magnetic fields of the co-propagating radiation generated inside an undulator[1]. For specific wavelengths (resonant wavelengths), energy transfer from the electrons to the radiations is sustained, leading to an amplification of the radiation power. One way to start up the radiation process is by using an external seed laser at the desired wavelength. Alternatively, the Self-Amplified Spontaneous Emission process (SASE) [KS80, BPN84, Kim86] can be adopted to initialise the radiation from an arbitrary wavelength of choice, which is a highly desirable property for the wavelength regimes of extreme ultra-violet and X-rays.

For a low-gain FEL, where the radiation is retained in an optical cavity and amplified in the undulator by being passed repetitively through the undulator and back, the power of the radiation increases by a few percent after each passage through the undulator. With the help of high reflectivity mirrors in the optical cavity, low gain FELs can be achieved for the optical and infra-red wavelength range. However for shorter wavelengths extending to the X-ray regime, such mirrors do not exist. Therefore, power gain of the radiation has to be accomplished during a single passage of the electron

[1] A periodic magnetic structure.

bunch through the undulator. Such high-gain FELs are based on the micro-bunching process of the electrons during the passage through the undulator: Electrons, which transfer energy to the initial light wave, travel on a longer trajectory through the undulator than electrons, which gain energy from the light wave. Different paths of electrons result in modulations in their longitudinal velocities. Evolution of such velocity modulation along the undulator eventually leads to longitudinally modulated micro-bunch structures with a periodicity of the resonant light wavelength inside the bunch. In each micro-bunch, which is shorter than the resonant light wavelength, the electrons radiate coherently, leading to an exponential gain in the radiation power.

To achieve a high radiation power gain from a single passage through the undulator, the following quality of an electron beam is required: a high peak current, a small energy spread and a small emittance[2]. When it is assumed that the electron bunch follows a Gaussian distribution, the photon pulse duration (at the saturation regime of power gain) can be estimated from the electron bunch length [SSY98, SSY00]. However in practice, collective effects (such as coherent synchrotron radiation, wakefields) in the magnetic bunch compressors [SSY02a, ZD11], which are essential for achieving short electron bunches with high peak currents, lead to significant variations of these electron parameters along the longitudinal direction. As a result, different portions of the electron bunch can contribute differently to the FEL amplification process in the undulator, making the estimation of the photon pulse duration an extremely challenging task. Ref.[DRAS+14] has experimentally studied the possible correlations between electron bunch length and photon pulse duration. An approximate upper limit of the latter can be derived from an estimation of the electron bunch length [BGG+12].

Longitudinal diagnostics on properties of slices in electron bunches, such as the current profile, the slice energy spread and the slice emittance, play a crucial role for X-ray FELs. They help control the longitudinal compression of the bunch during the set up of the accelerator to ensure a short pulse duration of the FEL pulses. Diagnosis of the slice parameters reveals information about the actual part of the bunch that could potentially contribute to the generation of FEL pulses, and are useful for the parameter optimization. Furthermore, monitoring the slice parameters during FEL operation offers the possibility of predicting and compensating potential drifts which may affect the properties of photon pulses.

Such demanding tasks on longitudinal diagnostics can be realized by transverse deflecting structures (TDS), which allow access to all three quantities, i.e. the current profile, the slice energy spread and the slice emittance, when used in combination with other devices. The versatility in application of TDS is further complemented by their high longitudinal resolution, large dynamic range and single-shot capability. In the latest development, application of TDS has been successfully extended to the field of photon diagnostics for determining the photon pulse duration [BDD+14]. Reliable performance of TDS has been validated with installations at various FEL facilities, such as the Linac Coherent Light Source [DBD+09], the Free-electron Laser in Hamburg [RGS+09] and the SPring-8 Angstrom Compact Free Electron Laser [HTT12].

The research presented in this thesis addresses the design and modelling of the online TDS diag-

[2]Detailed high-gain FEL theory has been derived in many textbooks, for example in Refs. [SDR08, SSY00]. A summary of the requirements on the electron beam is referred to Refs. [Beh12, Röh08].

nostic sections for the European X-ray Free-electron Laser (XFEL). The European XFEL is s super-conducting hard X-ray FEL located in Hamburg, Germany, with the commission of the injector section scheduled for the end of 2015. Three TDS diagnostic sections have been designed to fulfil the challenging requirements on the measurements of the various electron beam parameters including the longitudinal profile, the longitudinal phase space, the slice energy spread and the slice emittance.

Super-conducting technology [RST+01] makes it possible for the European XFEL to deliver thousands of electron bunches per second, leading to a high average brilliance of the photon pulses. Therefore it has been especially emphasized in the requirements of the three TDS diagnostic sections that the diagnostic system must be non-destructive to the generation of FEL pulses. Such online diagnostic of the electron beam in parallel to the generation of FEL pulses has seen an increasing demand in the operation of super-conducting FELs, and is highly appreciated by the photon user community. Realization of the online longitudinal diagnostic section with femtosecond resolution requires optimization of its accelerator optics and diagnostic components, and at the same time integration of its lattice into that of the accelerator.

The remainder of this thesis is organised as follows. In Chapters 1 and 2, the principles of transverse emittance and TDS diagnostics are explained, respectively. Chapter 3 presents the design of the online TDS diagnostic sections for the European XFEL, with extensive simulations of the measurement methods and analysis of their performance. In Chapter 4, suppression of coherence effects, which will be encountered in electron beam imaging in TDS diagnostics, is demonstrated with experiments performed at the Linac Coherent Light Source, Palo Alto, USA. Characterization of prototype devices responsible for the successful operation of the TDS diagnostic sections at the European XFEL, as well as realization of an online longitudinal profile diagnostic station at the Free-electron Laser in Hamburg, Germany, are described in Chapter 5. Chapter 6 deals with the performance of the multi-screen and quadrupole scan methods for emittance measurements, which have been investigated experimentally at the SwissFEL Injector Test Facility, Villigen, Switzerland. Following the summary given in Chapter 7, the appendices include the Monte-Carlo method for error analysis on emittance measurement, the optimization procedure for designing the accelerator optics of emittance measurements, the generalized formalism of transition radiation, and the algorithm for image processing.

1 Transverse emittance diagnostic

The emittance of the electron bunch is one of the most important parameters critical to the generation of FEL pulses. Reliable measurement of the emittance is highly demanded to characterize the quality of the electron beam. Furthermore, the actual accelerator optics in the accelerator can be determined alongside the emittance measurement. Deviation of the actual accelerator optics from the design values can lead to degradation of the beam quality as well [Rau00]. When the accelerator optics are measured, the actual values can be matched to the design values.

In this chapter, the basics of the accelerator physics are shortly reviewed, with emphasis on the definitions of emittance and Twiss parameters. The mathematical formalism of the method for measuring emittance is explained, followed by practical realization of the method. In the end, procedures for error analysis of the measurements, which are applied in the subsequent chapters of this thesis, are described.

1.1 Linear beam dynamics and definition of emittance

In this section, the basics of beam dynamics within linear approximation is introduced. The definition and interpretation of emittance and Twiss parameters, which are the main subjects of measurements presented in the subsequent chapters of this thesis, are described. Since the theory has been widely studied and presented in a variety of accelerator physics literature such as Refs. [Wie93, RS93], only the most relevant parameters are outlined. The content of this section is based on Ref. [Wie93], where more detailed derivations can be found.

1.1.1 Single particle motion

In accelerator physics, it is common to describe the motion of each particle using the coordinates along the design trajectory s of a reference particle. The 6-dimensional phase space vector in such a coordinate system is given by

$$\boldsymbol{u} = (x, x', y, y', z, \delta)^T, \tag{1.1}$$

where x and y are the horizontal and vertical distances from the design trajectory s, $x' = dx/ds$ and $y' = dy/ds$ the slopes of the particle trajectory[1], z the distance to the reference particle along the design trajectory s, and $\delta = (p - p_0)/p_0$ the relative deviation of the particle momentum $p = |\boldsymbol{p}|$ from the design momentum of the reference particle $p_0 = |\boldsymbol{p_0}|$.

[1]When the energy stays constant, the transverse momenta can be approximated by $p_x \approx px'$ and $p_y \approx py'$, since the slopes x' and y' are generally very small. It is common to use the slopes instead of the transverse momenta in the phase space.

In order to describe the motion of a particle through the accelerator beamline consisting of linear elements, such as the dipole magnet, the quadrupole magnet and the drift space, it is convenient to treat the individual beamline components separately, since the differential equation of the motion of a particle through the individual components can be established explicitly. The solutions of the equations of motion with linear approximation can be expressed as

$$\underbrace{\begin{pmatrix} x \\ x' \\ y \\ y' \\ z \\ \delta \end{pmatrix}}_{\boldsymbol{u}} = \underbrace{\begin{pmatrix} R_{11} & R_{12} & R_{13} & R_{14} & R_{15} & R_{16} \\ R_{21} & R_{22} & R_{23} & R_{24} & R_{25} & R_{26} \\ R_{31} & R_{32} & R_{33} & R_{34} & R_{35} & R_{36} \\ R_{41} & R_{42} & R_{43} & R_{44} & R_{45} & R_{46} \\ R_{51} & R_{52} & R_{53} & R_{54} & R_{55} & R_{56} \\ R_{61} & R_{62} & R_{63} & R_{64} & R_{65} & R_{66} \end{pmatrix}}_{\mathcal{R}} \cdot \underbrace{\begin{pmatrix} x_0 \\ x'_0 \\ y_0 \\ y'_0 \\ z_0 \\ \delta_0 \end{pmatrix}}_{\boldsymbol{u}_0} . \tag{1.2}$$

The 6-dimensional matrix $\mathcal{R}$ denotes the transfer matrix that characterizes the transportation of the particle phase space vector from the entrance to the exit of a beamline component. When a particle traverses through a beamline consisting of various components, the final phase space vector can be described using the product of the individual transfer matrices as

$$\boldsymbol{u} = \mathcal{R}_n \cdot \mathcal{R}_{n-1} \cdot \ldots \cdot \mathcal{R}_1 \cdot \boldsymbol{u}_0, \tag{1.3}$$

where $\boldsymbol{u_0}$ and $\boldsymbol{u}$ describe the phase space vectors of the particle at the initial position s_0 and the final position s, respectively, and $\mathcal{R}_1, \mathcal{R}_2, \ldots \mathcal{R}_n$ denotes the transfer matrix of the individual components in the sequence from s_0 to s.

In the following treatment, decoupled motion in the transverse planes is assumed. The transfer matrix of a beamline consisting of decoupled components simplifies to

$$\mathcal{R}_{\text{decoupled}} = \begin{pmatrix} R_{11} & R_{12} & 0 & 0 & 0 & R_{16} \\ R_{21} & R_{22} & 0 & 0 & 0 & R_{26} \\ 0 & 0 & R_{33} & R_{34} & 0 & R_{36} \\ 0 & 0 & R_{43} & R_{44} & 0 & R_{46} \\ R_{51} & R_{52} & R_{53} & R_{54} & R_{55} & R_{56} \\ 0 & 0 & 0 & 0 & 0 & R_{66} \end{pmatrix} . \tag{1.4}$$

A breakdown of the individual transfer matrices for the various components can be found in Ref. [Cha93].

1.1.2 Twiss parameters

An analytical solution of the decoupled equations of motion for an entire beamline is of particular interest, as it will reveal the characteristics of the particle trajectory. Using the ansatz $q(s) = \sqrt{\varepsilon}\sqrt{\beta(s)} \cdot \cos(\psi(s) - \psi_0)$ (q stands for one of the transverse coordinate x or y) into the (decoupled, linear) equations of motions leads to:

$$\gamma(s)q(s)^2 + 2\alpha(s)q(s)q'(s) + \beta(s)q'(s)^2 = \varepsilon, \tag{1.5}$$

with the abbreviations α and γ defined as

$$\alpha(s) = -\frac{1}{2}\beta'(s), \quad \gamma(s) = (1 + \alpha(s)^2)/\beta(s). \tag{1.6}$$

The three parameters β, α and γ are called *Twiss parameters*[2]. Equation 1.5 reveals that at a specific s, the single particle moves along an ellipse with an area of $\pi\varepsilon$ in the phase space (q, q'). The area of the ellipse, sometimes referred to as the Courant-Snyder invariant [CS58], remains constant, while the shape of the ellipse changes along s. The definition and meaning of the constant ε will be introduced in the following section.

The *phase function* $\psi(s)$ fulfils

$$\psi(s) = \int_0^s \frac{d\bar{s}}{\beta(\bar{s})} + \psi_0, \tag{1.7}$$

where ψ_0 is an integral constant. More often the *phase advance* is of interest as defined below

$$\mu = \int_{s_0}^s \frac{d\bar{s}}{\beta(\bar{s})}. \tag{1.8}$$

The matrix elements in the transverse plane of a transfer matrix from s_0 to s can be expressed by the Twiss parameters and phase advance as well. For example, the matrix elements in the horizontal plane (x, x') are equivalent to

$$\begin{pmatrix} R_{11} & R_{12} \\ R_{21} & R_{22} \end{pmatrix} = \begin{pmatrix} \sqrt{\frac{\beta_x(s)}{\beta_x(s_0)}}(\cos\mu_x + \alpha_x(s_0)\sin\mu_x) & \sqrt{\beta_x(s)\beta_x(s_0)}\sin\mu_x \\ \frac{\alpha_x(s_0)-\alpha_x(s)}{\sqrt{\beta_x(s)\beta_x(s_0)}}\cos\mu_x - \frac{1+\alpha_x(s)\alpha_x(s_0)}{\sqrt{\beta_x(s)\beta_x(s_0)}}\sin\mu_x & \sqrt{\frac{\beta_x(s_0)}{\beta_x(s)}}(\cos\mu_x - \alpha_x(s)\sin\mu_x) \end{pmatrix} \tag{1.9}$$

1.1.3 Particle beams and definition of emittance

Now we consider a particle beam containing a distribution of particles. Equation 1.5 implies that compared to a set of particles moving on the edge of a phase space ellipse with an area of $\pi\varepsilon$, all particles with a smaller beta-function $\beta(s)$ move on ellipses with areas smaller than $\pi\varepsilon$, and are enclosed in the phase space ellipse of this set. The parameter ε of the ellipse is termed *emittance*. The phase space distribution of particle beams can be expressed with the help of the *beam matrix* $\boldsymbol{\sigma}$ by

$$\boldsymbol{u}^T\boldsymbol{\sigma}^{-1}\boldsymbol{u} = 1. \tag{1.10}$$

[2] In this thesis, the term *Twiss parameter* is used to describe all three parameters at the same time. When the individual parameter is mentioned, the terms *beta-*, *alpha-* and *gamma-function* are used.

The transformation of the beam matrix $\boldsymbol{\sigma}_0$ from a position s_0 to the beam matrix $\boldsymbol{\sigma}$ at a position s can be derived from Eq. 1.10 using the relation in Eq. 1.2 as

$$\boldsymbol{\sigma} = \mathcal{R}\boldsymbol{\sigma}_0\mathcal{R}^T. \tag{1.11}$$

For a two-dimensional phase space vector (q, q') with a two-dimensional beam matrix $\boldsymbol{\sigma}_{2D}$, Eq. 1.10 leads to

$$\sigma_{22}q^2 - 2\sigma_{12}qq' + \sigma_{11}q'^2 = \det(\boldsymbol{\sigma}_{2D}), \tag{1.12}$$

where the relation $\sigma_{12} = \sigma_{21}$ is used. Comparing the coefficients in Eq. 1.12 with Eq. 1.5, the beam matrix can be determined as

$$\boldsymbol{\sigma}_{2D} = \varepsilon\begin{pmatrix} \beta & -\alpha \\ -\alpha & \gamma \end{pmatrix}, \quad \varepsilon = \sqrt{\det(\boldsymbol{\sigma}_{2D})} = \sqrt{\sigma_{11}\sigma_{22} - \sigma_{12}^2}. \tag{1.13}$$

In analogy, the 6-dimensional phase space ellipsoid has an emittance of $\varepsilon = \sqrt{\det(\boldsymbol{\sigma}_{6D})}$.

The emittance describes the area (or volume) of the phase space ellipse (or ellipsoid) containing a certain fraction of particles of the beams. The choice of the fraction is arbitrary and is commonly defined using the statistical definitions[3]

$$\boldsymbol{\sigma} = \begin{pmatrix} \langle x^2\rangle & \langle xx'\rangle & \langle xy\rangle & \langle xy'\rangle & \langle xz\rangle & \langle x\delta\rangle \\ \langle xx'\rangle & \langle x'^2\rangle & \langle x'y\rangle & \langle x'y'\rangle & \langle x'z\rangle & \langle x'\delta\rangle \\ \langle xy\rangle & \langle x'y\rangle & \langle y^2\rangle & \langle yy'\rangle & \langle yz\rangle & \langle y\delta\rangle \\ \langle xy'\rangle & \langle x'y'\rangle & \langle yy'\rangle & \langle y'^2\rangle & \langle y'z\rangle & \langle y'\delta\rangle \\ \langle xz\rangle & \langle x'z\rangle & \langle yz\rangle & \langle y'z\rangle & \langle z^2\rangle & \langle z\delta\rangle \\ \langle x\delta\rangle & \langle x'\delta\rangle & \langle y\delta\rangle & \langle y'\delta\rangle & \langle z\delta\rangle & \langle \delta^2\rangle \end{pmatrix} = \begin{pmatrix} \boldsymbol{\sigma}_{xx} & \boldsymbol{\sigma}_{xy} & \boldsymbol{\sigma}_{xz} \\ {\boldsymbol{\sigma}_{xy}}^T & \boldsymbol{\sigma}_{yy} & \boldsymbol{\sigma}_{yz} \\ {\boldsymbol{\sigma}_{xz}}^T & {\boldsymbol{\sigma}_{yz}}^T & \boldsymbol{\sigma}_{zz} \end{pmatrix}, \tag{1.14}$$

which describes the fraction of particles within one root-mean-square (rms) distance of the particle beams. The parameter $\varepsilon = \sqrt{\det\boldsymbol{\sigma}_{qq}} = \sqrt{\langle q^2\rangle\langle q'^2\rangle - \langle qq'\rangle^2}$ is called the *rms projected emittance* (onto the transverse planes), with $\langle q^2\rangle$ the projected squared rms beam size. If the particle beams are coupled in the transverse planes, i.e. $\boldsymbol{\sigma}_{xy} \neq 0$, the *intrinsic emittance* instead of projected emittance is required to fully describe the transverse phase space of the beam. A detailed definition of the intrinsic emittance and the method for measurement can be found in Ref. [Kub99].

In case of acceleration, it is convenient to introduce the *normalized emittance*

$$\varepsilon_N = \beta\gamma\varepsilon \tag{1.15}$$

with $\gamma = 1/\sqrt{1-\beta^2}$ the Lorentz-factor and $\beta = v/c$. The normalized emittance is invariant in the ideal situation of absent statistical processes[4].

In this thesis, the beam matrix is always used with the statistical (rms) definition, while the term "emittance" refers to the normalized rms emittance, unless otherwise stated. The quantity of interest

[3] The bracket $\langle \ldots \rangle$ is the operator for the statistical mean of the variables inside the bracket.
[4] Statistical processes refer to emission of synchrotron radiation of the particles or collisions with other particles [Wie93].

is the rms projected emmitance, which constitutes the subject of experimental measurements and further discussions in the subsequent chapters.

1.2 Method for emittance measurement

In order to determine the projected emittance ε, the quantities $\langle q^2\rangle, \langle qq'\rangle$ and $\langle q'^2\rangle$ have to be known. However, only the squared rms beam size $\langle q^2\rangle$ can be observed with direct methods (see Section 1.2.2). Applying the transfer matrix $\mathcal{R}_{\text{decoupled}}$ (see Eq. 1.4) from a decoupled beamline to Eq. 1.11, the beam matrix element σ_{11} can be expressed with

$$\langle x^2\rangle = \sigma_{11} = R_{11}^2\langle x_0^2\rangle + 2R_{11}R_{12}\langle x_0x_0'\rangle + R_{12}^2\langle x_0'^2\rangle + 2R_{11}R_{16}\langle x_0\delta_0\rangle + 2R_{12}R_{16}\langle x_0'\delta_0\rangle + R_{16}^2\langle \delta_0^2\rangle. \quad (1.16)$$

It can be seen that the squared beam size $\langle x^2\rangle$ at s is a linear combination of six beam matrix elements at the initial position s_0. By establishing 6 linear and independent equations with various $\mathcal{R}^{(i)}$, the 6 initial beam matrix elements can be uniquely determined, from which the projected emittance $\varepsilon = \sqrt{\langle x_0^2\rangle\langle x_0'^2\rangle - \langle x_0x_0'\rangle}$ can be obtained. The same procedure can be applied similarly for the vertical plane y.

If a transfer matrix with vanishing R_{16} is used, Eq. 1.16 simplifies to

$$\langle x^2\rangle = R_{11}^2\langle x_0^2\rangle + 2R_{11}R_{12}\langle x_0x_0'\rangle + R_{12}^2\langle x_0'^2\rangle. \quad (1.17)$$

Then only three measurements are enough to solve for the three initial beam matrix elements required to calculate the emittance. In the following, the simple case of $R_{16} = 0$ is treated.

1.2.1 Linear least square method

In practice, measurements of the squared beam size $\langle x^2\rangle$ are subject to errors. Increasing the number of measurements improves generally the accuracy of beam matrix estimation. When more than three measurements are available, the beam matrix elements can be obtained using the linear least square method. Detailed description of the linear least square method in emittance measurement can be found in Refs. [MZ03, Löh05].

The equations for the $n(n > 3)$ beam size measurements can be summarized into a linear equation system

$$\underbrace{\begin{pmatrix} \langle {x^{(1)}}^2\rangle \\ \langle {x^{(2)}}^2\rangle \\ \vdots \\ \langle {x^{(n)}}^2\rangle \end{pmatrix}}_{\boldsymbol{B}} = \underbrace{\begin{pmatrix} {R_{11}^{(1)}}^2 & 2R_{11}^{(1)}R_{12}^{(1)} & {R_{12}^{(1)}}^2 \\ {R_{11}^{(2)}}^2 & 2R_{11}^{(2)}R_{12}^{(2)} & {R_{12}^{(2)}}^2 \\ \vdots & \vdots & \vdots \\ {R_{11}^{(n)}}^2 & 2R_{11}^{(n)}R_{12}^{(n)} & {R_{12}^{(n)}}^2 \end{pmatrix}}_{\boldsymbol{A}} \cdot \underbrace{\begin{pmatrix} \langle x_0^2\rangle \\ \langle x_0x_0'\rangle \\ \langle x_0'^2\rangle \end{pmatrix}}_{\boldsymbol{o}} + \underbrace{\begin{pmatrix} \delta^{(1)} \\ \delta^{(2)} \\ \vdots \\ \delta^{(n)} \end{pmatrix}}_{\boldsymbol{\delta}}, \quad (1.18)$$

with $\boldsymbol{o}$ containing the beam matrix elements at the initial position s_0, $\boldsymbol{A}$ the elements of the transfer matrices from s_0 to s, and $\boldsymbol{B}$ the squared beam sizes of the n measurements. Each measurement of

$\langle x^{(i)2} \rangle$ is assumed with an uncorrelated error $\delta^{(i)}$ underlying a Gaussian distribution according to $\delta^{(i)} \sim \mathcal{N}(0, \Delta^{(i)\,2}_{\langle x^2 \rangle})$[5].

With the introduction of the following notations

$$\boldsymbol{a} = \begin{pmatrix} \frac{R_{11}^{(1)2}}{\Delta^{(1)}_{\langle x^2 \rangle}} & \frac{2R_{11}^{(1)}R_{12}^{(1)}}{\Delta^{(1)}_{\langle x^2 \rangle}} & \frac{R_{12}^{(1)2}}{\Delta^{(1)}_{\langle x^2 \rangle}} \\ \frac{R_{11}^{(2)2}}{\Delta^{(2)}_{\langle x^2 \rangle}} & \frac{2R_{11}^{(2)}R_{12}^{(2)}}{\Delta^{(2)}_{\langle x^2 \rangle}} & \frac{R_{12}^{(2)2}}{\Delta^{(2)}_{\langle x^2 \rangle}} \\ \vdots & \vdots & \vdots \\ \frac{R_{11}^{(n)2}}{\Delta^{(n)}_{\langle x^2 \rangle}} & \frac{2R_{11}^{(n)}R_{12}^{(n)}}{\Delta^{(n)}_{\langle x^2 \rangle}} & \frac{R_{12}^{(n)2}}{\Delta^{(n)}_{\langle x^2 \rangle}} \end{pmatrix}, \quad \boldsymbol{b} = \begin{pmatrix} \frac{\langle x^{(1)2} \rangle}{\Delta^{(1)}_{\langle x^2 \rangle}} \\ \frac{\langle x^{(2)2} \rangle}{\Delta^{(2)}_{\langle x^2 \rangle}} \\ \vdots \\ \frac{\langle x^{(n)2} \rangle}{\Delta^{(n)}_{\langle x^2 \rangle}} \end{pmatrix}, \tag{1.19}$$

the weighted linear least square method gives the estimation of $\boldsymbol{o}$ and its covariance matrix $\Sigma_{\boldsymbol{o}}$ as

$$\boldsymbol{o} = (\boldsymbol{a}^T \boldsymbol{a})^{-1} \boldsymbol{a}^T \boldsymbol{b}, \tag{1.20}$$

$$\Sigma_{\boldsymbol{o}} = (\boldsymbol{a}^T \boldsymbol{a})^{-1}. \tag{1.21}$$

It should be noted here that the covariance matrix $\Sigma_{\boldsymbol{o}}$ is *not* a diagonal matrix, and the non-vanishing off-diagonal matrix elements indicate a correlation between o_1, o_2 and o_3. The emittance ε as well as the Twiss parameters β_0, α_0 at the initial position s_0 can be then derived via

$$\varepsilon = \sqrt{o_1 o_3 - o_2^2}, \tag{1.22}$$

$$\alpha_0 = -o_2 / \sqrt{o_1 o_3 - o_2^2}, \tag{1.23}$$

$$\beta_0 = o_1 / \sqrt{o_1 o_3 - o_2^2}. \tag{1.24}$$

Mismatch parameter

The beam usually has Twiss parameters which are different from the design values $\beta_D, \alpha_D, \gamma_D$, leading to a mismatch between the actual and design shape of the beam ellipse. To understand the degree of the mismatch, it is useful to introduce the *mismatch parameter* [MZ03]

$$M = \frac{1}{2}(\beta \gamma_D - 2\alpha \alpha_D + \gamma \beta_D), \tag{1.25}$$

where the subscripts D denotes the design values. The mismatch parameter equals to 1, if and only if the Twiss parameters are identical to the design values.

In the normalized coordinate $(\tilde{q}, \tilde{q}')$, which is defined as

$$(\tilde{q}, \tilde{q}') = \left(\frac{q}{\sqrt{\beta_D}}, \frac{q\alpha_D + q'\beta_D}{\sqrt{\beta_D}}\right), \tag{1.26}$$

[5] The notation of $\mathcal{N}$ means that the probability distribution of the error is a Gaussian (normal) distribution centred at 0 and with standard deviation of $\Delta^{(i)}_{\langle x^2 \rangle}$.

the phase space area of a matched beam with $M = 1$ appears to be a circle with an area of $\pi\varepsilon$. The mismatched beam has the same area of $\pi\varepsilon$, but in a shape of a rotated ellipse, whose semi-major axis has a length of $\sqrt{\varepsilon\widetilde{M}}$ with $\widetilde{M} = M + \sqrt{M^2 - 1}$[6]. A graphical interpretation of the design and mismatched phase space ellipse in the normalized coordinates is illustrated in Fig. 1.1.

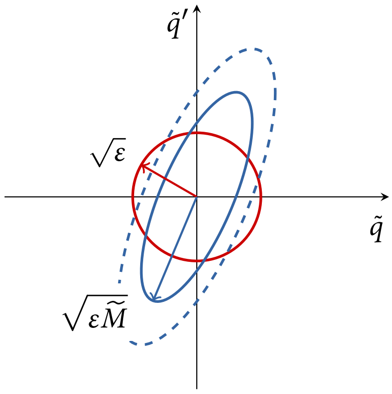

Figure 1.1: Phase space ellipse in the normalized coordinates $(\tilde{q}, \tilde{q}')$: (red solid) for a design beam with $M = 1$ and emittance of ε, (blue solid) for a mismatched beam with $M > 1$ and emittance of ε, (blue dashed) for a mismatched beam with the same mismatch parameter as that for the blue solid ellipse but with emittance larger than ε.

1.2.2 Realization of the method

As described in Section 1.2.1, the Twiss parameters β_0, α_0 and the emittance ε at an initial position s_0 can be reconstructed by measuring the beam sizes at downstream positions with various transfer matrices $\mathcal{R}^{(i)}$.

Typical devices for beam size measurement of high-energy electron beams are imaging screen systems and wire scanners. A wire scanner measures the one-dimensional beam profile integrated from multiple beam shots [HBC+08, RBH+92], while a screen system provides directly the two-dimensional projected transverse distribution of the beam with single-shot capability. Both devices are destructive to the beam. In recent developments, the critical problem of coherence effects in the emission process of radiation from the screens has been overcome (see Section 4.1.1), and the spatial resolution has been dramatically improved (see Section 4.3.1) to be competitive with that of the wire scanners, which stimulates the implementation of screen systems as electron beam profile diagnostics.

Variation of the transfer matrix can be achieved by changing the strength of the quadrupole field between the initial position s_0 and a fixed measurement location s, or by changing the locations s of the measurements without modifying the quadrupole settings. Changing the transfer matrix by employing single quadrupole or multiple quadrupoles at the same time is called the *quadrupole scan method*, whereas measuring the beam sizes at multiple locations is given the name *multi-screen (wire-scanners) method*. The two methods can be combined together in real applications.

[6] $\widetilde{M}$ is denoted as mismatch parameter in some literature, such as Ref. [San91].

Emittance and Twiss parameter measurements can be performed flexibly at any location using the quadrupole scan method with many available quadrupoles along the beam lines. The number of measurement steps i is defined by the change steps of the quadrupole field strengths, and can be chosen within a wide range. Since the accelerator optics between the initial position s_0 and the measurement locations s are actively modified, the change introduced for the measurement should be compensated, in case the electron beam is needed at a further location downstream of the measurement point s.

The multi-screen method is limited by the number of measurement steps n due to the constricting number of screens, which requires dedicated space in the accelerator beamline. One advantage of the multi-screen method is that it does not affect the transportation and beam dynamics of the electron beam to the downstream locations due to the fixed accelerator optics. This feature makes it a good candidate as a non-destructive method[7] for emittance measurement.

In practice, the Twiss parameters β_D, α_D at the initial position s_0 and the transfer matrices $\mathcal{R}^{(i)}$ used for the measurement are carefully designed. By assigning the designed $\mathcal{R}^{(i)}$ to the beamline and measuring the corresponding squared beam sizes $\langle {x^{(i)}}^2 \rangle$ at s, the emittance ε is reconstructed, and the calculated β_0, α_0 at the initial position s_0 are compared to the design values β_D, α_D. When a mismatch between the calculated and design values exists, accelerator optics upstream of the initial position s_0 can be adjusted (for example by utilizing the quadrupoles upstream of s_0) to match β_0, α_0 to β_D, α_D. Several iterations of such matching procedures might be needed to achieve a matched beam.

1.3 Error analysis

Measurement of emittance and Twiss parameters involves various beamline components, and can be sensitive to various sources of error. A robust and reliable measurement requires careful design with extensive error analysis. In this section, procedures for estimating the statistical and systematic errors are described. Different methods for analysing the statistical errors are investigated and compared with each other.

1.3.1 Statistical errors

First we concentrate on the statistical error, which describes the distribution of how much the estimated emittance and Twiss parameters deviate from their true values due to statistical beam size measurement noise $\delta^{(i)} \sim \mathcal{N}(0, {\Delta^{(i)}_{\langle x^2 \rangle}}^2)$. Since the parameter $\boldsymbol{o}$ estimated by the linear least square method (see Eq. 1.20) is a linear transform of the measured beam size, the error of $\boldsymbol{o}$ is then given by the same linear transform applied to the measurement noise. As a result, assuming a Gaussian measurement noise, the error on $\boldsymbol{o}$ also follows a Gaussian distribution with covariance $\Sigma_{\boldsymbol{o}}$ given in Eq. 1.21.

[7] Although the electron beam cannot be used for the generation of FEL pulses when it hits the screen, implementation of off-axis screens and fast kicker magnets can be considered effectively as non-destructive method in pulse-stealing mode (see Section 3.2.1).

Analysis of the error of the emittance and the Twiss parameters is more complicated since they are all non-linear functions of o_1, o_2 and o_3, which means their error distributions can no longer be captured in an analytical form. In the following sections, two different methods for estimating the statistical errors of the emittance and Twiss parameters will be introduced. The first method, called error propagation, makes a linear approximation to obtain an analytical expression of the error distribution; the second method, called direct sampling, retains the non-linearity of the expressions but have to resort to sampling methods to obtain the error distribution.

Error propagation with linear approximation

As derived in Eq. 1.22,1.23 and 1.24, the desired emittance and Twiss parameters are non-linear functions $f(o_1, o_2, o_3)$ of the solved elements of $\boldsymbol{o}$. Error propagation (termed EP) replaces the non-linear functions $f(o_1, o_2, o_3)$ with their linear approximations $f \approx f^0 + \frac{\partial f}{\partial o_1} o_1 + \frac{\partial f}{\partial o_2} o_2 + \frac{\partial f}{\partial o_3} o_3$. As a result, the errors on the emittance and Twiss parameters become a linear transform of o_1, o_2, o_3, and therefore also follows a Gaussian distribution with its standard deviation σ_{EP} given by:

$$(\sigma_{EP})^2 = \begin{pmatrix} \frac{\partial f}{\partial o_1} & \frac{\partial f}{\partial o_2} & \frac{\partial f}{\partial o_3} \end{pmatrix} \cdot \Sigma_{\boldsymbol{o}} \cdot \begin{pmatrix} \frac{\partial f}{\partial o_1} \\ \frac{\partial f}{\partial o_2} \\ \frac{\partial f}{\partial o_3} \end{pmatrix}, \tag{1.27}$$

where $\Sigma_{\boldsymbol{o}}$ is defined in Eq. 1.21.

Error propagation method using linear approximation is very convenient since it can be determined analytically. The error distributions obtained for the emittance and Twiss parameters follow a Gausssian distribution and can be characterized by its standard deviation σ_{EP}.

Monte-Carlo: sampling of the squared beam size

Monte Carlo simulation (termed MC) can be used to avoid making the linear approximation as used in the error propagation method. The exact distributions of the errors on the emittance and Twiss parameters can be obtained.

Since the measurements of $\langle x^{(i)^2} \rangle$ have uncorrelated Gaussian distributed errors (see Eq. 1.18), direct sampling of the squared beam size $\langle x^{(i)^2} \rangle$ is easy. From each sampled $\langle x^{(i)^2} \rangle$, $\boldsymbol{o}$ can be solved via Eq. 1.20, and the emittance as a non-linear function of $\boldsymbol{o}$ can be determined. Repeated sampling of $\langle x^{(i)^2} \rangle$ yields the probability distribution $\mathcal{P}(\varepsilon)_{MC}$ of the reconstructed emittance, from which the mean values $\bar{\varepsilon}$ and standard deviation $\sigma_{\varepsilon,MC}$ can be derived. The same procedure applies to the estimation of the error distribution of the Twiss parameters.

One alternative Monte-Carlo method is to sample $\boldsymbol{o}$ and then pass the sample through the non-linear functions to obtain the emittance and Twiss parameters. Sampling of $\boldsymbol{o}$ is, however, not directly possible due to the correlations between the variables o_1, o_2 and o_3. One method to sample from such a correlated multivariate Gaussian distribution is described in Appendix A using Cholesky decomposition.

Comparison of the two methods

The different methods for estimating statistical errors have been investigated using the design matrix $\boldsymbol{A}$ and the design Twiss parameters β_D, α_D taken from Section 3.3.1 and assuming an input normalized emittance $\varepsilon_N = 1\,\mu\text{m}$ and input energy $E_0 = 700\,\text{MeV}$. The relative standard deviation of the error distribution of the emittance is determined with error propagation (denoted as $\sigma_{\varepsilon,EP}/\varepsilon_N$) and Monte-Carlo simulation with direct sampling of $\langle x^{(i)^2} \rangle$ (denoted as $\sigma_{\varepsilon,MC}/\bar{\varepsilon}_{MC}$).

The probability distributions of ε from the Monte-Carlo simulation and the relative standard deviations are presented in Fig. 1.2. When the initial Twiss parameters α_0, β_0 are matched to the design values (top row for $M = 1$), the probability distribution of the reconstructed emittance ε has a Gaussian shape centring at the input reference value ε_N. The relative standard deviations determined with the two methods are identical.

In the case of a mismatch parameter of 2 (see Fig. 1.2 middle row), the errors differ largely for different initial Twiss parameters in spite of the same value of mismatch. Therefore it is not sufficient to study how the errors vary with the mismatch parameter M only. For case A with $M_A = 2$, the probability distribution is still symmetric and the relative standard deviations are identical. The expected value of emittance $\bar{\varepsilon}_{MC}$ is slightly underestimated to be 98.3% of ε_N. In the case of B with $M_B = 2$, Twiss parameters different from those of case A but with the same mismatch parameter have been chosen. A slightly asymmetric probability distribution is observed. The relative standard deviations are by a factor of ~ 2 larger than those for case A with $M_A = 2$. In contrary to case A with $M_A = 2$, the relative standard deviation determined from Monte-Carlo simulation is slightly larger than that from error propagation. The expected emittance $\bar{\varepsilon}_{MC}$ is 97.7% of ε_N.

The relative standard deviations increase significantly with mismatch parameters of 3 (see Fig. 1.2 bottom row). In the case of A with $M_A = 3$, the asymmetry of the probability distribution becomes more pronounced, with a long tail towards the smaller values of emittance. Although the expected value $\bar{\varepsilon}_{MC}$ is 96.9% of ε_N, the relative standard deviations determined from the two methods are identical. Deviation between the two methods becomes more distinct in the case B with $M_B = 3$, where the relative standard deviations obtained with the error propagation method is by a factor of 36% larger than that from Monte-Carlo simulation. The expected emittance is slightly overestimated to be 103.9% of ε_N.

In the three cases of observing asymmetric probability distributions (case B with $M_B = 2$, case A with $M_A = 3$ and case B with $M_B = 3$), the percentage of successful reconstructions of emittance with real values are less than 100%, and amount to 99.9%, 94.7% and 85.3%, respectively. With larger mismatch parameter, more failure in the reconstruction of emittance is expected.

The comparison has shown that when the linear approximation with the Taylor series is not accurate enough, the probability distribution deviates from Gaussian shape. In such cases, the error propagation method cannot correctly describe the standard deviation of the distribution. Significant differences in the probability distributions have been observed in the cases of different Twiss parameters, even when their corresponding mismatch parameters are identical. It indicates that it is not sufficient to compute the errors with respect to the mismatch parameter only.

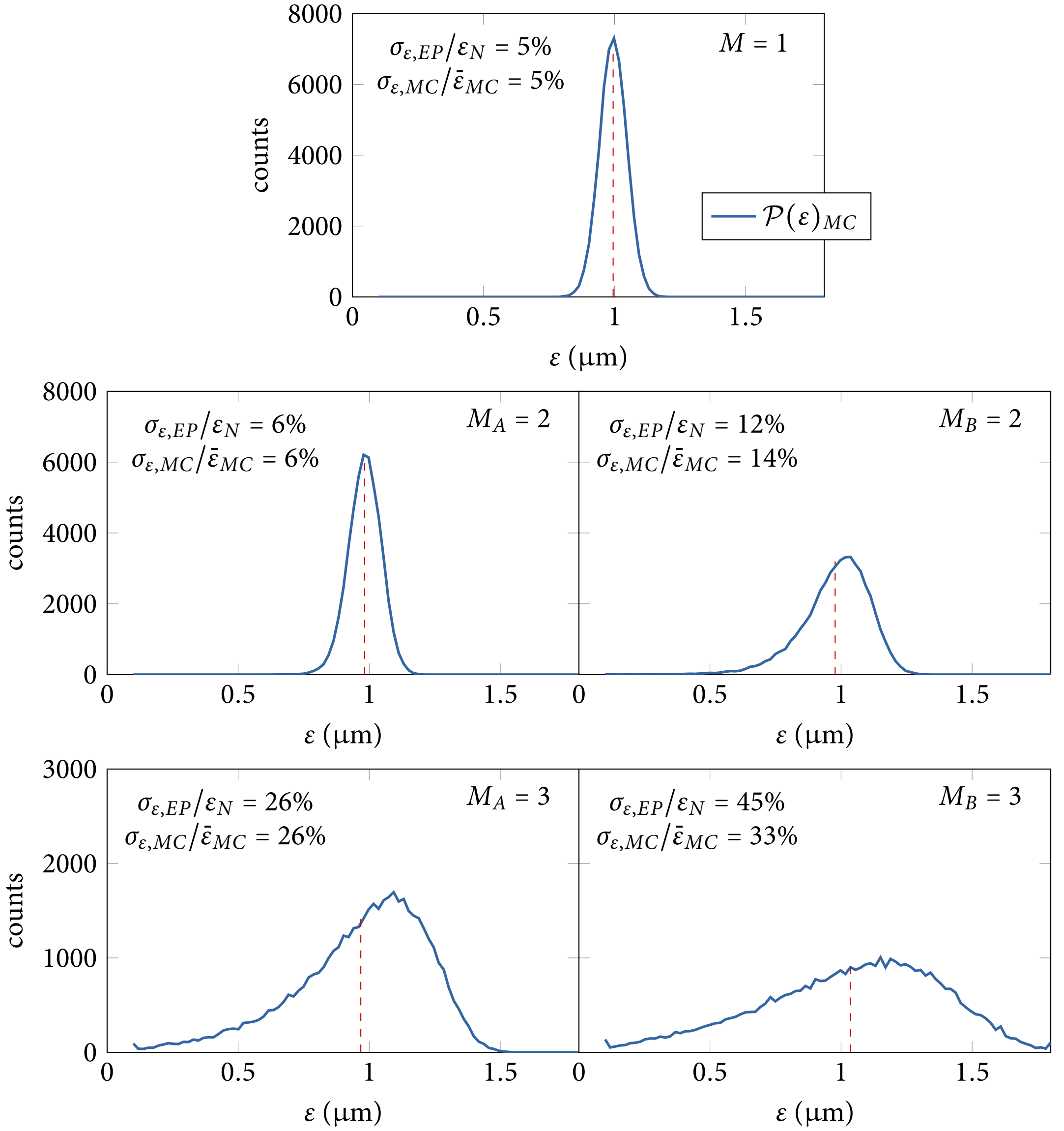

Figure 1.2: Comparison of the statistical error of the reconstructed emittance ε estimated with different methods. The blue lines represent the probability distribution $\mathcal{P}(\varepsilon)_{MC}$ of ε obtained with Monte-Carlo simulation using direct sampling of $\langle x^{(i)^2}\rangle$. In each of the Monte-Carlo simulations, 50000 samples have been drawn. The input beam energy is E_0 = 700 MeV and the normalized input emittance ε_N = 1 µm. The errors of $\langle x^{(i)^2}\rangle$ are assumed to be uncorrelated and follow a Gaussian distribution with $\Delta^{(i)}_{\langle x^2\rangle} = 10\%\langle x^{(i)^2}\rangle$[8]. Five different combinations of α_0, β_0 with mismatch parameters of $M = 1, 2, 3$ are considered. The (red dashed) vertical lines around ε = 1 µm in each plot denote the mean values $\bar{\varepsilon}_{MC}$ of $\mathcal{P}(\varepsilon)_{MC}$. The counts of imaginary values obtained for ε (failed reconstruction of emittance) are excluded from the results.

The advantage of the error propagation method is the analytical solution. The Monte-Carlo simu-

[8]Commonly, the measured rms beam size $\sqrt{\langle x^{(i)^2}\rangle}$ has a relative error of 5%, which equals to approximately a relative error of 10% for $\langle x^{(i)^2}\rangle$.

lation provides a better insight into the probability distribution of emittance, but has to be computed for each individual measurement. In this thesis, statistical errors determined with both methods are used, and explicitly labelled when encountered.

1.3.2 Systematic errors

Emittance estimation using the linear least square method is influenced by systematic errors as well. Among the various systematic errors, the most important and relevant sources of error are listed here and will be analysed and discussed in more details in Chapters 3 and 6.

- **System for beam size measurement** The beam sizes can be measured for example with imaging screens and wire scanners. Errors in the calibration and resolution of the systems lead to systematic errors in the beam size measurement. When screens are employed, the beam size measurements could be additionally influenced by coherent emission of the electron beam (see Section 4.1.1).
- **Dispersion** When the measurement is performed with transfer matrices with non-vanishing R_{16}, the model in Eq. 1.16 should be applied. In case of small R_{16} and negligible correlation terms, the model of assuming $R_{16} = 0$ can be applied by treating the influence of the dispersion as perturbation to the beam size measurement.
- **Quadrupole** Calibration errors of the quadrupole field strengths in the beam lattice result in uncertainties in the field strengths of the quadrupoles, which then lead to an erroneous transfer matrix $\mathcal{R}^{(i)}$.
- **Beam energy** Errors in the beam energy translate into errors in the calculation of the quadrupole field strengths, resulting in an erroneous transfer matrix $\mathcal{R}^{(i)}$ as well. Furthermore, errors in the beam energy affect the normalization of the emittance according to Eq. 1.15.

In Chapter 3 and 6, the systematic errors are investigated using analytical method as well as Monte-Carlo simulations, and are described individually for the specific cases.

2 Time-resolved diagnostic with TDS

High-gain FELs put demanding requirements on the driving electron bunches. As mentioned in the Introduction, high-brightness beams with high peak current, small transverse emittance and small energy spread are desired [SDR08, SSY00, Beh12]. While the overall beam parameters of the whole bunch are of importance, investigation into the evolution of the beam properties along the bunch reveals more insightful information. The longitudinal slices of the bunch can have pronounced variation in the beam parameters and thus make immensely different contribution to the generation of FEL pulses in the undulators. Therefore, time-resolved diagnostics providing access to the slice parameters is an important tool for optimizing the operation of the FELs.

Transverse deflecting structure (TDS) is one of the most robust devices among the various methods for time-resolved electron beam diagnostics, such as the electro-optics (EO) method [Ste07, YMG+00] and coherent radiation spectroscopy [Wes12, MBD+13] (when applying reconstruction technique from the frequency to the time-domain). Single-shot measurement, which allows the investigation of shot-to-shot fluctuation of the bunches, can be realized by the TDS (in the case of the bunch having no initial correlations, see Section 2.2.1) as well as the EO and coherent radiation spectroscopy method. The TDS can be applied to measure electron bunches with bunch length in a large dynamic range, from several picoseconds down to a few femtoseconds [BDD+14]. Whereas the EO and coherent radiation methods provide only the longitudinal current profile, TDS excels by allowing a variety of other beam parameters to be measured, including the slice energy spread, the longitudinal phase space and the slice emittance, when in combined use with other devices. Lately, the application of TDS has been successfully extended to the measurement of the temporal profile of FEL photon pulses [BDD+14].

Compared to other time-resolved electron beam diagnostics, TDS has the drawback of being a destructive device. The electron bunch that is used for measurements with TDS has dramatically degraded beam parameters and is not capable of generating FEL pulses. However, dispensing several bunches for diagnostic purposes per second is non-detrimental to a high-repetition rate superconducting FEL (e.g. FLASH and the European XFEL, see Section 5.3), which delivers thousands of electron bunches per second for the generation of FEL pulses.

As a promising and robust diagnostic tool, TDS is installed and planned at various FEL facilities, such as LCLS [EFK00, KDD+13], SwissFEL [CIL+13], SACLA [MEK+12], as well as FLASH (see Section 5.2) and the European XFEL (see Section 3.2). In this chapter, the beam dynamics of electrons travelling through a TDS is discussed with derivation of the transfer matrix of a TDS. Following that, some example applications of TDS for beam diagnostics are explained.

2.1 Principle of TDS

The idea of transverse deflecting structures was originally proposed for the separation and identification of charged high energy particles in particle physics [Phi61]. Based on the theorem from Panofsky and Wenzel [PW56], suitable RF separator imposing transverse deflecting field to separate particles was developed and investigated at SLAC [ALL64] in the 1960's. Figure 2.1 shows a schematic drawing in cutaway view of the LOLA-type[1] TDS invented at SLAC, which is an iris-loaded RF travelling wave waveguide.

With the invention of FELs, challenging requirements were put on the methods for measuring the short bunch length of relativistic electron bunches. The physics of the RF separators was reviewed in the 1990's, highlighting TDS as a promising tool for the time-resolved diagnostics of electron bunches [EFK00]. Successful applications of the existing LOLA-type structures incorporated at LCLS and FLASH have confirmed the reliable performance of the TDS for longitudinal electron beam diagnostics [Röh08]. Recent success in using the TDS to reconstruct the temporal profile of the FEL pulse has further raised its potentials [BDD+14].

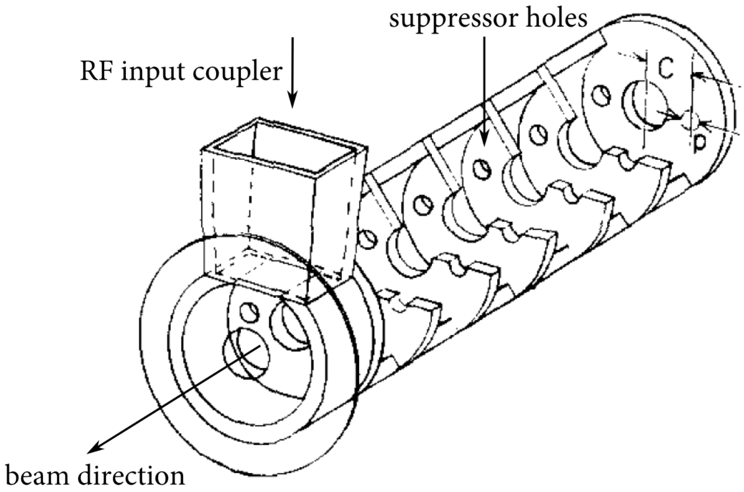

Figure 2.1: Schematic drawing in cutaway view of the LOLA-type TDS invented at SLAC. It is an S-band RF travelling wave structure operated at 2.856 GHz. The inner side cavity and the iris have a radius of 5.895 cm and 2.032 cm, respectively. To avoid possible rotation of the deflecting field, two suppressor holes with a diameter of $\rho = 1.905$ cm are added symmetrically aside each iris at a distance of $C = 3.620$ cm from the centre of the iris to the centre of the suppressor hole. The deflection direction of the illustrated structure is in the vertical plane. Figure adapted from Ref. [ALL64].

The LOLA-type TDS has proven to be a reliable design, and will be adopted at the European XFEL. In the following section, the beam dynamics of a relativistic electron passing through an iris-loaded RF travelling wave TDS is considered. The transformation of the transverse and longitudinal phase space of the particle is derived.

[1] Named after the inventors of the structures: O. H. Altenmueller, R. R. Larsen, and G. A. Loew [ALL64].

2.1.1 Beam dynamics within a TDS

A TDS deflecting in the horizontal direction x with a length of L is studied in the following. The electric and magnetic field distribution inside the structure are discussed and given in Ref. [ALL64]. After transformation from cylindrical to cartesian coordinate (x, y, z), the Lorentz force $\boldsymbol{F}$ experienced by an electron with a charge of e can be calculated:

$$F_x = e\mathcal{E}_0 \sin(\psi), \tag{2.1}$$
$$F_y = 0, \tag{2.2}$$
$$F_z = e\mathcal{E}_0 \cos(\psi) kx. \tag{2.3}$$

ψ is the RF phase relative to the phase with the maximum gradient of the transverse electric field component (i.e. RF zero-crossing). $\mathcal{E}_0$ describes the amplitude of a travelling wave $\mathcal{E}_0 e^{i(kz-\omega t)}$ and k is the wave number of the structure. The transverse force vanishes in the y direction, and remains constant in x independent of the positions in y and z, resulting in an aberration-free deflection in pure x direction. The longitudinal force F_z reduces to zero in the centre of the structure at $x = 0$. However, it increases linearly with the off-axis position x.

Due to the vanishing force in the vertical direction y, only the horizontal motion (x, x') of the particle and its momentum are affected by the TDS, and will be derived in the following. Now a relativistic electron ($|\boldsymbol{v}| \approx c$), travelling in a bunch of electrons, with an initial status of $(x_0, x'_0, z, p)^T$ before injection into the TDS is treated. Here x_0 is its distance from the design trajectory, $x'_0 = dx/ds$ the horizontal slope with respect to the design trajectory s, z the longitudinal distance to the bunch centre and $p = |\boldsymbol{p}|$ the momentum. When the energy stays constant, the slope x' describes the transverse momentum via $p_x \approx px'$ as well. The RF phase will be replaced with $\psi = kz + \psi_0$, where ψ_0 gives the RF phase between the centre of the bunch and the RF zero-crossing. The term kz is negligible, for example: for the LOLA-type TDS at FLASH with $f = 2.856\,\mathrm{GHz}$ and a typical uncompressed bunch length of 300 µm, kz amounts to $2\pi f/c \cdot z \approx 18 \cdot 10^{-3}$. As a result, the cosine and sine of the phase ψ can be approximated by their Taylor series around $kz = 0$ up to the first order: $\sin(kz + \psi_0) \approx kz\cos(\psi_0) + \sin(\psi_0)$ and $\cos(kz + \psi_0) \approx \cos(\psi_0) - kz\sin(\psi_0)$.

At a position s inside the TDS ($s < L$), the particle will undergo an accumulated deflection of

$$\begin{aligned} x'(s) &= x'_0 + \int_0^{p_x(s)} \frac{\mathrm{d}p_x}{p} = x'_0 + \int_0^s \frac{1}{p} F_x \frac{\mathrm{d}s}{c} = x'_0 + \frac{F_x}{pc} s \\ &\approx x'_0 + \frac{e\mathcal{E}_0 (kz\cos(\psi_0) + \sin(\psi_0))}{pc} s. \end{aligned} \tag{2.4}$$

For the purpose of beam diagnostics, a deflection with maximum linear dependence on the longitudinal position z is highly desirable and can be achieved by operating the TDS at the zero-crossings of the RF, which means setting ψ_0 to 0 or π. Therefore, Eq. 2.4 becomes

$$x'(s) = x'_0 \pm \frac{e\mathcal{E}_0 kz}{pc} s, \tag{2.5}$$

with the plus and minus sign corresponding to $\psi_0 = 0$ and π, respectively. In the following, only the situations of operating the TDS at $\psi_0 = 0, \pi$ are considered.

Using Eq. 2.5, the displacement $x(s)$ of the electron at a position s can be formulated as:

$$x(s) = x_0 + \int_0^s x'(s)\mathrm{d}s = x_0 + x_0's \pm \frac{e\mathcal{E}_0kz}{2pc}s^2. \tag{2.6}$$

The non-vanishing longitudinal force at the off-axis positions inside the TDS induces extra change of the momentum of the electron. After travelling the total length L of the TDS, the particle gains an amount of momentum Δp_z in the longitudinal direction (using Eqs. 2.3 and 2.6):

$$\begin{aligned} c\Delta p_z &= \int_0^L F_z\mathrm{d}s = \int_0^L e\mathcal{E}_0k(x_0 + x_0's \pm \frac{e\mathcal{E}_0kz}{2pc}s^2)\mathrm{d}s \\ &= e\mathcal{E}_0k[Lx_0 + \frac{1}{2}L^2x_0' \pm \frac{1}{6}\frac{e\mathcal{E}_0k}{pc}L^3z]. \end{aligned} \tag{2.7}$$

The transverse deflecting force has an effect changing the electron momentum as well. Since the deflecting force F_x is constant over the aperture of the structure (see Eq. 2.1), the resulting momentum change Δp_x of the particle in the transverse plane is given by

$$c\Delta p_x = F_x \cdot x(s = L) = e\mathcal{E}k(zx_0 + zLx_0' \pm \frac{1}{2}\frac{e\mathcal{E}_0k}{pc}L^2z^2), \tag{2.8}$$

where Eq. 2.6 is used. Compared to the longitudinal momentum gain $c\Delta p_z$ in Eq. 2.7, each term in the expression for the transverse momentum gain is much smaller due to the multiplication with z/L (typically $z < 100\,\mu\mathrm{m}$). The total momentum gain Δp induced by the TDS is dominated by the change in the longitudinal direction and can be approximated by $c\Delta p \approx c\Delta p_z$. Using the substitution $K = \frac{eV_0k}{pc}$ with the peak effective voltage defined as $V_0 = \mathcal{E}_0L$, the relative momentum deviation of the particle induced by the TDS can be obtained:

$$\Delta\delta = \frac{c\Delta p}{cp} \approx \frac{c\Delta p_z}{cp} = Kx_0 + \frac{1}{2}KLx_0' \pm \frac{1}{6}K^2Lz. \tag{2.9}$$

The first term describes a momentum gain due to the finite transverse beam size, the second term relates to the initial beam divergence and the last term is induced by the off-axis longitudinal force of the TDS.

Finally, the total displacement and deflection angle at the exit of TDS can be derived from Eqs. 2.6 and 2.5 using the substitution $s = L$, so the final states of the electron are given by:

$$x_{\mathrm{final}} = x_0 + Lx_0' \pm \frac{KL}{2}z, \tag{2.10}$$

$$x'_{\mathrm{final}} = x_0' \pm Kz, \tag{2.11}$$

$$\delta_{\mathrm{final}} = \delta + Kx_0 + \frac{1}{2}KLx_0' \pm \frac{1}{6}K^2Lz, \tag{2.12}$$

where δ describes the initial momentum deviation of a particle with respect to a reference momentum p_0 such that $p = p_0(1+\delta)$. For a relativistic particle with $|v| \approx c$, the particle energy E can be approximated by $E \approx cp$. Therefore, the relative momentum deviation describes the relative energy deviation $\delta \approx (E - E_0)/E_0$ with respect to the design energy E_0 as well.

2.1.2 Transfer matrix of TDS

Equations 2.10, 2.11 and 2.12 reveal that the final state of the particle is a linear combination of the initial status. It is convenient to summarize the beam dynamics of the TDS in matrix formalism (to the first order), yielding

$$\begin{pmatrix} x \\ x' \\ z \\ \delta \end{pmatrix}_{\text{final}} = \underbrace{\begin{pmatrix} 1 & L & \pm\frac{KL}{2} & 0 \\ 0 & 1 & \pm K & 0 \\ 0 & 0 & 1 & 0 \\ K & \frac{KL}{2} & \pm\frac{K^2L}{6} & 1 \end{pmatrix}}_{\mathcal{R}_{\text{TDS}}^{\text{thick}}} \cdot \begin{pmatrix} x_0 \\ x_0' \\ z \\ \delta \end{pmatrix}. \tag{2.13}$$

This transfer matrix of the TDS $\mathcal{R}_{\text{TDS}}^{\text{thick}}$ takes into account the finite length of the structure and is therefore referred to as "thick lens form". An approximation for $L \to 0$ yields the simplified transfer matrix in "thin lens form":

$$\mathcal{R}_{\text{TDS}}^{\text{thin}} = \begin{pmatrix} 1 & 0 & 0 & 0 \\ 0 & 1 & \pm K & 0 \\ 0 & 0 & 1 & 0 \\ K & 0 & 0 & 1 \end{pmatrix}. \tag{2.14}$$

The thin lens form is convenient to be used when only the transverse motion (x, x') is of interest. In thin lens form, a TDS with a total length of L is conceived to be composed of a drift space of $L/2$, an instantaneous deflection of Kz at the centre of the structure, followed by another drift space of $L/2$. The expressions of x and x' for such a thin lens TDS are exactly the same as that for a thick lens TDS as given in Eqs. 2.10 and 2.11.

Since the other transverse plane y is not affected by the TDS, the matrices presented in Eqs. 2.13 and 2.14 can be easily augmented to be

$$\mathcal{R}_{\text{TDS}}^{\text{thick}} = \begin{pmatrix} 1 & L & 0 & 0 & \pm\frac{KL}{2} & 0 \\ 0 & 1 & 0 & 0 & \pm K & 0 \\ 0 & 0 & 1 & L & 0 & 0 \\ 0 & 0 & 0 & 1 & 0 & 0 \\ 0 & 0 & 0 & 0 & 1 & 0 \\ K & \frac{KL}{2} & 0 & 0 & \pm\frac{K^2L}{6} & 1 \end{pmatrix} \text{ and } \mathcal{R}_{\text{TDS}}^{\text{thin}} = \begin{pmatrix} 1 & 0 & 0 & 0 & 0 & 0 \\ 0 & 1 & 0 & 0 & \pm K & 0 \\ 0 & 0 & 1 & 0 & 0 & 0 \\ 0 & 0 & 0 & 1 & 0 & 0 \\ 0 & 0 & 0 & 0 & 1 & 0 \\ K & 0 & 0 & 0 & 0 & 1 \end{pmatrix}. \tag{2.15}$$

The 6-dimensional matrices describe the beam dynamics in both the transverse phase space and the longitudinal phase space, and can be applied to the phase space vector $(x_0, x_0', y_0, y_0', z, \delta)^T$ of the electron. Expressions for a TDS deflecting in the y direction can be derived analogously.

2.2 Diagnostics with TDS

For high-gain FELs, not only the overall beam parameters of the bunch are important to the generation of FEL pulses, the parameters of the slices along the bunch are more decisive. However, the electron bunches for FELs are extremely short (from several femtoseconds to picoseconds) with longitudinal coordinates that are not directly accessible, which puts immense challenges on the highly sought-after longitudinal diagnostics.

According to the transfer matrices derived in Eq. 2.15, a TDS imposes a linear transformation[2] of the longitudinal position of the relativistic particle into one transverse plane. The transverse position, which is easily accessible with simple diagnostic tools, can be measured and translated linearly back to the longitudinal position. With the knowledge of the longitudinal coordinate, the properties of the electrons residing at different positions inside the bunch can be investigated. Therefore, longitudinal diagnostics can be achieved with TDS in combination with transverse diagnostic techniques.

The use of imaging screens, such as optical transition radiation (OTR) and scintillator screens (see Section 4.1), is one of the most easily and widely adopted methods for transverse beam diagnostics. In the case of beam imaging without coherence effects (see Section 4.1.1), which is presumed in the rest of this chapter, the intensity of the image scales linearly with the charge of the particles. By calibrating the spatial magnification of the imaging system, the transverse position of the particles can be determined. With the knowledge of charge and transverse position, the image of an electron bunch can be calibrated to represent the transverse density distribution of the bunch.

When used in combination with other diagnostic components, the TDS provides various longitudinal diagnostics such as measurements of the longitudinal current profile, the longitudinal phase space and the slice emittance. The principles of these diagnostics are described in the following sections.

2.2.1 Longitudinal current profile

High peak current is one of the essential electron bunch properties for high-gain FELs. It is important to measure and control the longitudinal density distribution of the bunch, which then yields the current profile for a given bunch charge. Often the portion within the bunch with high peak current is more likely to contribute to the FEL lasing process than the rest of bunch. Furthermore, the electron bunch length can be deduced from the current profile to give an estimation on the upper limit of the FEL pulse length [BGG+12].

Since only transverse motions are relevant in the measurement of the longitudinal current profile, it is justified to consider a TDS in thin lens form as described in Eq. 2.14: a drift space of $L/2$, an instantaneous horizontal deflection of Kz and another drift space of $L/2$ [Röh08]. Denoting the phase space vector of the particle after the first drift space (i.e. at the centre of the TDS s_0) as $\boldsymbol{u}_{s_0} = (x_{s_0}, x'_{s_0}, y_{s_0}, y'_{s_0}, z, \delta)^T$, the transformation of the phase space vector from s_0 to a downstream

[2] Linear transformation is valid for $kz \ll 1$, i.e. when the longitudinal position z is much smaller than the TDS RF wavelength $2\pi/k$ (see Section 2.1.1).

imaging screen at s is given by Eq. 1.3

$$\boldsymbol{u}_s = \mathcal{R}_{s_0\to s} \cdot \mathcal{R}_{\mathrm{TDS}}^{\mathrm{thin}} \cdot \boldsymbol{u}_{s_0}, \tag{2.16}$$

where $\mathcal{R}_{s_0\to s}$ is the transfer matrix from the centre of the TDS s_0 to the location of the screen at s. The horizontal position of the particle on the screen is of interest and can be found by

$$x_s = \underbrace{\left(R_{11,s_0\to s} x_{s_0} + R_{12,s_0\to s} x'_{s_0}\right)}_{x_s^0} \pm R_{12,s_0\to s} K z, \tag{2.17}$$

where the result from Eq. 2.14 has been used. The first part of this equation x_s^0 represents the horizontal displacement in the case of the TDS being switched off ($V_0 = 0 \to K = 0$), and the second part the deflecting effect of the TDS. Substituting the definition of the matrix element $R_{12,s_0\to s} = \sqrt{\beta_x(s)\beta_x(s_0)}\,\sin(\Delta\mu_x)$ from Eq. 1.9 into Eq. 2.17 leads to

$$x_s = x_s^0 + S_\pm z, \quad S_\pm = \pm\sqrt{\beta_x(s)\beta_x(s_0)} \cdot \sin(\Delta\mu_x) K, \tag{2.18}$$

where $\beta_x(s)$ and $\beta_x(s_0)$ are the horizontal beta-functions (see Eq. 1.6) at the screen and the centre of the TDS, respectively, and $\Delta\mu_x$ denotes the horizontal phase advance (see Eq. 1.8) between these two points. The parameter $S_\pm$ is commonly called *streak parameter* and describes the strength of the linear deflection of the TDS.

Without initial correlation

The simplest case is first considered for a bunch of electrons: the electrons display no correlation in (x, z) and (x', z) at the entrance of the TDS, and thus x_s^0 is not correlated to the longitudinal coordinate z either, i.e. $\langle x_s^0 z\rangle = 0$[3]. The second moment of the horizontal positions of the electrons at the screen, i.e. the squared rms beam size of the bunch σ_x^2 is given as

$$\sigma_x^2 = \langle (x_s^0)^2 \rangle + S_\pm^2 \langle z^2 \rangle = (\sigma_x^0)^2 + S_\pm^2 \sigma_z^2, \tag{2.19}$$

where it is presumed that the first moments of the electrons in a nominal bunch are $\langle x_s^0 \rangle = 0$ and $\langle z \rangle = 0$. By measuring the intrinsic beam size σ_x^0 (by switching off the TDS), the streaked beam size σ_x at S_+ (or S_-), and the corresponding streak parameter S_+ (or S_-, see Eq. 2.36), the bunch length σ_z can be determined to be

$$\sigma_z = \sqrt{\frac{\sigma_x^2 - (\sigma_x^0)^2}{S_\pm^2}}. \tag{2.20}$$

It is worth noting that the sought-after bunch length does not depend on the sign of the streak parameter (i.e. the value of the zero-crossing phase ψ_0) with this simplifying assumption of an uncorrelated initial transverse-longitudinal phase space.

[3] The bracket $\langle \ldots \rangle$ is the operator for the statistical mean of the variables inside the bracket.

The longitudinal resolution R_z of the bunch length measurement is determined by the intrinsic beam size, which is the smallest measurable transverse beam size on the screen, divided by the streak parameter:

$$R_z = \frac{\sigma_x^0}{|S_\pm|} = \frac{\sqrt{\beta_x(s)\varepsilon_N/\gamma}}{\sqrt{\beta_x(s)\beta_x(s_0)}\cdot\sin(\Delta\mu_x)K} = \frac{\sqrt{\varepsilon_N/\gamma}}{\sqrt{\beta_x(s_0)}\cdot\sin(\Delta\mu_x)K}, \tag{2.21}$$

with ε_N the normalized emittance and γ the Lorentz-factor of the bunch (see Eq. 1.15). In order to optimize the longitudinal resolution, a large horizontal beta-function $\beta_x(s_0)$ at the centre of the TDS and a horizontal phase advance of $\Delta\mu_x = \pi/2 + n\pi, n \in \mathbb{N}^0$ from the TDS to the screen are preferred. The beta-function $\beta_x(s)$ at the screen does not influence the longitudinal resolution, but should be chosen to give a beam size on the screen that is measurable taking into account the spatial resolution of the imaging system.

It is common to describe the longitudinal parameters using the time axis $t = z/c$ instead of the longitudinal axis z, which leads to the expressions of the bunch length σ_t and longitudinal resolution R_t in the time domain:

$$\sigma_t = \sigma_z/c, \quad R_t = R_z/c. \tag{2.22}$$

Influence of initial correlations

The assumption of no correlation in the transverse-longitudinal plane was an idealized case. A real electron bunch usually displays correlations in (x, z) or (x', z), or both of them. This initial correlation leads to a correlation between the intrinsic offset (when the TDS is switched off) and the longitudinal coordinate, which modifies Eq. 2.18 to give $x_s = x_s^0(z) + S_\pm z$. In this case, Eq. 2.19 becomes invalid for the determination of the bunch length due to $\langle x_s^0 z\rangle \neq 0$, and the longitudinal profile cannot be directly obtained. One simple method based on Refs. [Ban90, Loo] to reconstruct the longitudinal profile will be described in the following paragraphs, with one example of the application of the reconstruction method presented in Figs. 2.2 and 2.3.

Since the motion in y is not affected by TDS, it is convenient to consider only the x and z planes. The initial phase space density $\rho(x, z)$ of a bunch is assumed to be

$$\rho(x, z) = \lambda(z)\delta(x - f(z)), \quad z \in [z_{0-}, z_{0+}] \tag{2.23}$$

with $\lambda(z)$ being a line density function and z_{0-}, z_{0+} ($z_{0-} < z_{0+}$) the start and end position of the bunch, respectively. Two approximations are made here: (i) each longitudinal slice in z has an infinitesimal width in x (expressed by the δ-function in Eq. 2.23) and an infinitesimal divergence in x', (ii) the horizontal-longitudinal correlation of each slice is given by $x = f(z)$ and $x' = g(z)$, where $f(z)$ and $g(z)$ are two arbitrary correlation functions. The longitudinal density function equals to $\lambda(z)$ due to the relation

$$\rho_z(z) = \int \rho(x, z)\mathrm{d}x = \int \lambda(z)\delta(x - f(z))\mathrm{d}x = \lambda(z). \tag{2.24}$$

When the TDS is switched off, only the transverse plane (x, x') is transformed, while the longitudinal density function $\rho_z(z)$ remains unchanged. Therefore the intrinsic density distribution of the bunch on the screen $\rho^0(x,z)$ is given as

$$\rho^0(x,z) = \lambda(z)\delta(x - x^0(z)), \tag{2.25}$$

with $x^0(z)$ being a linear combination of $f(x)$ and $g(x)$ describing the horizontal-longitudinal correlation of the bunch at the position of the screen when the TDS is switched off.

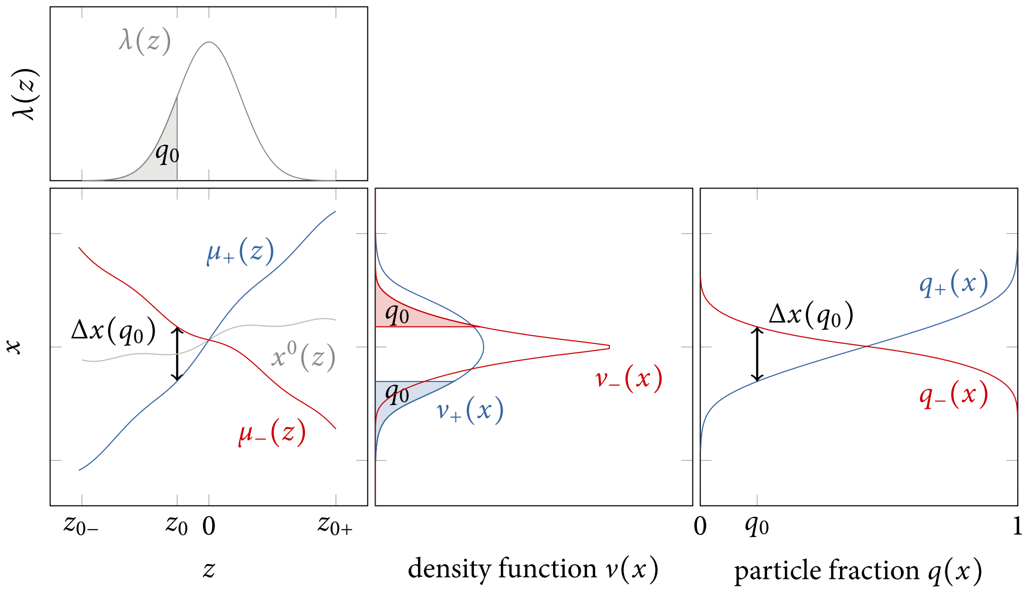

Figure 2.2: Illustration for the principle of the profile reconstruction method using measurements at both TDS RF zero-crossings. The example is shown for a Guassian distributed longitudinal density function $\lambda(z)$. An arbitrary correlation function $x^0(z)$ is assumed. The reconstructed longitudinal density function $q'(z)$ is compared with the reference $\lambda(z)$ in Fig. 2.3.

The TDS introduces extra correlation in the horizontal-longitudinal plane, resulting in

$$\mu_\pm(z) = x^0(z) + S_\pm z. \tag{2.26}$$

It is assumed that $\mu_\pm(z)$ is a monotonic function[4] due to the large value of the streak parameter $S_\pm$ (see Fig. 2.2 left). Replacing the correlation function $x^0(z)$ in Eq. 2.25 with $\mu_\pm(z)$ leads to the phase space density function of the streaked bunch

$$\rho_\pm(x,z) = \lambda(z)\delta(x - \mu_\pm(z)). \tag{2.27}$$

The measured horizontal density distribution on the screen is defined as the integral over the longi-

[4]for all $z \in [z_{0-}, z_{0+}]$, $\mu'_+(z) = x^{0\prime}(z) + S_+ > 0$ and $\mu'_-(z) = x^{0\prime}(z) + S_- < 0$.

tudinal coordinate (see Fig. 2.2 middle):

$$v_{\pm}(x) = \int \rho_{\pm}(x,z)\mathrm{d}z. \tag{2.28}$$

From the measured $v_{\pm}(x)$, the particle fraction $q_{\pm}$ can be calculated to be

$$q_{+}(x) = \int_{-\infty}^{x} v_{+}(x)\mathrm{d}x, \tag{2.29}$$
$$q_{-}(x) = \int_{x}^{\infty} v_{-}(x)\mathrm{d}x, \tag{2.30}$$

with the different integral limits indicating that they both give the particle fraction contained in the bunch part starting from the trailing end of the bunch (i.e. from the small longitudinal coordinate z_{0-}). The particle fraction functions $q_{\pm}(x)$ are invertible and their inverse functions are denoted as $x_{\pm}(q)$. For a given particle fraction $q = q_0 = \int_{z_{0-}}^{z_0} \lambda(z)\mathrm{d}z$ in the range of z_{0-} to z_0, the positions $x_{+}(q_0)$ and $x_{-}(q_0)$ refer to the transformation of the particles from the same longitudinal position z_0 (see Fig. 2.2 right):

$$x_{+}(q_0) = \mu_{+}(z_0) = x^0(z_0) + S_{+}z_0, \tag{2.31}$$
$$x_{-}(q_0) = \mu_{-}(z_0) = x^0(z_0) + S_{-}z_0. \tag{2.32}$$

Taking the difference of the above two equations, the following relation is obtained

$$\Delta x(q_0) = x_{+}(q_0) - x_{-}(q_0) = (S_{+} - S_{-})z_0. \tag{2.33}$$

This equation indicates that the longitudinal position z_0 can be solved for a given particle fraction q_0 by measurements at both TDS streak parameters S_{+} and S_{-}. By replacing q_0 with an arbitrary particle fraction q, the longitudinal position z can be expressed as a function of q

$$z(q) = \frac{\Delta x(q)}{S_{+} - S_{-}}. \tag{2.34}$$

The inverse function of $z(q)$ is $q(z)$, whose derivative gives the longitudinal line density function of the bunch (see Fig. 2.3)

$$\lambda(z) = q'(z). \tag{2.35}$$

This method retrieves the longitudinal distribution $\lambda(z)$ of a bunch with arbitrary initial transverse-longitudinal correlation using measurements at both TDS RF zero-crossings. The finite slice beam width and slice divergence is neglected.

Calibration of the streak parameter S

In both cases described above (with and without initial correlations), the reconstruction of the longitudinal profile using TDS requires the knowledge of the streak parameter $S_{\pm}$. The value of $S_{\pm}$ can be calculated directly according to Eq. 2.18 when the values of the beta-functions and phase advance

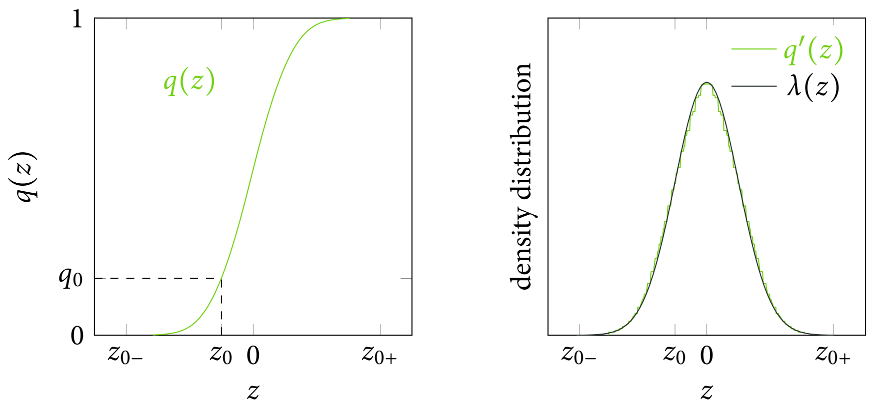

Figure 2.3: Illustration for the principle of the profile reconstruction method using measurements at both TDS RF zero-crossings. The longitudinal density function $q'(z)$ is reconstructed for the example shown in Fig. 2.2.

are known. The latter is usually not the case during real measurements, and therefore the streak parameter has to be determined experimentally.

From Eq. 2.18 the position of the centre of the bunch on the screen is given by $\langle x_s \rangle = \langle x_s^0 \rangle + S_\pm \langle z \rangle$, using the fact that the expectation is a linear operation. This relation is valid for both cases with and without initial transverse-longitudinal correlation. The change of the centre position of the bunch on the screen $\Delta\langle x_s \rangle$ depends linearly on the variation of the longitudinal centre position $\Delta\langle z \rangle$. According to $\Delta\langle z \rangle \approx c\Delta t = c\Delta\phi/2\pi f$ with f being the RF frequency of the TDS and $\Delta\phi$ a slight change of the TDS RF phase around the zero-crossing phase, the longitudinal centre position can be varied by changing the TDS RF phase as well:

$$\Delta\langle x_s \rangle = S_\pm \frac{c}{2\pi f}\Delta\phi. \tag{2.36}$$

By measuring the change of the horizontal position of the bunch centre $\Delta\langle x_s \rangle$ and the corresponding change of the TDS RF phase $\Delta\phi$, the streak parameter $S_\pm$ can be derived. One example of simulating the calibration procedure is shown in Fig. 3.36.

2.2.2 Longitudinal phase space

A horizontally deflecting TDS transforms the longitudinal coordinate into the horizontal plane and does not affect the vertical coordinate. Consequentially, a combined use with a vertically deflecting dipole magnet, which disperses the electrons vertically linearly with respect to their energy, allows for the measurement of the longitudinal phase space (z, δ).

The design deflection angle induced by a dipole magnet on a particle with design momentum of p_0 is given as

$$\alpha_0 = \frac{eB_0L}{p_0} \propto \frac{eI_0L}{p_0}, \tag{2.37}$$

where L is the length of the dipole magnet and B_0 the magnetic field at the design current I_0. The magnetic field usually has a small hysteresis, but can be approximated to be proportional to the dipole current at the nominal deflection angle. For example, the magnetic field of the dipole magnet used at the TDS diagnostic station at FLASH (see Section 5.2) scales as $B[\mathrm{T}] = 0.0022 + 0.0052 \cdot I[\mathrm{A}]$ and has a magnetic field of $B \approx 0.0052 \cdot 175\mathrm{A} = 0.91\mathrm{T}$ for electrons with a nominal energy of $p_0 c = 0.7\mathrm{GeV}$ at the design deflection angle of $\alpha_0 = 10°$.

A particle with a slightly deviated momentum of $p = (1+\delta)p_0$, $\delta \ll 1$ receives an additional deflection angle of

$$\Delta\alpha = \alpha_0 \frac{p_0}{p_0(1+\delta)} - \alpha_0 = \alpha_0 \frac{-\delta}{1+\delta} \approx \alpha_0(-\delta). \tag{2.38}$$

At a downstream screen, this extra angle is translated to a vertical displacement with the relation (see Eq. 1.2)

$$y = y^0 + R_{34}\Delta\alpha \approx y^0 - R_{34}\alpha_0\delta = y^0 + D_y\delta, \tag{2.39}$$

with y^0 being the intrinsic vertical position at the screen from betatron oscillation and R_{34} the corresponding element of the transfer matrix from the dipole to the screen. The term $D_y = -R_{34}\alpha_0$ is called the vertical *dispersion* and describes the linear dependency of the vertical position on the energy deviation. If there exists intrinsic correlation in the vertical-energy plane (y, δ), i.e. $y = y^0(\delta) + D_y\delta$, the same method as described in Section 2.2.1 can be used to retrieve the energy distribution using measurements at the dispersion D_y and $-D_y$. The latter requires an extra dispersive beamline deflecting the beam at the negative design angle. When there is no correlation in (y, δ), the rms energy spread $\sigma_\delta = \sqrt{\langle\delta^2\rangle}$ can be derived as

$$\sigma_\delta = \sqrt{\frac{\sigma_y^2 - (\sigma_y^0)^2}{D_y^2}}, \tag{2.40}$$

where $\sigma_y^2 = \langle y^2 \rangle$ is the squared vertical beam size and $(\sigma_y^0)^2 = \langle (y^0)^2 \rangle$ the squared intrinsic vertical beam size on the screen (with the dipole magnet turned off). We proceed with the assumption of no correlations in (y, δ), which is valid in most cases, for the following deviations.

The value of dispersion D_y can be obtained analytically with the relation $D_y = -R_{34}\alpha_0$, or determined more precisely experimentally. The same deflection angle $\Delta\alpha$ experienced by a particle with a momentum deviation of δ can be induced by changing the dipole current I_0 to $I_0(1+\delta_I)$ as well. With $\Delta\alpha = \alpha_0 \frac{I_0(1+\delta_I)}{I_0} - \alpha_0 = \alpha_0\delta_I$, the resulted vertical displacement on the screen can be then expressed as

$$y = y^0 + R_{34}\Delta\alpha = y^0 + R_{34}\alpha_0\delta_I = y^0 - D_y\delta_I, \tag{2.41}$$

which is a linear function of the relative change of the dipole current δ_I with the same coefficient D_y as in Eq. 2.39. The change of the vertical centre position of the beam $\Delta\langle y \rangle$ relates to the change of the dipole current δ_I as

$$\Delta\langle y \rangle = -D_y\delta_I, \tag{2.42}$$

from which the vertical dispersion D_y can be deduced.

The energy resolution is defined as

$$R_\delta = \sigma_y^0 / |D_y|. \tag{2.43}$$

However, σ_y^0 cannot be measured directly on the screen in the dispersive section when the dipole magnet is turned off. One possible way to obtain σ_y^0 is to duplicate the dispersive beamline in the forward direction (without deflection angle) downstream of the dipole magnet. When the dipole magnet is turned off, the measured beam size on the corresponding screen in the duplicated forward section represents the intrinsic beam size σ_y^0. The dispersion D_y and the vertical beta function on the screen β_y should be designed with considerations of the expected values of the energy spread in a real bunch.

The TDS induces an energy change as described in Eq. 2.9. Assuming there is no correlation in the transverse-longitudinal plane, the second moment $\sigma_{\Delta\delta}^2$ and first moment $\langle\Delta\delta\rangle$ of the relative energy deviation induced by the TDS can be obtained from Eq. 2.9 to be

$$\sigma_{\Delta\delta}^2 = K^2\sigma_{x_0}^2 + (\frac{1}{2}KL)^2\sigma_{x_0'}^2 + (\pm\frac{1}{6}K^2L)^2\sigma_z^2. \tag{2.44}$$

$$\langle\Delta\delta\rangle = K\langle x_0\rangle + \frac{1}{2}KL\langle x_0'\rangle \pm \frac{1}{6}K^2L\langle z\rangle. \tag{2.45}$$

Equation 2.44 shows that each slice at a position z (with a slice width of $\sigma_z = 0$) acquires an energy spread (termed as *induced energy spread* $\sigma_{IES} = \sigma_{\Delta\delta}$) resulted from the horizontal beam size σ_{x_0} and the divergence $\sigma_{x_0'}$ of the slice. Equation 2.45 reveals an increase or decrease of the mean energy of each slice as a linear function of the position $\langle z\rangle$ of the slice (with the assumptions $\langle x_0\rangle = 0$ and $\langle x_0'\rangle = 0$ for each slice). The effect of the energy change due to the TDS is described with calculations for FLASH in the following. A slice at $z = 60\,\mu$m of a compressed bunch with bunch length $\sigma_z = 60\,\mu$m and an energy of $cp = 700\,$MeV is considered. The TDS, with a length of $L = 3.826\,$m and a frequency of 2.856 GHz, was operated at an effective voltage of $V_0 = 20\,$MV. Assuming a design normalized emittance of $\varepsilon_N = 1\,\mu$m and design optics at the TDS of $\beta_x = 20\,$m and $\alpha_x \approx 0$, the induced energy spread and increase of the mean energy for this slice amount to $\sigma_{IES} \approx 2\cdot 10^{-4}$ and $\langle\Delta\delta\rangle \approx 1\cdot 10^{-4}$, respectively. Both the induced slice energy spread and the change of the mean slice energy are smaller than the initial bunch energy spread of typically $\sim 10^{-3}$. In the longitudinal phase space measurement using a TDS and a dipole magnet, the induced energy spread from TDS results in a larger vertical beam size on the screen:

$$\sigma_y = \sqrt{(\sigma_y^0)^2 + D_y^2\sigma_\delta^2 + D_y^2\sigma_{IES}^2}. \tag{2.46}$$

Determination of the initial energy spread σ_δ requires the knowledge of both the initial beam size σ_y^0 and the induced energy spread σ_{IES} from the TDS.

2.2.3 Slice emittance

The emittance of the bunch can be reconstructed using measurements of the beam size at locations with different transfer matrices (see Section 1.2). When the TDS is switched on, the longitudinal coordinate is mapped onto the horizontal plane, while the density distribution in the vertical plane is not changed. With the calibration of the streak parameter and the magnification of the imaging system, the vertical beam size of the slices along the bunch can be obtained. By measuring the slice beam sizes for various transfer matrices, the emittance of each slice can be retrieved by applying the same linear least square method as used for projected emittance measurements. In order to measure the slice emittance in both transverse planes x and y, two TDSs deflecting in different transverse directions are required.

3 Design of the TDS longitudinal diagnostic sections for the European XFEL

In order to fully exploit the photon beam capability of the European X-ray Free-electron Laser (XFEL), various electron bunch parameters, including the beam energy, the bunch charge, the bunch length, the bunch spacing, etc., will have to cover a wide range of values. This puts highly demanding requirements on the performance of the diagnostics for the electron bunch. Among the various diagnostics, transverse deflecting structures (TDS) stand out for their high-resolution, single-shot capability and large dynamic range. Applications of TDSs at the existing linear accelerators, as reported, for example, in Refs. [EFK00, KDD+13, Röh08], have proved their robust performance and versatile functionality as a time-resolved longitudinal diagnostic tool.

Three dedicated beamline sections equipped with TDS are planned for diagnosis of the electron bunches at different locations at the European XFEL. Measurements of a variety of parameters, such as the longitudinal profile, the longitudinal phase space, the slice emittance, the slice energy spread and the projected emittance, should be accomplished in the three TDS diagnostic sections. Fulfilling measurement requirements simultaneously for the diagnostics of multiple parameters of interest is a challenge in designing the accelerator optics. Furthermore, the three TDS diagnostic sections serve as matching sections, where the beam is matched to the design accelerator optics for transport into the subsequent main beamline with accelerating structures.

As a super-conducting FEL [RST+01], the European XFEL offers unique opportunity of delivering thousands of electron bunches per second. Therefore, diagnostics which are non-destructive to the generation of FEL pulses are highly appreciated. Such online diagnostics will be realized by using fast kicker magnets and off-axis screens in the pulse-stealing mode, in which single bunches out of the bunch train will be deflected for diagnostics and the remaining bunches stay unaffected. Implementation of the kicker magnets adds extra limitations to the design of the beamline lattice and accelerator optics.

Taking into account the requirements on the measurement resolutions and the limitations of diagnostic components, accelerator optics have been designed for all types of the measurements in the three TDS diagnostic sections. The performance of the measurements in terms of statistical and systematic errors has been studied analytically, and the achievable resolutions have been estimated.

Modelling of the measurements has been conducted using simulations with a particle tracking program. In order to investigate the expected performance under real accelerator operation conditions, particle distributions from start-to-end simulations have been adopted. Various issues that can be encountered in a real measurement process have been analysed, some of which may degrade the performance of the measurements and have to be avoided in practice.

In this chapter, the lattices of the three TDS diagnostic sections are presented with detailed description of their main components. The accelerator optics designed for the various types of measurements are explained, and possible error contributions are discussed. Finally, extensive modelling of the measurements using particle tracking simulations is presented.

3.1 The European X-ray Free-electron Laser

The European X-ray Free-electron Laser (XFEL) [EXF], which is being built in Hamburg, Germany, is an international project with currently contributions from 11 participating member states [Sha15]. The facility will run from the site of Deutsches Elektronen-Synchrotron (DESY) to the town of Schenefeld. The tunnel construction has been finished, and the beamline components are being installed. Commissioning of the injector section of the linac will commence by the end of 2015 and last approximately one year. First operation of the main linac is foreseen by the end of 2016.

The 3.4 km long European XFEL will be a hard X-ray FEL based on a super-conducting linear accelerator using the TESLA technology [RST+01]. The X-rays will be generated in the Self-Amplified Spontaneous Emission (SASE) [KS80, BPN84] process, and potentially with the self-seeding scheme.

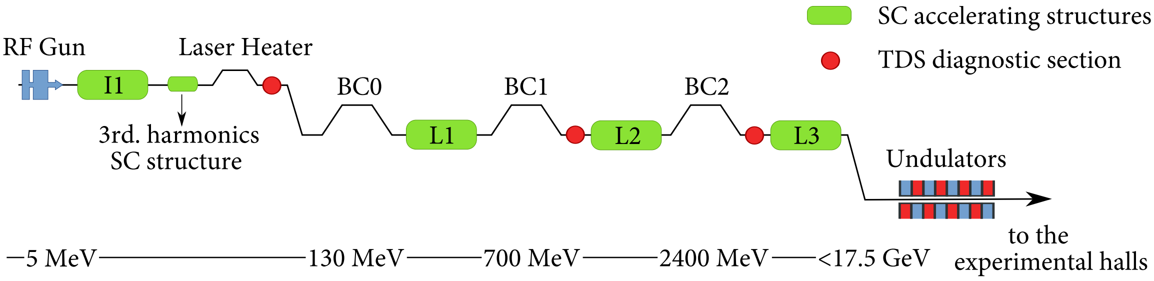

Figure 3.1: Simplified schematic layout of the European XFEL. The electron bunches are generated in a photocathode RF gun and accelerated in the super-conducting modules (I1, L1-3) operated at 1.3 GHz. Longitudinal compression of the electron bunches takes place in the magnetic chicanes BC0, BC1 and BC2 at beam energies of 130 MeV, 700 MeV and 2400 MeV, respectively. The three TDS diagnostic sections, which are relevant to this thesis, are represented by the red dots. Only one symbolic undulator section is depicted.

A simplified schematic layout of the European XFEL is depicted in Fig. 3.1. The electron bunches are generated in a photo-cathode RF gun and accelerated in the super-conducting accelerating modules operated at 1.3 GHz. After the first accelerating section I1, the beam energy reaches 130 MeV and the longitudinal phase space is linearised by a 3rd. harmonic system, operated at 3.9 GHz. A laser heater system is installed in the injector section to enable suppression of the micro-bunching instabilities by increasing the slice energy spread [SSY04]. In the following linac section, the electron bunches are successively accelerated and longitudinally compressed in the magnetic bunch compressors. Deflection of the electron bunch is in the horizontal plane in the laser heater system, and in the vertical plane in the bunch compressors BC0–BC2. After the maximum possible beam energy of 17.5 GeV is reached, the electron bunches are distributed through different undulator sections. At the moment, 5 photon beamlines are planned. The red dots in Fig. 3.1 represent the three TDS diagnostic sections, which are relevant to the content of this chapter and will be described in detail in the following sections.

The European XFEL will provide soft to hard X-rays with a wavelength down to 0.05 nm. Three electron beam energies of 10.5 GeV, 14 GeV and 17.5 GeV are chosen for the operation [DL13]. With variable bunch charges from 0.02 nC to 1 nC, electron bunches with a wide range of bunch lengths can be provided. Table 3.1 lists the expected bunch lengths at the locations of the three TDS diagnostic sections.

Table 3.1: Expected electron bunch lengths σ_t at the locations of the three TDS diagnostic sections for different bunch charges Q. The electron bunch lengths are rms values determined from start-to-end simulations for the European XFEL [BDG14].

Q (nC)	σ_t (fs)		
	Injector@130 MeV	after BC1@700 MeV	after BC2@2.4 GeV
0.02	3330	172	6
0.1	3600	189	16
0.25	4000	211	26
0.5	4630	258	46
1	5400	303	93

At the European XFEL, the RF accelerating field of the super-conducting structures will be pulsed at a macro frequency of 10 Hz[1] (see Fig. 3.2), i.e. the spacing between two macro pulses is 0.1 s. The RF macro pulse has a flat-top duration of up to 600 µs [DL13], where a train of electron bunches can be accelerated. The repetition rate defines the spacing between the bunches, and can be increased to up to 4.5 MHz (equal to a bunch spacing of 220 ns), which corresponds to a maximum of 2700 bunches per bunch train [DL13]. In future, it is envisioned to operate the accelerator with constant bunch filling patterns that are advantageous in terms of operation stability. The photon pulse pattern can be chosen by sending the unwanted electron bunches with fast kicker magnets into a local dump directly upstream of the undulator sections.

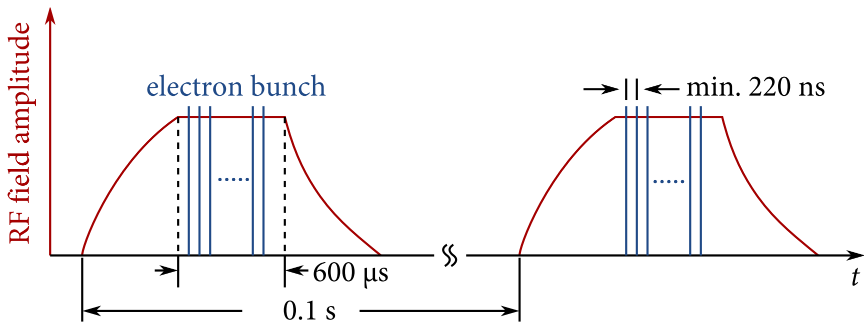

Figure 3.2: RF timing structure and electron bunch pattern of the European XFEL.

[1] Maybe later operation with 25 Hz or cw-operation.

3.2 Longitudinal diagnostic sections with TDS

The European XFEL will employ different longitudinal diagnostics, such as electro-optics (EO) methods, coherent radiation spectroscopy and TDS. Three complex beamline sections containing TDS are dedicated to measurements of the longitudinal profile, the longitudinal phase space, the slice emittance, the slice energy spread as well as the projected emittance at three different locations as indicated in Fig. 3.1: downstream of the laser heater system in the injector section, downstream of BC1 in the BC1 section and downstream of BC2 in the BC2 section.

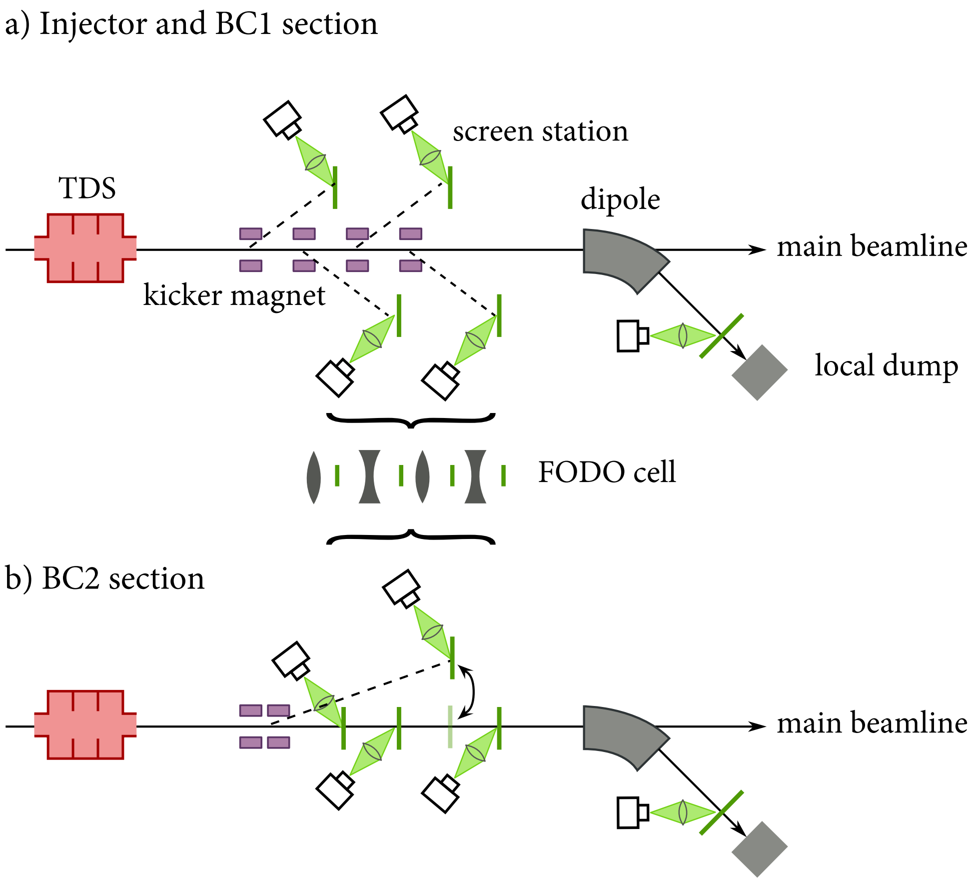

Figure 3.3: Schematic layout of the 3 TDS diagnostic sections at the European XFEL: a) in the injector and BC1 section, b) in the BC2 section.

The three TDS diagnostic sections have a similar layout. Figure 3.3 shows a schematic beamline of the three TDS sections. Each section comprises one TDS, several kicker magnets, four screen stations with off-axis and on-axis screens, one dipole magnet and one screen station in the dispersive section behind the dipole magnet. The four screen stations are located in a Focusing-Drift-Defocusing-Drift (FODO) cell structure, which allows for projected emittance measurement. When the TDS is switched on, slice emittance measurement can be performed with the four screen stations in the FODO cell structure, and longitudinal profile measurement with each of them as well. The electron bunch streaked by the TDS can be deflected by a dipole magnet into the dispersive section for the measurement of the longitudinal phase space. A local dump stops the electron bunch at the end of the dispersive section. When the dipole magnet is switched off, the electron bunches travel through the main beamline to the next accelerator section. The deflection direction and angle of the dipole magnets are different for the three sections and listed in Table 3.2. It should be noted that the streaking directions of the TDSs are decided to be perpendicular to the dispersion directions of the magnetic chicanes upstream of the TDSs, i.e. the laser heater, BC1 and BC2. This arrangement allows time-resolved investigation on possible degradation of the beam properties in the magnetic chicanes.

Each section has different total lengths, with different number and locations of the quadrupoles. The TDS, kicker magnet and screen station are described in the following section. The most important parameters of the three sections and their components are summarized in Table 3.2.

Table 3.2: Summary of the most important parameters of the three TDS sections and their components.

	unit	**Injector**	**BC1**	**BC2**
general				
design energy E_0	GeV	0.13	0.7	2.4
online diagnostics				
-longitudinal profile		yes	yes	yes
-longitudinal phase space		no	no	no
-projected emittance		yes	yes	no[2]
-slice emittance		yes	yes	no[3]
dispersive beamline				
deflection direction		horizontal	vertical	vertical
angle	degree	30	12	12
TDS				
streak direction		vertical	horizontal	horizontal
number of cells		16	46	2 × 46
flange-to-flange length	m	0.7	1.7	3.6
max. klystron power	MW	3	24	24
max. effective voltage $V_{0,max}$	MV	1.84	15.49	27.31
filling time	ns	117	337	673
kicker magnet				
deflection direction		horizontal	vertical	vertical
number		4	4	1 pair
max. kick strength	mrad	13.1	2.8	1.6

3.2.1 Online diagnostic in pulse-stealing mode

Online diagnostics, which are non-destructive to the generation of FEL pulses, are highly requested at the European XFEL. Such diagnostics will be realized in the three TDS diagnostic sections with

[2] Upgrade possible with extra kicker magnets.
[3] Upgrade possible with extra kicker magnets.

operation in the pulse-stealing mode. The TDS is capable of streaking up to four successive electron bunches out of each bunch train (at bunch repetition rate of 4.5 MHz and 1 MHz). The kicker magnets, which have a pulse duration short enough to deflect single bunches, kick the streaked bunches onto the off-axis screens for the measurements. The remaining bunches in the bunch train are not affected and continue travelling to the undulators for the generation of FEL pulses. Compared to the maximum number of bunches in a bunch train (2700 at a repetition rate of 4.5 MHz), the bunches lost for diagnostics purpose are negligible. On the other hand, the diagnostic bunches are usually added to the end of the long bunch train and will not be noticed by the photon users. Therefore, the pulse-stealing mode can be considered effectively as non-destructive to the generation of FEL pulses.

The three TDS diagnostic sections differ mainly in the variety of provided online diagnostics. In each of the injector and BC1 section, four fast kicker magnets are installed with each of them serving one corresponding off-axis screen in the FODO structure. This allows for online measurements of the slice emittance and longitudinal profile. In the BC2 section, the high beam energy of 2.4 GeV requires a pair of kicker magnets to deflect the electron bunch onto one off-axis screen. Due to the restraints on budgets, only two such pairs are foreseen for the moment. Online longitudinal profile measurement is possible in the BC2 section, with a potential upgrade option to slice emittance measurements.

3.2.2 Transverse deflecting structure

The TDSs, which are the key components in the three sections, are designed by the Institute for Nuclear Research of Russian Academy of Sciences, Russia [INR11]. Some of the most important requirements on the TDSs include:

- Short filling time to allow streaking bunches out of the bunch train at different repetition rates,
- Adjustable RF pulse flat-top duration to streak one to four bunches in a bunch train,
- High effective deflecting voltage to provide sufficient longitudinal resolution,
- Iris diameter of the TDS larger than the standard beam pipe diameter of 40.5 mm and tolerable impact from wakefields.

After optimization of the parameters, the well-known disk-loaded S-band RF waveguide structures [ALL64] are decided. The TDSs will be operated in travelling wave mode at a frequency of 2.997 GHz[4]. The group velocity of the structure and the phase shift per cell amount to -1.52% of the speed of light and $2\pi/3$, respectively.

The three disc-loaded waveguide structures are composed of the same waveguide cells as can be seen in Fig. 3.4 (left). Each cell has a length of 33.34 mm and a radius of $R_c = 55.28$ mm. The iris has a radius of $R_a = 21.71$ mm. Two suppressor holes with a radius of $R_{st} = 9$ mm are located symmetrically on each side of the iris to stabilize the direction of the deflecting field. The distance from the centre of the suppressor hole to the centre of the iris amounts to $L = 34.81$ mm.

[4] The frequency of the TDS f_{TDS} is generated from the frequency of 1.3 GHz of the master oscillator as $f_{TDS} = 332/144 \cdot 1.3$ GHz $= 2.997$ GHz, which is then an integer multiple of the bunch repetition rate of 4.5 MHz.

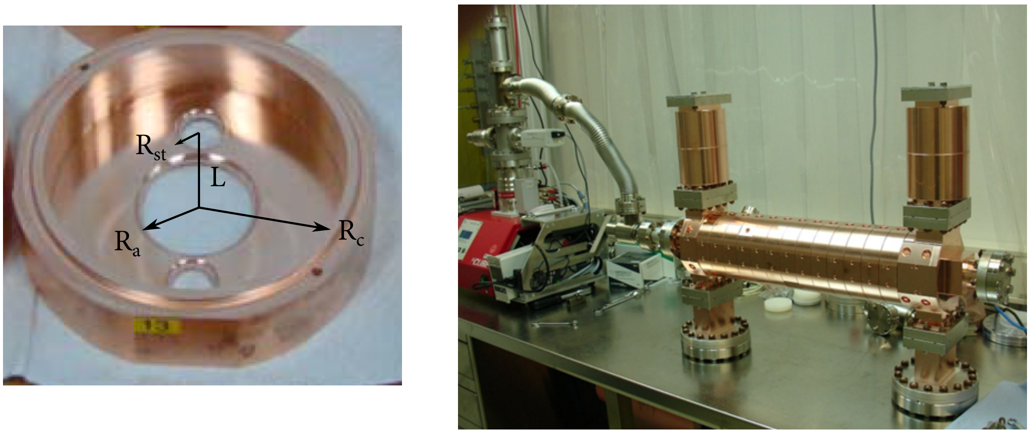

Figure 3.4: (Left) Photos of a single TDS cell. Figure adapted from Ref. [INR11]. (Right) Photo of a prototype TDS structure in tests at the Photo Injector Test Facility (PITZ), DESY Zeuthen.

Different numbers of the waveguide cells are chosen for the TDSs in the three sections. Mechanical designs of the TDSs are shown in Fig. 3.5. The TDS in the injector section is shorter with 16 cells. The TDS in the BC1 section comprises 46 cells, and the one in the BC2 section is assembled from two BC1 TDSs together. Using the known parameters of the TDS design, the effective deflecting voltage can be estimated and are listed in Table 3.2.

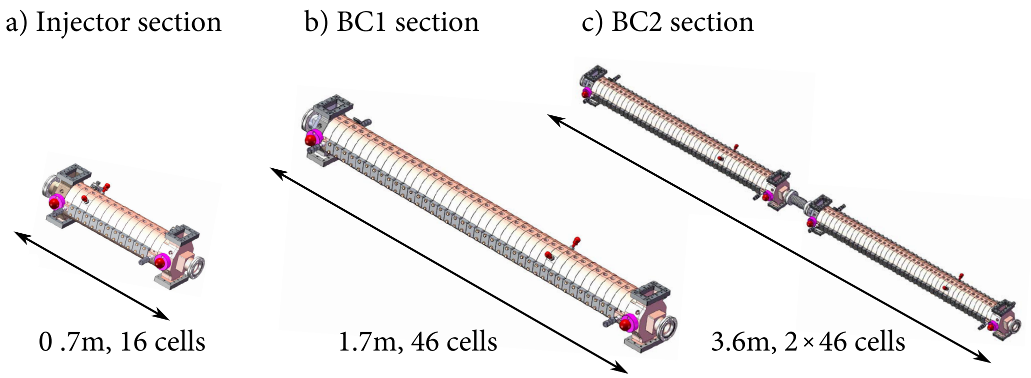

Figure 3.5: Designs of the TDSs in the three sections at the European XFEL. The waveguide cells have the same mechanical designs, but different numbers of the cells have been used to assemble the TDSs. The flange-to-flange lengths are given. Figure adapted from Ref. [INR11].

3.2.3 Kicker magnet

Downstream of the TDS in the three sections, kicker magnets will be installed to deflect the streaked bunch onto the off-axis screens. The kicker magnets have uniform designs, consisting of a ceramic vacuum chamber that has been sputtered at the inside with a layer of 1 μm thick stainless steel and two air coils, made of flat copper bars with a length of 350 mm, outside the vacuum beam pipe at opposite sides of the beam axis (see Fig. 3.6). A pulser that generates a half cycle of a sine wave with

10 Hz is directly attached to the kicker magnet. The pulse duration of $t_p = 380$ ns, which is shorter than $2 \cdot 220$ ns, enables deflection of single bunches out of a bunch train even at the highest repetition rate of 4.5 MHz. The maximum high voltage generated by the pulser is $U_p = 20$ kV.

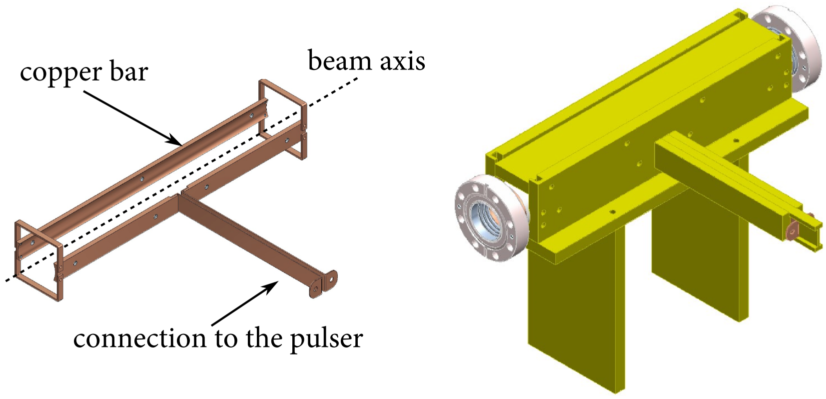

Figure 3.6: Mechanical design of the kicker magnet for the European XFEL. (Left) Two flat copper bars with a length of 350 mm are mounted outside the vacuum beampipe, and connected to a high voltage pulser. (Right) Ceramic housing for the kicker magnet. Courtesy of Frank Obier, DESY.

A prototype kicker magnet has been installed at the Free-electron Laser in Hamburg (FLASH), DESY (see Section 5.2.2). With the calibration performed at FLASH, the maximum kick strength of the kicker magnet for the European XFEL has been estimated and is listed in Table 3.2.

The kicker magnets deflect single bunches in the direction perpendicular to the streak direction of the TDS. In the injector and BC1 section, four kicker magnets are foreseen with each of them pairing to one off-axis screen in the FODO cell structure. In the BC2 section, a pair of two kicker magnets in sequence is needed to deflect the electron bunch with a beam energy of 2.4 GeV. At the moment only two such pairs are planned for online measurement of the longitudinal profile. Future upgrade with installation of more kicker magnets is possible to make use each of the off-axis screens in the BC2 section for the online slice emittance measurement.

3.2.4 Screen station

The screen stations installed in the TDS diagnostic sections are developed by the group MDI at DESY [WHK+13]. They have a uniform design as illustrated in Fig. 3.7. The screen is mounted perpendicular to the beam axis, and the imaging system is placed at an angle of 45° to the beam axis. With the application of scintillator screens, this configuration circumvents the problem of coherent emission of optical transition radiation using the spatial separation method (see Chapter 4).

The imaging system is located outside the vacuum chamber and assembled in a compact mechanical housing. Magnification of 1 : 1 and demagnification of 2 : 1 can be configured. For the image recording, CCD camera avA2300 from Basler AG, Germany [Bas07], will be used. With 2330×1750 pixels of squared size of $5.5\ \mu\text{m} \times 5.5\ \mu\text{m}$, the field of view is correspondingly $12.815\ \text{mm} \times 9.625\ \text{mm}$ and $25.63\ \text{mm} \times 19.25\ \text{mm}$ for the magnifications of 1 : 1 and 2 : 1, respectively. The CCD sensor of

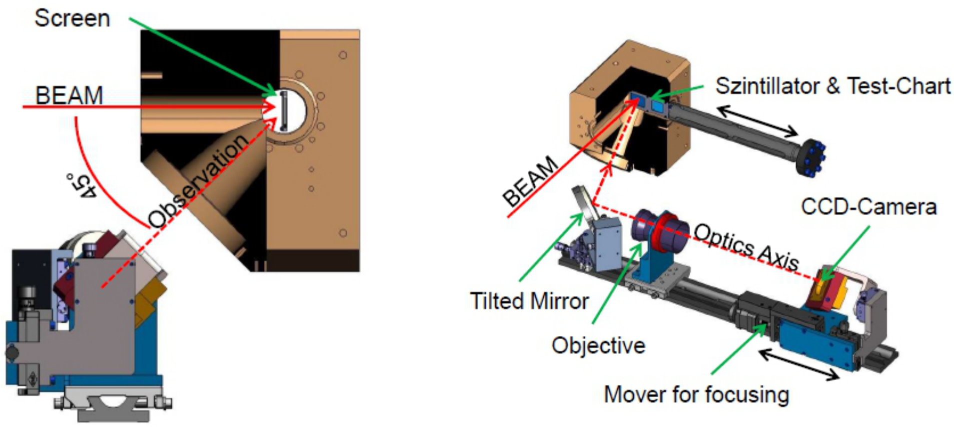

Figure 3.7: Mechanical design of the screen station for the European XFEL. Figure adapted from [WHK+13].

the camera is tilted according to the Scheimpflug principle[5] to be capable of imaging the whole area of the field of view in focus. It should be noted that the conventional micro lenses, which are attached parallel above each pixel of the CCD sensor, have been removed in order to strictly comply with the Scheimpflug principle. As a result, the screen stations will provide a constant spatial resolution of σ_{reso} = 10 µm (for the configuration with a magnification of 1 : 1) [WHK+13] in the x and y plane over the whole screen. The imaging system can be rotated in the transverse plane to provide different field of view in the x and y plane.

The screen holder is mounted with one calibration target, one on-axis and one off-axis scintillator screen. According to the studies in Refs. [KBL10, KBG+12], lutetium-yttrium oxyorthosilicate doped with cerium (LYSO:Ce) has been chosen due to its good spatial resolution and high light yield. A photo of an example of the screen holder is shown in Fig. 3.8. The on-axis screen has a dimension of 24 mm × 30.5 mm. The off-axis screen, with a dimension of 9.5 mm × 35.5 mm, are arranged in alternating positions, for example the first and third off-axis screen in the BC1 section are in the positive y-direction, while the second and fourth in the negative y-direction. The distance from the edge of the off-axis screen to the beam axis amounts to 6 mm. Both scintillator screens have a thickness of 200 µm. The orientation of the screen holder is different in the three TDS diagnostic sections. The longer side of the off-axis screen is parallel to the streaking direction of the TDS, since the beam size of the electron bunch is larger in that plane.

3.3 Accelerator optics

The accuracy of measurements of the the projected emittance, the slice emittance and the longitudinal phase space depends crucially on the accelerator optics in the TDS diagnostic section [Löh05]. In each of the three TDS diagnostic sections (Injector, BC1 and BC2 section) at the European XFEL, all three types of measurements, which put different demands on the accelerator optics, should be

[5]When the planes of the object, the lens and the detector intersect at the same axis, the whole object is in depth of field and can be imaged sharply [Sch04].

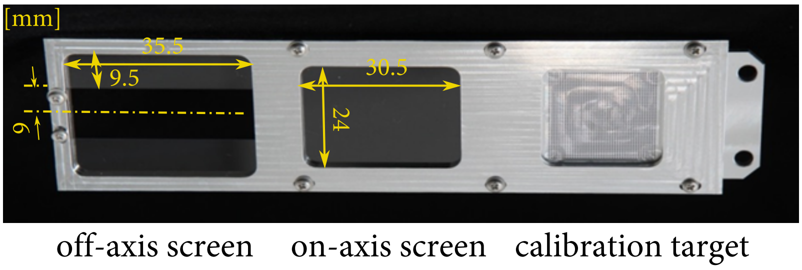

Figure 3.8: Photo of the screen holder in the screen station for the European XFEL. Two off-axis screens are mounted in this example. For the application in the TDS diagnostic sections, one of them is chosen. Photo courtesy of Dirk Nölle, DESY.

accomplished using the one and the same beamline. The requirements become more stringent in cases a combination of various types of measurements are needed simultaneously.

The three TDS diagnostic sections will employ the same concepts of the accelerator optics. Slight variations are necessary in the individual sections, since they have different available spaces and the different electron bunch parameters (such as the beam energy and electron bunch length) demand different measurement resolutions. In this section, the accelerator optics designed for the three types of measurements are presented, using the BC1 section as a representative for the detailed error analysis.

3.3.1 Slice emittance measurement

In order to provide online slice emittance measurements during the generation of FEL pulses, the multi-screen method is chosen in the three TDS diagnostic sections. With the kicker magnets and the four screen stations equipped with off-axis screens, the slice emittance measurements can be performed in the pulse-stealing mode (see Section 3.2.1).

The slice emittance is measured in the direction perpendicular to the streak direction of the TDS. In the streak direction, good longitudinal resolutions are required on the four screens to resolve the slices. In the slice emittance measurement plane, arrangements of the accelerator optics between the four screens are important to the accuracy of the emittance reconstructions. For all three TDS diagnostic sections, 1.5-cell FODO structures with phase advances of 30° and 76° per cell in the TDS streak plane and slice emittance measurement plane (will be denoted as 30/76-FODO), respectively, are chosen. The first screen is located at the beginning of the FODO structure, followed by three subsequent screens separated by a distance of half of one cell length. The slice emittance is reconstructed at the location of the first screen. The phase advance in the streak plane from the TDS to the centre of the 1.5-cell FODO structure (i.e. the centre of the second and third screen) is matched to 90°. Optimization procedure of the accelerator optics for slice emittance measurements is described in Appendix B.2.

An example of the design accelerator optics of the TDS diagnostic section in the BC1 section is shown in Fig. 3.9 with the beta-functions and phase advances in the streak plane x and emittance measurement plane y, respectively. A large $\beta_x = 30\,\mathrm{m}$ in the streak direction at the TDS ensures a

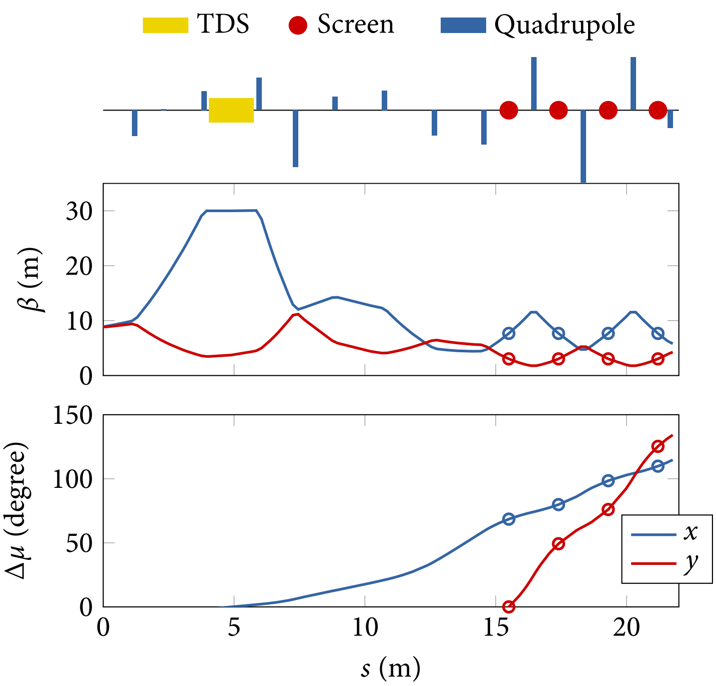

Figure 3.9: Accelerator optics for slice emittance measurements in the BC1 section (30/76-FODO). The height of the quadrupole in the symbolic beamline (top) scales with the value of the quadrupole strength. The kicker magnets are omitted in the plot.

large streak parameter S according to Eq. 2.18. The beta-functions at the four screens are $\beta_x = 7.7\,\mathrm{m}$ and $\beta_y = 3.0\,\mathrm{m}$ in the streak and slice emittance measurement plane, respectively.

Table 3.3 lists the most relevant parameters of the accelerator optics in the BC1 section. Since the beta-functions are identical at the four screens, the streak parameters S differ only due to the phase advance $\Delta\mu_{TDS\rightarrow screen}$. The largest streak parameter is achieved at the third screen S3, and the smallest at the first screen S1 with only a factor of 6% worse. Assuming the TDS operated at the maximum effective voltage $V_{0,max}$ and a normalized emittance of $\varepsilon_N = 1\,\mu\mathrm{m}$, the longitudinal resolutions obtained at the four screens are comparable and amount to ~ 12 fs. During online measurements with the kicker magnets turned on, deflection from the kicker magnets introduces additionally dispersion at the screens in the emittance measurement plane. Statistical and systematic errors from using this accelerator optics are analysed in the following.

Pulse-stealing mode

In the TDS diagnostic section in the BC1 section, four kicker magnets (K1-K4) will be installed. Each of the kicker magnet is capable of deflecting one electron bunch out of the bunch train onto one corresponding off-axis screen of the screen station, i.e. K1 is assigned to S1, etc. In order to reduce the secondary particle showers induced when the bunch hits the screen, unnecessary screens should be avoided on the trajectory of the kicked bunch. Therefore, the four off-axis screens are arranged

Table 3.3: Design parameters at the four measurement screens (S1-S4) for slice emittance measurements in the BC1 section.

	unit	Screens in BC1 section S1	S2	S3	S4
streak direction x					
$\Delta\mu_{TDS\rightarrow screen}$	degree	69	80	99	110
$\sin(\Delta\mu_{TDS\rightarrow screen})$		0.93	0.98	0.99	0.94
R_t @ $V_{0,max}$ @ε_N = 1 µm	fs	12.7	12.0	12.0	12.6
slice emittance measurement in y					
$\Delta\mu_y$ between the subsequent screens	degree	0	49	27	49
nominal kick strength	mrad	2.52	−2.10	2.52	−2.52
β_y	m	3	3	3	3
transfer matrix element R_{36}	mm	−4	8	−6	0

alternately on each side of the beam axis in the vertical plane. Figure 3.10 displays the subsection of the beamline presented in Fig. 3.9, in which the locations of the kicker magnets and the arrangement of the off-axis screens are shown. The vertical trajectory of the bunch centre $< y >$ is plotted for the four cases of the bunch being deflected by the individual kicker magnet. The kicker magnets are set to the nominal kick strengths as given in Table 3.3.

One problem might exist for the bunch kicked by K1: the bunch hits the designated screen S1, and arrives at the unwished screen S3 as well. As a result, both bunches kicked by K1 and K3 could be imaged on S3. An image of overlapping intensities from both bunches may lead to distortions of the beam size measurements and thus should be avoided. Separation of the intensities from two bunches at S3 becomes more challenging, when four consecutive bunches in each bunch train are deflected at the maximum repetition rate of 4.5 MHz, since it is critical for the CCD camera to resolve the images of the two bunches with a spacing below 1 µs. Test with the camera is presented in Section 5.2.3 and one remedy is proposed.

statistical error

Monte-Carlo simulations are performed to investigate the errors of the reconstructed emittance resulting from the statistical errors of the beam size measurements. The procedure of Monte-Carlo simulation is described in Section 1.3.1. The mean value $\bar{\varepsilon}$ and standard deviation σ_ε are calculated from the probability distribution of the reconstructed emittance from 1000 samples.

Figure 3.11 shows the results of Monte-Carlo simulations for the slice emittance measurement in the BC1 section, assuming a normalized emittance of $\varepsilon_N = 1$ µm, beam energy of $E_0 = 700$ MeV and normal distributed beam size error with a standard deviation of 5%. At the design Twiss parameters (indicated by the small white circle in Fig. 3.11), the deviation of the reconstructed emittance $(\bar{\varepsilon} - \varepsilon_N)/\varepsilon_N$ is 0.3% and the relative standard deviation of the reconstructed emittance $\sigma_\varepsilon/\bar{\varepsilon}$ amounts to 5%. For mismatch parameters smaller than 1.5, the deviation is smaller than 2%, and the relative standard deviation is below 15%. However, for mismatch parameters larger than 1.5, the relative

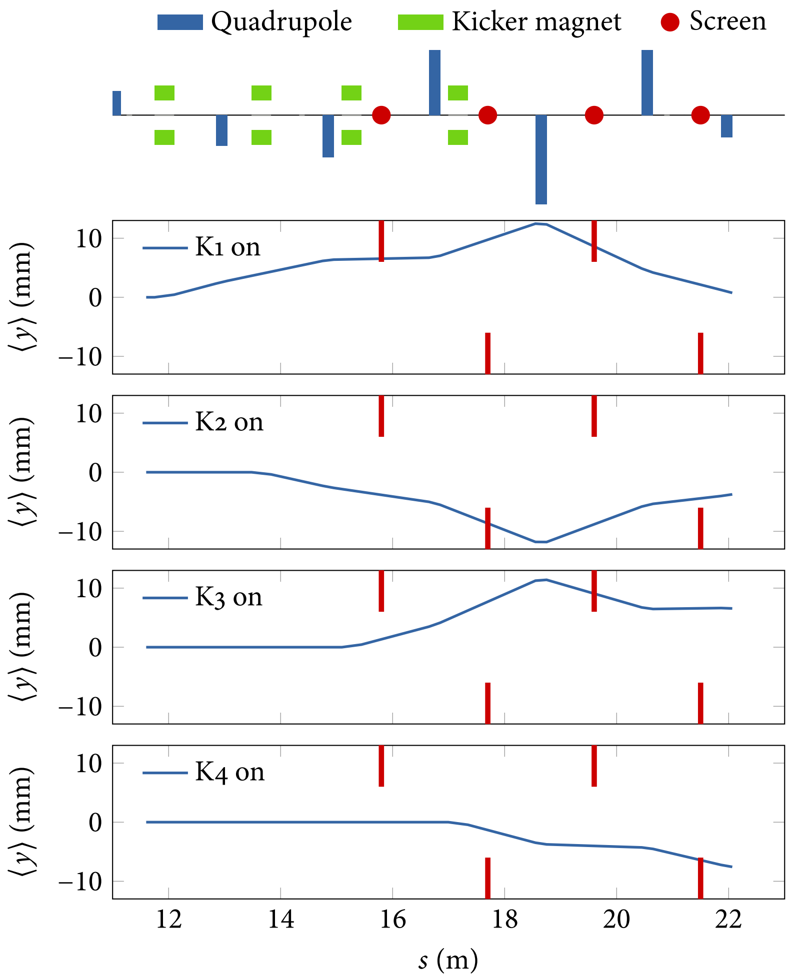

Figure 3.10: Trajectories of an electron bunch when deflected by one of the four kicker magnets (K1-K4) during online slice emittance measurements. The beamline shown in this plot is a subsection of that in Fig. 3.9. The location of the four off-axis screens (red bars) are illustrated for comparison with the bunch trajectories.

standard deviation could increase rapidly above 30%. It can be seen that different combinations of the initial beta- and alpha-functions with the same mismatch parameter can lead to various statistical errors. Therefore, four different values of the initial Twiss parameters, marked as black dots with the letters A, B, C, and D, will be further investigated in the following.

systematic error: screen resolution

Due to the limited spatial resolution σ_{reso} of the imaging system (see Section. 3.2.4), the measured beam size on the screen σ deviates from the real beam size σ_0, and is approximated by $\sigma \approx \sqrt{\sigma_0^2 + \sigma_{reso}^2}$. Depending on the values of the real beam sizes, the systematic errors of the reconstructed emittance arising from the screen resolution are different.

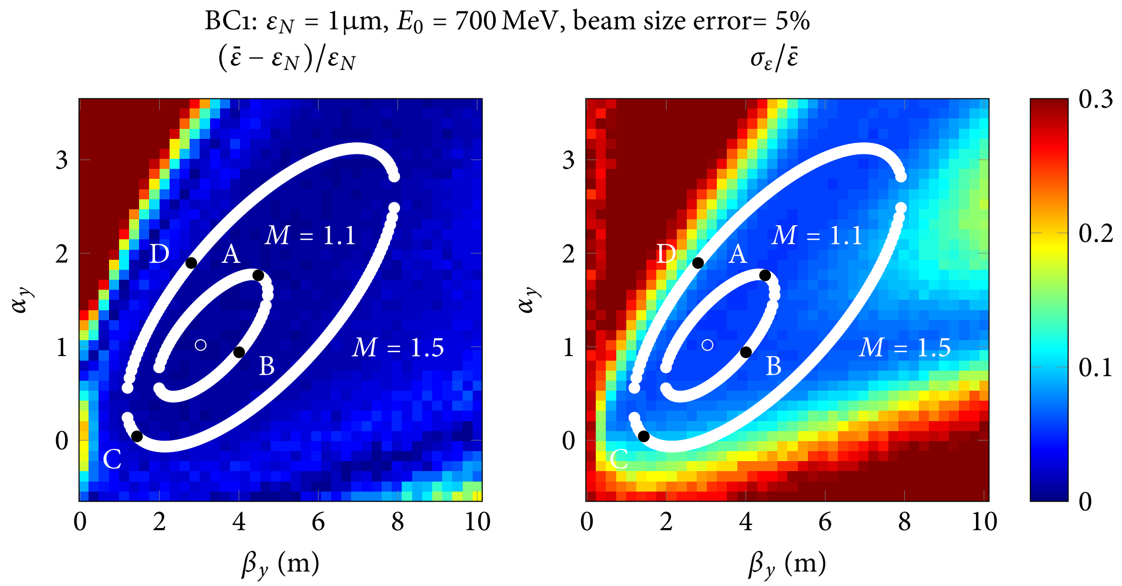

Figure 3.11: Statistical error resulting from beam size measurements in slice emittance measurements: Monte-Carlo simulations. The deviation of the reconstructed emittance from the design value (left) and the relative standard deviation of the reconstructed emittance (right) are shown. The design Twiss parameters as well as the Twiss parameters with $M = 1.1$ and $M = 1.5$ with respect to the design values are highlighted. Four specific combinations of beta- and alpha-functions, marked as A, B, C and D, will be referred to in Fig. 3.21. The colourmap is restricted to a value of 30% to be capable of presenting more details in the areas with smaller values.

Deviation of the reconstructed emittance $(\varepsilon - \varepsilon_N)/\varepsilon_N$ is investigated for different normalized emittances ε_N and initial Twiss parameters (see Fig. 3.12). At the design optics with a nominal beam with $\varepsilon_N = 1$ µm, the deviation is 4.5%. Deviations become smaller with increasing emittances, which means larger real beam sizes. When the initial Twiss parameters are not matched to the design values, the screen resolution results in larger systematic errors. It is worth noting that the deviation due to screen resolution depends on the mismatch parameter, but not on the values of the Twiss parameters (A and B with $M = 1.1$, C and D with $M = 1.5$).

In real measurements, the measured beam sizes can be corrected with the screen resolution. Section 6.5 describes one application with considerations of the screen resolution.

systematic error: screen calibration

The accuracy of beam size measurement is affected by the screen calibration error as well. The emittance is reconstructed from beam sizes measured at four screens, where each of them is subject to an uncorrelated calibration error of the factor of $\Delta_i \sim \mathcal{N}(0, c^2), \Delta_i \neq \Delta_j$[6]. The influence of the calibration errors of the individual screens can be investigated using Monte-Carlo simulation similar to that for the statistical errors (see Fig. 3.11). Typical calibration errors are expected to be smaller

[6]The probability distribution of Δ is a normal distribution centred at 0 and with a standard deviation of c.

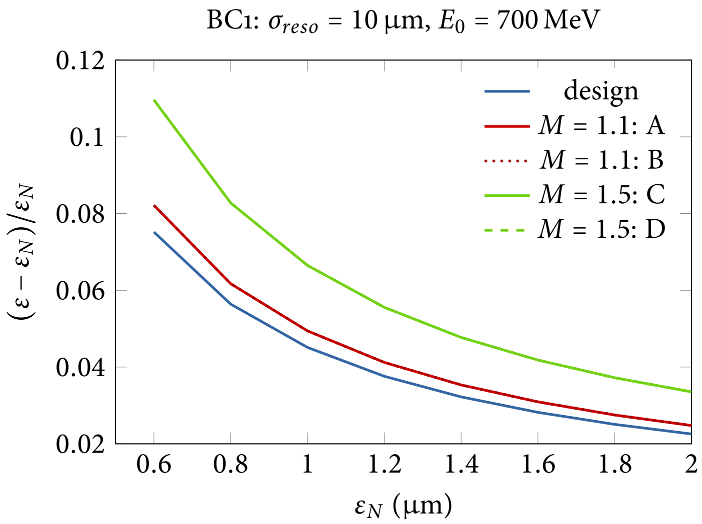

Figure 3.12: Systematic error in slice emittance measurements: influence of the screen resolution. The deviation of the reconstructed emittance is identical for different combinations of Twiss parameters with the same mismatch parameter (A and B, C and D).

than the statistical error of the beam size measurements and have smaller impact on the errors of the reconstructed emittance. For the assumption of $c = 1\%$, the relative standard deviation $\sigma_\varepsilon/\varepsilon_N$ of the reconstructed emittance at the design Twiss parameters is estimated to be 1%.

systematic error: dispersion from the kicker magnets

When the kicker magnets are turned on for online slice emittance measurements in pulse-stealing mode, dispersion can be generated in the emittance measurement plane at the screen locations. As listed in Table 3.3, the matrix element R_{36} of the transfer matrix from the first kicker magnet K1 to the individual screens does not vanish, when the individual kicker magnet is switched on.

In the presence of dispersion, the beam size σ_y at the screens can be expressed as a function of the beam matrix elements at the location s_0 of the first kicker magnet according to Eq. 1.16:

$$\sigma_y^2 = \sigma_{y,Twiss}^2 + 2R_{33}R_{36}\langle y_0\delta_0\rangle + 2R_{34}R_{36}\langle y_0'\delta_0\rangle + R_{36}^2\sigma_{\delta_0}^2, \tag{3.1}$$

with $\sigma_{y,Twiss}$ being the Twiss beam size when the kicker magnet is switched off, σ_{δ_0} the energy spread at s_0, $\langle y_0\delta_0\rangle$ and $\langle y_0'\delta_0\rangle$ the correlations in (y,δ)-plane and (y',δ)-plane of the electron bunch at s_0. The emittance can be reconstructed by at least 6 beam size measurements (see Section 1.2). In the FODO structures of the TDS diagnostic sections, where only 4 screens are available, determination of all the six beam matrix elements is not possible. However, when the values of the dispersion generated by the kicker magnets are small, the influences of the dispersions could be treated as perturbation to the Twiss beam size $\sigma_{y,Twiss}$. Depending on the order of magnitude of the energy spread and the correlation terms of the real particle distribution, application of the non-dispersion model as described in Eq. 1.18 on the perturbed beam sizes σ_y from Eq. 3.1 yields results with very different accuracies.

Systematic errors due to dispersions generated by the kicker magnets are investigated for the design Twiss parameters. In the first step, both correlation terms are assumed to be zero. Figure 3.13 shows the deviation of the reconstructed emittance in dependence of the energy spread. For typical slices with energy spread in the order of $\sigma_{\delta_0} \sim 10^{-4}$, deviation is well below 1% for all the three considered normalized emittances. A more extensive analysis including consideration of both correlation terms $\langle y_0\delta_0\rangle$ and $\langle y_0'\delta_0\rangle$ is presented in Fig. 3.14 for two cases of energy spread: (left) $\sigma_{\delta_0} = 10^{-4}$ as typical value of energy spread in slices, and (right) $\sigma_{\delta_0} = 10^{-2}$ typical for projected energy spread of the whole bunch. For a slice with an energy spread of $\sigma_{\delta_0} = 10^{-4}$, the values of both correlation terms are typically on the order of 10^{-9}, and the resulted perturbation to the beam sizes due to dispersion is negligible. The deviation of the reconstructed emittance is then far below 1%.

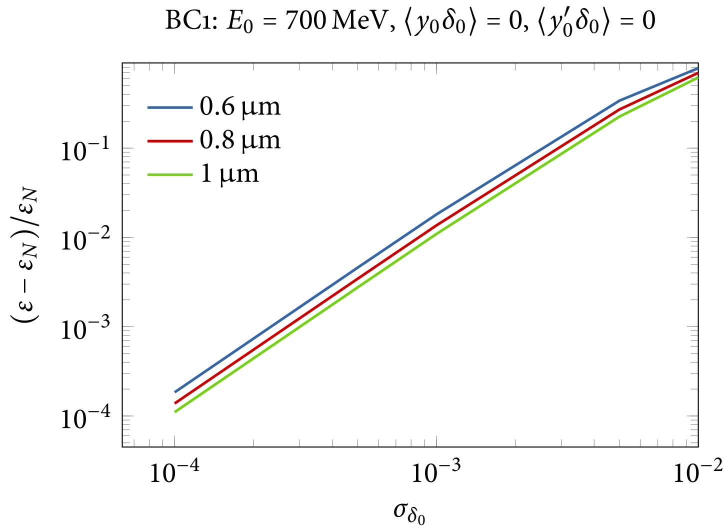

Figure 3.13: Systematic error in slice emittance measurements: influence of the dispersion generated by the kicker magnets. Vanishing correlation terms are assumed, i.e. $\langle y_0\delta_0\rangle = 0$ and $\langle y_0'\delta_0\rangle = 0$. The different colours correspond to three different values of the assumed normalized emittance.

systematic error: erroneous transfer matrix

In a real measurement, the design transfer matrix is assigned to the FODO section. The required currents I of the three quadrupoles are calculated based on the calibration of the quadrupole field gradient and the knowledge of the beam energy. Both the error in the calibration of the quadrupole field gradient $B = B(I)$ and measurement of the energy E lead to errors in the quadrupole coefficient $k \sim 0.299 \cdot \frac{B[\mathrm{T/m}]}{E[\mathrm{GeV}]}$, thus resulting in an erroneous transfer matrix. Furthermore, errors of energy measurement have influence on the normalization of the reconstructed emittance as well.

Monte-Carlo simulations have been performed with a normalized emittance of $\varepsilon_N = 1\,\mu\mathrm{m}$ for various initial Twiss parameters. The following assumptions are made:

- the three quadrupoles have uncorrelated calibration errors of $\Delta B_i \sim \mathcal{N}(0, 1\%^2)$, $\Delta B_i \neq \Delta B_j$,

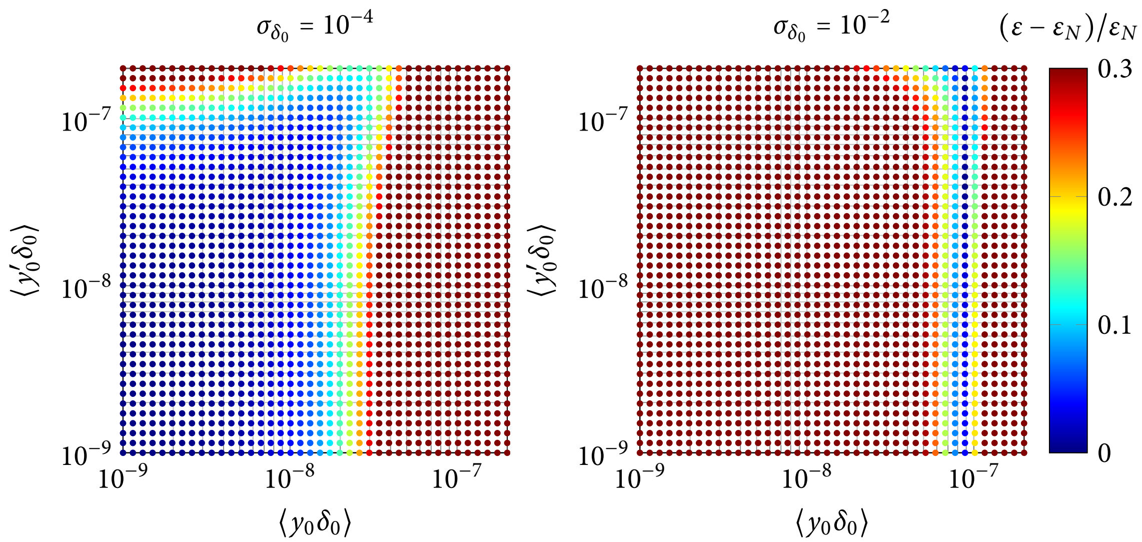

Figure 3.14: Systematic error in slice emittance measurements: influence of the dispersion generated by the kicker magnets. Deviations of the reconstructed emittance $(\varepsilon - \varepsilon_N)/\varepsilon_N$ for an energy spread of (left) $\sigma_{\delta_0} = 10^{-4}$ and (right) $\sigma_{\delta_0} = 10^{-2}$ are shown. The range of the correlation terms covers the values expected for a real bunch, as will be shown in Sections 3.4.1 and 3.4.2. The colourmap is restricted to 30%.

- the energy error is identical at the locations of the three quadrupoles and is assumed to be $\Delta E_i = \Delta E \sim \mathcal{N}(0, 1\%^2)$,
- the erroneous quadrupole coefficient k_i of each quadrupole is then $k_i = k_{0,i} \cdot \frac{1+\Delta B_i}{1+\Delta E}$, with $k_{0,i}$ being the design value for each of the quadrupoles.

The result of the Monte-Carlo simulation with 1000 samples is shown in Fig. 3.15. For a wide range of combinations of the initial Twiss parameters, the reconstructed emittance is in good agreement with the input emittance (Fig. 3.15 left). The relative standard deviation of the reconstructed emittance is 1% at the design Twiss parameters, and below 8% for mismatch parameters up to $M = 1.5$ (Fig. 3.15 right).

Simultaneous longitudinal profile measurement

During the slice emittance measurements, the images obtained at the four screens can be used to measure the longitudinal profile as well. The longitudinal resolutions at the four screens differ slightly due to the different phase advances in the TDS streak plane (see the parameter $\Delta\mu_{TDS\rightarrow screen}$ in Table 3.3). The best achievable longitudinal resolutions R_t at the screens S1-S4 in dependence of the normalized emittance are shown in Fig. 3.16. The longitudinal resolution has been determined according to Eq. 2.21.

In case no slice emittance measurement but only online longitudinal profile measurement is required, one pair of kicker magnet and off-axis screen can be employed using the same accelerator optics. Both S2 and S3, which provide the best longitudinal resolutions among the four screens, are

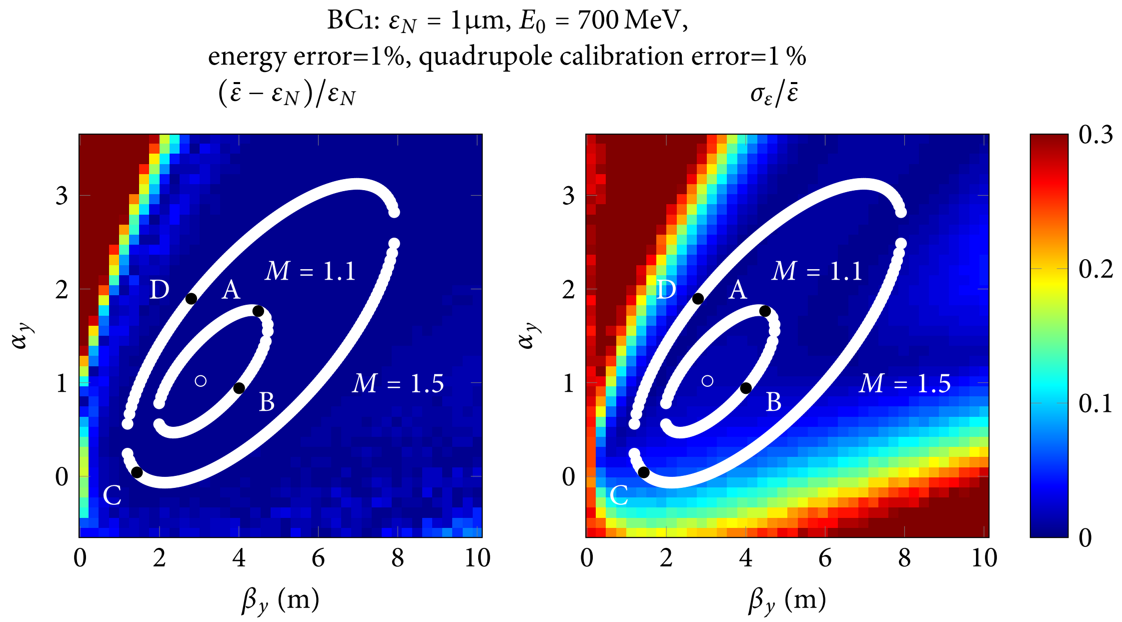

Figure 3.15: Systematic error in slice emittance measurements: influence of erroneous transfer matrices. Monte-Carlo simulations are performed assuming a quadrupole calibration error of 1% and energy measurement error of 1%. Deviation of the mean value of the reconstructed emittances $(\bar{\varepsilon} - \varepsilon_N)/\varepsilon_N$ (left) and the relative standard deviation of the reconstructed emittances $sigma_\varepsilon/\bar{\varepsilon}$ (right) are shown. The colourmap is restricted to a value of 30%.

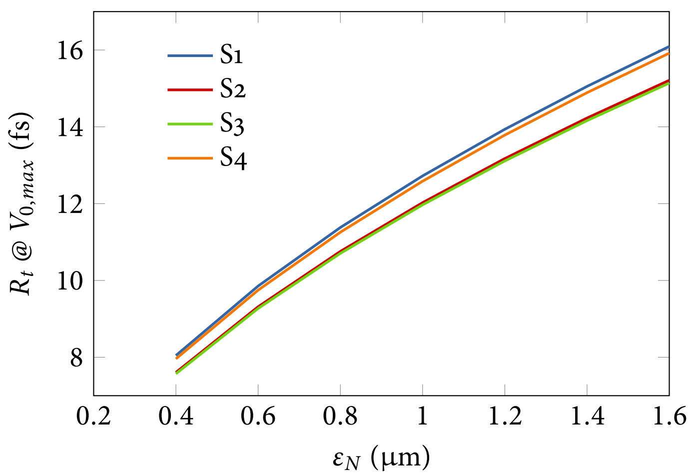

Figure 3.16: Longitudinal resolutions R_t at the four screens S1-S4 in dependence of the normalized emittance ε_N during the slice emittance measurements in the BC1 section. The TDS is assumed to be operated at the maximum effective voltage $V_{0,max}$.

suitable for the online longitudinal profile measurement.

3.3.2 Projected emittance measurement

The 30/76-FODO structure designed for the slice emittance measurement as described in the latter section is applicable for the projected emittance measurement in the vertical plane with the phase advance of $\Delta\mu_y = 76°$ as well. However, online projected emittance measurement in that plane in combined use with the kicker magnets will fail: the electron bunch has typically a total energy spread of $\sim 10^{-2}$ (see Section. 3.4.3), for which the dispersions from the kicker magnets may lead to a huge deviation of the reconstructed emittance. As can be seen in Fig. 3.14 (right), the deviation is above 30% for a large range of $< y_0\delta_0 >$ and $< y_0'\delta_0 >$.

When the kicker magnets are turned off, vertical projected emittance measurement in the 30/76-FODO structure can be performed using the on-axis screens in the four screen stations. This accelerator optics is not suitable for the measurement of the horizontal projected emittance due to the small phase advance of $\Delta\mu_x = 30°$.

More convenient accelerator optics allowing for measurements of the projected emittance in both transverse planes at the same time are favoured. An optics adopting FODO structures with 90° and 76° phase advance per cell in the horizontal and vertical plane (will be denoted as 90/76-FODO), respectively, is chosen (see Fig. 3.17). Measurements will be performed with the on-axis screens in the screen stations, which means the generation of FEL pulses is interrupted. It will be mainly used during the commissioning of the accelerator and for setting up the machine. The optimization procedure of the accelerator optics for projected emittance measurements is described in Appendix B.1.

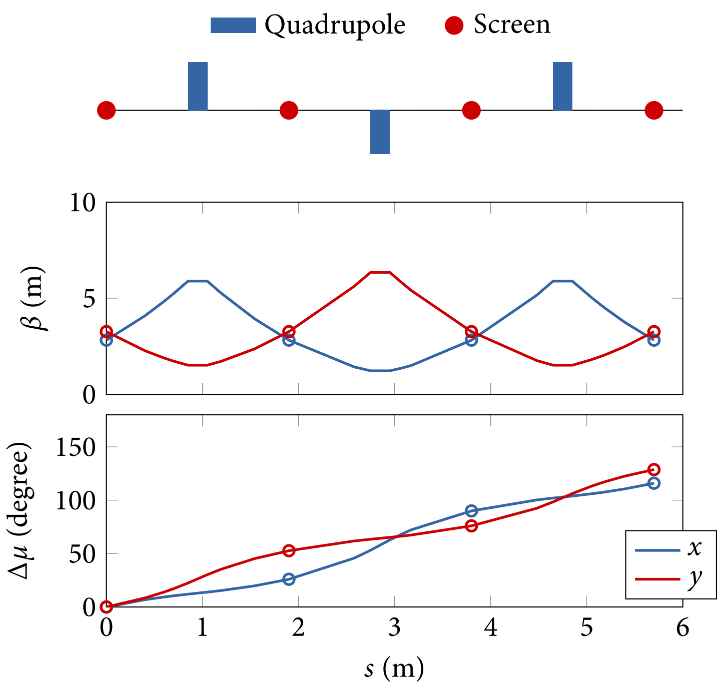

Figure 3.17: Accelerator optics for projected emittance measurements in the BC1 section (90/76-FODO). The kicker magnets are omitted in the plot.

The phase advances between the subsequent screens amount to $\Delta\mu_x = 26°, 90°, 113°$ and $\Delta\mu_y = 52°, 76°, 128°$. The statistical and systematic errors of the reconstructed emittance are analysed in the following.

Due to the different lengths of the FODO cells in the three sections, the optics are slightly different, i.e. the beam sizes on the screen locations are different. The phase advances are exactly the same. In the BC1 and BC2 sections, the optics from the start to the exit of TDS are exactly the same as these for the slice emittance measurement. However, it cannot be achieved in the injector section, since too few quadrupoles are available for optics matching.

statistical error

The standard deviations of the reconstructed emittance resulting from the statistical errors in the beam size measurements are determined using the error propagation method and calculated for different initial Twiss parameters in Fig. 3.18. The relative standard deviations are comparable in the x and y planes. When the optics is matched to the design optics, the relative standard deviations are expected to be ~ 5% in both planes for a typical beam size error of 5%. It can be seen that even for the same mismatch parameters, the relative standard deviations could differ largely. In the two examples shown for a mismatch parameter of $M = 1.5$, the relative standard deviation for the initial Twiss parameter D exceeds by a factor of 2 that for the Twiss parameter C (the values of the Twiss parameters C and D are denoted as black dots in Fig. 3.19).

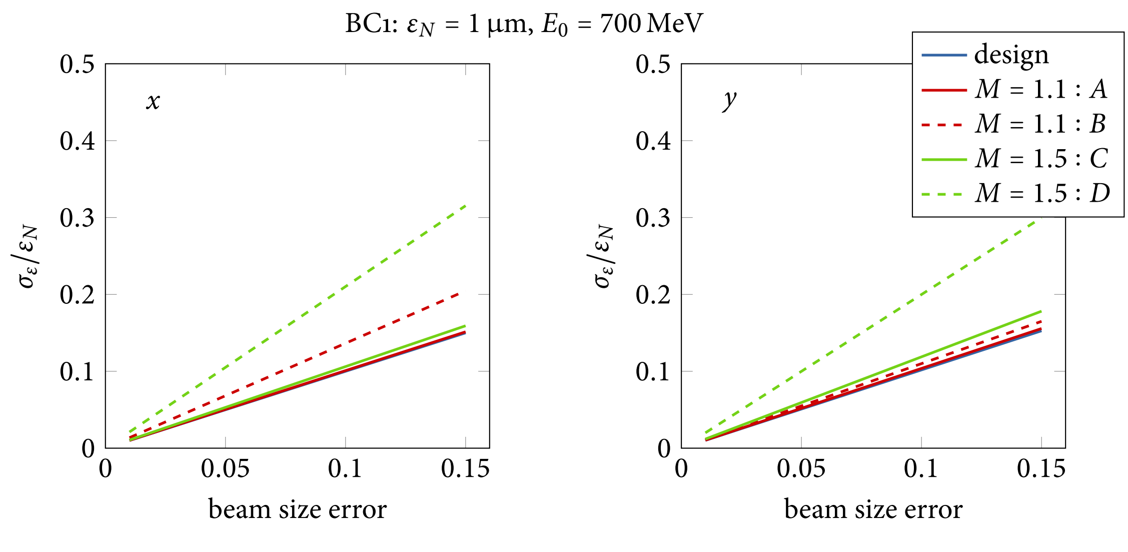

Figure 3.18: Statistical error in projected emittance measurements: error propagation method. The relative standard deviation of the reconstructed emittance $\sigma_\varepsilon/\varepsilon_N$ in the (left) x plane and (right) y plane is shown. Five initial Twiss parameters are considered: the design Twiss parameters (blue), Twiss parameters A and B with $M = 1.1$ (red), and Twiss parameters C and D with $M = 1.5$. The values for A, B, C and D are indicated with black dots in Fig. 3.19.

In order to investigate the statistical errors for a wider range of combinations of the initial beta- and alpha-functions, Monte-Carlo simulations are performed. The procedures and definitions used in the Monte-Carlo simulation are the same as described in Section 3.3.1. Figure 3.19 shows the deviation of the reconstructed emittance in both planes. For initial Twiss parameters with mismatch parameter $M < 1.5$, the deviations are smaller than 3% and 2% in the x and y plane, respectively, which proves the 90/76-FODO to be a robust option.

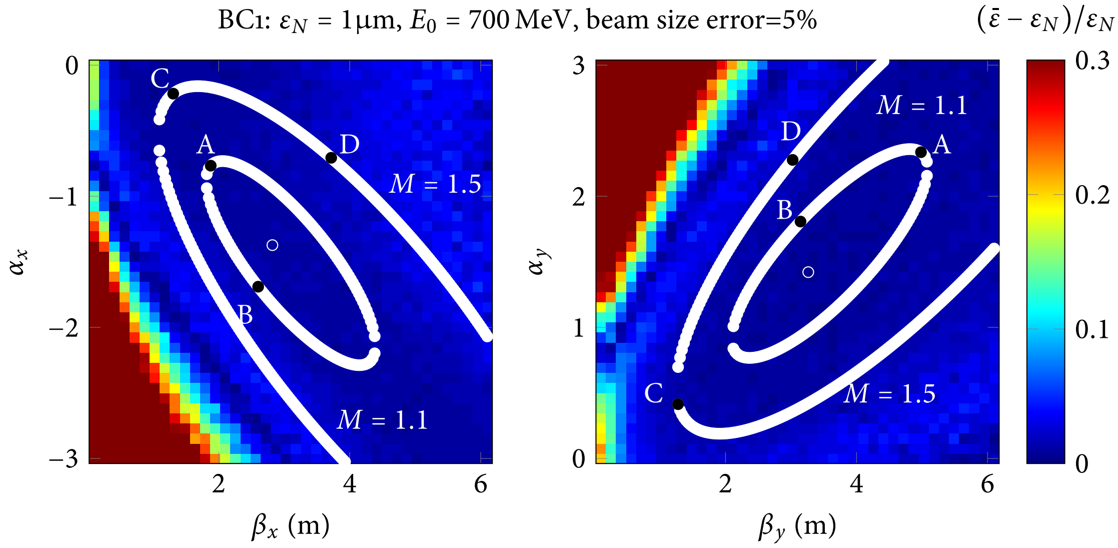

Figure 3.19: Statistical error in projected emittance measurements: Monte-Carlo simulations. Deviation of the mean value of the reconstructed emittances $(\bar{\varepsilon} - \varepsilon_N)/\varepsilon_N$ in the (left) x plane and (right) y plane is shown. The colourmap is restricted to 30%.

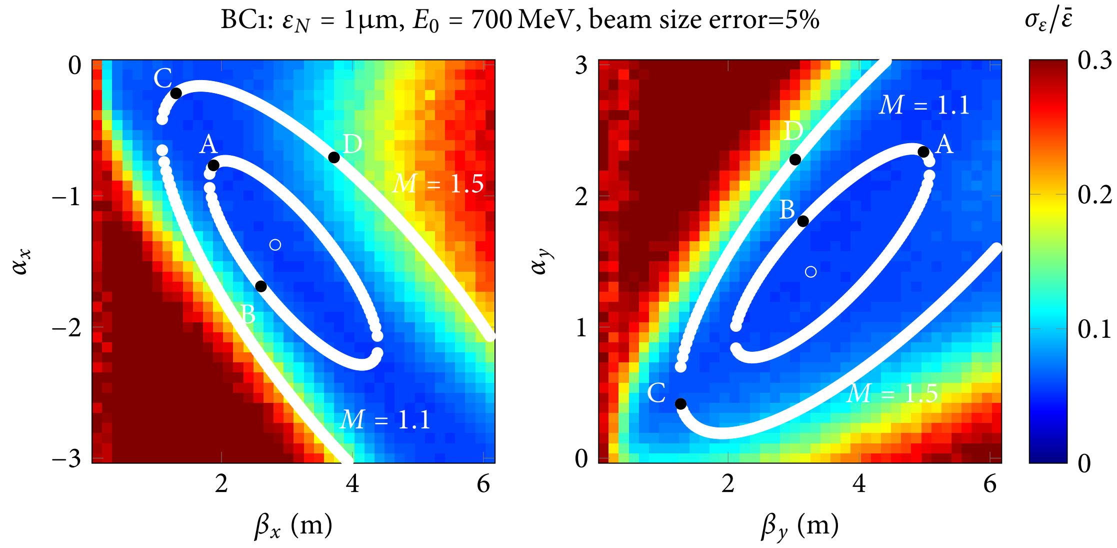

Figure 3.20: Statistical error in projected emittance measurements: Monte-Carlo simulations. The relative standard deviation of the reconstructed emittances $\sigma_\varepsilon/\bar{\varepsilon}$ in the (left) x plane and (right) y plane is shown. The colourmap is restricted to 30%.

The relative standard deviation of the reconstructed emittance determined from the Monte-Carlo simulation is shown in Fig. 3.20. In the x plane (left), the relative standard deviation is 5% for the Twiss parameters C, and increases to 11% for D, although they have the same mismatch parameters. In the y plane (Fig. 3.20 right), the relative standard deviations amount to ~ 6% and ~ 11% for C and D, respectively. In overall, the relative standard deviation in the y plane is slightly smaller than these in the x plane: for initial optics with mismatch parameter $M < 1.5$, the relative standard deviations are below 20% and below 12% in the x and y plane, respectively. It further confirms the phase advance of $\Delta\mu_y = 76°$, which is adopted in the design for slice emittance measurement as well, to be a reliable and robust choice for emittance measurement.

systematic error: screen resolution

The influence of the screen resolution of 10 μm (see Section 3.2.4) on the reconstructed emittance is shown in Fig. 3.21. For a normalized emittance of 1 μm and the design Twiss parameters, the deviations due to the screen resolution are 5% and 4% in the x and y plane, respectively. The impact in the y plane is in general slightly smaller than in the x plane. This might be explained by two reasons: (i) the beta-function at the screen locations is larger in the y plane, which means larger beam sizes with smaller perturbations due to the screen resolution, (ii) the transfer matrix in the y plane with $\Delta\mu_y = 76°$ per FODO cell is more suitable than that in the x plane with $\Delta\mu_x = 90°$ for emittance measurements. As mentioned in Section 3.3.2, the screen resolution can be corrected form the measured beam sizes in a real measurement.

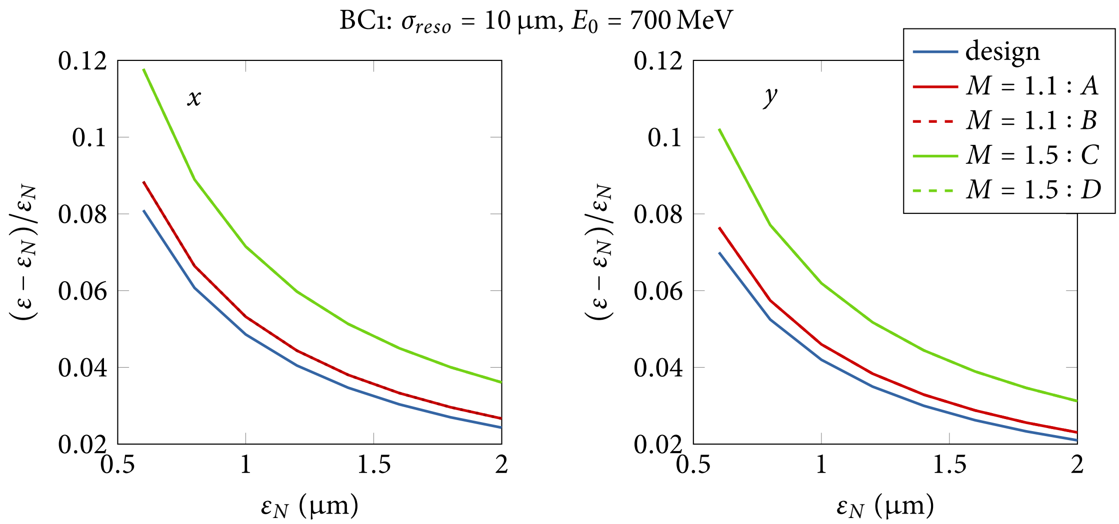

Figure 3.21: Systematic error in projected emittance measurements: influence of the screen resolution. The deviation of the reconstructed emittance $(\varepsilon - \varepsilon_N)/\varepsilon_N$ in the (left) x plane and (right) y plane is shown. The deviation is identical for different combinations of Twiss parameters with the same mismatch parameter.

systematic error: screen calibration

The errors resulting from inaccuracies of the screen calibration are investigated with Monte-Carlo simulation, in which uncorrelated Gaussian errors in the screen calibration are randomized for each of the screens (see Section 3.3.1). The results are similar to those for the statistical errors in the beam size measurements. Assuming the initial Twiss parameters are matched to the design values, a calibration error of 1% at all four screens leads to relative standard deviations of the reconstructed emittance of 1% in both planes.

systematic error: erroneous transfer matrix

The systematic errors due to the errors in the quadrupole field calibration and energy measurement are investigated using Monte-Carlo simulation with the same approaches as described for Fig. 3.15. Additionally, each sample of the 1000 erroneous transfer matrices is used in the reconstruction of the emittance in x as well as y plane, which resembles a real situation of measurements of projected emittance in both planes at the same time. As shown in Fig. 3.22, the reconstructed emittances deviate from the design value with less than 1% in both planes for mismatch parameters of $M < 1.5$.

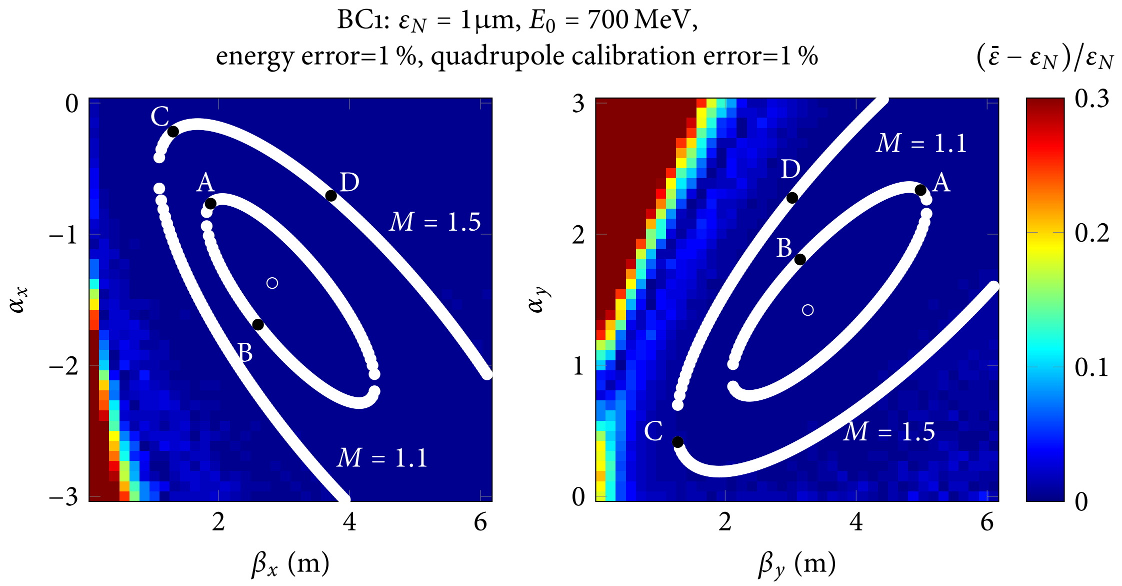

Figure 3.22: Systematic error in projected emittance measurements: influence of erroneous transfer matrices. Monte-Carlo simulations are performed assuming a quadrupole calibration error of 1% and energy measurement error of 1%. Deviations of the mean value of the reconstructed emittances $(\bar{\varepsilon} - \varepsilon_N)/\varepsilon_N$ in the (left) x plane and (right) y plane are shown. The colourmap is restricted to a value of 30%.

As shown in Fig. 3.23, the range of the Twiss parameters providing relative standard deviations below 10% is larger in the x plane than in the y plane. Compared to Fig. 3.20, the x plane is less sensitive to the quadrupole and energy errors than the y plane, whereas the x plane is more sensitive to beam size errors than the y plane.

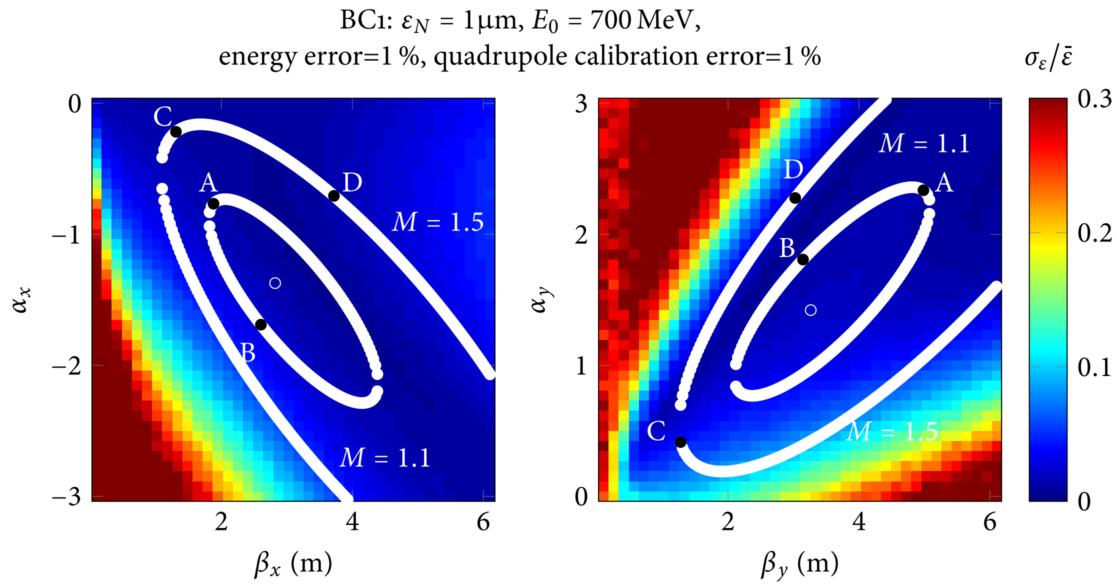

Figure 3.23: Systematic error in projected emittance measurements: influence of erroneous transfer matrices. Monte-Carlo simulations are performed assuming a quadrupole calibration error of 1% and energy measurement error of 1%. Relative standard deviations of the reconstructed emittances $\sigma_\varepsilon/\bar{\varepsilon}$ in the (left) x plane and (right) y plane are shown. The colourmap is restricted to a value of 30%.

3.3.3 Longitudinal phase space measurement

The longitudinal phase space measurements will be performed in the dispersive beamline in the TDS diagnostic sections. A good longitudinal resolution requires in the streak direction a large beta-function at the location of the TDS and a phase advance of about $\Delta\mu = 90° + n \cdot 180°, n \in \mathbb{N}^0$ from the TDS to the screen (see Eq. 2.21). Good energy resolution can be achieved with large dispersion and small beta-function at the location of the screen in the dispersion direction (see Section 2.2.2). For the European XFEL, the electron bunches will possess a large energy spread in the order of ~ 1% as determined from S2E simulations (see Section 3.4). This large energy spread puts especially restrictions on the value of dispersion at the screen to limit the beam size of the dispersed bunch.

In all three TDS diagnostic sections (i.e. in the injector, BC1, and BC2 section), the design optics for the longitudinal phase space measurement is identical to these for the slice emittance measurement in the parts from the start of the section to the last screen S4 in the FODO structures. This allows for a simultaneous measurement of slice emittance (using kicker magnets) and longitudinal phase space[7]. Furthermore, the resemblance of the optics for the two types of measurements eases the machine settings, and saves time when switching between the measurements. The most important parameters of the design optics for the longitudinal phase space measurements in all three TDS diagnostic sections are listed and compared in Table. 3.4.

[7]Except in the BC2 section, where not enough kicker magnets are available in the present design.

Table 3.4: Design parameters for the longitudinal phase space measurements in the three TDS diagnostic sections.

	unit	**Injector**	**BC1**	**BC2**
TDS parameters				
design energy E_0	GeV	0.13	0.7	2.4
$V_{0,max}$	MV	1.84	15.49	27.31
Optics in the streak plane				
β_{TDS}	m	9.5	30.0	49.7
β_{screen}	m	3.0	5.0	3.1
$\Delta\mu_{TDS\rightarrow screen}$	degree	234	262	270
$\sin(\Delta\mu_{TDS\rightarrow screen})$		−0.81	−0.99	−1.00
Optics in the dispersion plane				
β_{screen}	m	3.0	2.6	1.4
D_{screen}	m	0.423	0.539	0.812
S at $V_{0,max}$		−3.8	−16.9	−8.9

Induced energy spread from TDS

As described in Section 2.1.1, the TDS induces energy changes to the electrons inside the bunch. As a result, the slices of the bunch acquire extra induced energy spread, which is then measured together with the initial slice energy spread of the bunch.

Dependencies of the longitudinal resolution R_t (defined in Eq. 2.21), the energy resolution R_E (defined in Eq. 2.43) and the induced slice energy spread σ_{IES} (defined in Eq. 2.44) on the normalized emittance ε_N are shown in Fig. 3.24. With increasing values of the emittance, both resolutions R_t and R_E, as well as σ_{IES} become larger (i.e. worse). In the injector section, the induced energy spread is smaller than the energy resolution, while it is larger than the energy resolution in the BC1 and BC2 section.

Figure 3.25 shows the induced energy spread and the achievable resolutions for different TDS effective voltages V_0. Since the energy resolution R_E does not depend on the TDS effective voltage, it remains constant. The longitudinal resolution R_t is inversely proportional to the TDS effective voltage V_0, whereas the induced energy spread depends linearly on V_0. Improvement of the longitudinal resolution is correlated to an enhancement of the induced energy spread. Depending on the values of the initial slice energy spread of the bunch, the influence of the induced energy spread from TDS on the measurements could vary. For example of the BC1 section, one electron bunch has typically a bunch length of $\sigma_t \sim 300\,\text{fs}$ and slice energy spread of $\sigma_\delta \sim 5\cdot10^{-4}$, which equals to $\sigma_E = 5\cdot10^{-4}\cdot700\,\text{MeV} = 350\,\text{keV}$ (see Section 3.4.3). When the TDS is operated at $V_{0,max}$, the expected longitudinal and energy resolutions amount to $R_t = 12\,\text{fs}$ and $R_E = 57\,\text{keV}$, respectively. The bunch will acquire an induced slice energy spread of $\sigma_{IES} = 144\,\text{keV}$. The measured slice energy spread is then $\sqrt{\sigma_\delta^2 + R_E^2 + \sigma_{IES}^2} = 383\,\text{keV}$ and by a factor of 9% larger than the initial energy spread. The induced energy spread can be reduced by decreasing TDS effective voltage, at the cost of worsen-

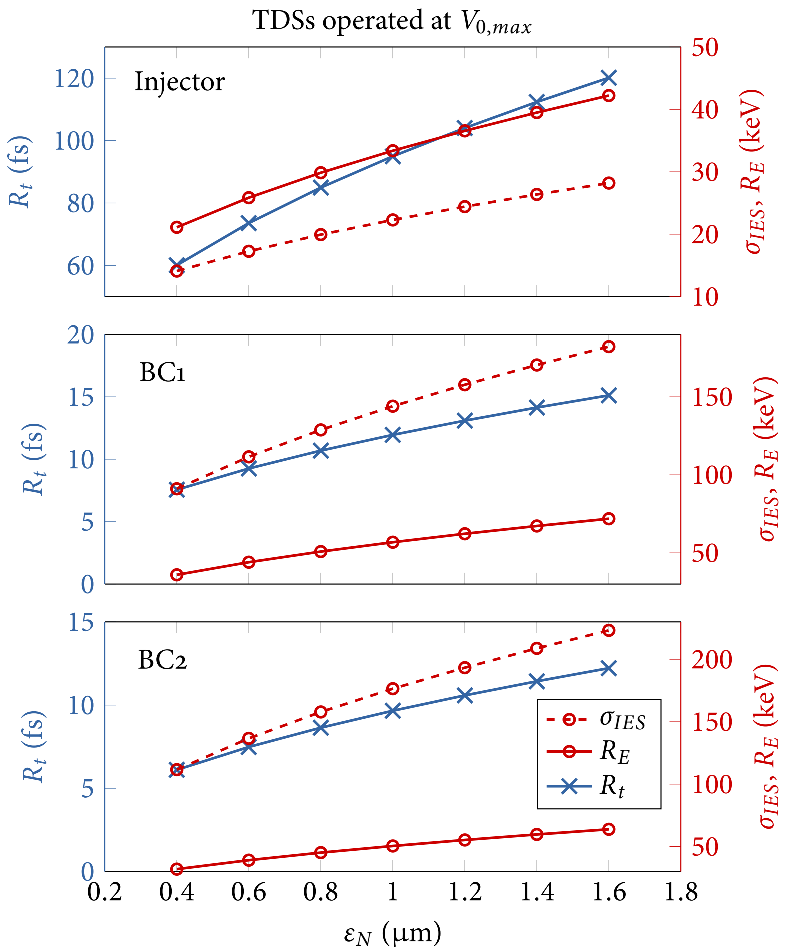

Figure 3.24: Expected longitudinal resolution R_t, energy resolution R_E and induced energy spread σ_{IES} from the TDS for electron bunches with different normalized emittances. In each TDS diagnostic section, the TDS is assumed to be operated with the corresponding maximum effective voltage $V_{0,max}$.

ing longitudinal resolution. At an effective voltage of $V_0 = 0.5V_{0,max}$, the longitudinal resolution of $R_t = 24$ fs is still sufficient to resolve the bunch with a bunch lengths of $\sigma_t \sim 300$ fs. With the induced energy spread reduced to $\sigma_{IES} = 72$ keV, the measured slice energy spread is then 362 keV, which is only by a factor of 3% larger than the initial slice energy spread.

3.4 Simulations with S2E bunch

In the latter Section 3.3, the accelerator optics designed for the different types of measurements have been presented and possible error contributions are discussed. The accuracy of the measurement differs for electron bunches with various parameters, such as emittance and energy spread. Particle tracking with the program `elegant` [Boroo] has been performed to model the measurements and investigate the performance of the TDS diagnostic sections for realistic electron bunches of the

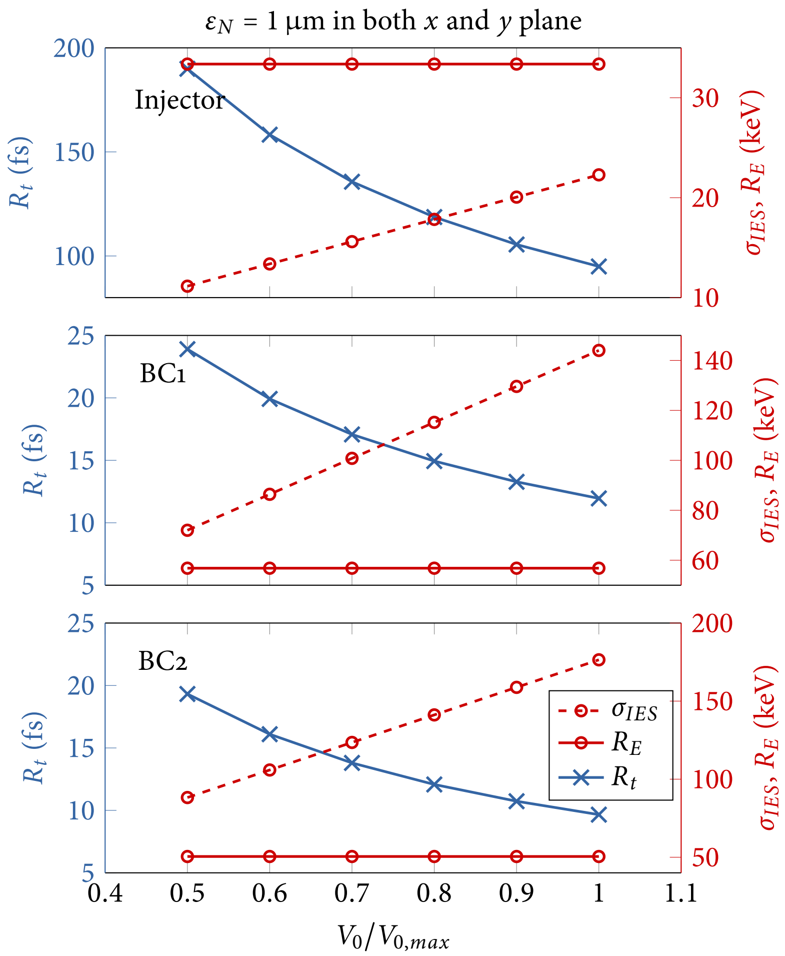

Figure 3.25: Expected longitudinal resolution R_t, energy resolution R_E and induced energy spread σ_{IES} from the TDS for different TDS effective voltages. A normalized emittance of ε_N = 1 µm is assumed in both x and y plane.

European XFEL.

Design RF working points for the European XFEL have been determined by start-to-end (S2E) simulations to provide electron bunches optimized for the generation of FEL photon pulses [BDG14]. In the following, simulation results of measurements in the TDS diagnostic section in the BC1 section are shown as an example. The electron bunch with a bunch charge of 1 nC at the entrance of the TDS diagnostic section is taken from the S2E simulation, and used for simulations of measurements in the TDS diagnostic section. The input particle distribution from the S2E simulation contains 200000 particles. In the simulation for each type of the measurements, the input particle distribution is matched to the design twiss parameter at the entrance of the TDS diagnostic section, and then tracked through the TDS diagnostic section to the position of the screens. The images of the bunch on the screens are simulated and analysed as they would be in a real measurement. A beam size error of 5% is assumed in the simulations for the estimation of the statistical errors using error propagation methods. When not specifically noted, the beam sizes are defined as rms beam sizes, and the emittances are given as normalized emittances with rms values.

3.4.1 Projected emittance measurement

As mentioned in Section 3.3.2, the 30/76-FODO structure designed for the slice emittance measurement is compatible for projected emittance measurement in the vertical plane with the phase advance of $\Delta\mu_y = 76°$ as well, provided that the perturbation of beam size measurements resulting from the dispersion of the kicker magnet is negligible. The S2E bunch of the 1 nC case has an energy spread of $\sigma_\delta = 1.05\%$, as well as correlation terms of $\langle y_0\delta_0\rangle = 8\cdot10^{-8}$ and $\langle y'_0\delta_0\rangle = 1.5\cdot10^{-7}$. As can be seen in Fig. 3.14 (right), the large energy spread and correlation terms can lead to a large deviation in the reconstructed emittance in the online measurement mode using the kicker magnets. Figure 3.26 compares the vertical beam sizes determined from the simulated images on the screens when the kicker magnets are switched on and off. At the second screen S2, where the R_{36} matrix element due to the kicker magnet is as large as 8 mm (see Table 3.3), the vertical beam sizes in the two cases of kicker magnet on and off differ from each other by a factor of ~ 75%. When the kicker magnets are switched off, the reconstructed emittance is in good agreement with the reference[8], whereas it is smaller and deviates by a factor of ~ 14% from the reference value in the case of the kicker magnets switched on. Therefore, the 30/76-FODO structure does not provide reliable projected emittance measurements in the vertical plane in combined use with the kicker magnets.

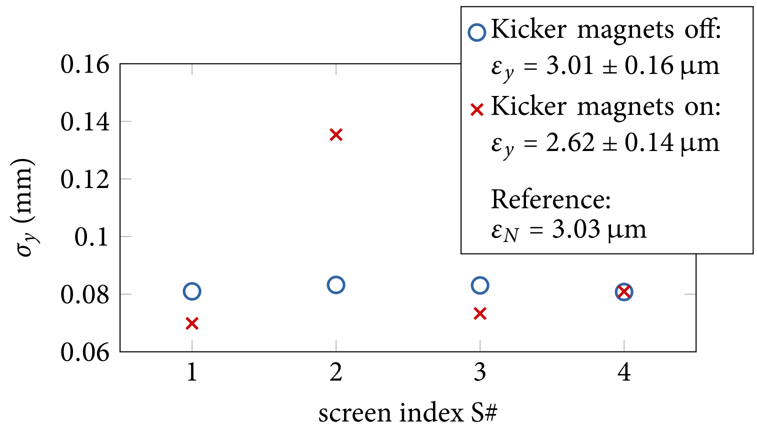

Figure 3.26: Vertical beam size σ_y determined from the simulated images at the screens S1-S4 using the optics with 30/76-FODO structures. Two cases with the kicker magnet switched on (blue) and off (red) are shown. The values of the reconstructed projected emittance are given, and compared to the reference value.

As an alternative, the 90/76-FODO structures will be employed for simultaneous measurements of the projected emittance in both transverse planes (in the off-line measurement mode). Figure 3.27 shows the expected beam sizes from the simulated images and the reconstructed projected emittance in the normalized coordinates (see Eq. 1.26). In both the horizontal and vertical planes, the

[8] Reference: the vertical normalized projected emittance of the input distribution from the S2E simulation.

reconstructed emittances are in good agreement with the reference one. The horizontal emittance amounts to $\varepsilon_x = 975 \pm 49$ nm, while the vertical one is much larger and has a value of 3025 ± 155nm. It is worth noting that in the vertical plane the slice emittance can be measured with the help of the TDS as well. A comparison of the projected and slice emittance from the simulations will be discussed in the following section.

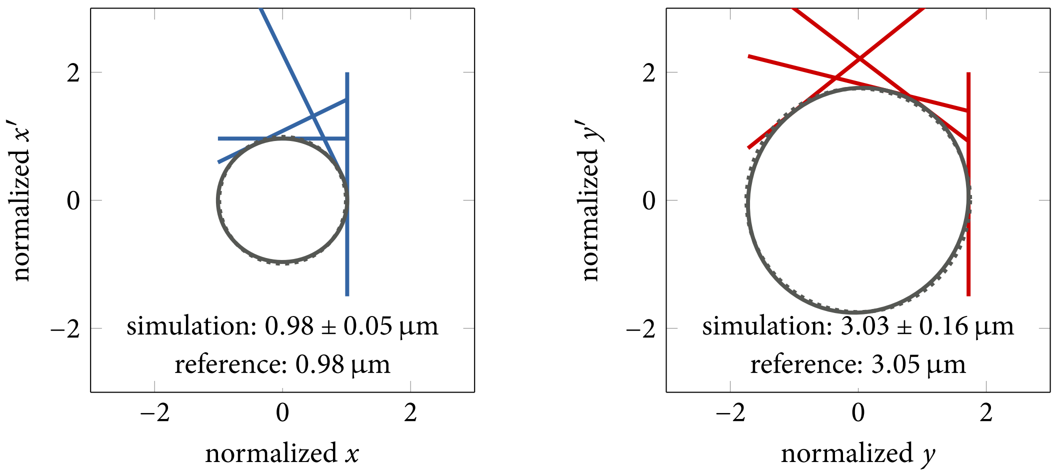

Figure 3.27: Simulation results of projected emittance measurements in the (left) x plane and (right) y plane using the accelerator optics with 90/76-FODO structures. The lines represent the beam sizes measured at the four screens in the normalized coordinates. The solid and dashed ellipses depict the transverse phase space ellipse of the reconstruction and reference, respectively. The values of the normalized emittances are given.

3.4.2 Slice emittance measurement

Simulations of online slice emittance measurements utilizing the TDS, the kicker magnets and the off-axis screens have been conducted. Various aspects in the settings of the diagnostics components (such as the effective voltage of the TDS, the phase of the TDS, etc.), and in the analysis procedure (such as definition of the beam size, determination of the slice width, etc.) are investigated step by step. The particle distribution tracked to the location of the first screen S1 with the TDS and the kicker magnet switched off is taken as a reference for the beam parameters for comparison.

Definition of beam size

The beam size of the electron bunch is commonly defined as the rms value of the profile (rms beam size) or the standard deviation of a Gaussian fit to the profile (Gaussian beam size). The rms beam size describes the standard deviation of the profile, but is very sensitive to the noises in the profile. In contrary, the Gaussian beam size is rarely affected by the noises, but cannot correctly reflect the attributes of the profile when a large discrepancy from a Gaussian shape exists.

Firstly, the influence of the definition of the beam size is investigated in the simulation for the online slice emittance measurement. In the simulation, the TDS is operated approximately at the maximum effective voltage of $V_0 = 15\,\mathrm{MV}$ and at the positive RF zero-crossing φ_+. The central slice of the input distribution, which is the slice containing the mean position of the profile, is matched to the design optics.

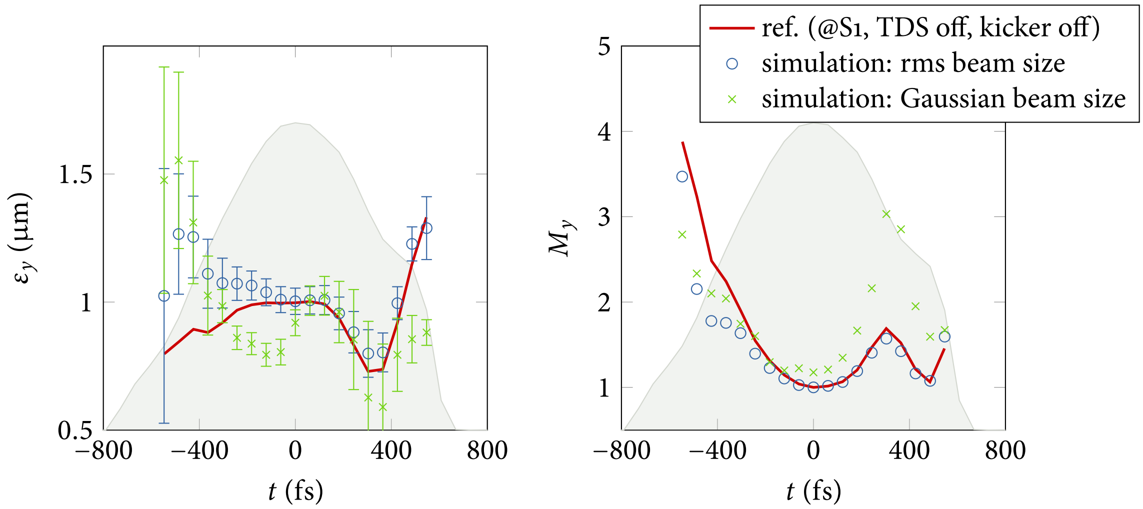

Figure 3.28: Simulation results of the slice emittance and mismatch parameter determined with (blue) rms and (green) Gaussian beam size definitions. The reference particle distribution (red) is obtained at S1 with both the TDS and the kicker magnets switched off in the particle tracking. The grey lines represent the scaled current profile (in arbitrary unit) obtained at the screen S1 in the simulations.

The slice emittance is reconstructed using the rms and Gaussian beam sizes from the simulated images at the four off-axis screens, and compared to the rms slice emittance of the reference particle distribution, as shown in Fig. 3.28. The good agreement between the reconstructed slice emittance with the rms beam size definition and the reference values demonstrates the feasibility of the online slice emittance measurement in the presence of dispersion due to the kicker magnets. The slices in the S2E bunch have an energy spread and correlation terms in the order of $\sigma_\delta \sim 10^{-4}$, $\langle y_0 \delta_0 \rangle \sim 10^{-9}$ and $\langle y_0' \delta_0 \rangle \sim 10^{-9}$. The dispersion arising from the kicker magnet has negligible influence on the reconstructed emittance, as expected in the analytical estimation (see Fig. 3.14 left) and proved in the particle tracking simulation (see Fig. 3.28 left). Deviation of the reconstructed rms emittance is observed in the slices towards the bunch head at the negative time axis, where the slices have large mismatch parameters.

The results with the Gaussian beam size definition show clearly larger deviation from the reference values. Comparison of the slice beam sizes at the screen S1 with the two definitions indicates discrepancies in the beam sizes with a factor of up to ~ 20% (see Fig. 3.29 left). A closer look at the vertical profile of the central slice at screen S1 (Fig. 3.29 right) reveals that the vertical profile does not have a Gaussian shape, and thus cannot be appropriately described by the Gaussian beam size. The definition of rms beam size is adopted in the rest of the simulations.

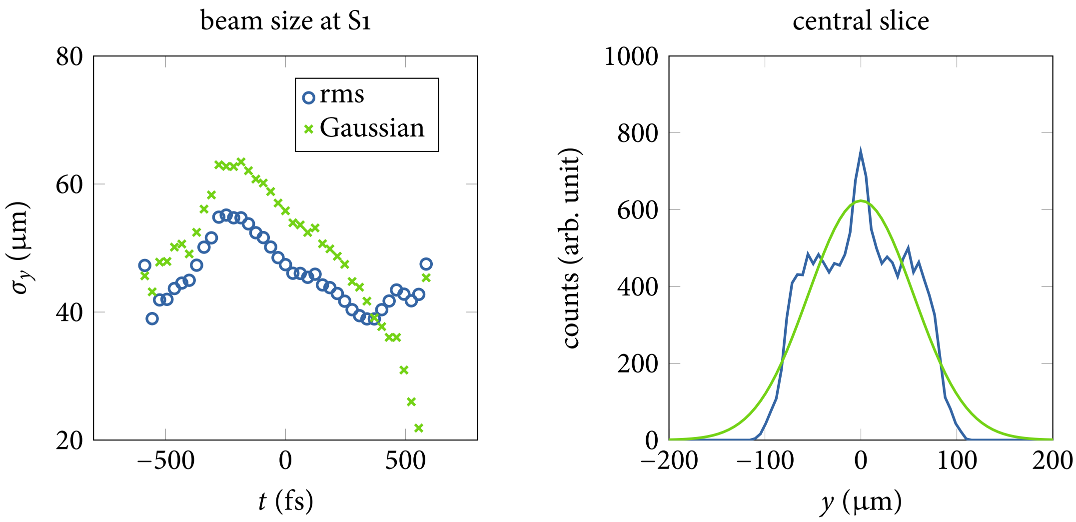

Figure 3.29: (Left) Vertical rms and Gaussian slice beam sizes determined from the simulated image at S1. (Right) Vertical beam profile of the central slice (blue) and its Gaussian fit (green).

Slice width

The emittance of one slice is reconstructed from the beam sizes of this slice measured at the four screens. In order to keep consistency of each slice, the four simulated images are subdivided into equal numbers of slices with the same slice width. The central slice is defined as the slice containing the mean position of the bunch as its centre. The width of the slices should be chosen according to two criteria: (i) the slice width should exceed the longitudinal resolution R_t at the screen to be capable of resolving the slices, (ii) the slice width should be small enough to display the evolution of the slice emittance along the bunch. Due to the different horizontal phase advances $\Delta\mu_{TDS\rightarrow screen}$ for the screens S1-S4 in the streak plane (see Table 3.3), the longitudinal resolutions at the four screens differ slightly from each other. In the accelerator optics designed, the first screen S1 provides the worst longitudinal resolution among them, and therefore defines the slice width.

Simulation results with the TDS operated at an effective voltage of $V_0 = 15$ MV are displayed in Fig. 3.30. From the simulation, the bunch length σ_t and the longitudinal resolution R_t at S1 is determined to be 302 fs and 15 fs, respectively. Three slice widths Δt_{slice} are considered in the reconstruction, as well as in the reference particle distribution for comparisons. For the slice widths of $\Delta t_{slice} = 60$ fs (equals to $4R_t$) and $\Delta t_{slice} = 30$ fs (equals to $2R_t$), the reconstructed slice emittances are in good agreement in most slices. Only at the very ends of the bunch (at $t \approx \pm 580$ fs), the details cannot be resolved in the case of $\Delta t_{slice} = 60$ fs. When the slice width is reduced to $\Delta t_{slice} = R_t = 15$ fs, local oscillations of the slice emittance start to appear in the reference distribution. Comparison of the mismatch parameters is shown in Fig. 3.31. It can be further concluded that the slice width definitions of $\Delta t_{slice} = 60$ fs and $\Delta t_{slice} = 30$ fs yield comparable results. In the following studies, the slice width of $\Delta t_{slice} = 60$ fs is used.

TDS RF zero-crossing phases

In order to examine the influence of the initial correlation in the transverse-longitudinal plane on the slice emittance measurement, simulations with the S2E bunch have been performed with the TDS operated at both RF zero-crossings ψ_+, ψ_-. In both cases, the TDS is assumed to be operated at the maximum effective voltage $V_{0,max}$ and the slice width is defined as $\Delta t_{slice} = 60\,\text{fs}$. As shown in Fig. 3.32, the reconstructed slice emittance and the slice mismatch parameter are consistent in the cases of ψ_+ and ψ_-, which implies that there is no pronounced initial correlation inside the bunch.

In the slices residing at the coordinates $t \geq -300\,\text{fs}$, where the mismatch parameters are $M \leq 2$, the reconstructed slice emittances are in agreement with the reference values (within the error bars). At $t < -300\,\text{fs}$, the mismatch parameter increases rapidly up to $M = 4$ and the reconstructed slice emittances deviate from the reference values by a factor of up to 50%. However, it is very likely that these slices at $t < -300\,\text{fs}$ may not contribute to the FEL gain, as they contain altogether a fraction of 15% of the total charge of the bunch and the currents of these slices are below 50% of the peak current of the bunch.

Compared to the projected emittance of $\varepsilon_y = 3.05\,\mu\text{m}$ in the y plane as shown in Fig. 3.27 (right),

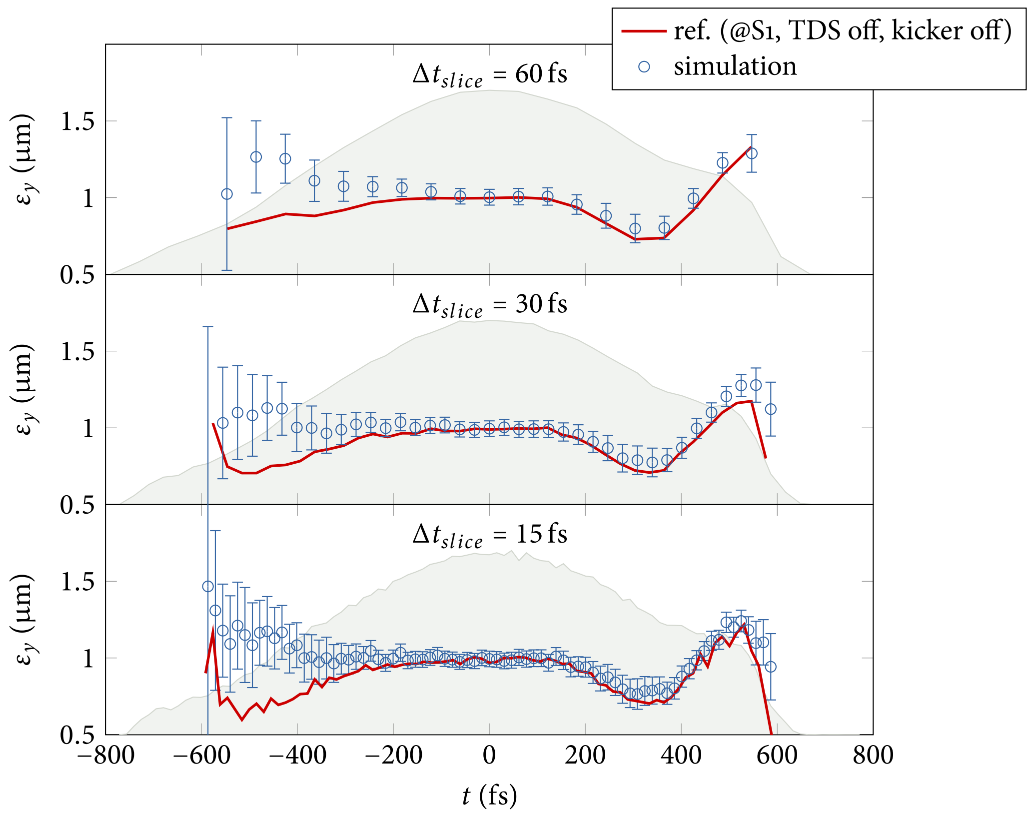

Figure 3.30: Slice emittance ε_y determined for three different slice widths Δt_{slice}. From top to bottom, the slice width Δt_{slice} relates to the longitudinal resolution R_t at S1 as $4R_t$, $2R_t$ and R_t accordingly. The grey lines represent the scaled current profile (in arbitrary unit) obtained at the screen S1 in the simulations.

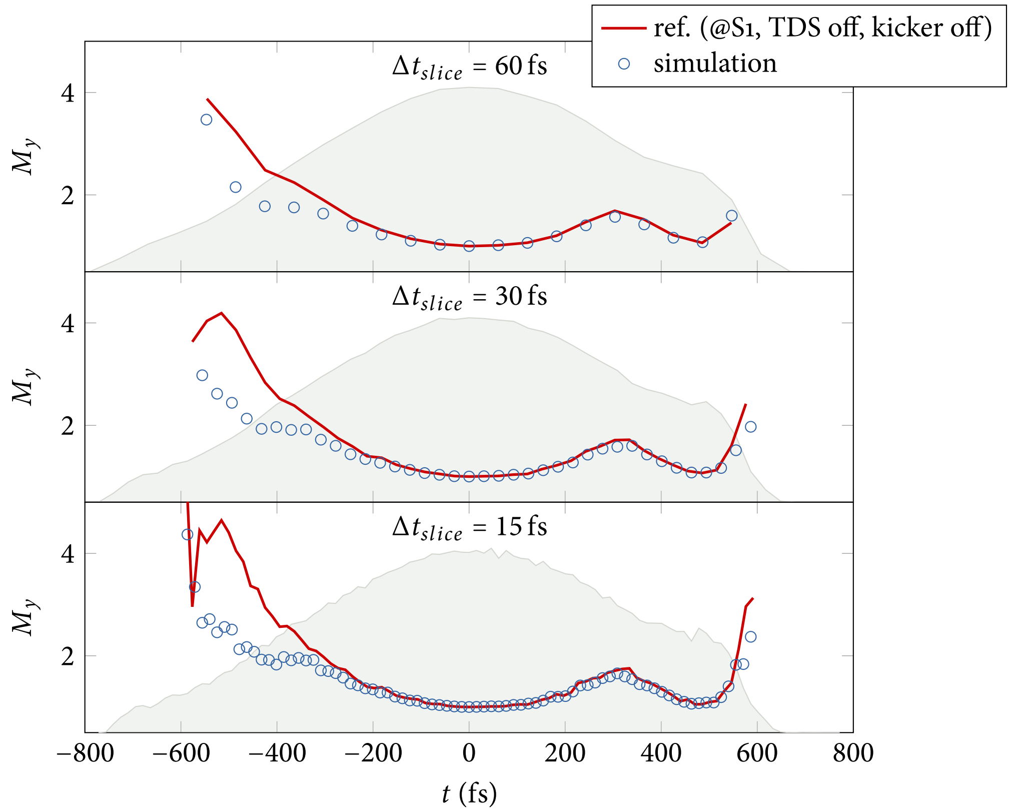

Figure 3.31: Slice mismatch parameter M_y determined for three different slice widths Δt_{slice}. From top to bottom, the slice width Δt_{slice} relates to the longitudinal resolution R_t at S1 as $4R_t$, $2R_t$ and R_t accordingly. The grey lines represent the scaled current profile (in arbitrary unit) obtained at the screen S1 in the simulations.

the slice emittances in the y plane are significantly smaller, for example the value of the emittance of the central slice is only ~ 32% of that of the projected emittance. Reason for the large deviations can be explained by possible offsets of the slices in position and angle. It can be seen that the projected emittance may be an overestimated parameter for the quality of the beam, and measurements of slice emittance are necessary to comprehensively characterize the electron bunch.

TDS effective voltages

The longitudinal resolution scales inversely with the effective voltage V_0 of the TDS (see Eq. 2.21). A weak streaking effect of the TDS could lead to overlapping of the adjacent slices and thus a poor longitudinal resolution. The overlapping of the slices induces furthermore perturbations in the measured slice beam sizes and results eventually in inaccuracies in the reconstructed slice emittance.

Two TDS effective voltages have been studied. From the simulations, the effective voltages of V_0 = 15 MV and V_0 = 4 MV are determined to provide a corresponding longitudinal resolution of R_t = 15 fs and R_t = 55 fs at S1, respectively. The slice width is chosen as Δt_{slice} = 60 fs, which equals approximately to the longitudinal resolution in the case of V_0 = 4 MV.

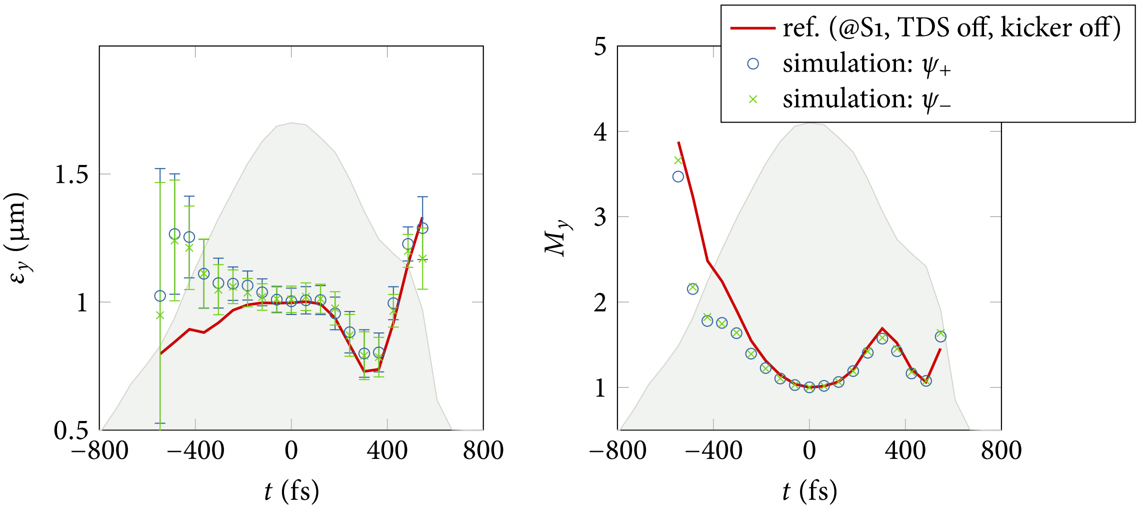

Figure 3.32: Slice emittance ε_y and mismatch parameter M_y determined at both TDS RF zero-crossing phases ψ_+ and ψ_-. The TDS is assumed to be operated at the maximum effective voltage $V_{0,max}$. In both cases, a slice width of Δt_{slice} = 60 fs is chosen, which equals to $4R_t$. The grey lines represent the scaled current profile (in arbitrary unit) obtained at the screen S1 with the TDS RF phase set to ψ_+ in the simulations.

The simulation results are shown in Fig. 3.33. In the slices in the range of -200 fs $< t <$ 400 fs, the reconstructed slice emittances and slice mismatch parameters are in agreement with the reference values (within the error bars) in both cases of V_0 = 15 MV and V_0 = 4 MV. Large discrepancy is observed in the case of V_0 = 4 MV in the slices towards the negative end of the time axis ($t < -200$ fs). In these slices, the reconstructed slice emittance is by a factor of more than 100% larger than the reference value, although the mismatch parameters in these slices are smaller than M = 1.5. The reason for the large discrepancy in these slices is possibly their larger initial beam sizes σ_{x_0} in the streak direction. Figure 3.34 shows the horizontal slice beam size σ_{x_0} in the streak direction of the reference distribution. For comparison, the uncalibrated equivalent slice width Δx_{slice} at S1, which is defined as $\Delta x_{slice} = S \cdot c\Delta t_{slice}$ with S the streak parameter and c the speed of light, is indicated for the case of V_0 = 4 MV as well. It is interesting to note that some slices have initial slice beam sizes σ_{x_0} larger than the equivalent slice width Δx_{slice}, even though the slice width is deliberately chosen with a value equivalent to the longitudinal resolution R_t as $\Delta x_{slice} = S \cdot c\Delta t_{slice} = S \cdot cR_t$. Successful reconstruction of slice emittance can be achieved in the slices where the initial slice beam size σ_{x_0} is smaller than the equivalent slice width Δx_{slice}. When σ_{x_0} becomes comparable to and exceeds Δx_{slice}, overlapping of the slices cannot be avoided, resulting in large discrepancy of the reconstructed slice emittance. For the case of V_0 = 15 MV with an equivalent slice width at S1 of 347 µm, the TDS streak effect is strong enough to minimize the overlapping of the adjacent slices.

Matching of the slices

It has been seen in the latter studies that the reference particle distribution has varying twiss parameters along the slices. Matching of the beam optics can only be performed for one set of values of twiss

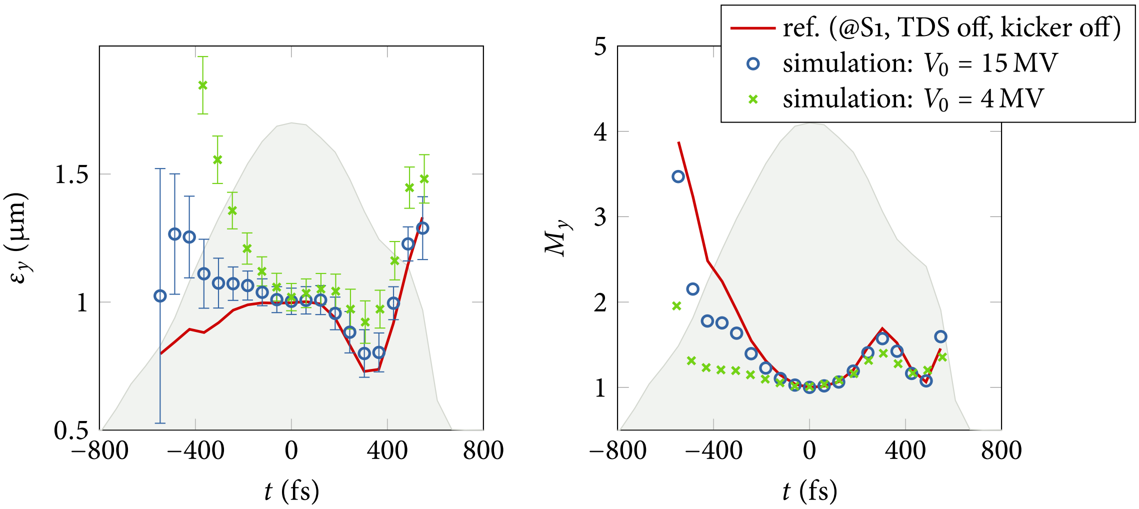

Figure 3.33: Slice emittance ε_y and mismatch parameter M_y determined from simulations with the TDS operated at the effective voltages of (blue) V_0 = 15 MV and (green) 4 MV. The grey lines represent the scaled current profile (in arbitrary unit) obtained at the screen S1 with the TDS effective voltage of V_0 = 15 MV in the simulations.

parameters due to the variation of the twiss parameters in the slices along the bunch. It is common to match the central slice of the bunch, the slice containing the peak current[9] or the projection. For example, when the central slice is matched to the design twiss parameters (see, e.g., Fig. 3.31), which is in particular for the S2E bunch at the same time the case of matching the slice containing the peak current, the mismatch parameter increases up to M = 4 towards the ends of the bunch. Figure 3.35 compares the simulation results using input distributions with matched central slice and matched projection. No obvious difference is observed in the two cases. Since the twiss parameters of the central slice are similar to these of the projected bunch, the two different matching procedures do not differ much from each other. The evolutions of the slice mismatch parameters in the reference distribution of the case with matched central slice (red solid) and matched projection (red dashed)are comparable.

3.4.3 Longitudinal phase space measurement

Longitudinal phase space measurements will be performed in the dispersive beamline. In addition to the longitudinal phase space, further bunch parameters can be obtained from the measurements: the longitudinal profile, the energy profile and the slice energy spread. Simulations using the S2E bunch with a bunch charge of 1 nC have been performed. The TDS effective voltage was set to V_0 = 15 MV.

[9]The slice containing the peak current is more likely to contribute to the generation of FEL pulses, since high peak current is desired for the FEL process.

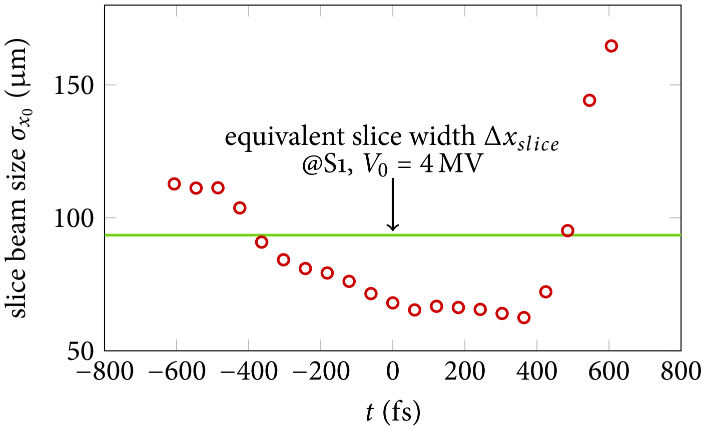

Figure 3.34: Initial horizontal slice beam size σ_{x_0} determined from the reference particle distribution. The equivalent slice width Δx_{slice} at S1 in the case of $V_0 = 4\,\text{MV}$ is indicated for comparison.

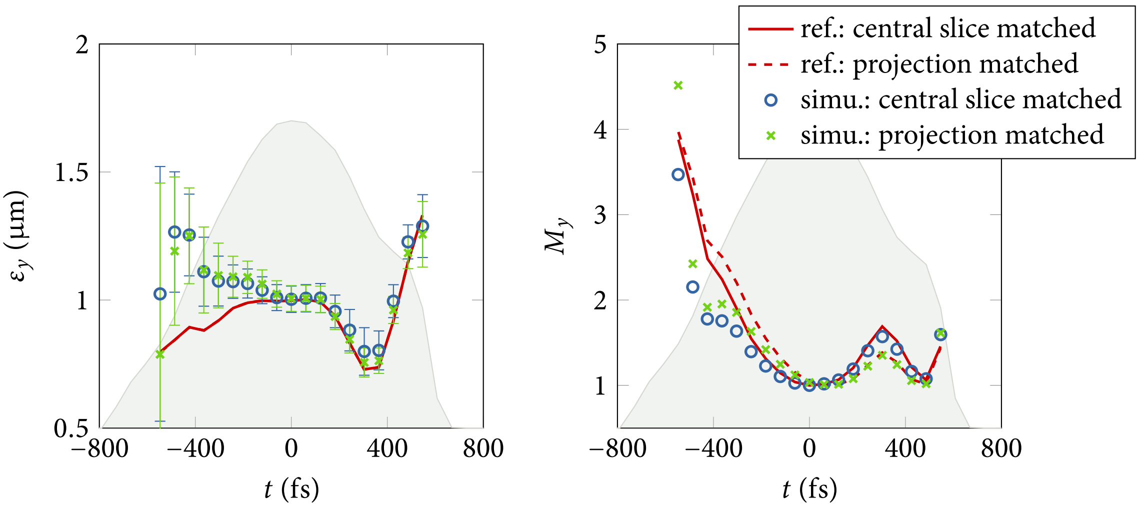

Figure 3.35: Slice emittance ε_y and mismatch parameter M_y determined from simulations using input particle distribution with (blue) matched central slice and (green) matched projection. The slice parameters of the reference particle distribution with (red solid) matched central slice and (red dashed) matched projection are shown. The TDS is assumed to be operated at an effective voltage of $V_0 = 15\,\text{MV}$, and the slice width is chosen as $\Delta t_{slice} = 60\,\text{fs}$. The grey lines represent the scaled current profile (in arbitrary unit) obtained at the screen S1 using a bunch with matched central slice in the simulations.

Calibration

Calibration of the streak parameter S is simulated by determining the horizontal position of the bunch centre on the screen in dependence of the change of the TDS RF phase around the zero-crossing (see Eq. 2.36). Calibration of the dispersion D_y at the screen location is simulated by recording the vertical position of the bunch centre in dependence of the change in the current of the dipole magnet (see Eq. 2.43). The simulation results of the calibrations are shown in Fig. 3.36. The obtained calibration constants are comparable to the design values as listed in Table 3.4. Using the streak parameter obtained from the simulation, the longitudinal resolution measurement can be simulated (see Eq. 2.21) and has been determined to be $R_t = 12\,\text{fs}$.

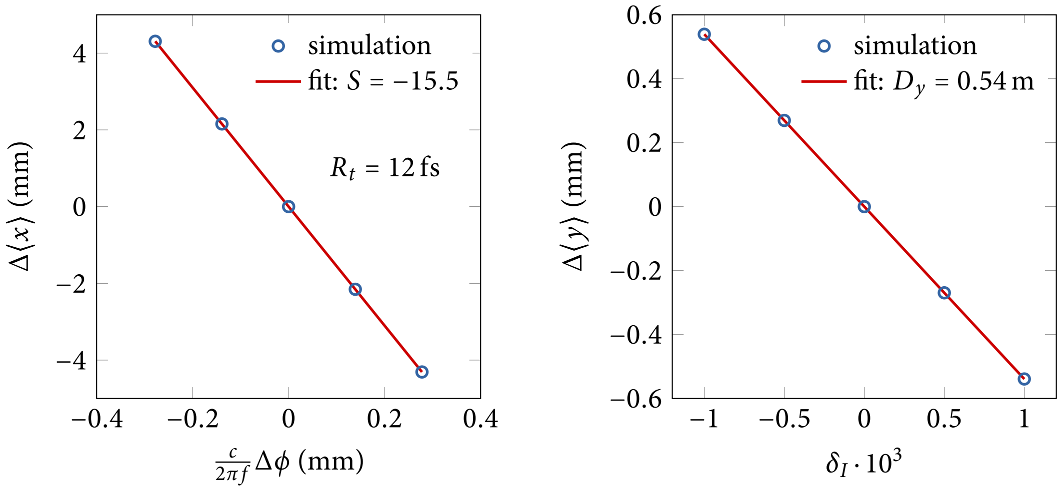

Figure 3.36: Simulation of the calibration measurement for (left) the streak parameter S and (right) the vertical dispersion D_y in the longitudinal phase space measurement. In the calibration of the streak parameter, the horizontal position change of the bunch $\Delta\langle x\rangle$ at the screen is determined for different TDS RF phases. The TDS phases are changed to an offset $\Delta\phi$ from the zero-crossing phase, and scaled to $\frac{c}{2\pi f}\Delta\phi$ with c being the speed of light and f the frequency of the TDS. The linear fit to the simulation data yields the streak parameter. The longitudinal resolution R_t at the screen is determined to be 12 fs from the simulation. In the calibration of the dispersion, the current of the dipole magnet is changed by δ_I and the corresponding vertical position change of the bunch $\Delta\langle y\rangle$ is recorded. The linear fit yields the additive inverse value of the dispersion.

Longitudinal phase space

The longitudinal phase space can be then reconstructed by calibrating the horizontal and vertical axis of the simulated image on the screen with the calibration constants. Figure 3.37 compares the reconstruction at the screen with the reference longitudinal phase space of the input particle distribution at the entrance of the TDS. The colour code of the simulated image scales with the electron density. Very good agreement has been achieved, except in the leading part (at $t < -600\,\text{fs}$) and trailing part (at $t > 550\,\text{fs}$) of the bunch, which contain only a fraction of 2% and 3% of the total charges in the bunch, respectively.

Projection of the image onto the two axis yields the longitudinal and energy profile (see Fig. 3.38). Both profiles are in excellent agreement with these of the reference particle distribution. The rms bunch length of $\sigma_t = 304\,\text{fs}$ and rms energy spread of $\sigma_\delta = 10.5 \cdot 10^{-3}$ determined from the profiles are within a deviation of < 1% compared to the reference values.

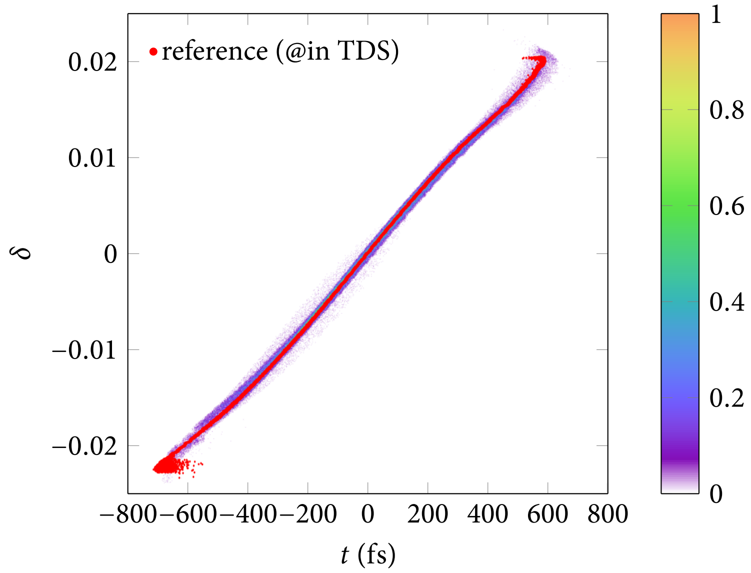

Figure 3.37: Calibrated image from the simulation representing the longitudinal phase space. The colour code of the image scales with the electron density. The longitudinal phase space of the reference particle distribution at the entrance of the TDS is shown in red.

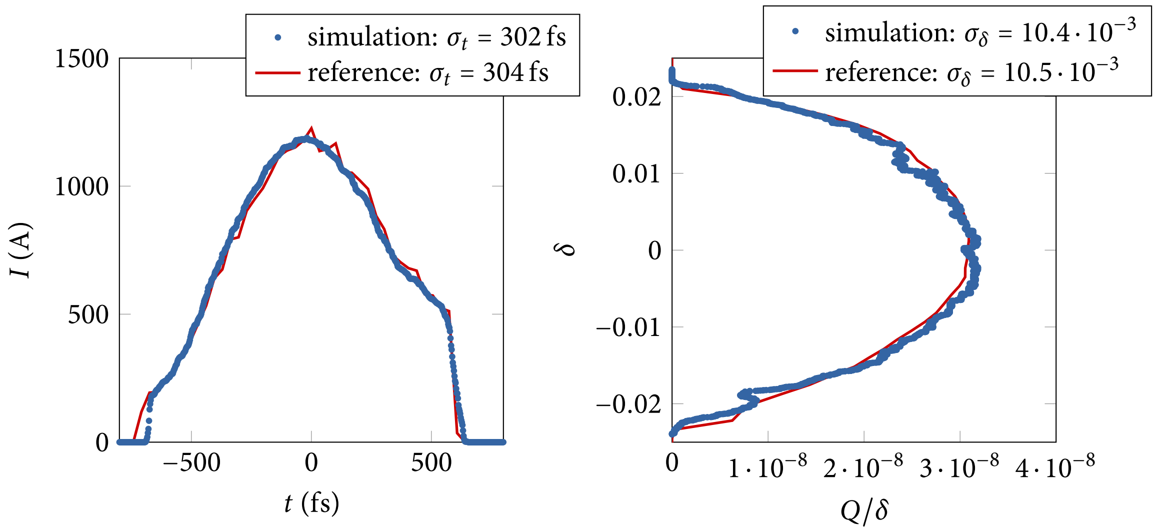

Figure 3.38: Longitudinal current profile (left) and energy profile (right) obtained from the simulated image as shown in Fig. 3.37.

Slice energy spread

When the simulated image of the longitudinal phase space is divided into longitudinal slices, the slice energy spread can be derived from the measurement as well. Firstly, a slice width of $\Delta t_{slice} = 60\,\text{fs} = 5R_t$ is chosen. As shown in Fig. 3.39 (left), the rms slice energy spread of the simulated longitudinal phase space (blue dotted) is compared with that of the reference particle distribution at the entrance of the TDS (red solid, noted as @in TDS). All slices of the simulation display significantly larger energy spreads than those of the reference. The same behaviour is observed in the results with smaller slice widths of $\Delta t_{slice} = 30\,\text{fs} \approx 2.5R_t$ and $\Delta t_{slice} = 10\,\text{fs} \approx R_t$ as well (see Fig. 3.39 middle and right). In all three cases with different definitions of the slice width, the evolution of the slice energy spread along the slices from the simulation has similar shape to that of the reference. With smaller slice width, the discrepancy of the simulation from the reference becomes larger. It is worth to note that the slice energy spreads decrease with reduced slice width in both the simulation and reference. It can be explained by the fact that the large energy chirp (correlation in (t, δ)) of the bunch contributes a lot to the rms value of the energy distribution in the slices.

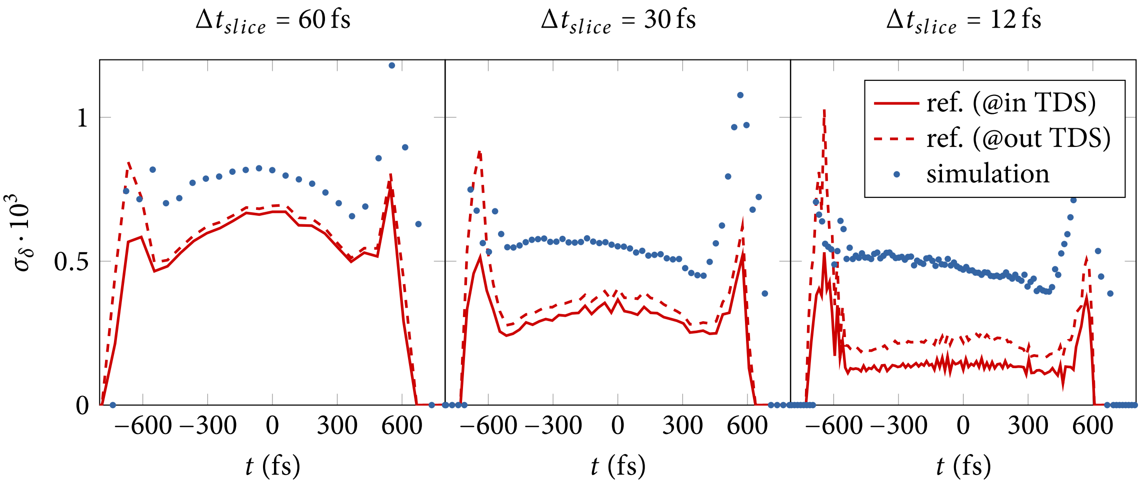

Figure 3.39: Slice energy spread determined from: (red solid) reference particle distribution at the entrance of the TDS, (red dashed) reference particle distribution at the exit of TDS and (blue dot) simulated image as shown in Fig. 3.37. From left to the right, the different definitions of the slice width Δt_{slice} relate to the longitudinal resolution on the screen as $5R_t$, $2.5R_t$ and R_t, respectively.

In order to understand the discrepancy, the particle distribution directly at the exit of the TDS (noted as @out TDS) is taken as a second reference and its slice energy spread is plotted in Fig. 3.39 as well (red dashed). The bunch at the exit of the TDS has slightly increased slice energy spread resulting from the induced energy gain from the TDS as expected from Eq. 2.44. However, the induced energy spread from the TDS σ_{IES} is in the order of $\sigma_{IES} \sim 10^{-4}$ and still cannot explain the large discrepancy between the slice energy spreads of simulations and reference.

Another speculation on the reason for the discrepancy is the initial vertical beam size σ_y^0 of the slices in the dispersion direction. The measurable beam size from the simulated image is given as $\sigma_y = \sqrt{(\sigma_y^0)^2 + D_y^2\sigma_\delta^2 + D_y^2\sigma_{IES}^2}$, from which the energy spread is then determined as σ_y/D_y. As a result, the derived energy spread is actually larger than the real one. In a real longitudinal phase space measurement, the initial vertical beam size σ_y^0 in the slices is not accessible and cannot be corrected for the calculation of the slice energy spread[10]. With the help of `elegant` simulations, such virtual beamline has been designed. The correction to the slice energy spread due to the initial slice beam size is estimated to be approximately $\sigma_y^0/D_y = 0.05 \cdot 10^{-3}$, which does not account for the large discrepancy as well.

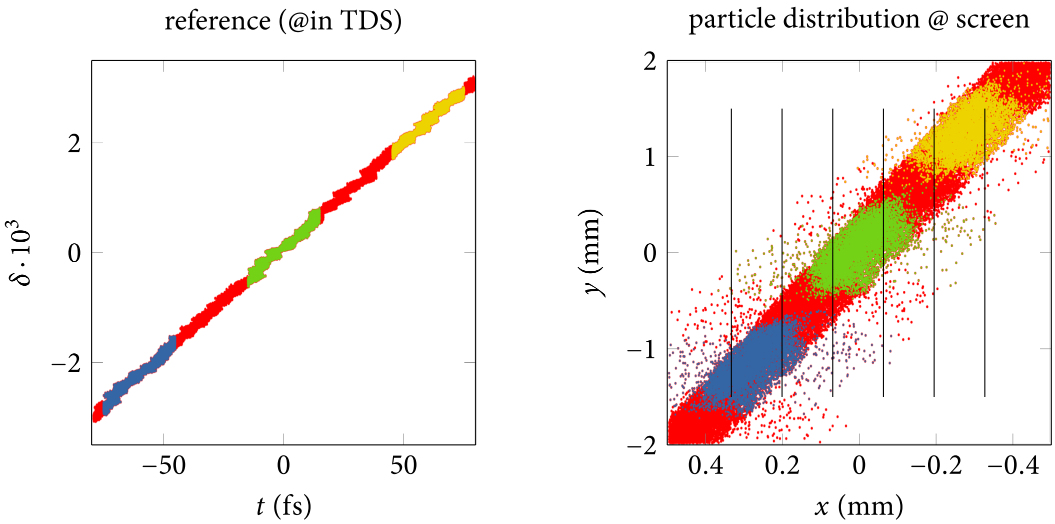

Figure 3.40: (Left) Longitudinal phase space of the central part of the reference particle distribution at the entrance of the TDS. Electrons in three different slices are marked in blue, green and yellow. Slices with a separation of $2 \cdot \Delta t_{slice}$ from each other are highlighted for clarification. (Right) Tracked particle distribution at the screen in the transformed longitudinal phase space (x, y). The horizontal and vertical axis can be then calibrated to t and δ, respectively. The vertical black lines represent the subdivision of the slices, which is applied for the determination of the slice energy spread presented in Fig. 3.39.

Figure 3.40 (left) shows electrons in three slices (marked as blue, green and yellow) in the longitudinal phase space of the reference particle distribution. The tracked distribution in the transverse plane (x, y) (the transformed longitudinal phase space) at the screen is shown in Figure 3.40 (right), with the electrons in the three slices being marked accordingly. It can be seen that the original slices are distorted in the transformed coordinates (x, y). The initial finite slice beam size in the streak direction x causes the shearing of the slices in that direction. Slicing of the bunch in the x direction, which is represented by the black lines in Fig. 3.40 (right), is not appropriate.

Special slicing procedure

A special slicing procedure has been introduced to take into account the effect of the finite slice beam size in the streak direction. As illustrated in Fig. 3.41 (left), the mean position of each row on the energy axis (blue line) is determined from the simulated image. The boundary of the slices are parallel to the time axis, in contrast to the common slicing procedures where the slices are perpendicular to

[10] In order to measure the initial vertical beam size in the slices, it requires to switch off the dipole magnet and measure the slice beam size at a screen downstream of the dipole magnet in a straight beamline that has the same beamline layout as the dispersive beamline.

the time axis. The definition of the slice width is illustrated in the plot. In order to have slices with identical slice width, the boundaries of the slices do not necessarily have equal distances any more. Comparison of the slice boundaries defined using the special slicing procedure with the tracked electrons in the three slices is shown in Fig. 3.41 (right). The central slice around $y = 0$ contains 82% of the electrons in the original green slice, while in case of the common slicing only 74%.

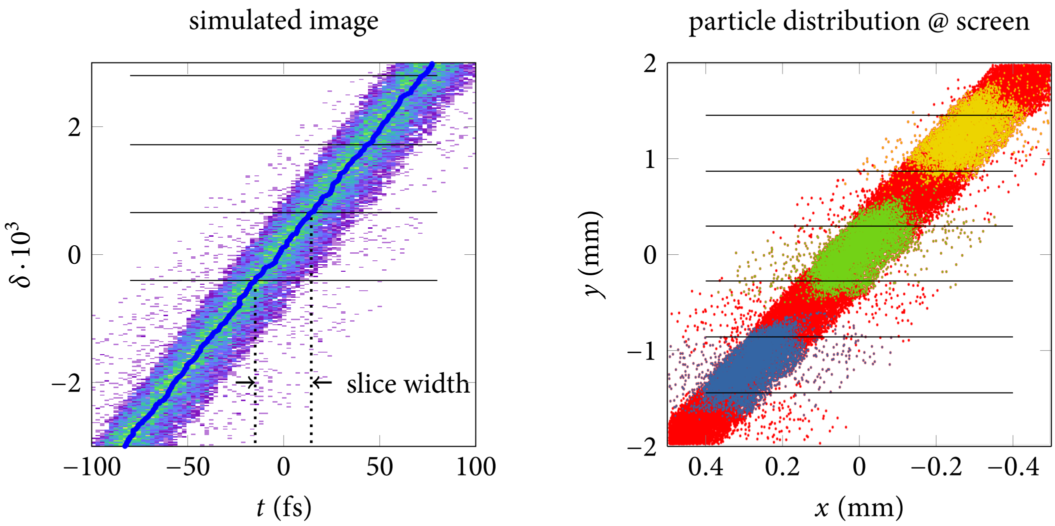

Figure 3.41: (Left) Principle of the special slicing procedure for determining the slice energy spread. The mean position of each row of the simulated image is calculated (blue line). The image is then subdivided into slices with boundaries parallel to the longitudinal axis. The slice width is defined as the distance between the mean positions of the slice boundary, and kept constant for all slices. (Right) Subdivision of the slices using the special slicing procedure in comparison to the three highlighted slices as shown in Fig. 3.40.

The slice energy spreads obtained using the special slicing procedure are compared to those of the reference particle distribution in Fig. 3.42. In all three cases of different slice widths, the results obtained with the special slicing procedure achieve much improved agreement with the reference at the exit of the TDS. When a slice width of 60 fs is chosen (see Fig. 3.42 left), deviation of the measured energy spread in the central slice from the reference value has been reduced significantly from 18% using the common slicing method to < 1% using the special slicing procedure. However in the cases with a slice width of $\Delta t_{slice} = 30$ fs and $\Delta t_{slice} = 12$ fs, the slice energy spreads obtained with the special slicing procedure are slightly underestimated compared to the reference values at the exit of the TDS. It can be explained by the fact that the special slicing procedure minimizes the dominating effects of the initial beam size in the streak direction, while it neglects the effects of the initial beam size in the dispersion direction.

3.5 Summary

Three online TDS diagnostic sections have been designed for the European XFEL. They will provide high-resolution measurements of the longitudinal profile, the longitudinal phase space, the slice en-

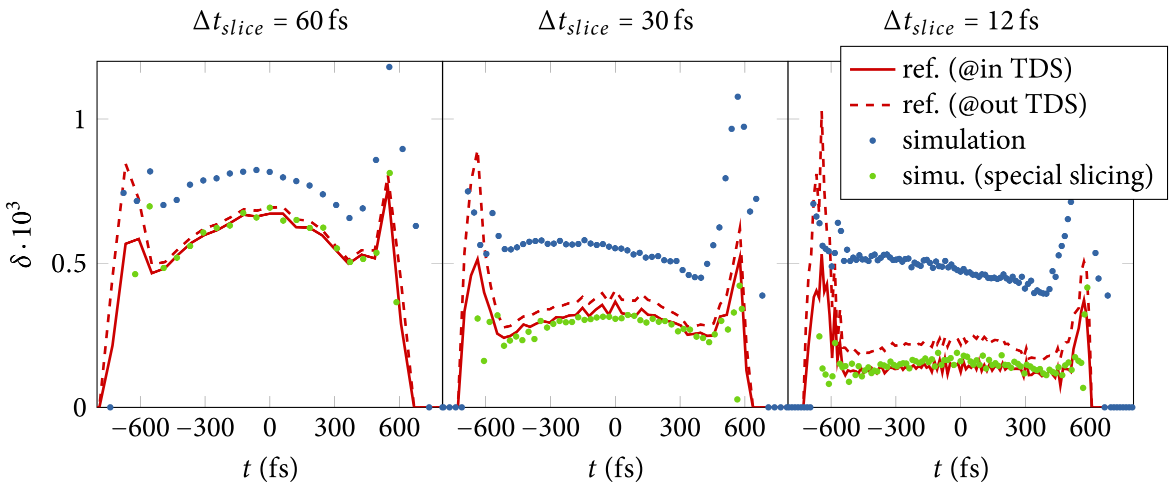

Figure 3.42: Slice energy spread determined by applying the special slicing procedure (green). The values obtained with (blue) the common slicing method and (red) from the reference as shown in Fig. 3.39 are displayed for comparison.

ergy spread and the slice emittance. The target of providing online diagnostics without disturbing the generation of FEL pulses is realized by the implementations of the fast kicker magnets and the off-axis screens.

Extensive error analysis has been performed for emittance measurements using the example of the TDS diagnostic section in the BC1 section. When a beam with a normalized emittance of 1 µm is matched to the design optics, statistical beam size errors of 5% lead to statistical errors of 5% on the measurement of both the slice and projected emittance. Systematic errors resulting from various sources including screen resolution, screen calibration, energy measurement and quadrupole field calibration have been studied. Special attention needs to be paid to the influence coming from the dispersions generated by the kicker magnets. Systematic error in slice emittance measurements due to dispersions can be negligible (below 1%) or dramatic (above 30%), depending on the actual parameters of the electron bunch.

In the measurement of the longitudinal phase space, the achievable longitudinal resolutions of the TDS diagnostic sections are designed to be in the 100 fs range in the injector section, and 10 fs in the BC1 and BC2 sections. In the BC1 and BC2 sections, the energy spread induced by the TDS exceeds the energy resolution, and is measured together with the initial energy spread of the bunch.

Simulations with S2E bunches have shown several aspects that have to be carefully taken into account in future measurements. The measurements of the projected emittance should be performed with the kicker magnets switched off, since the energy spread of 1.05% of the bunch leads to large errors of the measured emittance in the presence of dispersion. For slice emittance measurement, different results can be obtained by using the definitions of the beam size as rms value or Gaussian standard deviation. A large TDS streaking effect is essential for achieving reliable results. In the case of the bunch having differing Twiss parameters along the slices, matching of the beamline optics can only be performed for one set of the Twiss parameters. It is common to match to the central slice, the slice with the peak current or to the projected beam.

Simulations of longitudinal phase space measurements have validated the performance of the designed TDS diagnostic sections. Reliable longitudinal profile measurement is expected with a longitudinal resolution of 12 fs. However, the measured slice energy spread deviates remarkably from the reference value, which can be explained neither by the induced energy spread from TDS nor by the initial beam size in the dispersive plane. In contrast, the proposed special slicing procedure has achieved excellent improvement on the results of slice energy spread measurements. When a slice width of 60 fs is chosen, deviation of the measured energy spread in the central slice from the reference value has been reduced significantly from 18% using the common slicing method to $< 1\%$ using the special slicing procedure.

4 Measurement at LCLS

suppression of coherent optical transition radiation

Electron bunches with high peak current and high brightness are demanded to drive a high-gain FEL. These requirements are fulfilled by longitudinal compression of the electron bunches in the magnetic chicanes. During the bunch compression process, an initial density perturbation of the bunch, e.g. caused by shot noise from the gun, may be amplified, and an initial energy modulation of the bunch may be transformed into density modulation [SSY02a]. As a result of the so-called micro-bunching instabilities, microstructures are generated inside the compressed bunch. Micro-bunching instabilities have been studied extensively and are suggested to be induced by collective effects, such as coherent synchrotron radiation (CSR) [BCE+02, SSY02b], longitudinal space charge (LSC) [SSY04] and geometrical wakefields [HEBK03].

The modulation lengths of the microstructures can be on the scale of the visible wavelengths, which leads to coherence effects in the same wavelength range in the emitted radiation of the bunch, such as synchrotron radiation, transition radiation and diffraction radiation. Such coherence effect has drastically compromised the widely used electron beam imaging diagnostics with optical transition radiation (OTR) screens at several FEL facilities. Application of scintillator screens as an alternative has been hampered as well due to the coherent OTR (COTR) generated at the surface of the screen.

Different techniques, including temporal, spatial and spectral separation methods, have been proposed to suppress the COTR and image the beam with the incoherent scintillation light. Both the European XFEL and SwissFEL, which are now under construction, will implement transverse profile monitors utilizing the method of spatial separation to circumvent the problem of COTR. They will incorporate different designs regarding the observation geometry, screen materials and detection systems, but will both provide adequate spatial resolution required for the facility. The profile monitor for the European XFEL has been described in Section 3.2.4 and will be discussed at the end of this chapter. One exemplar of the profile monitor designed for the SwissFEL has been installed at the Linac Coherent Light Source (LCLS) for experimental tests under real conditions, in which the feasibility of the spatial separation method is investigated in the presence of COTR.

In this chapter, the theory of (C)OTR is shortly reviewed and the different suppression techniques are summarized. The high-resolution profile monitor developed for the SwissFEL is described. Finally, demonstration of successful COTR suppression is presented with experiments performed at the LCLS.

4.1 Beam imaging with OTR and scintillator screen

Transition radiation (TR) screens have been widely used for high energy electron beam imaging. The radiation from the electron bunch in the optical wavelength regime can be easily detected using commercially available camera systems. However, these diagnostics are impeded by coherence effects in the emission process of optical transition radiation (OTR). Scintillator screens, which have been commonly used for low-energy accelerators due to their much higher light yield than OTR screens, are considered as an alternative. The incoherently radiated scintillation light has drawn an increasing amount of attention for application in high-energy electron beam diagnostics since the observation of coherent OTR (COTR) at FEL facilities such as LCLS.

However, the problem of COTR cannot be avoided in the applications with scintillator screens as well due to the fact that the incoherent scintillation light is overlaid with the COTR generated at the boundary between the vacuum and the scintillator surface. Three methods have been suggested to circumvent the problem of COTR in beam imaging with scintillator screens: temporal, spatial and spectral separation. Reference [Yan12] has described in details the problematic of COTR and summarized the different techniques with experimental proof of the temporal separation method.

4.1.1 Problem of COTR

When a relativistic charged particle crosses the intersection between two media with different dielectric constants, TR is emitted in the forward direction along the incidence and in the backward direction around the specular reflection of the incident particle. The energy per spectral and spatial interval of the backward radiated TR from one single electron transiting from vacuum to a perfect conducting metal can be described using the Ginzburg-Frank formula [GF35]

$$\frac{d^2 U_{GF}}{d\omega d\Omega} = \frac{e^2}{4\pi^3 \varepsilon_0 c} \cdot \frac{\beta^2 \sin^2\theta}{(1-\beta^2\cos^2\theta)^2} \quad , \tag{4.1}$$

if the *effective source size*[1] and *far-field*[2] conditions are fulfilled [CSS05]. In Eq. 4.1, $\beta = v/c$ describes the velocity of the electron, θ the angle with respect to the backwards axis, $-e$ the charge of one electron and ε_0 the vacuum permittivity. The detailed formalism of TR is described in Appendix C. Typical TR profile monitors use aluminium coated silicon wafers as the radiation source due to their good resistance in thermal heatings [HBF+03], and detect the TR in the optical wavelength regime (OTR) using a high-resolution CCD[3] or CMOS[4] camera.

In case of an electron bunch of incoherently radiating electrons, the intensity recorded from the individual electrons add up linearly to the total intensity. The image of the intensity radiated from the whole bunch is the real transverse particle distribution convoluted with the image of a single electron, which is in analogy to the point spread function (PSF) in classical optics [Kub08] and determines the

[1] $a \geq \gamma\lambda$ with a being the radius of the screen, γ the Lorentz factor of the electron and λ the wavelength of the radiation.
[2] $D \geq \gamma^2\lambda$ with D being the distance from the screen to the detection point.
[3] Charge-coupled device.
[4] Complementary metal–oxide–semiconductor.

spatial resolution of the imaging system.

If the electrons of the bunch radiate coherently in the optical wavelength regime (COTR), superposition of the radiation fields from individual electrons leads to non-linear dependence of the total intensity on the electron density. As a result, the image of the radiated intensity of the whole bunch cannot represent the true transverse distribution of the bunch any more. The energy of COTR radiated per spectral and spatial interval from one electron bunch with N electrons can be expressed by

$$\frac{d^2 U_{bunch}}{d\omega d\Omega} = \frac{d^2 U_{GF}}{d\omega d\Omega} \cdot N + \frac{d^2 U_{GF}}{d\omega d\Omega} \cdot N\,(N-1)\,|F(\boldsymbol{k})|^2\,, \tag{4.2}$$

where $\boldsymbol{k}$ is the wavenumber and $F(\boldsymbol{k})$ the form factor of the bunch. The second part of Eq. 4.2 describes the coherent radiation and dominates the total intensity, since N is in the order of 10^9 for typical bunch charges of ~ 1 nC. COTR occurs if the bunch length is comparable to the optical wavelength or there exist microstructures with modulation lengths on the scale of the optical wavelengths. The latter might result from micro-bunching instabilities induced by e.g. CSR [BCE+02, SSY02b], LSC [SSY04] and geometrical wakefields [Cha93], and is the main origin of COTR at the FEL facilities (see Fig. 4.1).

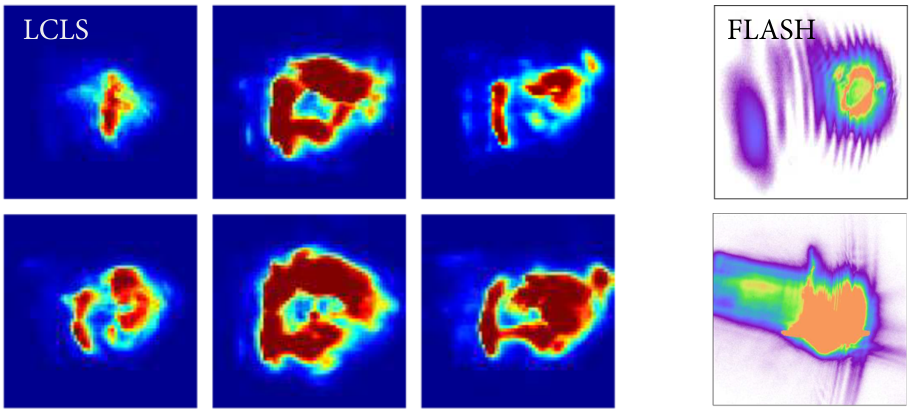

Figure 4.1: Observation of COTR has been reported at FLASH, LCLS and SACLA [WBSS09, LABD08, MMIO12]. The examples show COTR images taken at LCLS (adapted from Ref. [LABD08]) and FLASH with typical characteristics of ring-like structures and extremely high intensity resulting in saturation of the CCD sensor.

4.1.2 Incoherent imaging with scintillator screen

A scintillator screen is an alternative to an OTR screen for transverse beam imaging. Emission of scintillation light is a statistical process taking place in the luminescence centres inside the scintillator crystal [LAG+06]. The luminescence centres are excited independently by each electron, and then radiate incoherently after certain relaxation time, which makes scintillator a good candidate for beam imaging without disturbance from coherent effects. The most important characteristics of scintillation light are:

- spectral distribution at characteristic wavelengths,
- exponentially decreasing intensity with a decay time of typically a few hundred nanoseconds,
- isotropic direction of emission.

Scintillator material with a central wavelength in the optical regime can be easily adapted for beam imaging diagnostics using commercially available CCD and CMOS cameras.

While the scintillator screen has in general higher light yield (conversion rate from incident electron to photon) than the OTR screen, its spatial resolution is usually worse than that of OTR screen and could differ largely depending on the geometry of the imaging system. Considering a point-like single electron source, emission of scintillation light takes place along the trajectory of the electron inside the crystal, resulting in an elongation of the point-like source. The resolution could be further degraded due to the total reflection of the light inside the crystal. References [Yan12, KBL10] have investigated the influence of the observation geometry on the resolution of beam imaging systems with scintillator screens. Furthermore, saturation of the luminescence centres may occur when the localized incident particle density is too high and leads to non-linearity in light yield [MJR+00].

Although coherence effects are not expected in the scintillation light, OTR is generated at the scintillator surface and, in case of coherent emission (COTR), the application of scintillator screen for transverse beam profile measurements may be rendered impossible. Proper incoherent beam imaging with scintillator screens demands suppression of the coexisting (C)OTR in the image detection process. In the following, the temporal, spatial and spectral separation techniques to separate (C)OTR from the incoherent scintillation light are described.

Temporal separation

Emission of transition radiation from single electron is a prompt process, whose duration time is much shorter than the time an electron bunch needs to pass through the screen. The pulse duration of (C)OTR from one bunch is approximately on the same scale as the bunch length, which ranges typically from a few femtoseconds to a few picoseconds. In contrast, the emission of scintillation light is a slow process with typical decay times of a few hundred nanoseconds and exceeds the pulse duration of (C)OTR by several orders of magnitude.

The principle of the temporal separation method is illustrated in Fig. 4.2. The opening of the camera gate is postponed to a moment after the emission of (C)OTR, and the CCD sensor is exposed only to the incoherent scintillation light emitted during the exposure time. Separation of the (C)OTR, with pulse length in the picoseconds range, from the scintillation light, with pulse length of several hundreds of nanoseconds, cannot be realized by using CCD cameras, whose electronic shutter has typical rising and falling time of several hundreds of nanoseconds (see Section 5.2.3). One camera system suitable for temporal separation is, for example, the intensified CCD camera (ICCD). It basically consists of a photo cathode, a micro channel plate (MCP) as well as a CCD sensor, and provides possibility of delaying the camera gate in the nanoseconds range. First demonstration of successful temporal separation of COTR for incoherent beam imaging has been performed at FLASH

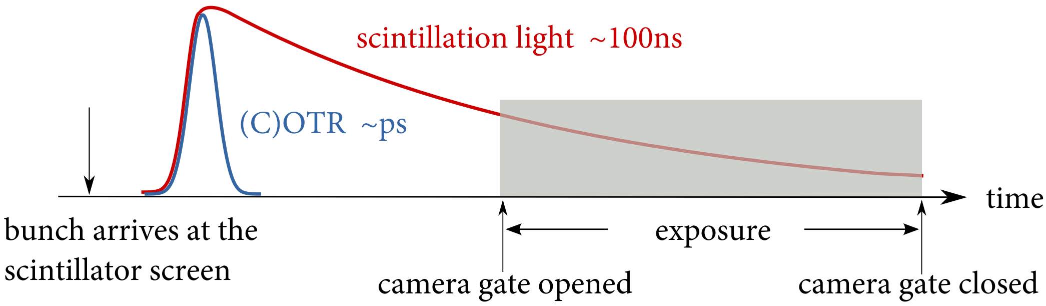

Figure 4.2: Illustration of the temporal separation method. The camera gate is delayed and opened after the emission of (C)OTR. The CCD sensor is exposed only to the incoherent scintillation light.

[Yan12, BGK+12]. Temporal separation has been proven to be capable to fully suppress COTR in the beam images, while the spatial and spectral separation still detect remaining small amount of COTR intensity as will be discussed in the following section.

The high price of such ICCD camera will not allow it being employed for standard screen stations at most existing and future FELs. For example, the ICCD camera dicam pro from PCO AG, Germany [PCO], which was used for the first demonstration of the temporal separation method in Refs. [Yan12, BGK+12], is by a factor of about 20 more expensive than the CCD camera Basler avA2300 from Basler AG, Germany [Bas], which will be installed for the screen stations at the European XFEL. ICCD cameras are originally designed for the purpose of intensity amplification. Due to the limited lifetime of the sensitive photo cathode, they are not compatible with continuous long-time operation in the screen stations for the accelerator. In addition, space charge effects in the MCP might result in unstable gain for different densities of the incoming photons. As investigated in Ref. [LBEU09], the camera gain stays constant up to a certain photon density, and then decreases rapidly at higher photon densities. Instability of the camera gain of ICCD cameras could worsen the resolution of the imaging system. Therefore, an alternative to the temporal separation method is desired.

Spatial separation

As can be seen in Eq. 4.1, the intensity of transition radiation has a spatial dependence on the angle θ with respect to the backwards axis. The intensity reaches its maximum at $\theta_{max} \sim 1/\gamma$ (see Eq. C.3), with γ being the Lorentz factor of the electron, and drops rapidly with increasing θ. Figure 4.3 shows the angular distribution of backwards TR for electrons with energies of $E = 0.5\,\mathrm{GeV}$, $E = 4.2\,\mathrm{GeV}$ and $E = 13.1\,\mathrm{GeV}$.

While the intensity of TR is spatially centred in a narrow cone with small opening angle around the backwards axis, scintillation light is emitted in a solid angle of 4π. The principle of spatial separation is illustrated in Fig. 4.4. The camera is positioned at an angle far away from θ_{max}. The detectable intensity of TR is then extensively suppressed and negligible compared to the scintillation light. However, as the angular TR intensity does not fully vanish at any angle $\theta > 0$, the N^2 dependent coherent part of the transition radiation (see Eq. 4.2) may still dramatically enhance the intensity and dominates the incoherent scintillation light. Careful design for the application of the spatial separation

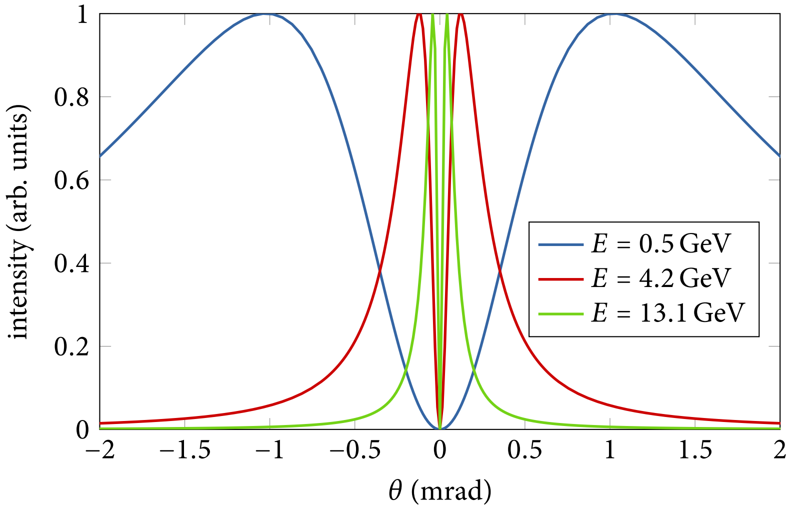

Figure 4.3: Angular distribution of TR intensity $\frac{d^2 U_{GF}}{d\omega d\Omega}$ according to the Ginzburg-Frank formula in Eq. 4.1 for different electron energies. There is no intensity at the centre ($\theta = 0$), and the maximum intensity is obtained at the angle $\theta_{max} = 1/\gamma$.

method has to be considered, depending on the coherence level and observation geometry of the imaging system.

Spectral separation

The principle of the spectral separation is to filter out the coherent wavelength content of the transition radiation. It requires knowledge of the COTR spectrum. Proper choice of the filter and the scintillator material in terms of its characteristic emission wavelength are important. Since the spectrum could vary depending on the compression settings, and the COTR usually extends into the whole optical wavelength regime, this method has to be considered explicitly for each specific application.

Reference [LSB+09] has reported one attempt using spectral separation method to mitigate coherence effects at the Advanced Photon Source (APS) [APS]. With the evidence that the intensity of COTR is dominant at the near infrared (NIR) end of the spectrum measured at APS, mitigation of COTR was achieved by using a 400 nm bandpass filter in combination with a cerium-doped lutetium oxyorthosilicate (LSO:Ce) scintillator screen which has peak emission at 415 nm.

4.2 The Linac Coherent Light Source

The experiments for the spatial separation of COTR are performed at the Linac Coherent Light Source (LCLS) at the SLAC national accelerator laboratory [SLA], Palo Alto, USA. LCLS is a linac-based FEL, delivering soft and hard X-ray photon beams [EAA+10]. A layout of the machine is shown in Fig. 4.5. The electron bunches generated in the photo cathode injector are accelerated in normal-conducting S-band RF structures ($f = 2856$ MHz) up to 3.5 – 14 GeV and compressed

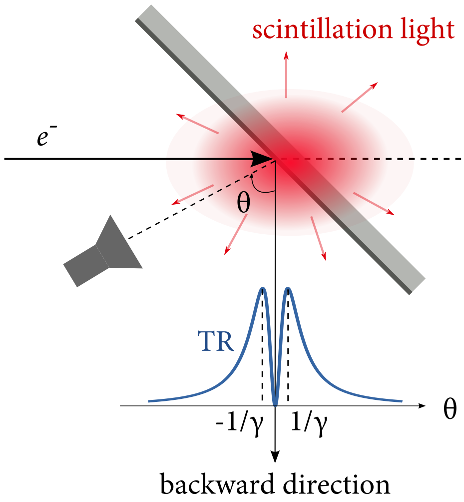

Figure 4.4: Illustration for the principle of the spatial separation method. The camera is placed at an angle θ far away from $\theta_{max} = 1/\gamma$. The TR intensity is drastically decreased at the angle $\theta \gg \theta_{max}$.

successively in two bunch compressors down to a few femtoseconds. A special laser heater system, which increases the uncorrelated energy spread of the electron bunch by ~ 20 keV, is installed after the first accelerating section L0, and can be operated to effectively suppress micro-bunching instability [SSY04, HBE+04, HBD+10].

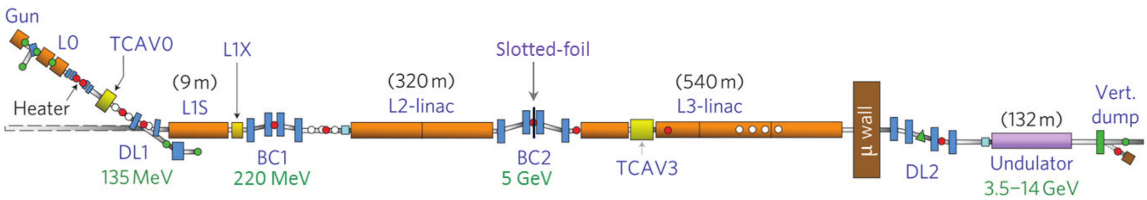

Figure 4.5: Schematic layout of LCLS. The electron bunches are accelerated in the normal-conducting accelerating structures (L0 to L3) and compressed in two bunch compressors (BC1 and BC2). The high-resolution profile monitor is installed in the section upstream of the undulator. Figure adapted from Ref. [EAA+10].

Various diagnostic stations are available, including one TDS section at low energy, one at high energy, and recently an X-band TDS system after the undulators serving as time-resolved photon pulse diagnostics with femtosecond resolution [BDD+14]. LCLS has been suffering from intense COTR effects even with the laser heater in operation. The laser heater system has been proven to have intensely reduced the COTR intensity but not fully suppressed it [HBD+10]. The functionality of all the existing screen monitors are hampered for diagnostics with compressed bunches.

4.3 Experimental details of the spatial separation of COTR

For the purpose of incoherent imaging using the spatial separation method, one high-resolution profile monitor has been developed by the diagnostic group at PSI for application at the future SwissFEL. The high-resolution profile monitor has been installed at the SwissFEL Injector Test Facility (SITF) and tested for beam diagnostics such as projected emittance and slice emittance measurements. The monitor achieves a spatial resolution of 8 µm [IKL+14] and its routine use at the SITF has verified its capability for operation with bunch charges down to 1 pC [PAB+14].

In order to investigate the performance of the monitor in a real environment in the presence of COTR, an exemplar of the high-resolution profile monitor is installed at the Linac Coherent Light Source (LCLS). Experiments were performed at different machine conditions to study the capability of the spatial septation method to suppress COTR using the high-resolution profile monitor.

In this section, the design of the profile monitor is presented, and the setup at the LCLS is described.

4.3.1 High-resolution profile monitor designed for the SwissFEL

The high-resolution profile monitor for the SwissFEL has been designed by the beam diagnostic group of Paul Scherrer Institute (PSI) [IT14]. The observation geometry of the monitor has been optimized taking into account the Snell's law of refraction to achieve better spatial resolution. Analytical calculation using simple model shows that broadening effect due to the finite thickness of the scintillator screen is minimized if the following relation is fulfilled [IKL+14]:

$$\beta = -\arcsin(n \sin \alpha), \tag{4.3}$$

where β is the angle between the observation point and the screen normal, n the refractive index of the scintillator and α the angle between the incident beam and the screen normal.

A prototype monitor equipped with different scintillator materials has been tested at the SITF at PSI. Yttrium aluminum garnet doped with cerium (YAG:Ce[5]) has achieved the best resolution [IKL+14]. Figure 4.6 shows the layout of the high-resolution profile monitor. The YAG screen has a thickness of 30 µm and a refractive index of 1.82 at the central emission wavelength of 550 nm. The crystal angle α and observation angle β amount to 8.1° and 15°, respectively. With the help of an in-vacuum mirror, the scintillation light is directed to a detection system consisting of a lens[6] with $f = 200$ mm and a CCD camera[7] with 1390 × 1037 pixels of pixel size of 6.45 µm × 6.45 µm. In order to image the whole scintillator screen in the focus plane, the camera is tilted according to the Scheimpflug principle[8].

[5] Crytur Ltd., Czech Republic [Cry].
[6] Nikon Corporation [Nik].
[7] UNIQ VISION INC. [UNI].
[8] When the planes of the object, the lens and the detector intersect at the same axis, the whole object is in depth of field and can be imaged sharply [Sch04].

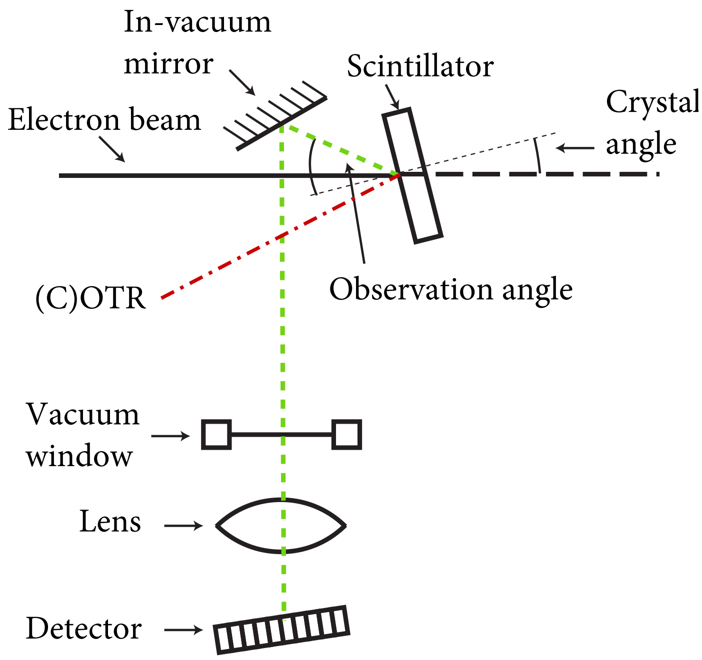

Figure 4.6: Observation geometry of the high-resolution profile monitor developed for the SwissFEL. The crystal angle α is 8.1° and the observation angle β is 15°. The CCD sensor is slightly tilted to fulfil the Scheimpflug principle.

4.3.2 Installation at LCLS

One exemplar of the high-resolution profile monitor has been installed upstream of the undulator section at the LCLS. Since LCLS has been suffering from strong COTR intensities, neutral density filters with optical density of 2 (transmission of 1%) are mounted onto the vacuum window to protect the camera.

The imaging system installed at LCLS has a demagnification of 1.8 : 1, which corresponds to an effective pixel size of 11.63 µm × 11.63 µm. The Ginzburg-Frank formula is not valid for the configuration of the high-resolution profile monitor at LCLS, since the far-field condition is violated. A generalized equation (see Eq. C.4) is applied for the estimation of the angular distribution of the TR intensity and is shown in Fig. 4.7. In comparison to the peak value, the measurable intensity at the detector, which is placed at an angle of 23.1° (~ 0.4032 rad) away from the backward axis of COTR, is expected to be reduced to $2.05 \cdot 10^{-6}$ and $1.65 \cdot 10^{-6}$ at a beam energy of 4.2 GeV and 13.1 GeV, respectively. Due to the quadratic dependence on N, which is in the order of 10^9, suppression of COTR could fail depending on the coherence level of the electron bunch and has to be tested experimentally.

4.4 Experimental results

Since the scintillation light is emitted incoherently, the total radiated intensity is expected to have a linear dependency on the bunch charge provided that COTR is suppressed. During each measure-

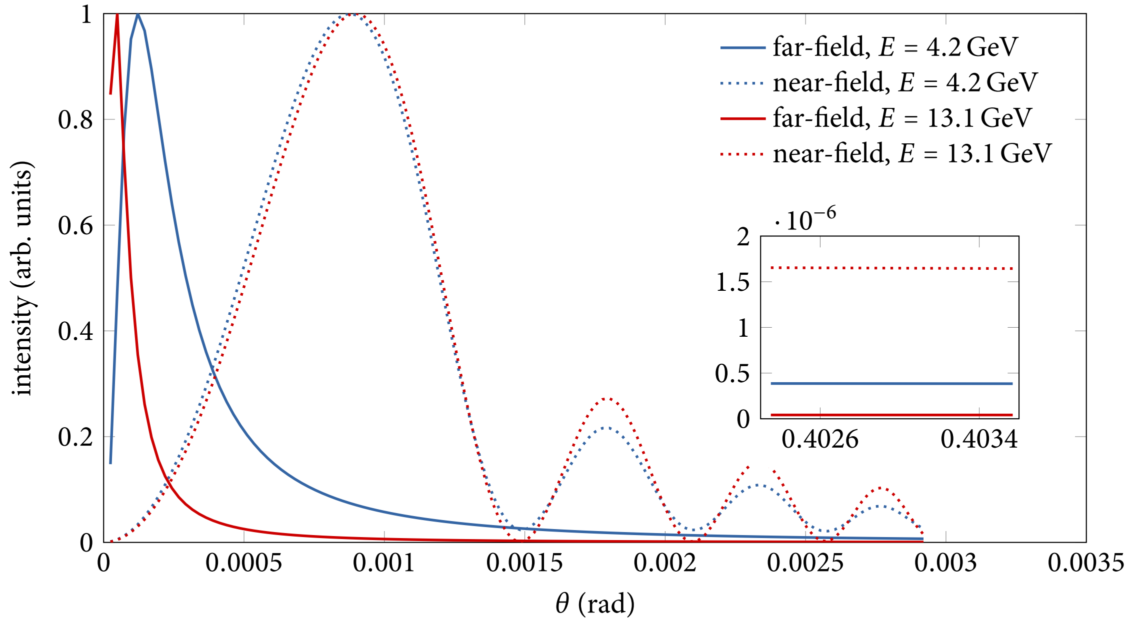

Figure 4.7: Angular distribution of TR in (solid lines) far-field and (dotted lines) near-field. The inset plot shows the TR intensity around the angle of 23.1° (~ 0.4032 rad), at which the camera is installed at LCLS.

ment scan, the bunch charge is kept constant, while the transverse or longitudinal bunch structures are changed. The integrated camera counts in the beam area of each image, which is a measure for the radiation intensity, is calculated. Constant camera counts for each scan are expected for incoherent beam imaging diagnostics.

The experiments were performed at three different machine settings (see Table. 4.1) covering low to high charge and energy for soft and hard X-rays operations. Both cases with the laser heater turned on and off are investigated. The case of laser heater on is the nominal operation setting for LCLS, while the case of laser heater off is explicitly chosen to generate intense COTR.

Table 4.1: Machine settings for the spatial separation experiments at the LCLS.

	unit	**A**	**B**	**C**
Charge	pC	20	20	150
Energy	GeV	4.2	13.1	13.1

4.4.1 Compression scan

As indicated by Eq. 4.2, the coherence level of the COTR intensity depends on the longitudinal form factor $F(\boldsymbol{k})$, which is then determined by the longitudinal structures inside the bunch. The compression settings of the machine are accordingly varied from under-compression to over-compression in order to change the longitudinal structures of the bunch. Two configurations of the laser heater are studied at all three machine settings: (i) the laser heater is turned off (laser energy 0 μJ) and (ii) the laser heater is turned on with a laser energy of 42 μJ (corresponding to a heated rms energy spread of 45 keV [HBD+10]).

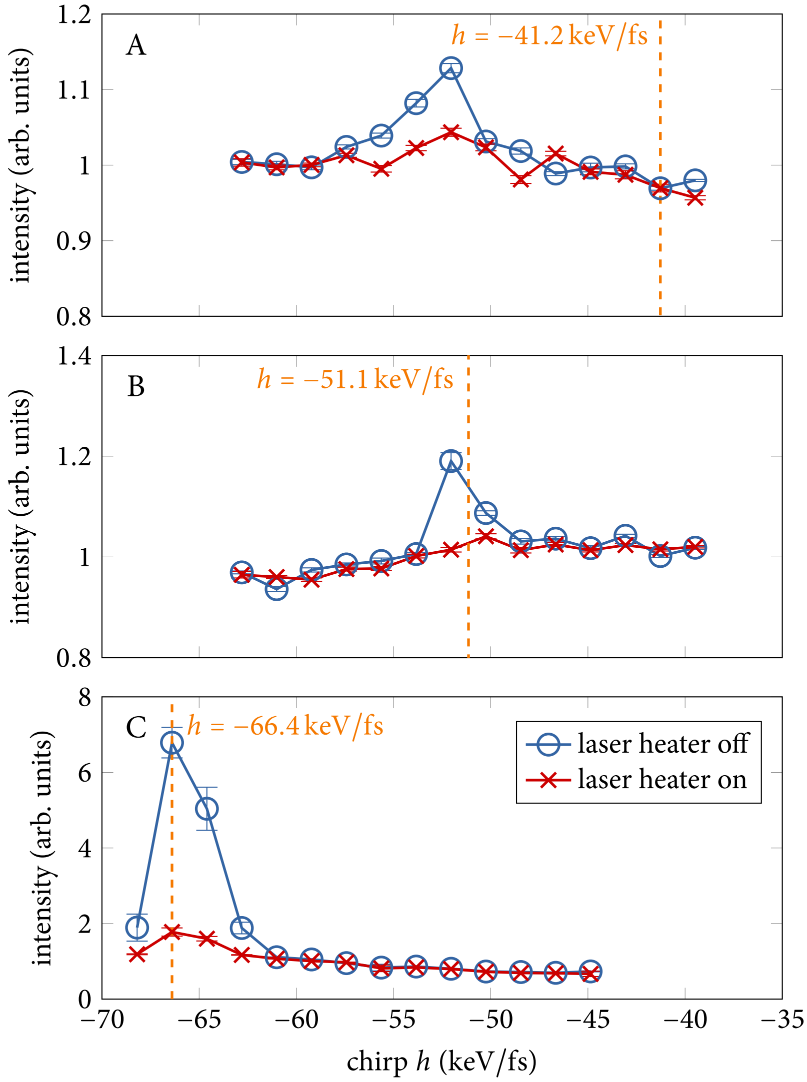

Figure 4.8: Compression scan at the settings A, B and C with the laser heater turned off (blue) and on (red). During the compression scan at each setting, the RF amplitude and phase of the L2-linac (see Fig. 4.5) are changed simultaneously to provide different chirps h (energy per length) to the electron bunch while keeping the beam energy constant. Different chirps of the electron bunch lead to different compressions in the downstream bunch compressor BC2 (see Fig. 4.5). The dashed vertical lines mark the compression settings which were used during the measurements presented in Figs. 4.9, 4.11 and 4.13.

The results of the compression scans are shown in Fig. 4.8. At all settings, the scans with laser heater off (blue line) show notable variations of the intensity. The enhancements of the intensities all occur at the high compression setting with high peak currents. In the worst case (setting C with high charge and high energy), fluctuation of the beam shape in the camera images is observed from shot to shot. The intensity increases up to a factor of 7, which clearly indicates the presence of COTR.

In the case of the laser heater turned on (red line), the intensity remains constant within a variation of less than 10% for setting A and B. For setting C, the intensity measured with laser heater on reaches an enhancement of a factor of 2. A closer look at the single images taken at the compression setting where the maximum intensity enhancement is observed indicates disturbances from an other radiation source. As can be seen in Fig. 4.9, the images exhibit on the one edge some stripes pattern resembling the structure on the chamfer of the in-vacuum mirror (see Fig. 4.10). Since the mirror is located at a close distance of nominally 3.73 mm to the beam axis, there is coherent optical diffraction radiation (CODR) generated on the edge of the mirror and reflected back to the camera. This CODR pattern overlaps with the beam image and results in a slight gradient in the background intensity (see Fig. 4.9). The fact that CODR is produced when the beam is present makes it very difficult to be separated from the beam image for data analysis. Mirrors with sharper edges are considered in the future upgrade of the high-resolution profile monitor [Isc].

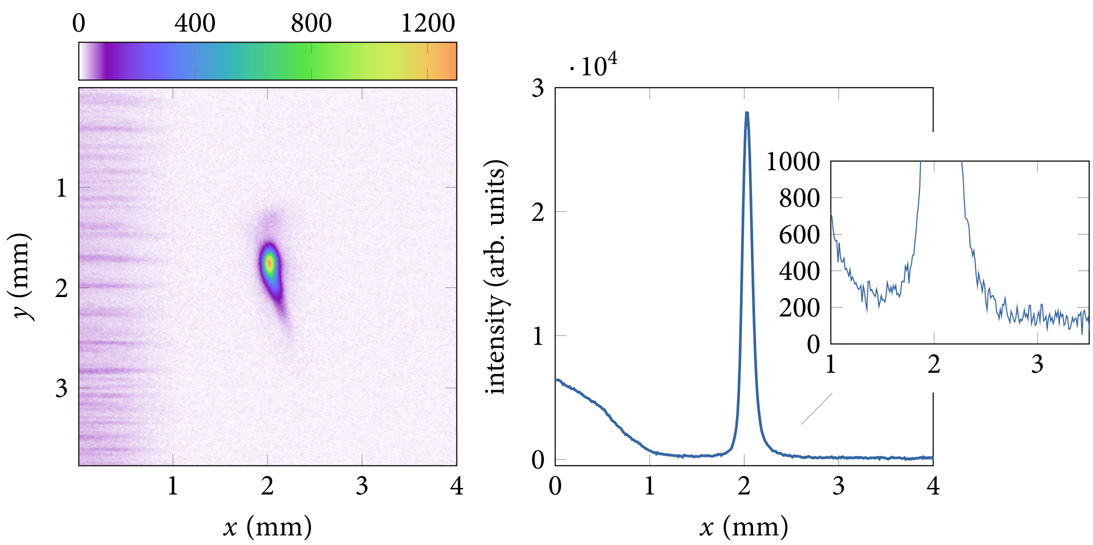

Figure 4.9: (Left) Single image containing stripes pattern taken at the machine setting C with the chirp $h = -66.4\,\mathrm{keV/fs}$ (referred to the dashed line in Fig. 4.8 C), where the intensity enhancement is maximum. The laser heater was turned on. (Right) Horizontal profile with a slight gradient in the background intensity.

4.4.2 Beam size scan

In the beam size scans, the transverse beam size of the bunch is varied by changing the quadrupole strength. The transverse beam size could have an influence on the transverse coherence level. The other purpose of the beam size scan is to investigate the performance of the scintillator crystal for different electron densities. When the electron bunch is transversely focused to a small area, the high electron density may induce saturation of the luminescence centres in the scintillator crystal. As a result, the intensity of the emitted scintillation light is not in linear dependence of the electron density any more.

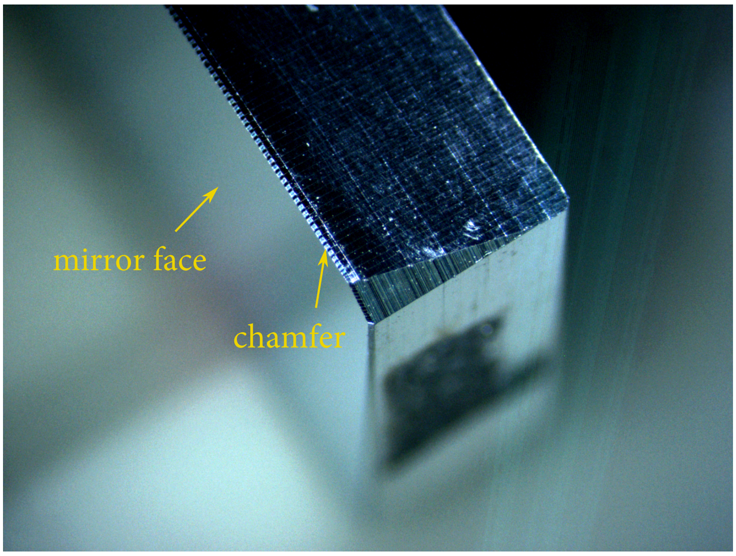

Figure 4.10: Microscopic photo of the in-vacuum mirror. The structures on the chamfer induces CODR and are imaged together with the beam by the camera. Photo courtesy of Rasmus Ischebeck, PSI.

The first scan was performed with low-compression scheme at the machine setting A (referred to the dashed line at $h = -41.2\,\mathrm{keV/fs}$ in Fig. 4.8 A) and is presented in Fig. 4.11 A. While the beam sizes are changed by a factor of 10, the intensity stays constant within a variation of less than 10%.

Another scan was performed with high-compression scheme at the machine setting B (referred to the dashed line at $h = -51.1\,\mathrm{keV/fs}$ in Fig. 4.8 B). At this high-compression setting, the intensity measured with the laser heater turned off exceeds generally that with the laser heater on, regardless of the transverse beam sizes. A small decrease of the intensity of about 5% with the laser heater on is observed for one particular beam size. Figure 4.12 shows the vertical beam sizes of the bunches with different beam areas measured at the setting B with the laser heater turned on. At the beam area of $0.55 \cdot 10^4\,\mu\mathrm{m}^2$, where the intensity drops about 5%, the vertical beam size is in waist and the vertical profile has some flat-top feature (see the inset plot of Fig. 4.12), which is a typical evidence for saturation in the scintillator crystal.

4.4.3 Laser heater energy scan

It has been shown in the previous two scans that the laser heater system has drastic influence on the mitigation of the micro-bunching instabilities and effectively reduced the coherence level in the emission of OTR. One scan of the laser heater energy was performed with the high-compression scheme at the machine setting B (referred to the dashed line at $h = -51.1\,\mathrm{keV/fs}$ in Fig. 4.8 B). The results are presented in Fig. 4.13. With increasing laser heater energy, COTR is quickly suppressed. Starting from $17.4\,\mu\mathrm{J}$, the variation of the measured intensity remains within 1%.

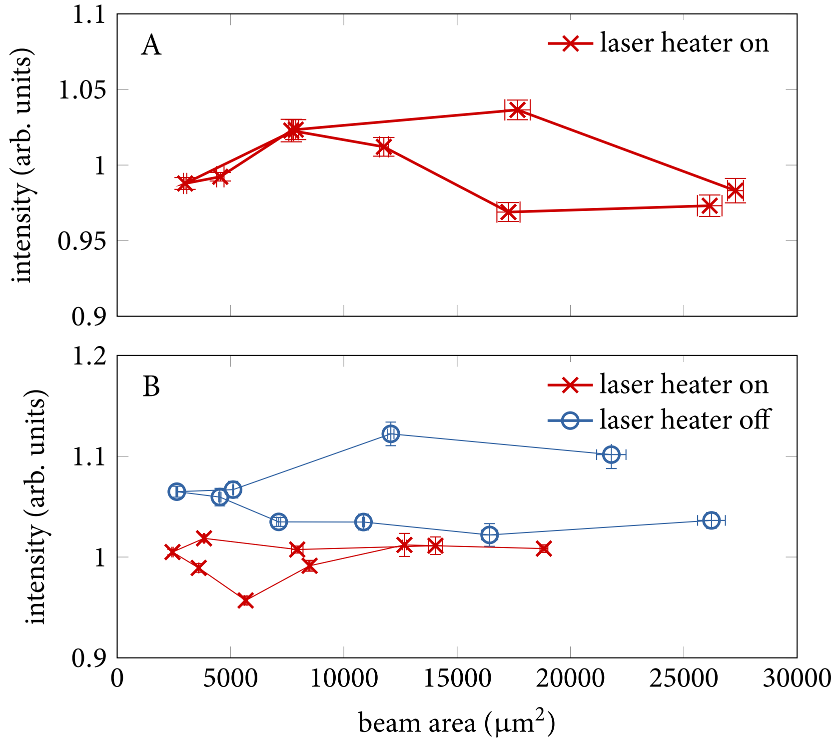

Figure 4.11: Beam size scan at the settings A and B with the compression-scheme referred to the dashed lines in Fig. 4.8 A (at $h = -41.2\,\mathrm{keV/fs}$) and B (at $h = -51.1\,\mathrm{keV/fs}$), respectively. The beam sizes are changed by varying the quadrupole field strength. The beam area is defined as the product of the beam sizes in the x and y planes.

4.5 Summary

The experiments at LCLS have shown the performance of the high-resolution profile monitor in beam imaging diagnostics in the presence of coherent emission. Capability of the spatial separation method to suppress COTR has been proved. Investigations at machine settings with various beam energies, bunch charges and compression schemes have verified that no distortion of COTR to the beam images has been observed for the nominal operation settings (laser heater on and normal compression).

The laser heater system has demonstrated to be effectively helping in reducing COTR. At one machine setting with high bunch charge and high compression (setting C), an enhancement of the total radiated intensity up to a factor of 2 is observed even with the laser heater turned on, which could result from the disturbing intensity of CODR originating from the in-vacuum mirror chamfer. The configuration of the imaging system has to be carefully reconsidered.

The high-resolution profile monitor installed at the LCLS has brought back the possibility of emittance and slice emittance measurements using imaging screens. First comparison of the measured projected emittance with the results from using wire-scanners showed agreements.

The experiments at the LCLS have provided much experiences for the European XFEL. A laser

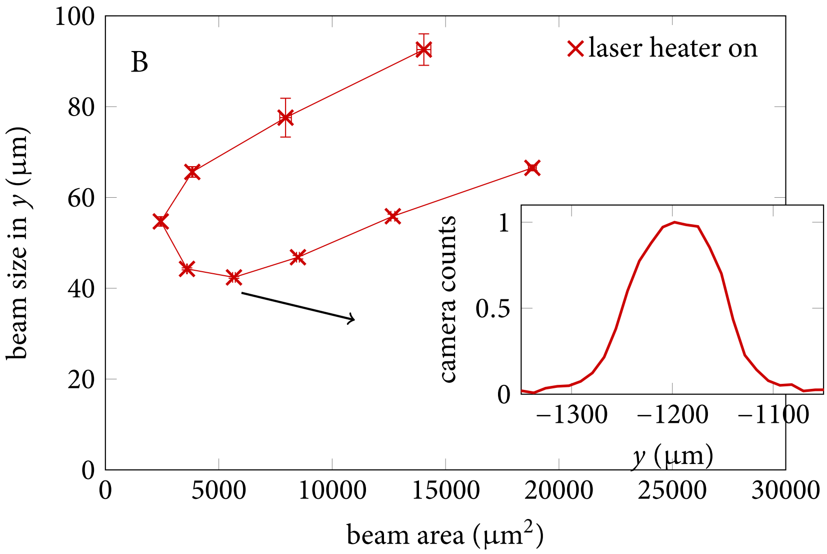

Figure 4.12: The vertical beam waist is reached exactly at where the dip of intensity in Fig. 4.11 B is observed. Flat-top feature in the vertical profile could be an indication for the saturation in the crystal.

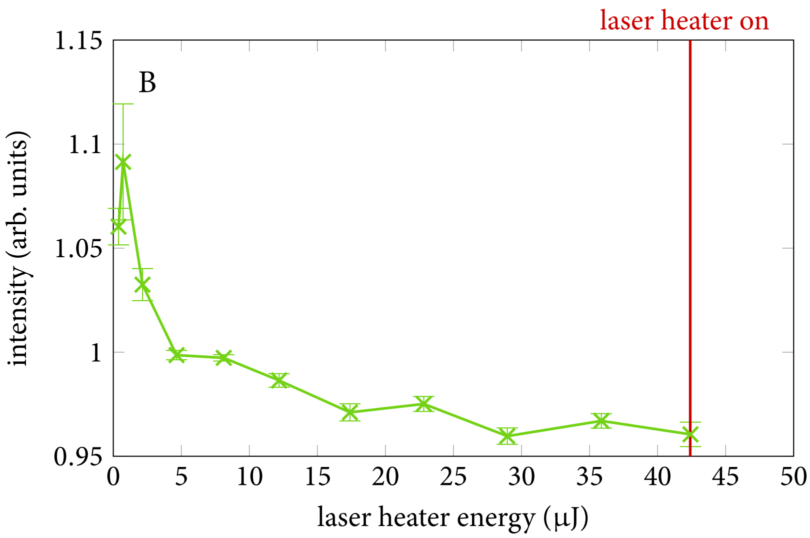

Figure 4.13: Scan of the laser heater energy with the high-compression scheme at the machine setting B (referred to the dashed line at $h = -51.1\,\mathrm{keV/fs}$ in Fig. 4.8 B).

heater system will be installed at the European XFEL as well to mitigate the micro-bunching instabilities. For the profile monitor developed for the European XFEL, the camera is placed at an angle of 45° away from the backward axis of (C)OTR, which is larger than the 23.1° of the SwissFEL design. Therefore, with more suppression of COTR intensity, the profile monitor for the European XFEL is expected to have good performance for most machine settings.

5 Measurement at FLASH

Longitudinal diagnostics with TDS and off-axis screen

High-resolution longitudinal diagnostics are desired to control and characterize the driving electron bunches of the linac-based FELs. Transverse deflecting structure (TDS) is one of the most robust diagnostics providing high-resolution as well as single-shot capability. With the advancement of the super-conducting technology, much higher repetition rate of the electron bunches in the linac has been achieved in comparison to the normal-conducting FELs. Bunch trains containing thousands of intense photon pulses per second can be generated and delivered to the experiments. The high average FEL power is highly welcomed by the FEL user community. The successful operation of the Free-electron Laser in Hamburg (FLASH) has demonstrated the excellent performance of the TESLA super-conducting technology [RST+01], and motivated the project of the European XFEL.

Diagnostics which are non-disruptive to the generation of FEL radiation become more important to high repetition rate FELs, such as FLASH and the European XFEL. On the other hand, the photon users have requested continuous monitoring of the electron bunch length in order to be noticed of its possible drifts and investigate its potential correlation to the pulse length of the photon pulses. Diagnostics fulling these requirements can be realized by a TDS in combination with a kicker magnet and an off-axis screen.

At FLASH, one longitudinal profile monitor of this kind has been constructed and commissioned at a location directly upstream of the undulators. The monitor is operated in the pulse-stealing mode, in which only one bunch out of a bunch train is used for diagnostic purposes and lost for the generation of FEL pulses. The remaining bunches are not affected. The monitor helps the operator setting up the machine and has been routinely used by the FEL users to monitor the longitudinal profile as well as possible electron bunch length variations.

This monitor at FLASH serves as a test platform for the European XFEL, which is foreseen with three online longitudinal diagnostic sections in the pulse-stealing mode. In addition, some prototype components for the European XFEL are installed for the monitor, and are characterized. One close-by dispersive section, where the longitudinal phase space of the electron bunch can be measured, allows for comparison of the longitudinal profiles with these obtained with the monitor, which makes an investigation on the performance of the monitor possible.

In this chapter, the setup of the longitudinal profile monitor at FLASH and the implementation of the data analysis software of the monitor are described. After the commissioning of the monitor, systematic errors due to initial correlations inside the bunch are investigated.

5.1 The Free-electron Laser in Hamburg

The Free-electron Laser in Hamburg (FLASH) is a high-gain SASE FEL which can deliver thousands of femtosecond photon pulses per second in the wavelength range from vacuum ultraviolet (VUV) to soft X-rays [SFF+10]. At a maximum electron beam energy of 1.25 GeV, the corresponding wavelength of 4.12 nm reaches the water window, offering exciting possibilities to research [GHM+11]. After the last upgrade, the second undulator beamline FLASH 2 with variable gap has been commissioned and achieved the milestone of first lasing, which accredits FLASH as the first facility serving independently two undulator beamlines with the same electron source [SF14].

A schematic layout of FLASH is shown in Fig. 5.1. The laser-driven RF gun generates electron bunches with a variable charge from 0.1 nC to 3 nC. The bunches are then accelerated with the seven super-conducting TESLA modules [RST+01], operated at 1.3 GHz, up to about 1.25 GeV and compressed longitudinally in two stages with the magnetic chicanes. A third harmonic system operated at 3.9 GHz (depicted as the red RF station in Fig. 5.1) is added after the first accelerating structures for linearising the longitudinal phase space (t, E). As a FEL user facility based on super-conducting technology, thousands of electron bunches per second are allowed to provide photon pulses to the FEL users.

After the linear accelerator section, the electron bunches are distributed towards the FLASH 1 and 2 undulator beamlines. Photon pulses with different wavelengths can be delivered by the two undulator beamlines at the same time. FLASH 1 beamline uses fixed-gap undulators, where the photon pulse wavelength is determined by the electron beam energy. The FLASH 2 undulators are with variable gaps, so that the electron bunches with beam energy required for FLASH 1 can produce FEL radiation at a different wavelength.

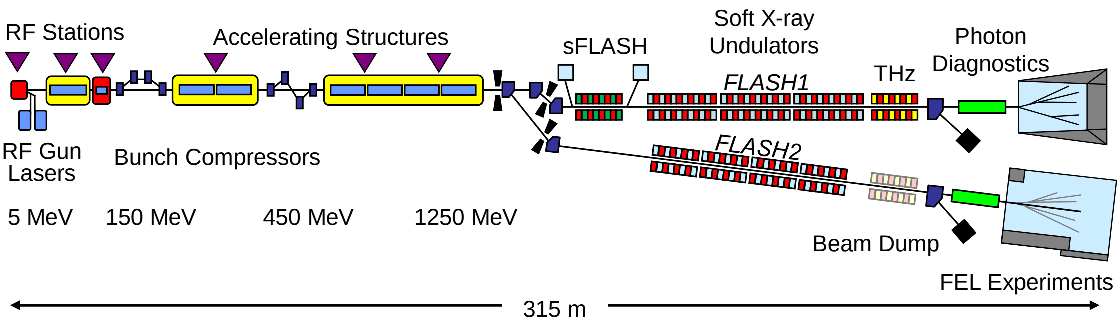

Figure 5.1: Schematic layout of FLASH with the two undulator beamlines FLASH 1 and 2. Figure adapted from Ref. [FLA].

5.2 Experimental details of the longitudinal diagnostics

The experiments are carried out at FLASH 1, using the existing longitudinal diagnostic section, where a TDS system together with a dipole magnet as well as a fast kicker magnet are available.

The TDS is a LOLA-type disc-loaded RF waveguide structure [ALL64], and located upstream of the FLASH 1 undulators. It is operated at a frequency of 2.856 GHz and streaks the bunch in the vertical direction. The short filling time of 0.645 μs of the RF pulses allows for measurements of single bunch even at 1 MHz repetition rate.

Two possible operation modes for use with the TDS are illustrated in Fig. 5.2. The first mode (Fig. 5.2 (a)) incorporates the non-dispersive section for the so-called pulse-stealing mode, where only one bunch out of the bunch train is used for the measurement and lost for the generation of FEL pulses. As usually one extra bunch added to the end of the long bunch train is used for diagnostics, the pulse-stealing mode appears effectively as non-destructive to the FEL operation. Downstream of the TDS, a fast kicker magnet deflects the electron bunch horizontally onto an off-axis screen. The kicker magnet is capable of separating single bunch out of a bunch train with spacing down to 1 μs as well, attributed to its short pulse length of 1.2 μs. By setting the trigger timings of the TDS and the kicker magnet to the one and the same bunch, the longitudinal beam profile is obtained for the selected bunch, while the remaining bunches of the bunch train are not affected and continue traversing through the undulators for the generation of FEL pulses. The off-axis imaging screen is a scintillator screen (CRY19 [1], 25 mm × 20 mm, 100 μm thickness) with a horizontal offset of 15 mm from the screen centre to the beam axis. The angle between the screen normal and the beam axis amounts to 35° and the scintillation light emitted in the direction perpendicular to the beam axis is captured by the camera system[2]. This configuration utilizes the spatial separation method (see Section 4.1.2) to avoid the problem of coherence effects.

Alternatively (Fig. 5.2 (b)), the TDS can be operated together with a dipole magnet for the measurement of the longitudinal phase space (t, δ). The downstream horizontal dipole diverts the beam path with 10° into the dispersive section towards to local beam dump. The horizontal dispersion at the screen amounts to $D_x \sim 750$ mm. The imaging screen is a scintillator screen (YAG:Ce[3], 40mm × 30 mm, 100 μm thickness) mounted at an angle of 45° between the screen normal and the beam axis. The camera system[4] is positioned perpendicular to the beam axis. Coherence effects have not been observed and proved to be suppressed in the dispersive section [BGK+12]. In this operation mode, FEL delivery is disrupted, and the number of bunches is limited to two bunches due to the capacity of the local beam dump at the end of the dispersive beamline. Usually single-bunch mode is used for the longitudinal phase space measurement in the dispersive section, which is very useful for beam studies and setting up the compression. However, variations of the parameters of the bunches are expected when the machine is switched from single- to multi-bunch mode. The dispersive section is not usable in multi-bunch operation and thus does not allow measuring the variations of different bunches in the bunch train.

[1] Crytur Ltd., Czech Republic [Cry].
[2] Manta G145B, Allied Vision Technologies GmbH, Germany [AVT].
[3] Yttrium aluminum garnet doped with cerium, Crytur Ltd., Czech Republic [Cry].
[4] GC1380, Allied Vision Technologies GmbH, Germany [AVT].

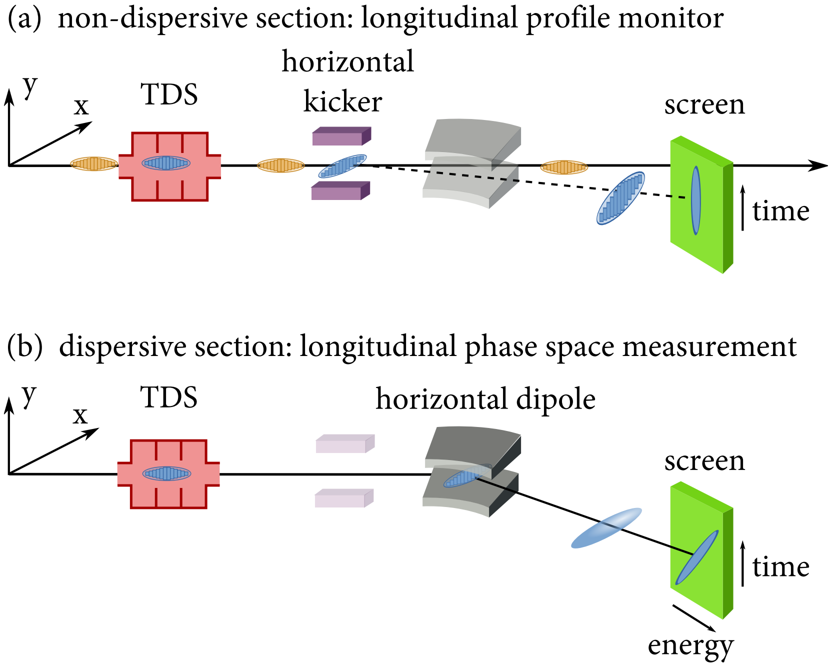

Figure 5.2: TDS diagnostic section at FLASH 1. (a) The non-dispersive section incorporates the longitudinal profile monitor operated non-disruptive to the FEL delivery. (b) The dispersive section provides measurements of the longitudinal phase space.

5.2.1 Image processing

The raw data for all the measurements utilizing the TDS are camera images, from which the beam parameters (e.g. the beam size , beam profile) may be derived. Therefore, the images have to be carefully processed to filter out the noisy contents. An algorithm for image processing has been implemented at FLASH and proved to be adaptable to beams of arbitrary shape. The algorithm is described in detail in Appendix D.

The basic principle involves the following steps:

1. subtraction of background signals arising from dark current and noise in the CCD sensor,
2. estimation of the threshold intensity for the beam,
3. determination of the region of interest (ROI) area containing the beam,
4. setting the intensity of all pixels outside the ROI to zero.

Figure 5.3 shows an example of a simulated 2-dimensional Gaussian beam added with normal distributed noises, and the corresponding image after image processing. The calculated beam size of the processed image agrees with the simulated one. Another example of the application of the algorithm on real electron beam is shown in Fig. 5.4. The algorithm has successfully distinguished the on-crest beam in sinusoidal shape from the noisy backgrounds.

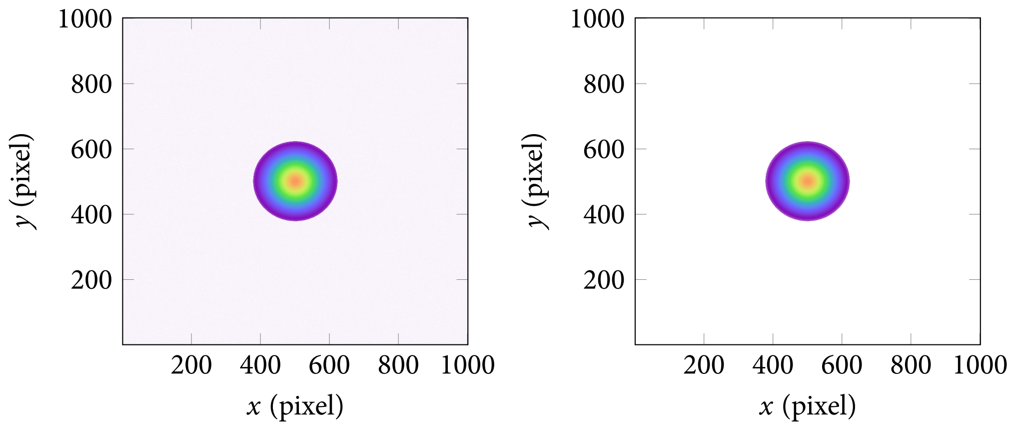

Figure 5.3: (Left) Simulated 2-dimensional symmetric Gaussian beam with normal distributed noises. (Right) After image processing. The rms beam size of the processed image is determined to be 45.86 pixel and is identical to that of the originally simulated beam.

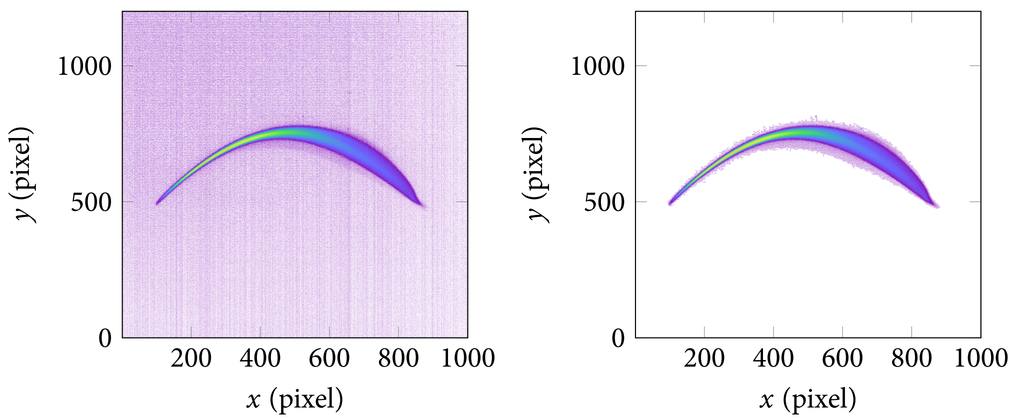

Figure 5.4: (Left) Raw camera image with real beam. (Right) After image processing. The beam image is recorded with the YAG:Ce screen in the dispersive section.

5.2.2 Calibration of the kicker magnet

The European XFEL will employ four fast kicker magnets in each of the three TDS diagnostic sections (see Section 3.2). In order to estimate if the kick strength of the kicker magnet to be installed at the European XFEL is sufficient, the knowledge of the calibration of the kicker magnet is needed. For this purpose, a modified version of the prototype kicker magnet for the European XFEL has been installed at FLASH. Table 5.1 lists the main parameters of the test kicker magnet compared to the one to be installed at the European XFEL.

Different methods were used to calibrate the strength of the kicker magnet. The kick strength scales according to

$$k[\mathrm{mrad}] = c \cdot \frac{N \cdot L[\mathrm{mm}] \cdot U[\mathrm{kV}]}{D[\mathrm{mm}] \cdot E[\mathrm{GeV}]}, \tag{5.1}$$

Table 5.1: Comparison of the main parameters of the prototype kicker magnet at FLASH with that of the design version for the European XFEL .

	unit	FLASH	European XFEL
No. of copper bar N		1	2
voltage U	kV	0 – 20	0 – 20
beam energy E	GeV	0.4 – 1.25	0.15 – 2.4
length L	mm	580	350
beampipe diameter D	mm	34	40

where N is the number of the copper bars, L the length of the copper bars, D the diameter of the beam pipe, E the energy of the electron bunch, c a dimensionless scaling factor. The calibration measurements were carried out at an electron energy of $E = 700\,\text{MeV}$ and the results are presented in Fig. 5.5. The deviation of the method C from the others results very likely from a systematic error (i.e. error in the calibration of the screen employed in this method). Based on the calibration measurement at FLASH, a characteristic scaling factor of $c = 0.0056$ is obtained for the prototype kicker magnet. By substituting the according parameters from Table 5.1, the kicker magnet for the European XFEL is estimated to provide a kick strength of $k[\text{mrad}] = 0.098 \cdot U[\text{kV}]/E[\text{GeV}]$.

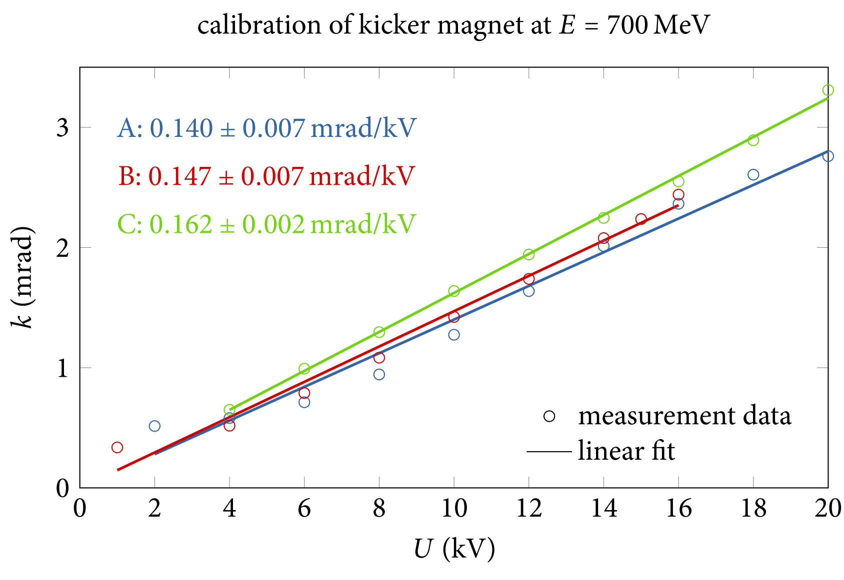

Figure 5.5: Calibration of the prototype kicker magnet at FLASH with 3 different methods. In method A, the beam position at a downstream beam position monitor (BPM) is recorded at different voltages of the kicker magnet. Method B compensates the steering effects of the kicker magnet by using a steerer to keep the beam at a fixed position. Method C is similar to A, with the beam position being measured with a downstream imaging screen. The proportionality $c \cdot \frac{N \cdot L}{D \cdot E}$ is determined from the slope of the fits to the measurement data, and listed in the figure.

5.2.3 Timing of the camera gate

The TDS diagnostic sections at the European XFEL will encounter the situation that the kicked bunch will arrive at the designated off-axis screen as well as at a subsequent one (see Fig. 3.10) during the slice emittance measurement. The spacing between these two bunches could be as small as 220 ns (at the maximum repetition rate of 4.5 MHz), when four consecutive bunches are necessary for providing online slice emittance at 10 Hz. As a result, images recorded on the subsequent screen may contain radiation intensities from both bunches, since the minimum exposure time of the CCD camera to be used at the European XFEL is 18 µs [Bas]. It is important to verify that the rising and falling time of the camera gate are fast enough to resolve the two bunches separately. Otherwise an overlap of them will lead to a distorted image, resulting in inaccurate beam sizes.

Tests of the camera gate timing have been conducted with the camera[5] in the dispersive section at FLASH. Two bunches with a spacing of 1 µs (corresponding to the maximum repetition rate of 1 MHz at FLASH) are transported onto the screen. The TDS is switched on with a minimum RF voltage to steer the second bunch, so that it is spatially separated from the first one, which eases the data analysis. Two possible methods are tested and illustrated in Fig. 5.6. The method A triggers the camera gate in-between the two bunches and images only the second bunch, while the method B images only the first bunch by setting the falling edge of the camera gate in-between the two bunches. During the tests, the trigger timing of the camera is scanned in 110 ns steps (the smallest interval in the timing system for FLASH), and the intensity of the images of the two bunches is calculated. The exposure time of the camera is set to the minimum value of 8 µs.

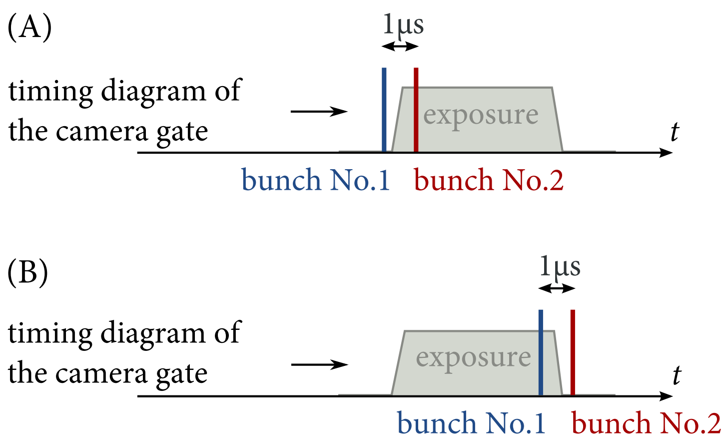

Figure 5.6: Illustration of the test for the timing of the camera gate at FLASH. Method A triggers the camera gate in-between the two bunches, and images the second bunch at the rising edge of the camera gate. Method B images the first bunch at the falling edge of the camera gate.

The results obtained with method A is presented in Fig. 5.7. The scan starts with both bunches being fully imaged and ends with both bunches vanishing. As can be seen in the inset image for $t = 15 \cdot 110$ ns, the image of the first bunch (to the right edge) does not fully disappear before the image of the second bunch (in the middle) starts to vanish. Since the scintillation light has a certain

[5] GC1380, Allied Vision Technologies GmbH, Germany [AVT].

decay time, the intensity of the first bunch is reduced to about 4%, but not fully suppressed. A clear temporal separation of the images of these two bunches is not possible.

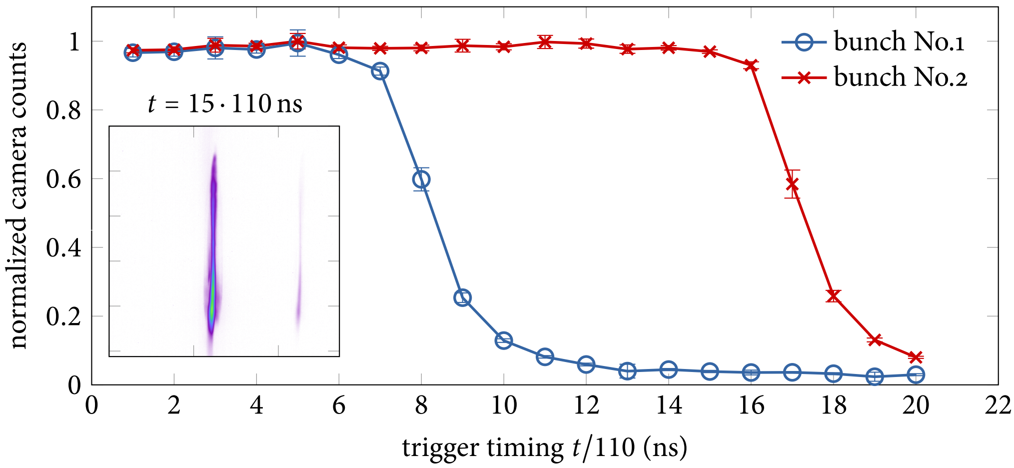

Figure 5.7: Test of the camera gate timing with the method A. The trigger timing of the camera is scanned in 110 ns step. Bunch No.1 (blue line) is spatially separated from bunch No.2 (red line) with the help of the TDS. Intensity of the image of the two bunches is measured at different trigger timings of the camera. The inset plot shows the image taken at the trigger timing of $t = 15 \cdot 110$ ns.

Figure 5.8 shows the results obtained with the method B. The scan starts with both bunches disappearing and ends with both bunches being fully imaged. The first bunch is completely imaged starting at the trigger timing of $t = 9 \cdot 110$ ns. The second bunch becomes visible later at $t = 10 \cdot 110$ ns (see the inset image), which makes a temporal separation of the two bunches possible. However, this method becomes critical when the bunch spacing is smaller than 1 µs.

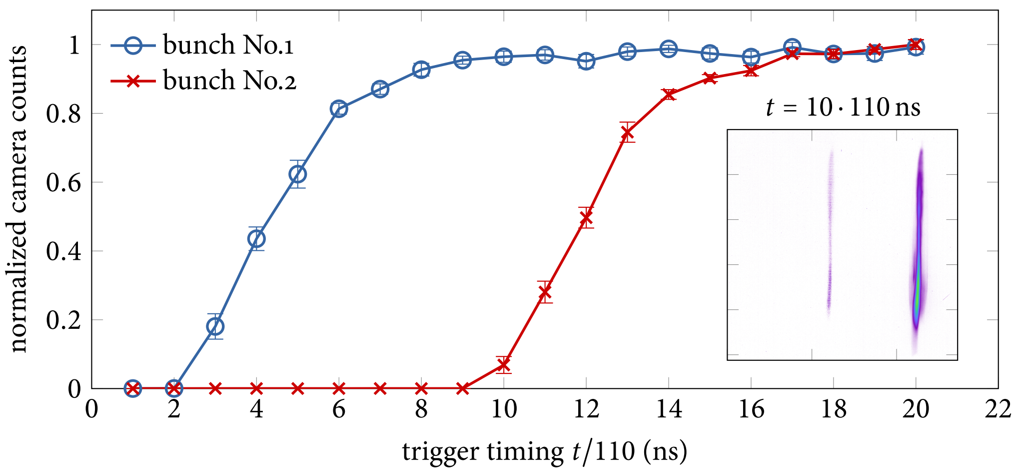

Figure 5.8: Test of the camera gate timing with the method B. The inset plot shows the image taken at the trigger timing of $t = 10 \cdot 110$ ns. It should be noted that the start of the trigger timing at $t = 0$ ns is a relative value, and cannot be compared to the one presented in Fig. 5.7.

One remedy for the European XFEL is illustrated in Fig. 5.9 using the method B. The pattern for the bunch and the kicker magnet combination is configured in the way that the overlapping bunches on the camera No.3 are temporally separated with as much time interval as possible. In this example, the bunch No.1 is kicked onto the designated screen S3, while the bunch No.4 is assigned to the screen S1 but continues to the screen S3 as well. The two bunches on the screen S3 can be resolved separately at 1 MHz, but requires explicitly spatial separation at the full repetition rate of 4.5 MHz. It should be noted that the camera trigger test at FLASH was not performed with the same camera to be installed at the European XFEL. The performance of the camera for the European XFEL is expected to be comparable, but has to be characterized in the real conditions after installation.

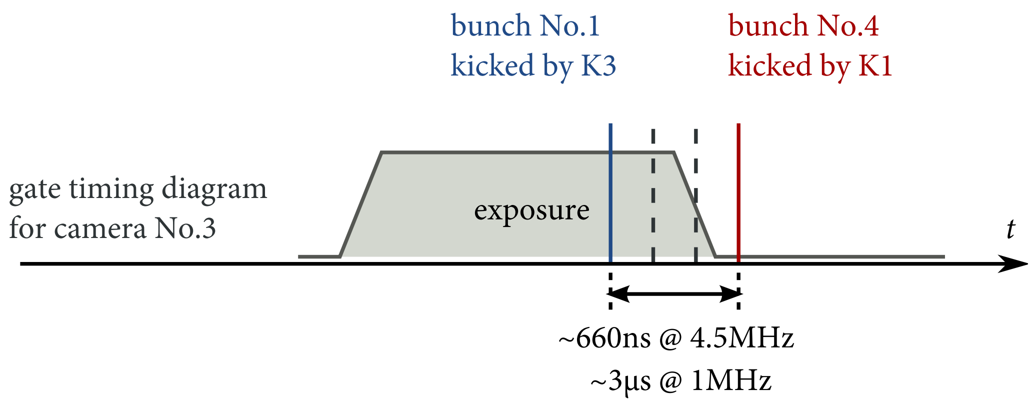

Figure 5.9: Remedy for the European XFEL using the method B to resolve two overlapping bunches. The camera No.3 sees two bunches within one bunch train: bunch No.1 kicked by the third kicker magnet K3 onto the designated screen S3, and bunch No.4 kicked by the kicker magnet K1 to the screen S1 but arriving at the screen S3 as well.

5.3 Longitudinal profile monitor

The longitudinal profile monitor utilizes the non-dispersive section, as illustrated in Fig. 5.10 with its main components. By setting the trigger timings for the TDS, the kicker magnet and the camera to one and the same bunch, the monitor is configured in bunch-stealing mode, in which one bunch out of the bunch train is streaked and deflected onto the off-axis screen for the measurement while the remaining bunches continue to the generation of FEL radiation. Shifting the trigger timings for all components by the same amount allows for monitoring any bunch within the bunch train.

The algorithm of the longitudinal profile measurement has been implemented on the MATLAB interface as well as the control system platform. Reliable operation of the longitudinal profile monitor requires comprehensive measures concerning technical aspects, such as induced beam loss. In addition, RF drifts of the TDS cause drifts of the transverse bunch position, which has to be compensated.

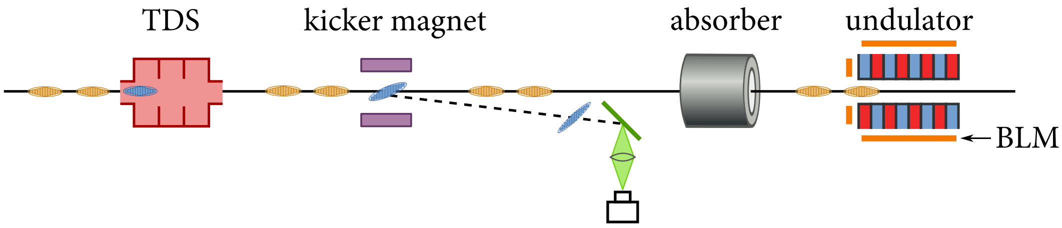

Figure 5.10: Schematic layout of the longitudinal profile monitor. The main components are the TDS, the kicker magnet, the off-axis screen and the copper absorber. Three bunches are illustrated, with the blue one used for the measurement, the yellow ones for the generation of the FEL pulses.

5.3.1 Beam loss

In order to prevent damage to the accelerator, especially the undulators, in case of beam loss, a machine protection system (MPS) [FHL+06] including beam loss monitors (BLM) and a toroid protection system (TPS) [HLN+07] are in operation at FLASH. The MPS stops the generation of electron bunches in case of beam loss by utilizing a fast shutter in the photo-cathode injector laser with a total response time of below 4 µs. Online TDS measurements in bunch-stealing mode intentionally cause beam losses. The electron bunch that is kicked out of the bunch train onto the off-axis screen is stopped in a copper absorber with a length of 256 mm behind the off-axis screen (see Fig. 5.10) and generates a shower of secondary particles. Most of the secondary particles are blocked by a lead wall of 100 mm located directly behind the absorber. Nevertheless, the BLMs in the downstream undulator section are very sensitive to protect the undulators from demagnetization, and generate alarms, although these alarms do not represent unwanted beam loss inside the undulators. Furthermore, the absence of the kicked bunch downstream of the off-axis screen is detected by the TPS and an alarm is generated as well.

Electronic circuits have been developed to mask both the analogue signals generated by the BLMs [Göt04] and a bunch gate received by the TPS for the duration of the kicked bunch (~ 1 µs). The timing of the BLM and TPS mask can be set in accordance with the kicked bunch used for diagnostics.

5.3.2 Implementation on MATLAB interface

Control and data analysis of the monitor is first implemented using the MATLAB® interface to the control system. A screen shot of the MATLAB graphical user interface (GUI) is shown in Fig. 5.11, where the second bunch out of two bunches are used for the monitor. The processed image, the longitudinal profile as well as the histories of the peak current, the rms bunch length and the full-width-at-half-maximum (FWHM) bunch length are displayed. Depending on the size of the image, results are provided with ~ 1 Hz.

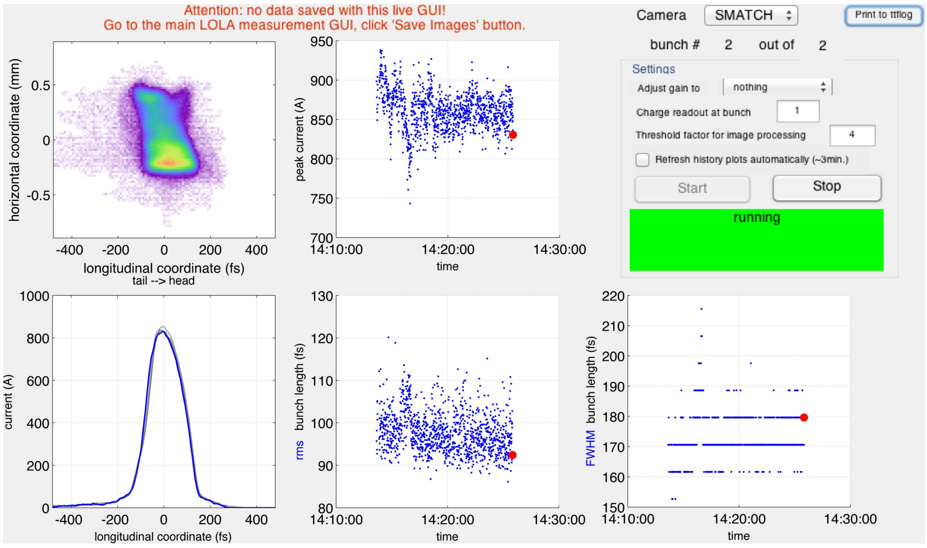

Figure 5.11: Screen shot of the MATLAB GUI for operation with the longitudinal profile monitor. The displayed beam parameters are: (First row from left) the processed image, the history of the peak current; (Second row from left) the longitudinal current profile, the history of the rms bunch length, the history of the FWHM bunch length.

5.3.3 Integration in the control system

After the successful operation on the MATLAB interface, the algorithm has been adapted and integrated as a C++ based middle layer server of the accelerator control system [YBG+13, Wyc]. The longitudinal profile server adds more functionality to the monitor and enables full data utilization rate at 10 Hz.

A simplified diagram which illustrates the data flow for the longitudinal profile server is depicted in Fig. 5.12. At FLASH, communication with hardware is realized by front-end servers of the distributed object-oriented control system [DOO]. Both beam images taken with the camera and the bunch charge recorded with the toroid are read out by their corresponding front-end servers, and the data is transferred to the shared memory of the data acquisition system (DAQ) [AAD+08]. All front-end servers receive unique identifiers from the timing system for each bunch train, and collector processes take care that the data from all distributed front-end servers is sorted according to the bunch train in the shared memory of the DAQ. In case data is received, the DAQ delivers the raw image and bunch charge to the longitudinal profile server. The server performs the image processing and sends calculated parameters of the bunch back to the shared memory of the DAQ.

The longitudinal profile monitor is extended with a TDS RF phase feedback server. Any timing change between the arrival time of the bunches at the TDS and the TDS RF phase results in a centroid deflection of the bunches. Arrival time changes can be caused by RF amplitude or phase changes of the accelerating modules upstream of the bunch compressors, leading to path lengths changes in the magnetic chicanes. Changes of the TDS RF phase may originate from length changes of the RF cables due to temperature drifts. In order to keep the beam in the centre of the imaging screen, a slow TDS

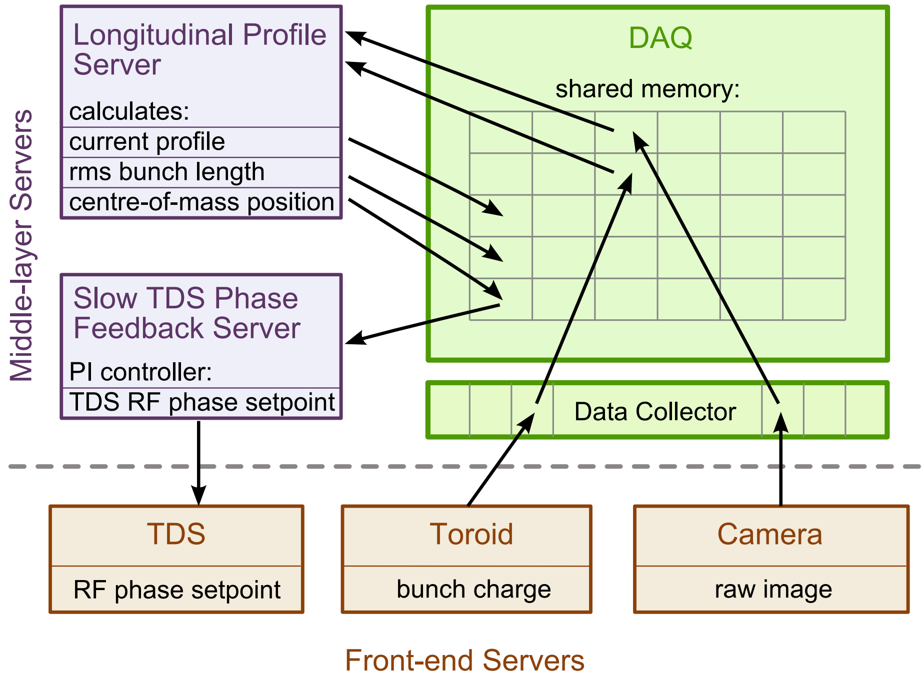

Figure 5.12: Flow diagram of the longitudinal profile monitor in the DOOCS [DOO] control system. For a detailed description see the text.

RF phase feedback has been implemented as a middle-layer server. The server is an adaptation of the slow phase feedback [KS13] for the accelerating modules. When the longitudinal profile server sends a centre-of-mass beam position to the shared memory of the DAQ, the position is sent to the slow TDS RF phase feedback server. The value of the centre-of-mass position is compared to the target value, and a proportional-integral (PI) controller calculates the corrected TDS RF phase set-point which is then written to the corresponding property of the TDS RF front-end server.

5.4 Studies on initial correlations in bunch

As described in Section 2.2.1, longitudinal profile measurements with the help of TDS are affected by the initial correlations in the transverse-longitudinal plane inside the bunch. Largely different results could be yielded at different TDS RF zero-crossings. Influence of the initial correlations on the measured longitudinal profiles has been observed at FLASH. In order to obtain the real longitudinal profile, measurement at one TDS RF zero-crossing is not sufficient, and reconstruction method requiring measurements at both TDS RF zero-crossings, as described in Section 2.2.1, has to be applied.

The TDS diagnostic section at FLASH provides the opportunity to measure the longitudinal profiles at two different sections, allowing for an investigation of the effectiveness of the reconstruction method. At three accelerator settings with different compression schemes, the longitudinal profiles are measured in the dispersive and non-dispersive section with the TDS operated at two different RF zero-crossings. The electron bunches have an energy of 700 MeV and a bunch charge of 0.33 nC. The

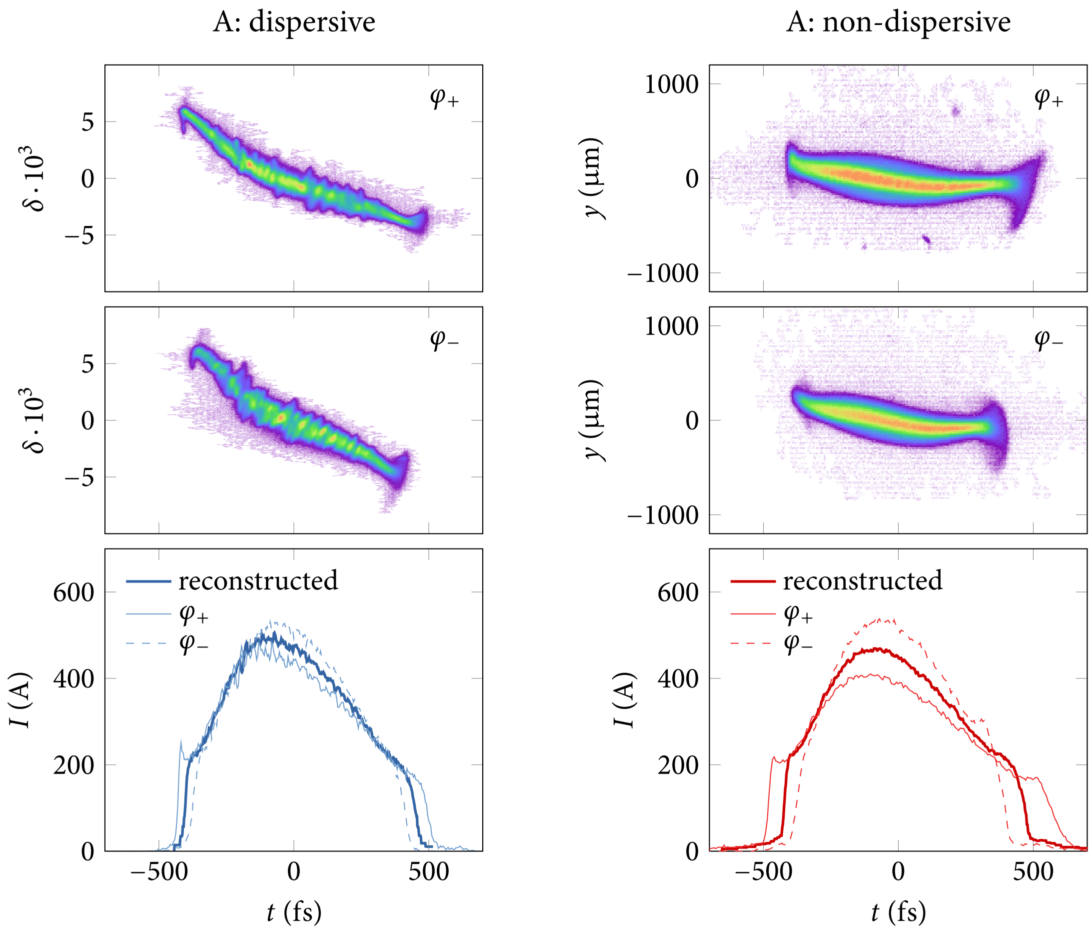

Figure 5.13: Longitudinal profiles measured with the TDS operated at the RF zero-crossings $\varphi_{+,-}$: Setting A with low compression. The images are single-shot images.

reconstructed profiles obtained in the two sections are compared with each other.

Figure 5.13 shows the longitudinal profiles measured at the machine setting A in the dispersive (blue) and non-dispersive (red) section with the TDS operated at the RF zero-crossings $\varphi_{+,-}$. The electron bunch is slightly compressed with a linear chirp. Small variations of the profiles are visible at the two phases. Both sections measured a wider profile at φ_+ with a small local peak at the bunch tail on the negative time axis. In the images taken in the dispersive section (left), microstructures are visible in the longitudinal phase space.

Comparison of the results obtained at the machine setting B with moderate compression is presented in Fig. 5.14. The non-dispersive section measured profiles with pronounced discrepancies at the two phases, while the dispersive section measured comparable profiles. The local peaks at the tail of the bunches, measured at the TDS RF phase φ_+, are underestimated in the longitudinal profiles measured at φ_-.

Figure 5.15 shows the longitudinal profiles measured at the machine setting C with strong compression. Large energy spread of ~ 2% peak-to-peak leads to cut-off of the beam on the screen in the

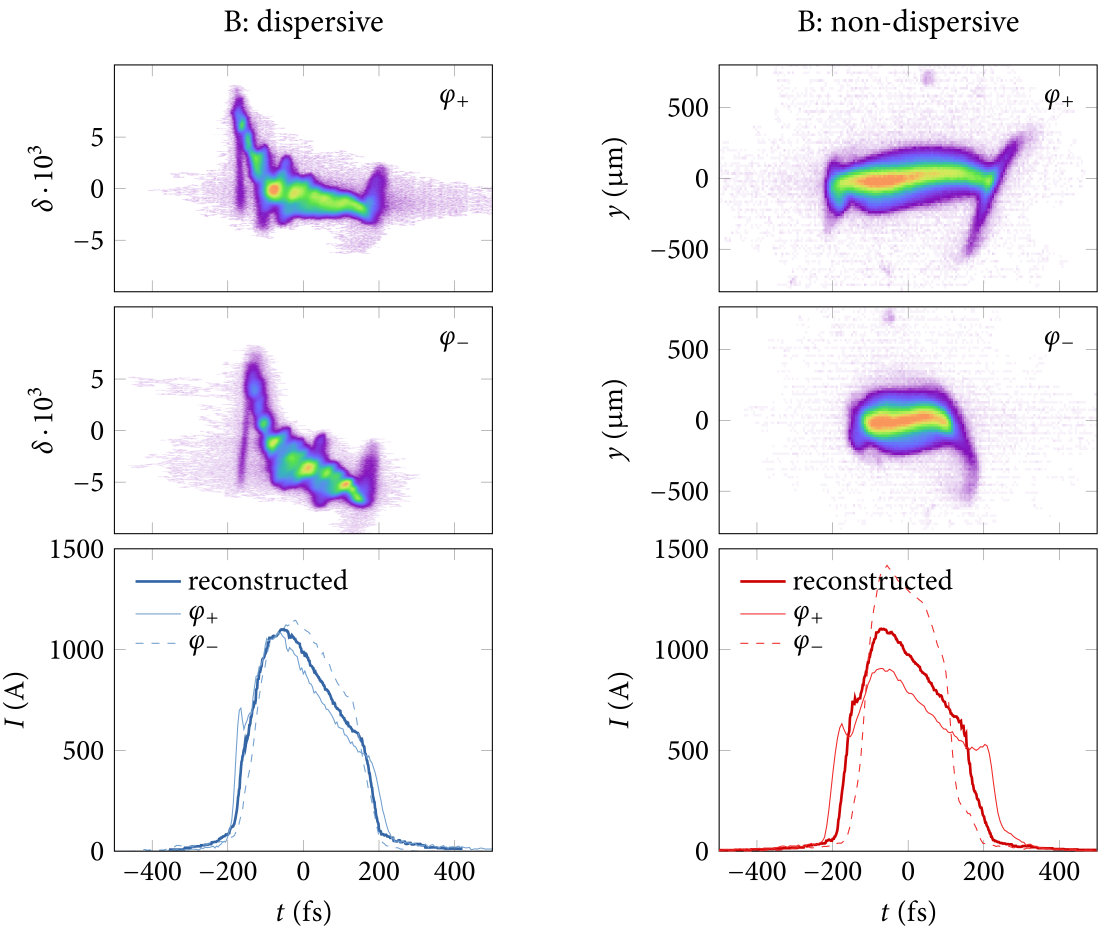

Figure 5.14: Longitudinal profiles measured with the TDS operated at the RF zero-crossings $\varphi_{+,-}$: Setting B with moderate compression.

dispersive section, as can be seen in the middle left image. Both sections observed large deviation in the longitudinal profiles measured at the two phases. In general, the non-dispersive section is more sensitive to the initial correlation due to the relatively weak streaking effect from the TDS resulted from the accelerator optics.

Figure 5.16 compares the reconstructed profiles with indication of the calculated rms bunch length. Although the individual profiles measured at each RF phase display noticeable deviations, very good agreement is achieved in the reconstructed profiles. In setting C with very short bunches (< 70 fs), the two small local peaks at the edges of the bunch cannot be resolved in the non-dispersive section. This might result from the worse rms longitudinal resolution of ~ 38 fs compared to ~ 12 fs in the dispersive section.

The rms bunch lengths of the profiles measured at the two TDS phases $\varphi_{+,-}$ and these of the reconstructed profiles, as well as the measured longitudinal resolutions are listed in Table 5.2. The statistical errors are given. The successful application of the reconstruction method proves it to be necessary and useful.

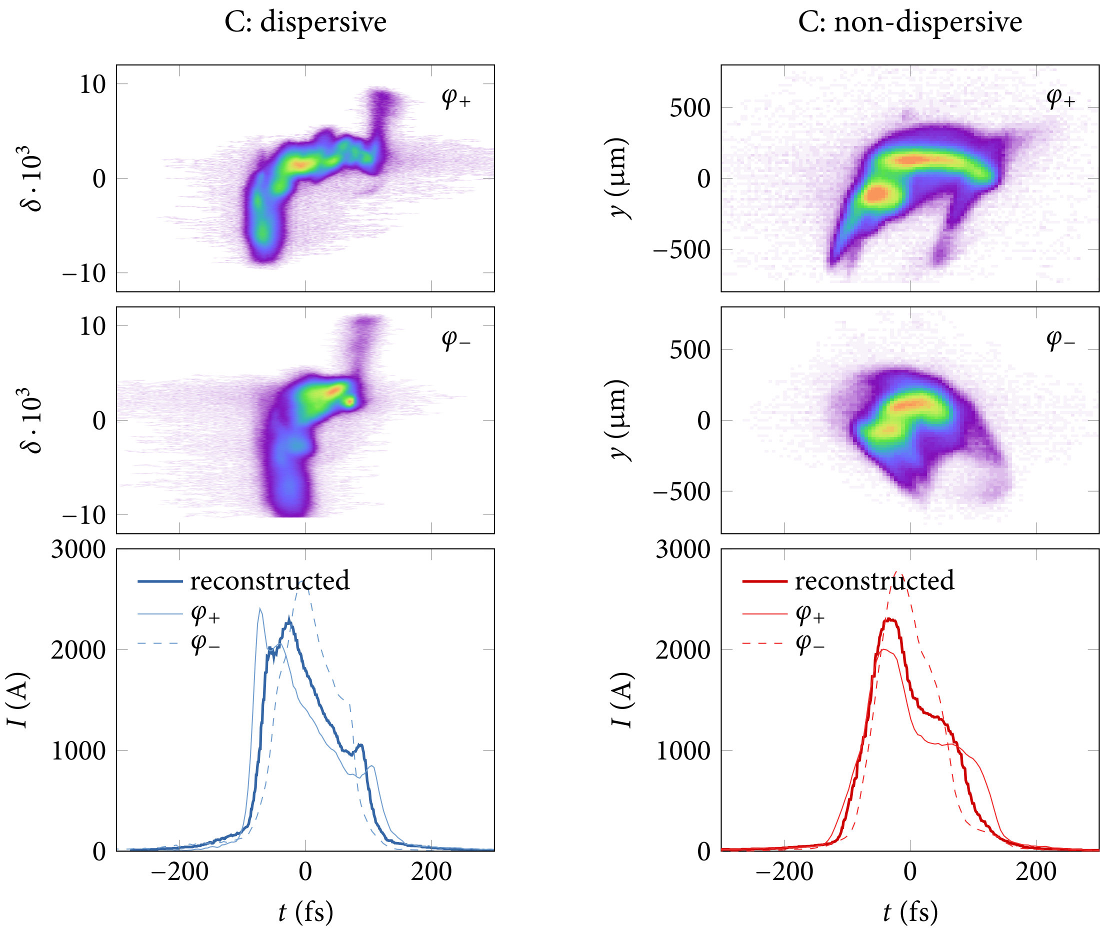

Figure 5.15: Longitudinal profiles measured with the TDS operated at the RF zero-crossings $\varphi_{+,-}$: Setting C with strong compression.

5.5 Comparison with the coherent intensity spectrometer

Complementary to the time-domain longitudinal profile measurements using TDS are frequency-domain measurements, which are realized at FLASH with the coherent intensity spectrometer [Wes12]. The spectrometer measures the spectral-resolved intensity in the 5 µm – 430 µm wavelength range of the transition radiation emitted from the electrons. In this wavelength range, the intensity is dominated by the coherent part of the transition radiation. Taking into account the bunch charge, the absolute value of the longitudinal form factor $|F(\lambda)|$, the Fourier transform of the normalized longitudinal profile (see Eq. 4.2) can be computed. Furthermore, an approximate longitudinal profile can be retrieved from $|F(\lambda)|$ with the help of the Kramers-Kronig relations for phase retrieval [LS97, GS06]. Detailed descriptions of the coherent intensity spectrometer and the method for reconstructing the longitudinal profile can be found in Refs. [Wes12, WSB+11].

For all three machine settings studied in Section 5.4, the longitudinal profiles have been retrieved using the coherent intensity spectrometer as an independent diagnostic method. The spectrometer

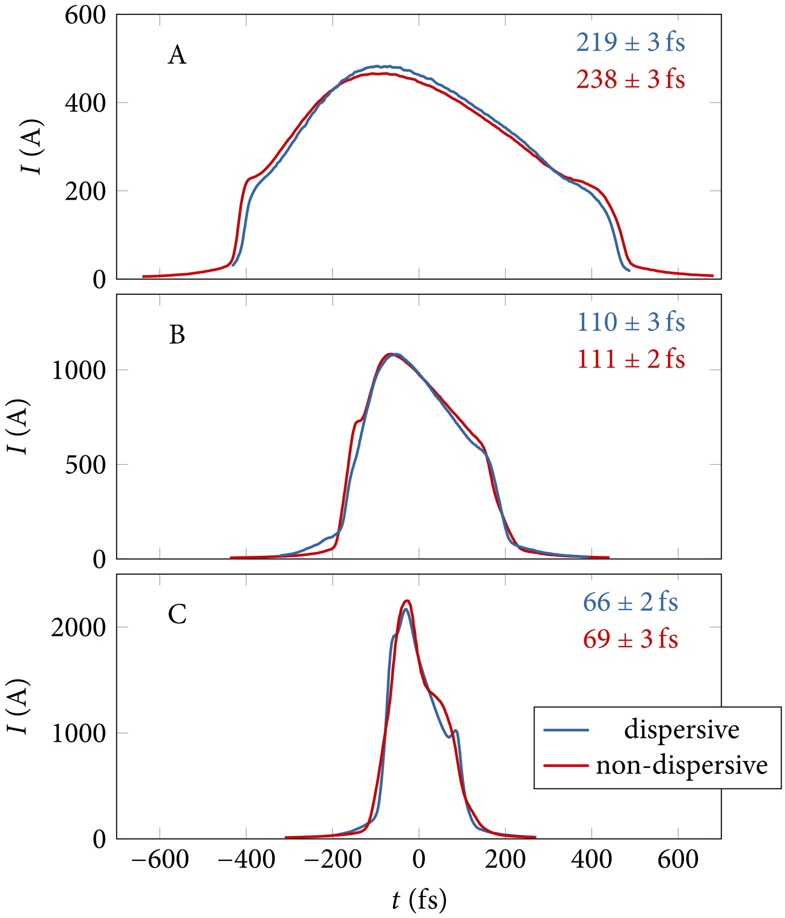

Figure 5.16: Comparison of the reconstructed longitudinal profiles measured in the dispersive and non-dispersive section. The profiles are averaged over 20 single-shots. The rms bunch lengths are indicated with statistical errors.

is located directly after the last accelerating structures (see Fig. 5.1). In Fig. 5.17, the retrieved profiles from the spectrometer measurements are compared with the reconstructed profiles obtained from the measurements at both TDS RF phases. The overall shapes of the profiles from TDS measurements agree with those from spectrometer measurements. At the machine setting C, a pronounced local peak current at $t \sim -70$ fs is observed in the retrieved profile from spectrometer measurements (green). This local peak current is underestimated in the reconstructed profile from TDS measurements in the dispersive section (blue), and not resolved in the measurements in the non-dispersive section (red). The limited longitudinal resolutions of TDS measurements (see Table 5.2) might account for the suppression of the local current peak. At the ends of the bunch towards the positive time axis, the retrieved profiles from spectrometer measurements show small oscillations containing currents with negative values. The rms bunch lengths are determined from the retrieved profiles excluding the oscillations. The bunch lengths obtained with different methods agree with each other, except in case C where the bunch length from spectrometer measurements exceeds those from TDS

Table 5.2: Summary of the rms bunch lengths $\sigma_{t,+}$, $\sigma_{t,-}$, $\sigma_{t,recon}$ measured at the two TDS phases φ_+, φ_- and of the reconstructed profile, as well as the measured rms longitudinal resolution R_t. The values are given with statistical errors in the unit of [fs].

	dispersive section	non-dispersive section
	setting A	
$\sigma_{t,+}$	232 ± 4	279 ± 7
$\sigma_{t,-}$	201 ± 9	209 ± 5
$\sigma_{t,recon}$	219 ± 3	238 ± 3
R_t	~ 15	~ 34
	setting B	
$\sigma_{t,+}$	122 ± 4	140 ± 5
$\sigma_{t,-}$	103 ± 6	89 ± 4
$\sigma_{t,recon}$	110 ± 3	111 ± 2
R_t	~ 17	~ 45
	setting C	
$\sigma_{t,+}$	74 ± 4	84 ± 4
$\sigma_{t,-}$	64 ± 5	58 ± 5
$\sigma_{t,recon}$	66 ± 2	69 ± 3
R_t	~ 12	~ 38

measurements by ~ 30%.

5.6 Summary

A system consisting of a longitudinal profile monitor utilizing a TDS, a fast kicker magnet and an off-axis screen has been commissioned at FLASH, which is now used routinely by the operators and other users. In order to comply with long-time machine operation, different technical obstacles have been overcome and software for data analysis has been prepared.

The monitor serves as a platform to test various prototype components and ideas for the European XFEL. Calibration of the prototype kicker magnet has been performed and the value adopted in the design of the accelerator optics for the European XFEL. In order to resolve the problem that two consecutive bunches arriving at the same screen may not be distinguishable, a remedy has been proposed based on the results of the investigation on the camera gate timing.

Deviation of the longitudinal profiles measured at different TDS RF zero-crossings indicates the existence of systematic errors resulting from the initial correlation in the transverse-longitudinal plane of the electron bunch. The reconstruction method as described in Section 2.2.1 has been applied. Comparison with the longitudinal profiles obtained in longitudinal phase space measurements has demonstrated good agreements of the reconstructed profiles, and proved the efficiency of the reconstruction method. Comparison with the results of the independent spectrometer measurements has further confirmed the reliability of the reconstruction method.

Stable performance of the monitor during FEL deliveries has validated the feasibility of the idea

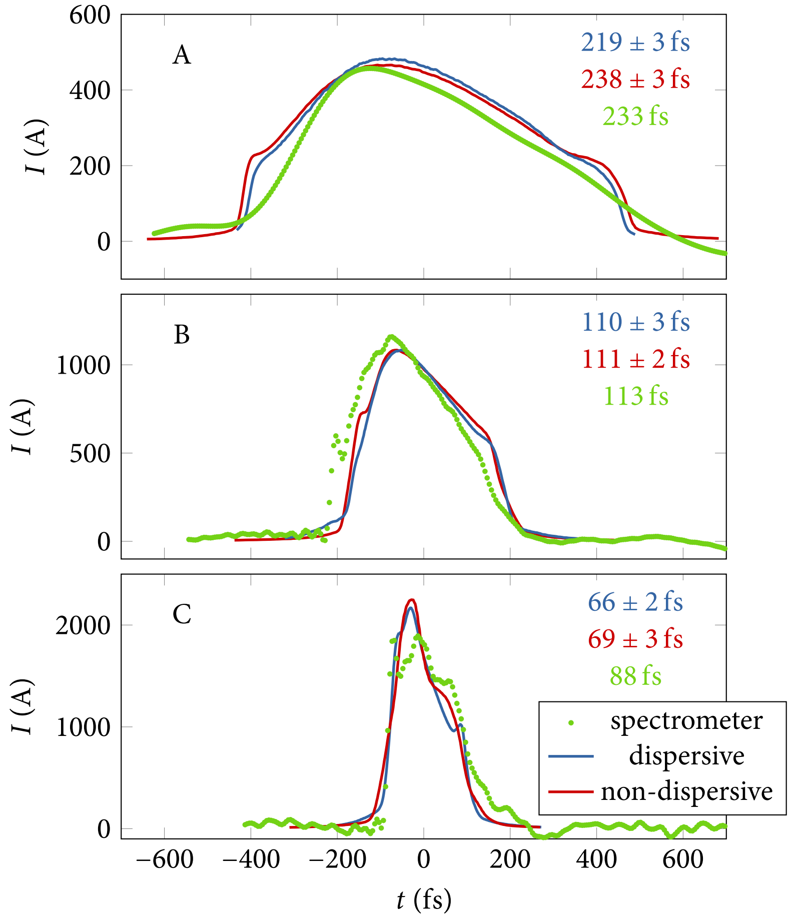

Figure 5.17: Comparison of the reconstructed profiles (presented in Fig. 5.16) with the retrieved longitudinal profiles from spectral measurements using the coherent intensity spectrometer. The rms bunch lengths are indicated.

of online longitudinal diagnostics with TDS in pulse-stealing mode, and provided valuable practical experiences for the implementation of similar systems at the European XFEL. It should be especially emphasized that measurement of the longitudinal profile at one TDS RF zero-crossing is not sufficient, when there exist initial correlations inside the electron bunch. Measurements at two different TDS RF zero-crossings are necessary to reconstruct the longitudinal profile, and to calculate the length of the electron bunch.

6 Measurement at SITF

Comparative emittance measurements using quadrupole scan and multi-screen method

The projected emittance and slice emittance of electron bunches are crucial parameters to the performance of the FELs. Reconstruction of projected and slice emittance can be realized by measuring the beam sizes of the bunch at locations with different transfer matrices (see Section 1.2). Quadrupole scan and multi-screen method are the two most widely used methods for emittance measurements. The quadrupole scan varies the transfer matrices by changing the strengths of the quadrupoles, and thus the accelerator optics between the reconstruction and the measurement point. When multiple quadruples are used, the accelerator optics can be changed freely and the steps of the variations can be organized with flexibility. However, it cannot be performed parasitically during the generation of FEL pulses. In the multi-screen method, the accelerator optics remain unchanged, and measurements are performed at different locations to obtain various transfer matrices. It requires dedicated diagnostic section, where the number of the screens defines the number of measurement points. The multi-screen method provides the possibility of parasitic emittance measurements without interrupting the generation of FEL pulses in a so-called pulse-stealing mode: One or several bunches from a bunch train are deflected onto off-axis screens for diagnostic purpose, and the remaining bunches are not affected and traverse through the undulator for the generation of FEL pulses. Such online diagnostics are highly demanded for high repetition multi-bunch FELs.

The European XFEL will employ the multi-screen method with off-axis screens for online emittance measurements during the generation of FEL pulses in the pulse-stealing mode (see Section 3.2.1), and at the same time retain the possibility of using the quadrupole scan method for the commissioning period. The implementation of off-axis screens and fast kicker magnets for online diagnostics has been validated at FLASH (see Section 5.3). It is important to gather experience with the procedures of emittance measurement and investigate the performance of these two methods compared to each other.

The SwissFEL Injector Test Facility (SITF) at PSI, Villigen, Switzerland provides an existing diagnostic section, where the quadrupole scan method has been established as a standard tool for routine use in emittance measurements [PA14, Pra14]. With the installation of a transverse deflecting structure, the diagnostic section allows furthermore longitudinal diagnostics, such as longitudinal profile, longitudinal phase space and slice emittance [PAB+14]. Multiple screens that are originally planned for emittance measurements using the multi-screen method have been installed and are available in the diagnostic section. In this thesis, first application of the multi-screen method for emittance measurements at SITF has been achieved. Results of the projected and slice emittance measurements using the multi-screen method have been compared with those using the established quadrupole scan method. Measurements with both compressed and uncompressed bunches have been performed.

In this chapter, the experimental setup at the SITF is described and the results of the measurements of projected and slice emittance using both methods are presented. Following that, discussion of the deviation in the results and correction of the results with systematic errors are described. In the end, a summary with learnt experience for the European XFEL is given.

6.1 The SwissFEL Injector Test Facility

The SwissFEL, a normal-conducting X-ray free-electron laser, is under construction at the Paul Scherrer Institut (PSI) in Switzerland and will commence commissioning in 2016, with first FEL operation expected by 2017. It will serve two undulator beamlines delivering FEL pulses in the range from 0.1 – 7 nm [G+12]. In order to demonstrate the feasibility of the SwissFEL, the SwissFEL Injector Test Facility (SITF) [P+10] has been built, where different concepts and prototype components are tested.

A schematic layout of the SITF is shown in Fig. 6.1. The electron bunches are generated in a laser-driven RF gun and then further accelerated in four S-band normal-conducting accelerating structures, which are operated at a frequency of $f \approx 3\,\text{GHz}$. An X-band system working at the fourth harmonic of the S-band structures with $f \approx 12\,\text{GHz}$ is installed to linearise the longitudinal phase space before the electron bunches are compressed longitudinally in the magnetic chicanes. The maximum beam energy after compression is 250 MeV and the nominal charge for machine operation can be varied from 10 pC to 200 pC.

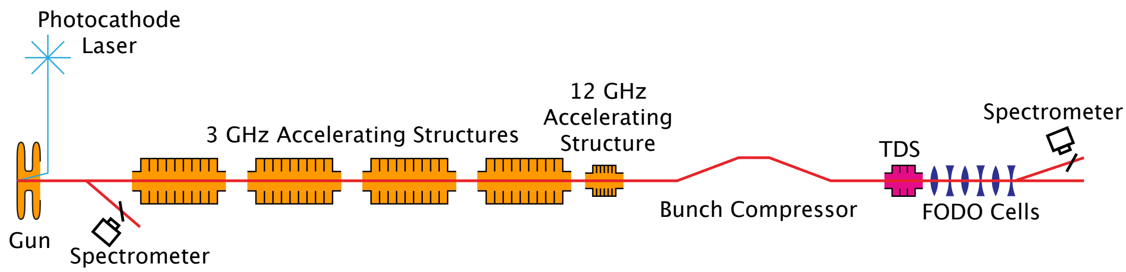

Figure 6.1: Schematic layout of the SwissFEL Injector Test Facility at PSI. Figure adapted from Ref. [IBSS09].

The compact and complete diagnostic section is located downstream of the bunch compressor and comprises various components for different diagnostic purposes. An S-band transverse deflecting structure (TDS), which provides a maximum effective voltage of 5 MV, streaks the bunch in the vertical direction. It allows for time-resolved longitudinal diagnostics and enables slice emittance measurement in the horizontal plane. A Focusing-Drift-Defocusing-Drift (FODO) section is installed downstream of the TDS for the emittance measurements, where multiple transverse imaging screens can be employed for both quadrupole scan and multi-screen method. At the end of the SITF beamline, the bunches can be deflected by a dipole magnet into the energy spectrometer. In combined use with the TDS, the longitudinal phase space can be obtained there.

6.2 Experimental details for the multi-screen and quadrupole scan method

The emittance measurements based on the quadrupole scan and multi-screen method are performed in the diagnostic section. Figure 6.2 shows the detailed arrangement of the accelerator components starting from the TDS to the last transverse imaging screen. The TDS is followed by five quadrupoles, which are used for the quadrupole scan method, and a 3.5-cell FODO section with seven standard screen stations (marked as red dots in Fig. 6.2), which are designed for the multi-screen method. The seven standard screen stations are equipped with optical transition radiation (OTR) and scintillator screens. A high-resolution transverse profile monitor [IT14] (marked as a green dot in Fig. 6.2) is available at the end of the section.

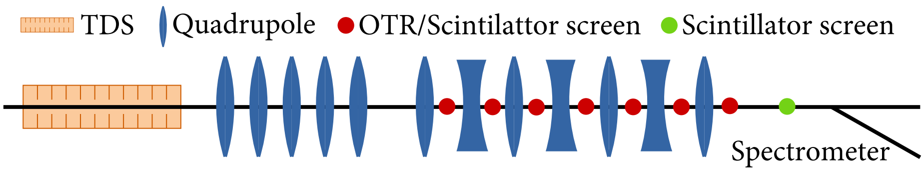

Figure 6.2: Schematic layout of the diagnostic section for emittance measurements. It comprises one S-band TDS, five quadrupoles used in the quadrupole scan method, and a FODO section with multiple screen stations used in the multi-screen method.

6.2.1 Accelerator optics

As can be seen in Eq. 1.21, accuracy of emittance measurement is sensitive to the accelerator optics. In addition, accelerator optics influence the longitudinal resolution of the TDS measurement as well. Careful calculation in the accelerator optics is essential for a robust emittance measurement. Different accelerator optics are designed for the projected and slice emittance measurements using these two methods.

Multi-screen method

Figure 6.3 shows the symbolic beamline layout of the diagnostic section starting from the TDS (top) and the design optics for the multi-screen method (bottom). The same accelerator optics is adopted for both projected and slice emittance measurements. It should be mentioned that although there exists different optimum accelerator optics for them, a shared optics simplifies the measurement procedures by avoiding changing and matching the optics.

At the TDS, a large β_y = 40 m in the streaking direction is essential for a good time resolution (see Eq. 2.21). The beam is then matched with help of five quadrupoles into the 3.5-cell asymmetric FODO section with phase advances of 72° and 52° in each cell in the x and y plane, respectively. Seven OTR and scintillator screens (i.e. seven data points) are available for each measurement. The value of the emittance is reconstructed at the entrance of the first quadrupole. In addition, the Twiss parameters at the reconstruction point are designed to share the same value as these for the slice emittance measurement using the quadrupole scan method, making an extra comparison of the Twiss parameters possible.

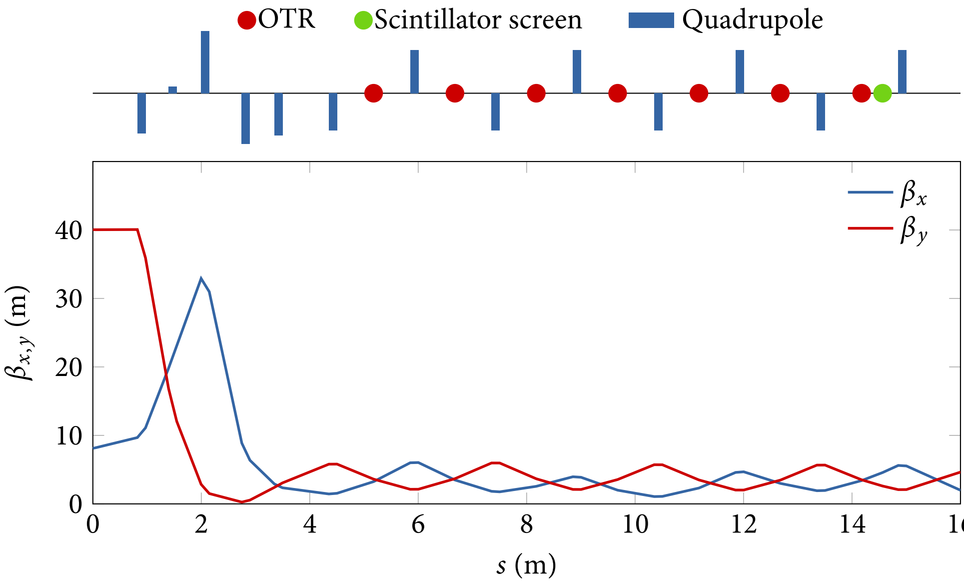

Figure 6.3: Symbolic beamline layout (top) and design optics (bottom) for the emittance measurement using the multi-screen method. The beamline from the TDS to the end of the FODO section is depicted. The orientation of the blue bars, representing the quadrupoles, indicates the sign of the quadrupole field (positive and negative orientation means focusing in the x and y plane, respectively), and the height of the bars scales with the strength of the quadrupole field. The multi-screen method employs the same optics for both slice and projected emittance measurements.

The phase advances $\Delta\mu_x$ and $\Delta\mu_y$ from the TDS to the individual screens are shown in Fig. 6.4 (left). For the measurement of projected emittance, a total phase advance of 206° and 153° are covered in the x and y plane, respectively. Only five screens are utilized for the measurement of slice emittance, as measurements at the first and last screen in the FODO cell with phase advances of $\Delta\mu_y = 189°$ and $\Delta\mu_y = 342°$, respectively, have worse longitudinal resolution from the TDS due to the $\sin(\Delta\mu_y)$ term in Eq. 2.21. Compared to the fourth screen with $\Delta\mu_y = 270°$, the obtainable longitudinal resolutions at the first and last screen are expected to increase by a factor of 6.4 and 3.2.

Quadrupole scan method

The quadrupole scan method is the standard method for measuring projected and slice emittance at the SITF [PAB+14, Pra14]. It is well established and has been used routinely during machine setup.

A high-resolution profile monitor, dedicated for the quadrupole scan method, has been installed at the end of the FODO section (denoted with a green dot in Fig. 6.3). The large space and number of available quadrupoles between the TDS and the high-resolution profile monitor provide more flexibility and easier realization in designing the accelerator optics for the quadrupole scan method.

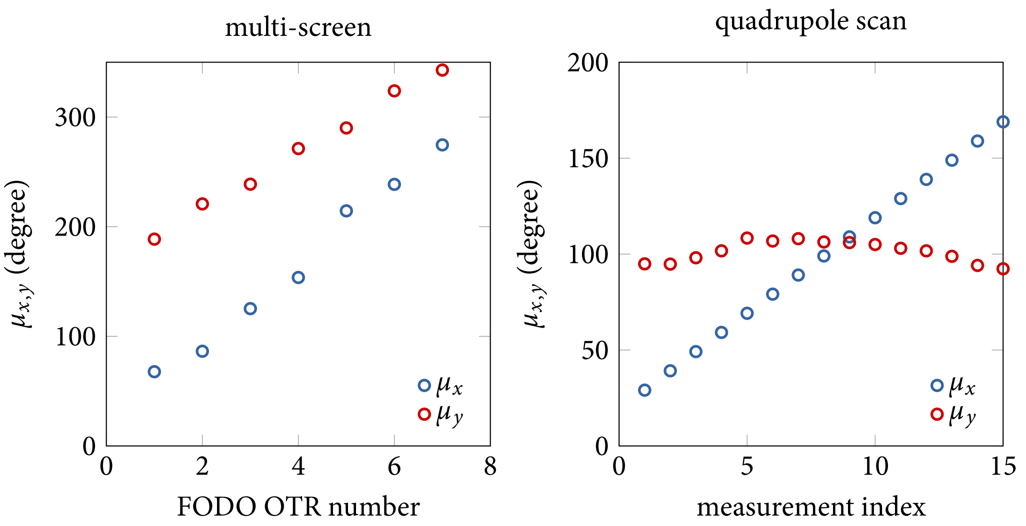

Figure 6.4: Phase advances of the optics designed for the slice emittance measurement: (left) from the TDS to each screen for the multi-screen method and (right) from the TDS to the high-resolution profile monitor at each quadrupole setting for the quadrupole scan method.

One single quadrupole (the fifth quadrupole in Fig. 6.3) is scanned for the measurement of projected emittance, covering phase advances in total of approximately 180° in both x and y planes at the same time [Pra14]. Five quadrupoles (the first five quadrupoles in Fig. 6.3) are employed together for the measurement of slice emittance [PAB+14]. The reconstruction point for the slice emittance and its value of Twiss parameters are the same as those in the multi-screen method, which makes additionally a comparison of the reconstructed optics using these two methods possible. The phase advances for the measurement of slice emittance are displayed in Fig. 6.4 (right). With the combined use of the five quadrupoles, the horizontal phase advance $\Delta\mu_x$ covers from 30° to 180° with equal steps. Relative constant $\Delta\mu_y$ around 90° is achieved to maximize the streaking effect of the TDS and maintain constant longitudinal resolution throughout the scans. In addition, the horizontal beta-functions at the high-resolution profile monitor are designed to be constant at $\beta_x = 40.5 \pm 3.1$ m during the scan. The large value of beta-function leads to a large beam size on the screen, thus improving the accuracy of beam size measurement. The constant beam sizes ensure comparable error contributions from the screen resolution.

6.2.2 Imaging system

The screen monitors inside the FODO section [IBO+10] are equipped with multiple screens and optical systems (see Fig. 6.5). One OTR (aluminium-coated silicon mirror) and one scintillator screen (LuAG:Ce, i.e. lutetium aluminium garnet doped with cerium) are rotated in the horizontal plane at an angle of 45° between the screen normal and the incoming beam axis. The optical system, consisting of a room-temperature CCD camera[1] and a commercial macro lens[2], is positioned to detect the light emission at an angle of 90° to the beam axis. With a calibration of 4.55 µm/pixel, the field of view of the imaging system amounts to 5.46 mm and 7.28 mm in the x and y plane, respectively. As the Scheimpflug criterion [Sch04] is not fulfilled in the imaging system, only the central horizontal part of the screens with a width of about 1 mm can be imaged within depth of field to achieve reasonable resolution. The LuAG screen has much higher light yield than the OTR screen, which is very desired for operation with low-charge bunches, but it provides worse spatial resolution due to the finite thickness of the scintillator screen (compare Section 4.3.1). Therefore, the OTR screens are chosen for the emittance measurements using the multi-screen method. The spatial resolution is determined according to ISO12233 standards [IOS00] to be 150 lp/mm using uniform illumination. Taking into account the angular distribution characteristic of OTR, the resolution with real beam is estimated to be below 15 µm full-width-at-half-maximum (FWHM) [IBO+10].

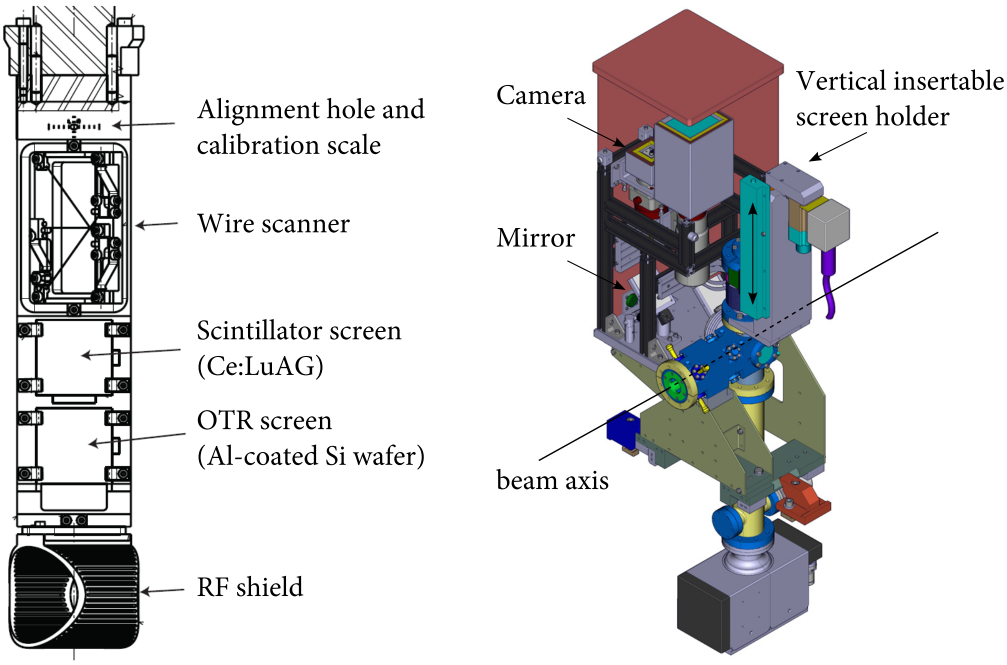

Figure 6.5: Screen monitor used for the multi-screen method at the SITF. (Left) The screen holder with scintillator and OTR screens. (Right) Chamber of the screen monitor containing the camera, mirror and vertical insertable screen holder. Figure adapted from Ref. [IBO+10].

The high-resolution profile monitor, which is employed for the quadrupole scan method, is designed in a special configuration to achieve a resolution much smaller than the thickness of the scintillator. It is more robust than the OTR screen for operation with low-charge bunches due to its higher light yield. A detailed description of the profile monitor can be found in Section 4.3.1.

[1] Sony ICX274AL.
[2] Micro Nikkor 200 mm f/4.

6.2.3 Error discussion

statistical error

As given in Eq. 1.27, error propagation method can be used to estimate the statistical error of the reconstructed emittance resulting from statistical error in the beam size measurements. However, when the optics have a large mismatch parameter, the probability distribution of the measured emittance is no longer in a Gaussian shape and cannot be sufficiently described by the approach of error propagation. One more elaborate method is to use Monte-Carlo simulation to compute the probability distribution of the emittance.

Monte-Carlo simulations are performed for slice emittance measurements with the transfer matrices (from the reconstruction point to the individual measurement point) that are used later in the real measurements, and the parameters similar to that in the real measurements, i.e. normalized emittance of $\varepsilon_N = 0.5\mu\text{m}$, beam energy of $E_0 = 200\,\text{MeV}$. A beam size error of 5% is assumed, which is comparable to the beam size errors measured in the experiments presented in Sections 6.3 and 6.4. The Twiss parameters at the reconstruction point are varied. For each combination of beta- and alpha-function, reconstruction of the horizontal emittance is repeated for 1000 samples of beam sizes with Gaussian distributed error. From the probability distribution of the 1000 reconstructed emittance values, the mean value $\bar{\varepsilon}$ and the standard deviation σ_ε are evaluated. Detailed explanation of the procedure of Monte-Carlo simulations can be found in Section 1.3.1.

Figure 6.6 shows the relative deviation of the mean value of emittance $\bar{\varepsilon}$ from the design emittance ε_N in a colour code. The quadrupole scan method (right) works for a slightly larger range of the initial Twiss parameters than the multi-screen method (left). For initial Twiss parameters of mismatch parameter up to $M = 1.5$, both methods yield reconstructed emittances with deviations of smaller than 4% from the design emittance. Outside of a certain range, the deviation could increase rapidly so that both methods fail.

Figure 6.7 shows the relative standard deviation $\sigma_\varepsilon/\bar{\varepsilon}$ of the probability distribution of the reconstructed emittance from the 1000 samples for different combinations of the initial Twiss parameters. For matched beams ($M \approx 1$), the probability distribution of the measured emittance is still in Gaussian shape, and its standard deviation agrees with the error obtained from the error propagation method. At the design optics ($M = 1$) using the assumed statistical beam size error of 5%, the deviation of the mean value $\bar{\varepsilon}$ from the design emittance is determined to be less than 0.2% for both methods, and the relative standard deviation $\sigma_\varepsilon/\bar{\varepsilon}$ is 5.7% and 2.9% for the multi-screen and quadrupole scan method, respectively. The quadrupole scan method is more robust for mismatched beam: the error is below 10% for bunches with mismatch parameter up to $M = 1.5$, while in case of the multi-screen method the error exceeds 10% for bunches with mismatch parameter of $M > 1.1$. For mismatched beams with $M > 1.5$, the multi-screen method expects relative standard deviations larger than 30%, although the mean value could still have discrepancy of less than 10% from the design emittance.

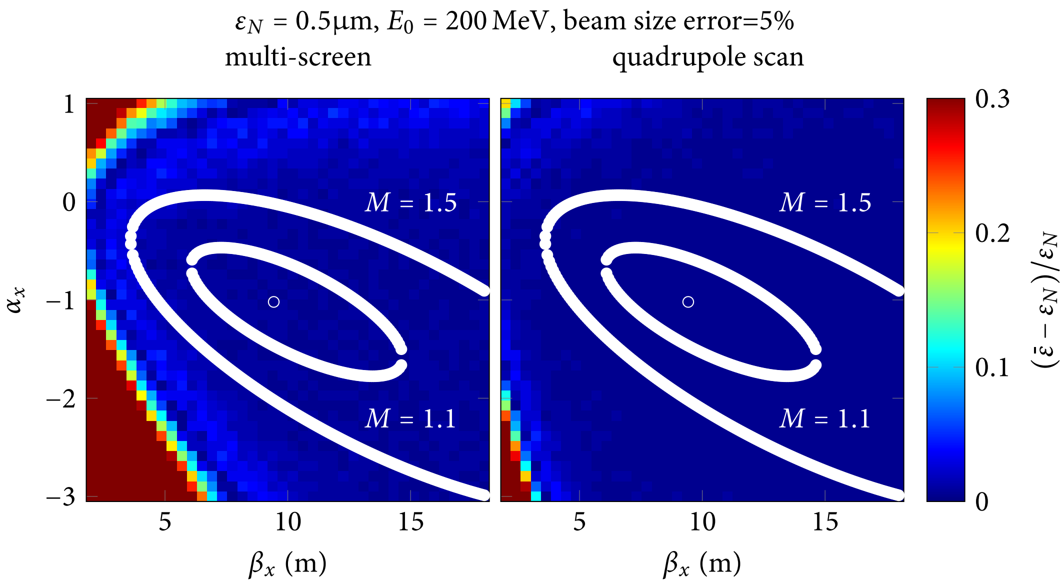

Figure 6.6: Statistical error in slice emittance measurements estimated with Monte-Carlo simulations: Deviation of the mean value of the reconstructed emittances $\bar{\varepsilon}$ from the design emittance ε_N using (left) the multi-screen method and (right) the quadrupole scan method. The colourmap is limited to the value of 30% to be capable of displaying more details in the areas with smaller values. The design optics is indicated by the circle in the middle, and the Twiss parameters with mismatch parameters of $M = 1.1$ and $M = 1.5$ are highlighted in the figure as well.

systematic error

One of the main contribution to the systematic error is the screen resolution. The different spatial resolutions of the OTR screens (15 µm [IBO+10]) and high-resolution profile monitor (8 µm [IKL+14]) result in different systematic errors of the two methods. Depending on the actual beam size, the influences of the screen resolutions could differ strongly, and be dominating in some cases. Therefore, systematic errors due to screen resolution are discussed individually in Section 6.5.

The accuracy of beam size measurement is affected by the screen calibration error as well, which is estimated to be in the order of 1% at SITF. In the quadrupole scan method, all beam sizes σ_i are measured using the same one screen, and have errors of the same factor of $\Delta_i = \Delta \sim \mathcal{N}(0, 1\%^2)$[3] from the real beam sizes. The emittance, which is reconstructed from the squared beam size $\sigma^2 \sim (1 + \Delta)^2$, has accordingly an error of $(1 + \Delta)^2 - 1$. In case of a small calibration error of 1%, the error of the measured emittance can be approximated by the first order term $2\Delta = 2\%$. The situation is different for the multi-screen method, where beam size measurements were performed using different screens. Each measured beam size σ_i has an uncorrelated error of the factor of $\Delta_i \sim \mathcal{N}(0, 1\%^2)$, $\Delta_i \neq \Delta_j$. The influence of the calibration errors of the individual screens can be investigated using Monte-Carlo simulation similar to that for the statistical errors (see Fig. 6.6 and 6.7). When the beam is matched to the design optics, the calibration error of 1% leads to a relative standard deviation of < 1% of the

[3]The probability distribution of Δ is a normal distribution centred at 0 and with a standard deviation of 1%.

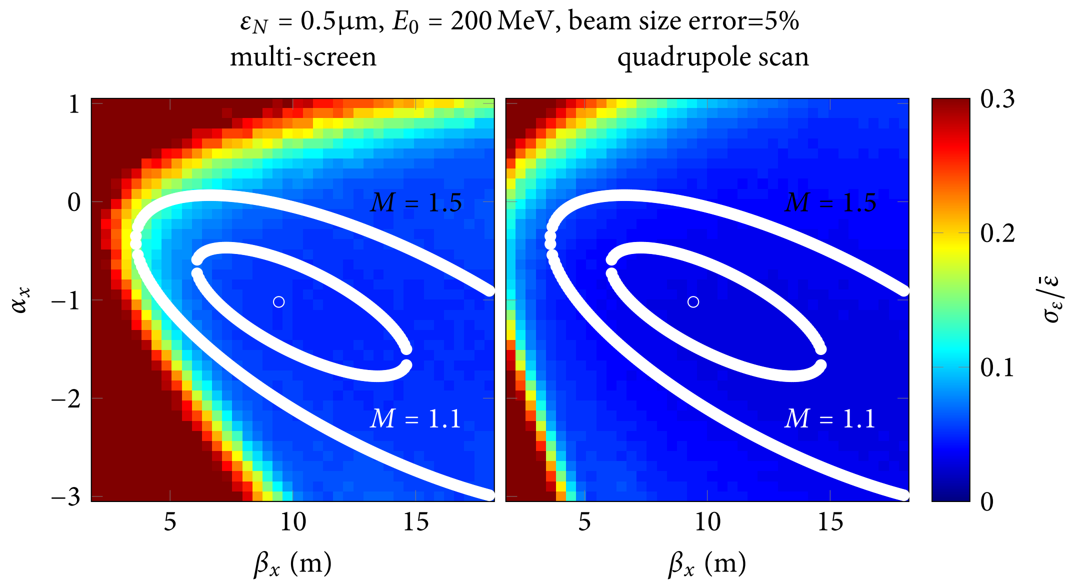

Figure 6.7: Statistical error in slice emittance measurements estimated with Monte-Carlo simulations: Relative standard deviations of the reconstructed emittance using (left) the multi-screen method and (right) the quadrupole scan method. The colourmap is limited to the value of 30% to be capable of displaying more details in the areas with smaller values. The design optics is indicated by the circle in the middle, and the Twiss parameters with mismatch parameters of $M = 1.1$ and $M = 1.5$ are highlighted in the figure as well.

reconstructed emittance in the multi-screen method.

Other important systematic errors include quadrupole field error (0.2% at SITF), error in energy measurement (0.1% at SITF) [PA14] and beam size definitions. Both quadrupole field and energy error translate into inaccuracy of the transfer matrix. Furthermore, the errors in energy measurement affect the normalization of the measured emittance to normalized emittance. Compared to the influences from optics mismatch and beam size errors, the errors from these sources are negligible.

6.3 Experimental results for uncompressed bunches

Comparative measurements were performed using uncompressed electron bunches with an energy of 200 MeV. All accelerating modules were operated on-crest. The highest possible charge of 200 pC was chosen in order to maximize light emission from the unstreaked and streaked bunches using the OTR screens.

The quadrupole scan has been used routinely for optimizing the slice emittance at the SITF [PAB+14] and usually the optics can be matched within 2 to 3 matching iterations. Before starting the comparative measurements, the necessary matching of the accelerator optics was performed using the quadrupole scan method. For the matching of the optics used in the multi-screen method, the quadrupole scan method was employed, since they share the same Twiss parameters at the reconstruction point. It should be noted that for the multi-screen method, the optics is not matched for the projected bunch, but for the central slice of the bunch.

During the measurements, the last OTR screen in the FODO section was defect, which left 6 screens available for the projected emittance measurement using the multi-screen method, and 5 for the slice emittance measurement. For each beam size measurement, multiple images were recorded for statistical reason (20 single shot images for the multi-screen method, 10 for the quadrupole scan method). Each image was first subtracted with background images and then processed to reduce noise (see Appendix D). Since the beam profiles were in Gaussian shape for measurements with both the uncompressed and compressed bunches, the beam sizes are determined by using Gaussian fit to the transverse profiles. On the other hand, determination of beam sizes from Gaussian fit is more robust than rms values in the case that the OTR screens have very low signal to noise ratio. The errors given in the following sections include only statistical errors and are determined according to error propagation (see Eq. 1.27).

During the slice emittance measurements, the bunch length is determined from Gaussian fit. Each slice is defined with a width of 1/5 of the bunch length and the central slice as the one at the longitudinal mean position of the bunch. The same definition is used in both methods for consistency.

6.3.1 Projected emittance

During the measurement using the multi-screen method, the images taken with the 4th. OTR screen displayed two beamlets similar to the features of the OTR point spread function (see Fig. 6.8) and therefore were omitted for the reconstruction of the emittance.

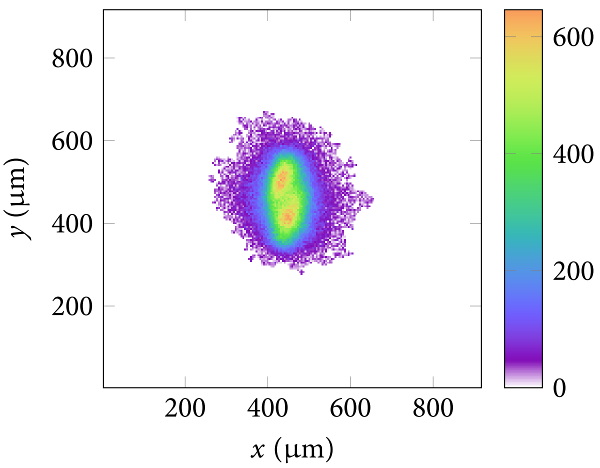

Figure 6.8: Example beam image taken with the 4th. OTR screen during the projected emittance measurement with uncompressed beam. Two beamlets are visible.

For each of the method, one measurement was performed. The results of the projected emittance measurements are presented in Fig. 6.9, and the reconstructed normalized projected emittances $\varepsilon_{x,y}$ together with the mismatch parameters $M_{x,y}$ are summarized in Table 6.1. The results obtained with these two methods are comparable, but the normalized emittances derived using the multi-screen method are slightly larger than that using the single quadrupole scan method in both planes. Errors from optics mismatch are minimized in the single quadrupole scan method, while the mismatch parameters of 1.13 and 1.07 in the multi-screen method indicate that there is still an error contribution stemming from the optics mismatch.

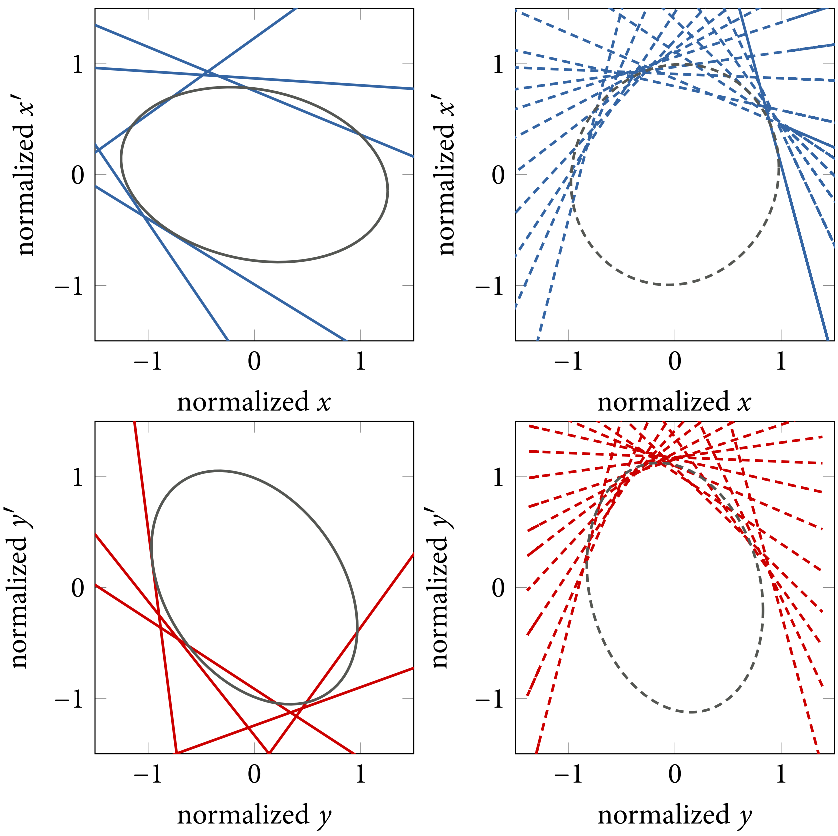

Figure 6.9: Fits of the beam ellipses using (left, solid lines) the multi-screen method and (right, dashed lines) the single quadrupole scan for the measurement of horizontal (blue) and vertical (red) projected emittance with uncompressed bunches. The lines represent each measured beam size. The results are presented in normalized coordinates as given in Eq. 1.26.

Table 6.1: Summary of projected emittance measurements with uncompressed bunches.

	multi-screen method	single quadrupole scan
ε_x	487 ± 8 nm	486 ± 2 nm
M_x	1.13	1.00
ε_y	479 ± 6 nm	458 ± 3 nm
M_y	1.07	1.06

6.3.2 Slice emittance

The accelerator was operated with the same settings as for the projected emittance measurement. Several matching iterations were performed to match the central slice to the design optics. The bunch length was determined from Gaussian fit and amounts to approximately 3 ps. Each slice was chosen to have a width of ~ 0.6 ps.

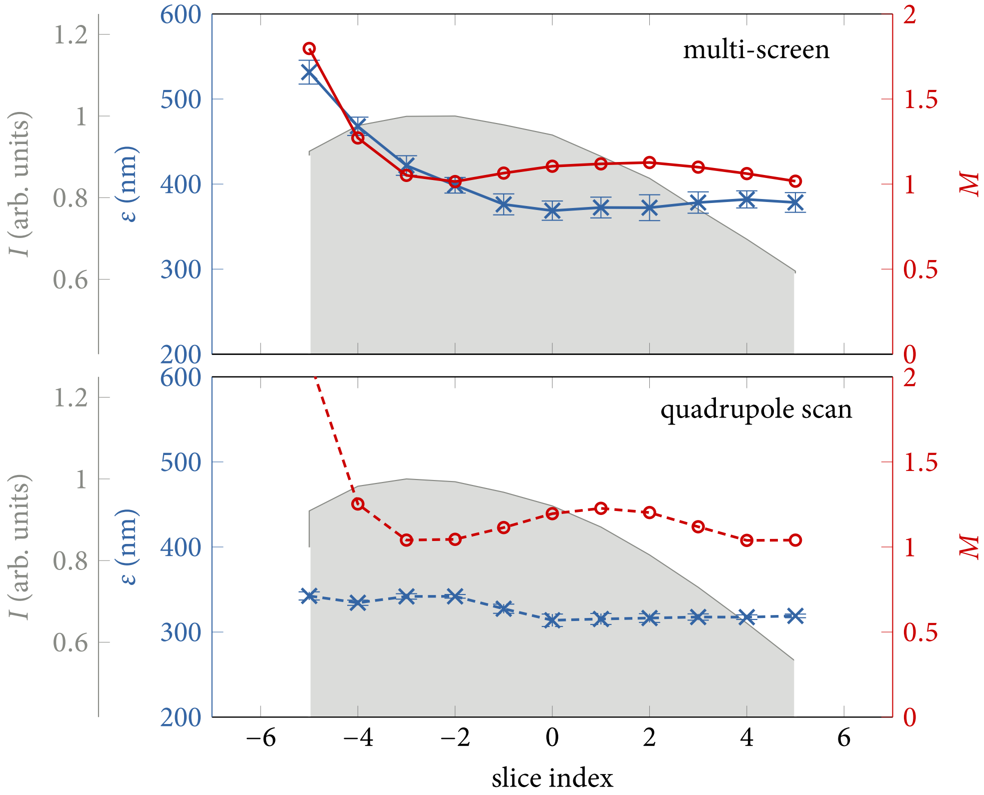

Figure 6.10: Slice emittance measured at the first TDS RF zero-crossing with uncompressed bunches using (top, solid) multi-screen and (bottom, dashed) quadrupole scan method. The red lines represent the mismatch parameter with respect to the design optics. The grey lines (with filled areas) represent the longitudinal profile in arbitrary units. The head of the bunch is on the right hand side of the horizontal axis.

The deflecting power of the TDS P_{TDS} was kept at a moderate value complying with the following restrictions: (i) The beam size of the streaked bunch on the OTR screens should be relatively small so that there will be still enough light emission from the OTR screens, (ii) The longitudinal resolution is still enough to resolve the slices. The TDS power P_{TDS} remained constant for all the measurements using the multi-screen method (P_{TDS} = 0.07 MW) and quadrupole scan method (P_{TDS} = 0.11 MW), so that influence from the TDS induced effects can be excluded in the reconstruction of emittance. Due to the significant differences in the spatial resolutions and light yields of the OTR and high-resolution screens, as well as the accelerator optics, an identical TDS power for both methods was not possible. As expected from Fig. 6.4, the measured longitudinal resolution on the first OTR screen was only 1/2 of the bunch length and therefore not usable for slice emittance measurement.

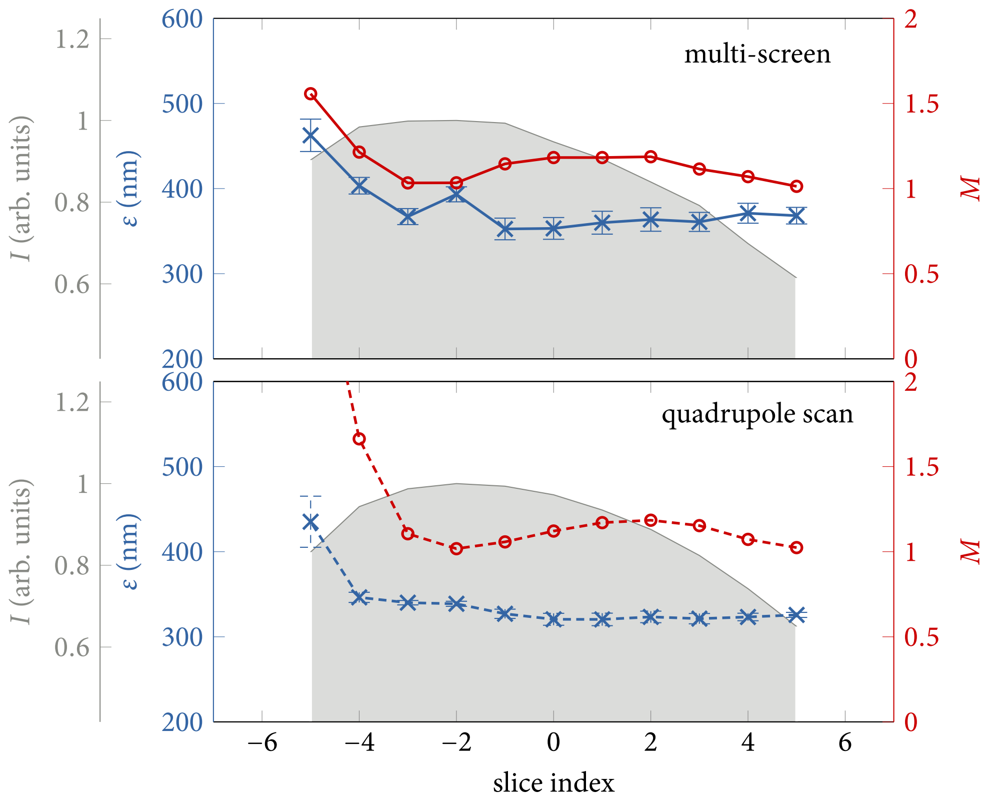

Figure 6.11: Slice emittance measured at the second TDS RF zero-crossing (i.e. with 180° phase shift compared to Fig. 6.10) with uncompressed bunches using (top, solid) multi-screen and (bottom, dashed) quadrupole scan method. The red lines represent the mismatch parameter with respect to the design optics. The grey lines (with filled areas) represent the longitudinal profile in arbitrary units.

Figure 6.10 shows the normalized horizontal slice emittance and slice mismatch parameter obtained using (top) multi-screen and (bottom) quadrupole scan method with the TDS operated around the RF zero-crossing. The grey lines (with filled areas) represent the current in each slice. The reconstructed slice emittance from these two methods shows the same behaviours along the slices: constant emittance for the slices with positive indices and increasing emittance values towards the negative indices. The slice mismatch parameter from these two methods show the same feature as well. The slice emittance values obtained with the multi-screen method are in general larger than those obtained with the quadrupole scan method.

In order to investigate the influence of the TDS streak and the initial bunch correlation in (y, z) and (y', z) on the reconstructed longitudinal distribution, the slice emittance measurement was repeated at the other TDS RF zero-crossing (see Fig. 6.11), i.e. with 180° phase shift compared to Fig. 6.10. The consistency of the reconstructed slice emittance and slice mismatch parameter derived for these two TDS RF zero-crossings excludes the influence of an initial bunch correlation and further confirms the reliability of the measured results. The fact of measuring larger slice emittance from the multi-screen method than the quadrupole scan method is still observed.

Table 6.2: Summary of the central slice parameters measured with uncompressed bunches.

	unit	**multi-screen**	**quadrupole scan**
		1st. TDS phase	
ε_x	nm	369 ± 11	314 ± 7
M_x		1.10	1.19
β_x	m	6.58 ± 0.32	5.73 ± 0.18
α_x		-0.95 ± 0.05	-0.90 ± 0.02
		2nd. TDS phase	
ε_x	nm	353 ± 13	321 ± 7
M_x		1.18	1.12
β_x	m	6.23 ± 0.31	6.19 ± 0.21
α_x		-1.03 ± 0.04	-0.86 ± 0.02
$\beta_{\text{Design},x}$	m	9.43	
$\alpha_{\text{Design},x}$		-1.02	

Since the design Twiss parameters at the reconstruction point are the same in the measurements using these two methods, they can be compared as well. Table 6.2 summarizes the reconstructed parameters for the central slice, which was the one matched during the matching iterations. Although the slice emittance measured with the multi-screen method is larger than that measured with quadrupole scan method, the Twiss parameters measured with both methods and at both TDS RF zero-crossings show good consistency. In all cases, the measured beta-function has a large deviation of ~ 40% to the design value, while the alpha-function is matched within ~ 10% to the design value. Better matching could not be achieved during the matching iterations at the beginning of the measurement series. According to Figs. 6.6 and 6.7, the relative deviation of the reconstructed emittance (measured at the initial optics of $\beta \approx 6$ m and $\alpha \approx -1$) from the real value is estimated to be below 2% for both methods, and the relative standard deviation of the reconstructed emittance below 10%. It cannot fully explain the discrepancy of the emittance of ~ 15% measured using the two methods. Possible systematic errors resulted from the screen resolution are discussed in Section 6.5.

6.4 Experimental results for compressed bunches

It is important to measure and control the slice parameters for compressed bunches, since they are required for the SASE process to generate FEL pulses. Comparison of the two methods, as described in the latter section, is repeated for compressed bunches with identical beam energy and bunch charge. The bunches were compressed slightly[4] with a compression factor of ~ 6. The measured bunch length amounts to ~ 500 fs as determined from a Gaussian fit.

[4]The compression factor of 6 is comparable to the design nominal compression factor of 8 to 12 at the first bunch compressor for the SwissFEL.

6.4.1 Projected emittance

Figure 6.12 compares the results of the projected emittance measurements for compressed bunches. The reconstructed normalized projected emittances ε_N together with the mismatch parameters $M_{x,y}$ are summarized in Table 6.3. The results obtained with these two methods are comparable in the x plane, while a large discrepancy is observed in the y plane. It can be seen in Fig. 6.12 (bottom left) that one beam size measurement has large offset to the fit with the ellipse probably due to systematic error, which could then result in inaccuracy of the reconstructed emittance.

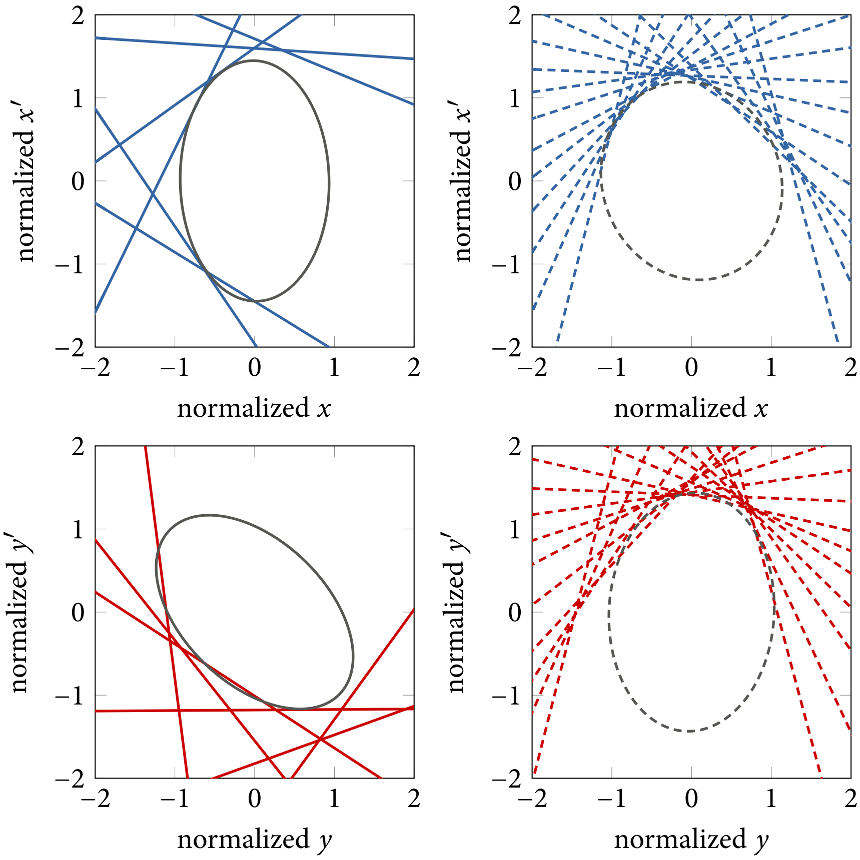

Figure 6.12: Fits of the beam ellipses using the (left, solid lines) multi-screen method and (right, dashed lines) the single quadrupole scan for the measurement of the horizontal (blue) and vertical (red) projected emittance with compressed bunches. The lines represent each measured beam size.

6.4.2 Slice emittance

For slice emittance measurements with compressed bunches, the deflecting power of the TDS was increased to have better longitudinal resolution than for the measurements with uncompressed bunches. In order to have enough signal to noise ratio in the images taken with the OTR screens with the multi-screen method, the TDS power was chosen to be below the maximum value. The TDS power for the multi-screen and quadrupole scan method was 0.76 MW and 1.99 MW, respectively. The slice width

Table 6.3: Summary of projected emittance measurements with compressed bunches.

	multi-screen method	single quadrupole scan
ε_x	676 ± 11 nm	675 ± 8 nm
M_x	1.10	1.00
ε_y	639 ± 12 nm	743 ± 11 nm
M_y	1.13	1.05

is chosen to be 1/5 of the bunch length, i.e. 100 fs. The relative small TDS power for the multi-screen method leads to relatively worse longitudinal resolution at the OTR screens, whose influence on the slice emittance measurements are discussed later in Section 6.5.

Figure 6.13 shows a comparison of the slice emittance and mismatch parameter measured with the multi-screen (top) and quadrupole scan method (bottom). An increase of the mismatch parameter along the slices with negative indices is observed in both methods. The multi-screen method shows a slow increase, while the quadrupole scan method displays rapid growth. Large discrepancy of the slice emittance appears in the slices with large mismatch parameters.

Results obtained at the second TDS RF zero-crossing are shown in Fig. 6.14. Both methods show the same tendency in the evolution of the slice mismatch parameters as those observed at the first TDS RF zero-crossing. The multi-screen method yields larger emittance than the quadrupole scan method, which is observed in the comparative measurement with uncompressed bunches as well. The parameters for the central slice are summarized in Table. 6.4. Although both the beta- and alpha-function deviate from the design values, the emittance measured at this mismatched optics will have deviation of less than 1% and an error of less than 5% according to Figs. 6.6 and 6.7. The discrepancy of the measured emittance with the two methods is more than 15%, and cannot be fully explained by optics mismatch. A possible systematic error accounting for this discrepancy is discussed in Section 6.5.

Comparison of the Twiss parameters measured with uncompressed and compressed bunches reveals that different optics were generated during the matching iterations at the beginning of each measurement series. The values of projected and slice emittance measured with compressed bunches are larger than these with uncompressed bunches. This emittance growth (~ 40% in the projected emittance and ~ 25% in the central slice emittance) is probably induced by coherent synchrotron radiation (CSR) and longitudinal space charge (LSC) in the bunch compressor chicanes, as well as systematic errors due to dispersive effects and coupling in the transverse plane.

6.5 Correction with screen resolution

In general, it has been observed that with the multi-screen method larger emittances have been measured than with the quadrupole scan method. One possible explanation for this discrepancy of the values obtained with these two methods could be the worse resolution of the imaging systems used for the multi-screen method. The resolution of the OTR screen stations in the FODO section was

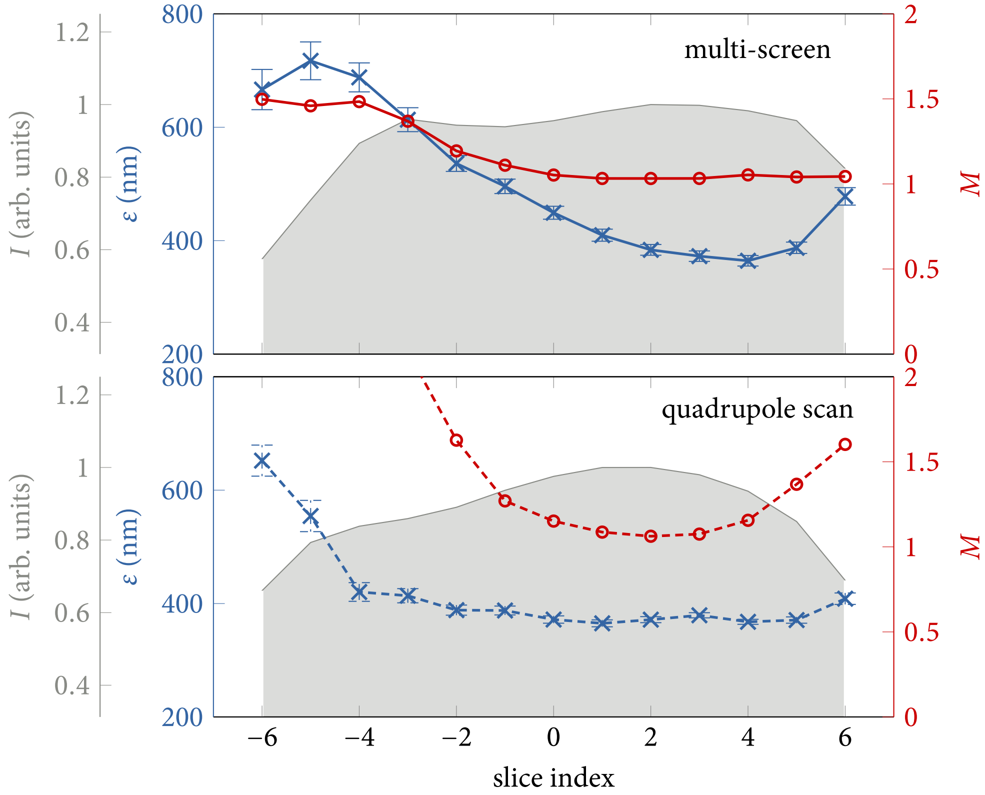

Figure 6.13: Slice emittance measured at the first TDS RF zero-crossing (the same as for Fig. 6.10) with compressed bunches using (top, solid) the multi-screen and (bottom, dashed) the quadrupole scan method. The red lines present the mismatch parameters with respect to the design optics. The grey lines (with filled areas) represent the longitudinal profile in arbitrary units.

estimated to be 15 µm. With a design beta-function of 3 m, the beam sizes at the OTR screens are expected to be 62 µm (assuming a normalized emittance of 0.5 µm and beam energy of 200 MeV), which is significantly influenced by the errors arising from the screen resolution. The measured beam size σ is larger than the real one, and given by $\sigma = \sqrt{\sigma_0^2 + \sigma_{resol}^2}$, with σ_0 the real beam size and σ_{resol} the screen resolution. Correction with this systematic error is performed: the resolution has been subtracted quadratically from the measured beam sizes, and the emittance has been reconstructed then with the corrected beam sizes. Since the high-resolution profile monitor has better resolution of 8 µm and the beam sizes are expected to be 226 µm (calculated for the design beta-function of $\beta_{x,screen} \sim 40$ m assuming a normalized emittance of 0.5 µm and beam energy of 200 MeV), the correction with the screen resolution in case of the quadrupole scan method is within error bars of statistical error. For example of the real measurement, the smallest beam size 125.7 ± 4.1µm of the central slice will be corrected to 125.4 µm.

Figure 6.15 shows the results of slice emittance measurements with uncompressed bunches after the corrections with screen resolutions. Compared to the results without corrections with the screen resolutions (see Fig. 6.10 and 6.11), the discrepancy of 15% of the measured emittance for the central

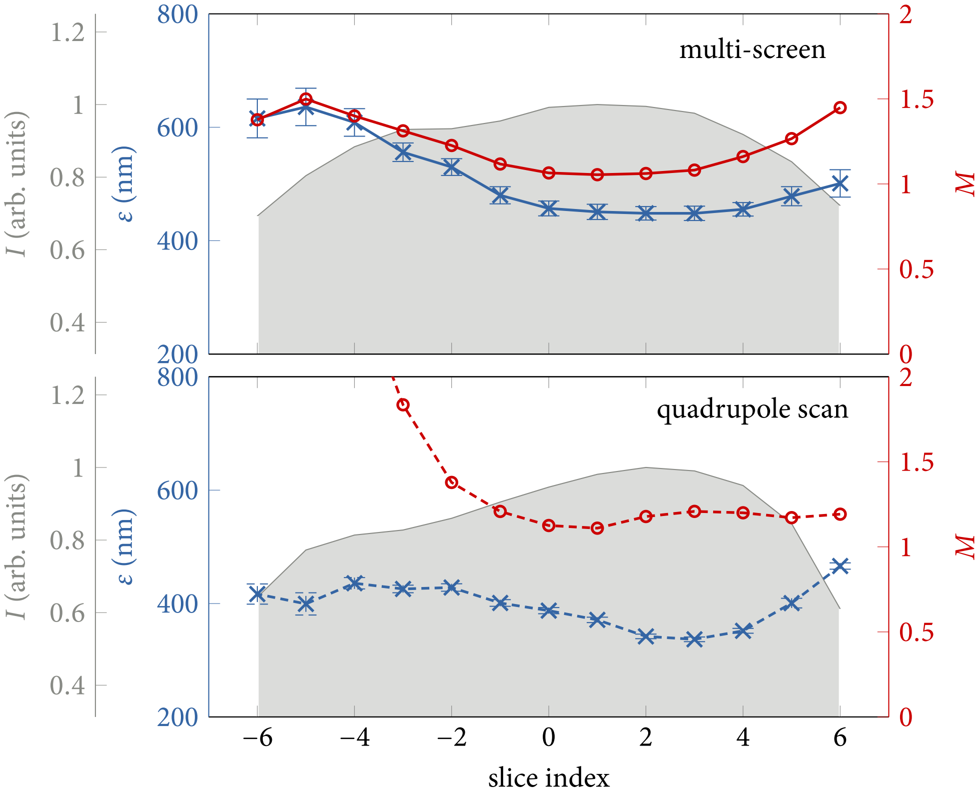

Figure 6.14: Slice emittance measured at the second TDS RF zero-crossing (the same as for Fig. 6.11) with compressed bunches using (top, solid) the multi-screen and (bottom, dashed) the quadrupole scan method. The red lines present the mismatch parameters with respect to the design optics. The grey lines (with filled areas) represent the longitudinal profile in arbitrary units.

slice is significantly reduced. At both TDS RF phases (top and bottom), excellent agreements of the measured values (within the error bars) of slice emittance and mismatch parameter are achieved in most slices.

In the case of compressed bunches (see Fig. 6.16), these two methods show much improved consistency in the results after corrections with screen resolutions. A good agreement especially in the slices with small mismatch parameter ($M < 1.5$) is obtained. For the central slice, the deviation of the measured value for the slice emittance is reduced from 15% to 7%, which is then in the order of the statistical and systematic error. For the slices at the tails of the bunch (with negative slice indices), where the mismatch parameter measured with the quadrupole scan method is larger than 1.5, errors in the reconstructed emittance could increase rapidly above 10% as indicated in Fig. 6.7.

For the measurements with compressed bunches, the limited longitudinal resolution on the OTR screens used in the multi-screen method has pronounced influences on the dividing of the slices. For example, the measured longitudinal resolution on the 6th. OTR screen was approximately 1/5 of the bunch length, which then equals to the chosen width of each slice, whereas the one on the 4th. OTR screen was 1/16 of the bunch length. Although the slices have the same length, the same slice in the

Table 6.4: Summary of the central slice parameters measured with compressed bunches.

	unit	**multi-screen**	**quadrupole scan**
		1st. TDS phase	
ε_x	nm	449 ± 11	372 ± 6
M_x		1.05	1.15
β_x	m	12.57 ± 0.51	15.18 ± 0.18
α_x		−1.19 ± 0.06	−1.28 ± 0.03
		2nd. TDS phase	
ε_x	nm	457 ± 13	388 ± 5
M_x		1.06	1.13
β_x	m	13.26 ± 0.63	14.92 ± 0.3
α_x		−1.30 ± 0.07	−1.35 ± 0.04
$\beta_{\text{Design},x}$	m	9.43	
$\alpha_{\text{Design},x}$		−1.02	

measurement on each screen do not contain the identical electrons due to the different longitudinal resolutions. As can be seen in Fig. 6.13 and 6.14, the longitudinal current profiles measured with the multi-screen method differ slightly from these measured with the quadrupole scan method, which is an indication of inconsistencies of the slices. The worse and differing longitudinal resolutions at the OTR screens in the measurements with the multi-screen method can account for the deviation of the results. Taking into account this influence, excellent agreements of the measured values have been achieved using the two methods.

6.6 Summary

Comparative measurements of projected and slice emittance have been performed using the multi-screen and quadrupole scan method at the SITF. The measured projected emittance is larger than the emittance of the central slice by a factor of about 1.5 and 1.7 for the uncompressed and compressed bunches, respectively. It has been observed that the optics and emittance of the slices vary quickly along the slices, which may result in different lasing performance of the slices when the bunch is used for the generation of FEL pulses. Therefore, the time-resolved slice parameters are necessary and more crucial to describe the quality of the bunch than the projected parameter.

Emittance growth of compressed bunches has been measured: ~ 40% in the projected emittance and ~ 25% in the central slice emittance. It could be probably induced by CSR and LSC in the bunch compressor chicanes, as well as systematic errors due to dispersive effects and coupling in the transverse plane.

Monte-Carlo simulations for the multi-screen and quadrupole scan method reveal that the emittance error resulted from statistical beam size error of 5% is small when the beam is matched: 5.7% and 2.9%, respectively. Errors below 10% are expected in the quadrupole scan method for bunches with mismatch parameter $M < 1.5$, and in the multi-screen method for $M < 1.1$. The quadrupole scan is more robust for mismatched beams due to the larger number of measurement points.

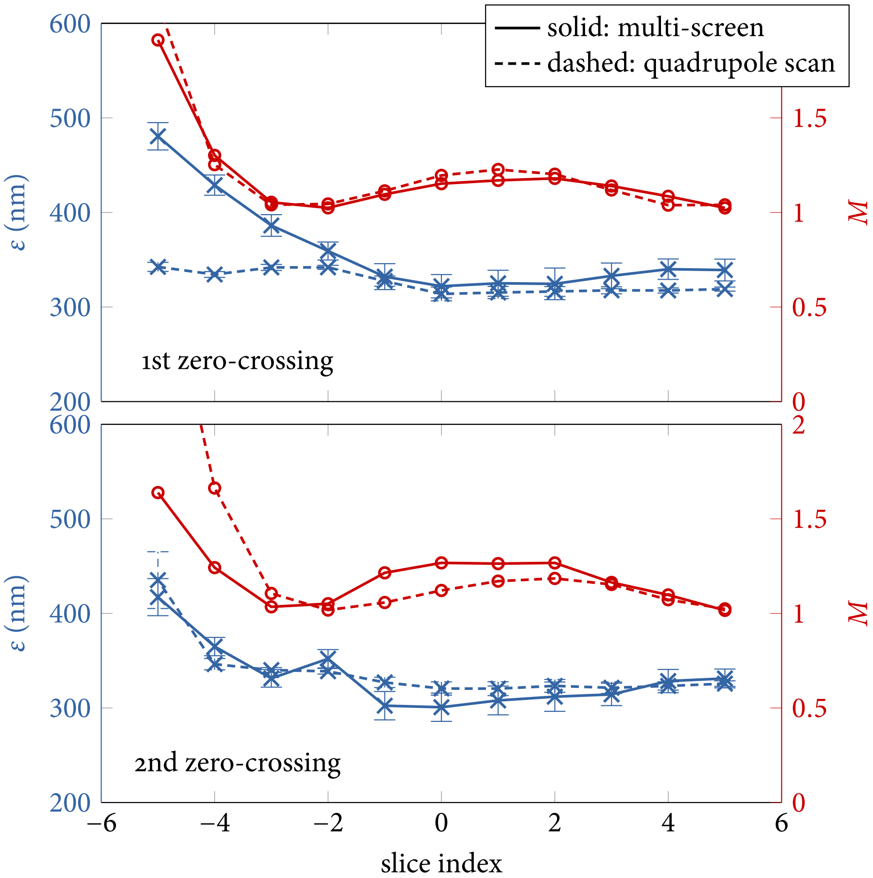

Figure 6.15: Results of slice emittance measurements with uncompressed bunches after the beam sizes corrected with the screen resolution. The values of slice emittance and slice mismatch parameter obtained with (solid line) the multi-screen and (dashed line) the quadrupole scan method are compared. Results measured at both TDS RF zero-crossings are displayed (top: 1st. zero-crossing, bottom: 2nd. zero-crossing).

The first experimental results has shown slight discrepancy of the values obtained with the two methods. The screen resolution was the dominating factor in the systematic errors and has strong influence on the beam size measurements in the multi-screen method, in which the screen resolution was worse and the beam size was smaller due to a smaller beta-function. After correction with the screen resolution, excellent agreement (within error bars) of the central slice emittance measured with the two methods has been achieved for uncompressed bunches. In the case of compressed bunches, deviation of the central slice emittance measured with the two methods has been reduced from 15% to 7%. In order to minimize the crucial influence of the screen resolution on the emittance measurement, either an imaging system with high-resolution is required, or the beta-function at the screens should be large to have large beam size. The latter can be more easily achieved in the quadrupole scan.

Consistency of the slice parameters obtained at both TDS RF zero-crossings excludes systematic errors due to initial correlation in the transverse-longitudinal plane. For the multi-screen method, the

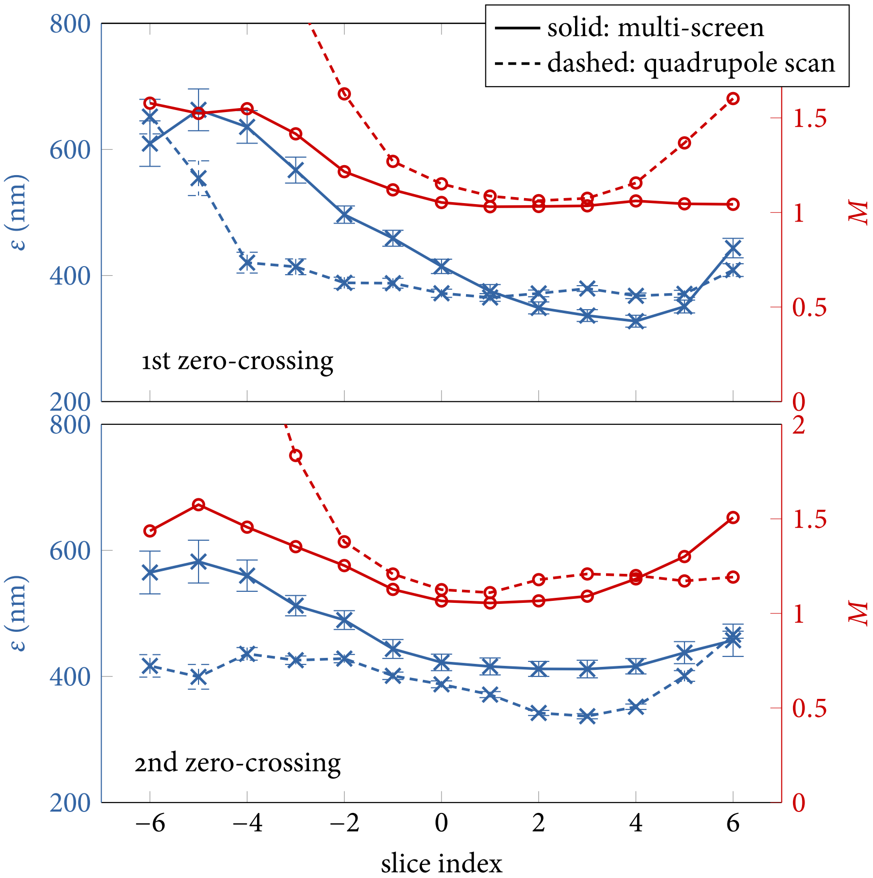

Figure 6.16: Results of slice emittance measurements with compressed bunches after beam sizes corrected with the screen resolution. The values of slice emittance and slice mismatch parameter obtained with (solid line) the multi-screen and (dashed line) the quadrupole scan method are compared. Results measured at both TDS RF zero-crossings are displayed (top: 1st. zero-crossing, bottom: 2nd. zero-crossing).

low light yield of the OTR screens put restraints on the streaked beam sizes, resulting in a limited TDS power and thus worse longitudinal resolution on the screens. Furthermore, different longitudinal resolutions have been measured on different OTR screens, which leads to inaccuracies of the slice definitions. In contrast, it is easier in the quadrupole scan method to achieve comparable longitudinal resolutions for the measurement points by using multiple quadrupoles at the same time.

Matching iterations are essential, since confidential measurements require matched beam for both methods. For the slice emittance measurement, where the slice parameters could differ largely along the bunch, the matching procedure should be applied to the slices instead of the projected bunch.

The measurements at the SITF provide valuable experience for the design of the emittance measurement procedure at the European XFEL, where the multi-screen method will be mainly employed for the emittance measurements, accredited to its capability of carrying out measurements during the generation of FEL pulses by implementing off-axis screens and fast kicker magnets. Taking into account the experiences from theSITF, optimization of the design accelerator optics of emittance measurements for the European XFEL has put especially emphasis on the error sensitivity due to optics mismatch, the longitudinal resolutions at the screens and the influence of screen resolution on the relatively small beam sizes on the screens in the multi-screen method.

7 Summary

The European XFEL will generate coherent X-rays with wavelengths in the (sub-)Ångström-range for the study of ultra-fast processes in the femtosecond regime. In this thesis, three high-resolution longitudinal diagnostic sections with transverse deflecting structures (TDS), which will provide measurements of the longitudinal profile, the longitudinal phase space, the slice energy spread and the slice emittance, have been designed for the European XFEL. The requirement of being (quasi) non-destructive to the generation of FEL pulses has been fulfilled by the implementation of fast kicker magnets and off-axis screens.

Extensive modelling of the measurements have been conducted for the designed diagnostic sections. Error analysis using both analytical and numerical methods has proved the reliability of the design for the emittance measurements. In the studies presented for the BC1 section, statistical beam size errors of 5% lead to statistical errors of 5% on the measurements of both the slice and projected emittance, when the normalized emittance is assumed to be 1 μm. Investigation on the systematic errors resulting from various sources has revealed that errors caused by the dispersions generated by the kicker magnets are especially sensitive to the variation of the actual beam parameters of the electron bunch. Particle tracking simulations using S2E bunches have verified that reliable slice emittance measurements can be obtained in the online mode with the kicker magnets switched on, while projected emittance measurements should be performed in the offline mode. Influences of other issues that can be encountered in practice on the performance of the slice emittance measurements have been studied using simulations which lead to the following conclusions: (i) The beam size definitions using rms value and Gaussian standard deviation yield different results, (ii) Large TDS effective voltage is desired to minimize overlapping of the slices, (iii) The slice width should be chosen with respect to the longitudinal resolution, (iv) As the variation of the Twiss parameters along the bunch increases, accurate emittance measurements can be only achieved in the slices with small mismatch parameters.

For the longitudinal phase space measurement designed, the achievable longitudinal resolutions are expected to be in the 100 fs range in the injector section, and 10 fs in the BC1 and BC2 sections. Simulations using S2E bunches have shown good agreement between the measured longitudinal profile and the reference. However, the measured slice energy spread has shown significant deviation from the reference value, which can be explained neither by the induced energy spread from TDS nor by the energy resolution in the dispersive plane. A special slicing procedure has been developed and applied, which results in remarkable improvement in slice energy spread measurement. When a slice width of 60 fs is chosen, deviation of the measured slice energy spread from the reference value has been reduced significantly from 18% using the common slicing method to < 1% using the special slicing method.

Several aspects of the concept have been investigated at various existing FEL facilities. Coherent emission of transition radiation in the optical wavelength regime may hamper the beam imaging diagnostics, which is an essential part of the longitudinal diagnostic sections. Incoherent beam imaging can be achieved using a scintillator screen together with the spatial separation method to suppress the co-existing COTR. First experimental study of the spatial separation method has been performed at LCLS, which proves the method capable of fully suppressing COTR at nominal operation settings. These experimental results predict successful future operation of the TDS diagnostic sections designed for the European XFEL, where the same spatial separation method with different geometrical layout will be employed.

First implementation of the concept of using fast kicker magnets and off-axis screens to realize diagnostics that are (quasi) non-destructive to the generation of FEL pulses has been achieved at FLASH in the form of an online longitudinal profile monitor, the high demand of which proves the importance of longitudinal diagnostics with online capability for the European XFEL. During the operation of the monitor, disagreements have been observed in the profiles obtained at different TDS RF phases. It has been concluded for the future operation at the European XFEL that longitudinal profile measurement at one TDS RF phase will be insufficient, when there exists a transverse-longitudinal correlation inside the bunch. Systematic studies on the reconstruction method have been performed, in which the bunch lengths measured at the two TDS diagnostic sections have been compared to those determined independently using the coherent intensity spectrometer. Deviation between the bunch lengths are below 6% at the investigated machine settings where the bunch lengths are comparatively long. At a setting where the electron bunch length is below 100 fs, the deviation increases to 30%, which may be attributed to the limited resolution of the TDS measurements and the systematic errors in the phase retrieval using the spectrometer measurement.

Practical experiences with emittance measurements have been gained at the SITF, with emphasis on the comparison of the multi-screen method with the quadrupole scan method. The screen resolution has dominated the systematic errors of the measurements using the multi-screen method due to the small beam sizes in the FODO cells. After the measured beam sizes have been corrected with the screen resolution, deviation between the central slice emittances measured with the two methods has been removed from the initial 15% for uncompressed bunches, and reduced from 15% to 7% for compressed bunches. The longitudinal resolution has strong influences on the slice definitions in the measurements using the multi-screen method, and should be kept as constant as possible on all screens. The experience gained at SITF has been applied to the design for the European XFEL.

A Monte-Carlo sampling of correlated multivariate Gaussian distribution

As described in Section 1.2.1, the vector $\boldsymbol{o}$ and its covariance matrix $\Sigma_{\boldsymbol{o}}$ can be determined using linear least square methods. The sought-after emittance ε (see Eq. 1.22) and Twiss parameters α_0, β_0 (see Eqs. 1.23 and 1.24) are non-linear functions of the variables o_1, o_2, o_3. For the error analysis of ε and α_0, β_0, Monte-Carlo method can be applied to sample the variables o_1, o_2, o_3 of $\boldsymbol{o}$ and then pass the sample through the non-linear functions to obtain samples of the emittance and the Twiss parameters.

As noted in Eq. 1.21, the covariance matrix $\Sigma_{\boldsymbol{o}}$ is not diagonal matrix, which indicates correlations between the variables o_1, o_2 and o_3. One way to sample from a correlated multivariate Gaussian distribution is to use Cholesky decomposition such that the covariance matrix $\Sigma_{\boldsymbol{o}}$ can be decomposed as [GHM12]

$$\Sigma_{\boldsymbol{o}} = \boldsymbol{L} \cdot \boldsymbol{L}^*, \tag{A.1}$$

where $\boldsymbol{L}$ is a lower triangular matrix[1] with non-negative diagonal elements and $\boldsymbol{L}^*$ its conjugate transpose matrix. Let $\boldsymbol{\delta}$ be an uncorrelated random vector of the form $\boldsymbol{\delta} = (\delta_1, \delta_2, \delta_3)^T$ with $\delta_i \sim \mathcal{N}(0,1)$, then $\boldsymbol{o} + \boldsymbol{L} \cdot \boldsymbol{\delta}$ is a random variable that follows a multivariate Gaussian distribution with covariance matrix $\Sigma_{\boldsymbol{o}}$.

From each sample $\boldsymbol{o} + \boldsymbol{L} \cdot \boldsymbol{\delta}$, the Twiss parameters and emittance can be calculated. Repeated sampling yields the probability distribution of the parameters, denoted as $\mathcal{P}_{MC_{ch}}$. Furthermore, the mean value and standard deviation $\sigma_{MC_{ch}}$ of the probability distribution can be determined.

As a demonstration, Fig. 1.2 is augmented with the probability distribution $\mathcal{P}(\varepsilon)_{MC_{ch}}$ of the emittance estimated using this method. Comparison of the relative standard deviations obtained with the error propagation method (denoted as $\sigma_{\varepsilon,EP}/\varepsilon_N$), the Monte-Carlo simulation with direct sampling of $\langle {x^{(i)}}^2 \rangle$ (denoted as $\sigma_{\varepsilon,MC}/\bar{\varepsilon}_{MC}$) and the Monte-Carlo simulation with sampling of $\boldsymbol{o}$ (denoted as $\sigma_{\varepsilon,MC_{ch}}/\bar{\varepsilon}_{MC_{ch}}$) is shown in Fig. A.1. As expected, the two Monte-Carlo methods are equivalent to each other.

[1] $\boldsymbol{L}$ is a lower triangular matrix, if $L_{ij} = 0$ for $j > i$.

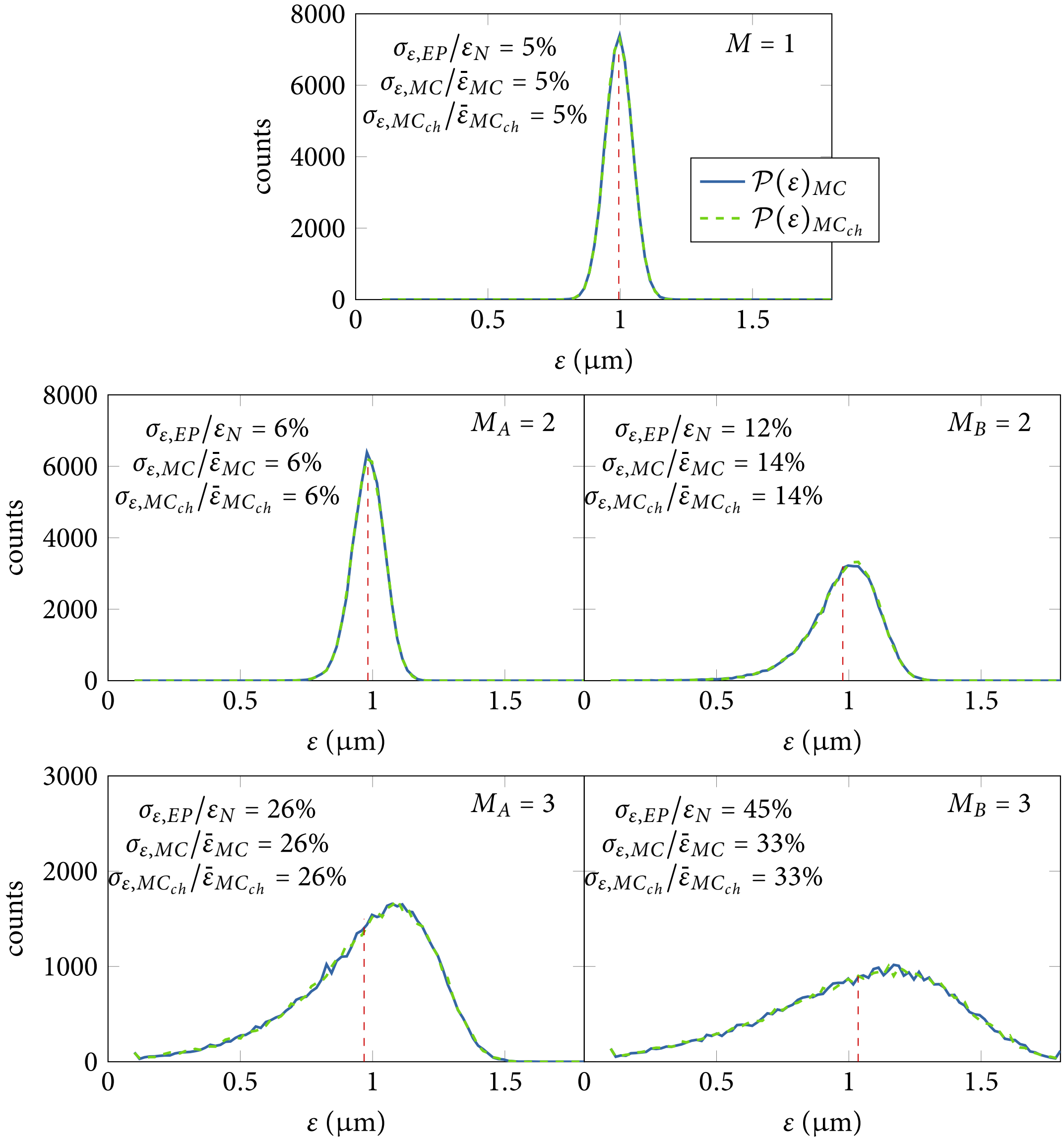

Figure A.1: Comparison of the distribution of the emittance ε obtained with different methods: (blue) Monte-Carlo simulation with direct sampling of $\langle x^{(i)^2} \rangle$, (green) Monte-Carlo simulation with sampling of $\boldsymbol{o}$. This figure is an augmentation to Fig. 1.2, where more details can be found.

B Optimization of the accelerator optics design for emittance measurements

At the European XFEL, the multi-screen method is adopted for online diagnostics (see Section 3.2.1). The accuracy of emittance measurement depends on the transfer matrices $\mathcal{R}^{(i)}$ from the initial position to the screens, the initial Twiss parameters α_0, β_0, as well as the errors in the computation of the beam sizes (see Eq. 1.27). The latter is obtained individually during each real measurement, whereas the transfer matrices $\mathcal{R}^{(i)}$ and the initial Twiss parameters α_0, β_0 can be fixed to their optimal values in the design. For an emittance measurement performed with n screens, i.e. n different transfer matrices $\mathcal{R}^{(i)}$, the values of $\mathcal{R}^{(i)}$ and α_0, β_0 are optimized when the covered phase advances $\Delta\mu^{(i)}$ (see Eq. 1.9) of the subsequent screens are increased from $0°$ to $180°$ in equal separation of $180°/n$ [Röh08].

Optimization of $\mathcal{R}^{(i)}$ and α_0, β_0, which will be referred to as optimization of the accelerator optics, have many degrees of freedom: the beamline lattice (including the number of quadrupoles and screens, the locations of the quadrupoles and screens, and the quadrupole field strengths) and the values of the initial Twiss parameters α_0, β_0. Optimization of the accelerator optics for the projected and slice emittance measurements are presented in this chapter.

B.1 Projected emittance measurements

A beamline lattice consisting of symmetric FODO cells[1] with screens located at the end of each cell is an ideal candidate for fulfilling the requirement of equal phase advance steps in the x and y planes simultaneously. However, a lot of space and a large number of quadrupoles are needed for such a lattice. Due to the constraints on the available space in the beamlines, 1.5-cell FODO structures with 4 screens each located in the middle of the subsequent quadrupoles are chosen for the European XFEL instead. Asymmetric FODO cells are considered for optimizing projected emittance measurement in both transverse planes at the same time. The Twiss parameters have identical values at the four screens (when the optics are matched to the periodic solution of the asymmetric FODO cell), which means identical beam sizes are expected. This allows an easy and quick estimation on the matching of the accelerator optics.

At the start of this Ph.D. research, the allowed positions of the quadrupoles in the beamlines

[1] A FODO cell consists of a focusing quadrupole, a drift space, a defocusing quadrupole and again a drift space. The Twiss parameters at the entrance and exit of a FODO cell are identical. As a result, a series of FODO cells have periodic Twiss parameters. A FODO cell is described as "symmetric" when the field strengths of the focusing and defocusing quadrupoles have the same value with opposite signs.

were quite limited. The optimization procedures are then based on the provided arrangements of the quadrupoles and screens. One example of the BC1 section of the European XFEL is shown in Fig. B.1. Taking into account the fixed positions of the quadrupoles and screens together with the constraints on the periodic Twiss parameters of a FODO cell, a given pair of the phase advances $(\Delta\mu_{x,\text{cell}}, \Delta\mu_{y,\text{cell}})$ in one cell determines uniquely the quadrupole field strengths and the initial Twiss parameters $\alpha_{x,0}, \beta_{x,0}, \alpha_{y,0}, \beta_{y,0}$ in both the x and y planes. Therefore, the degrees of freedom in the optimization of the accelerator optics are reduced to the two variables $\Delta\mu_{x,\text{cell}}$ and $\Delta\mu_{y,\text{cell}}$.

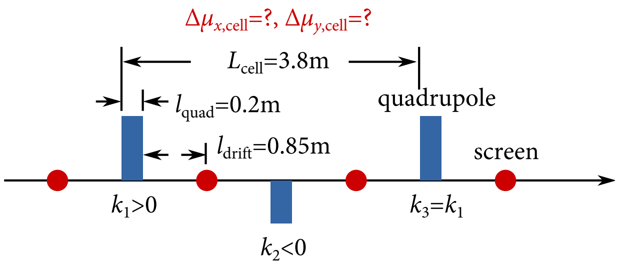

Figure B.1: Arrangement of the beamline components for the optimization of projected emittance measurement in the BC1 section of the European XFEL. A 1.5-cell asymmetric FODO structure with a cell length of $L_{\text{cell}} = 3.8\,\text{m}$ is equipped with four screens (red dots), each located at an equal distance of $l_{\text{drift}} = 0.85\,\text{m}$ to the nearest quadrupoles (blue bars). The first and the third quadrupoles have identical positive values for the field strengths, i.e. $k_1 = k_3 > 0$, whereas the second quadrupole has negative field strength $k_2 < 0$. A periodic solution of the Twiss parameters (identical Twiss parameters at the entrance and exit of a FODO cell) is sought for the asymmetric FODO structure. These preconditions reduce the degrees of freedom to the phase advance $\Delta\mu_{x,\text{cell}}$ and $\Delta\mu_{y,\text{cell}}$ per cell in the x and y plane, respectively.

The following parameter values are adopted for the optimization procedures: a normalized emittance of $\varepsilon_N = 1\,\mu\text{m}$ in both x and y planes, a beam energy of 700 MeV and a relative statistical error of 5% in beam size measurement. For each pair of $(\Delta\mu_{x,\text{cell}}, \Delta\mu_{y,\text{cell}})$ with unique transfer matrices, the standard deviation $\sigma_{\varepsilon,x}$ of the reconstructed emittance is computed using the error propagation method (see Eq. 1.27) for the following 5 different initial Twiss parameters:

- the periodic solutions $\alpha_{x,0}, \beta_{x,0}$ of the FODO cell,
- a set of the initial beta-function of $\beta_{x,1} = 90\%\beta_{x,0}$ and the alpha-function $\alpha_{x,1}$, which together correspond to a mismatch parameter of $M = 1.1$ with respect to $\alpha_{x,0}, \beta_{x,0}$,
- the second set[2] of the initial beta-function of $\beta_{x,2} = 90\%\beta_{x,0}$ and alpha-function $\alpha_{x,2}$, which together correspond to a mismatch parameter of $M = 1.1$ with respect to $\alpha_{x,0}, \beta_{x,0}$,
- a set of the initial beta-function of $\beta_{x,3} = 110\%\beta_{x,0}$ and the alpha-function $\alpha_{x,3}$, which together correspond to a mismatch parameter of $M = 1.1$ with respect to $\alpha_{x,0}, \beta_{x,0}$,
- the second set of the initial beta-function of $\beta_{x,4} = 110\%\beta_{x,0}$ and the alpha-function $\alpha_{x,4}$, which together correspond to a mismatch parameter of $M = 1.1$ with respect to $\alpha_{x,0}, \beta_{x,0}$.

[2] The mismatch parameter is a second order function of the alpha-function (see Eq. 1.25). For a given mismatch parameter and beta-function, there exist up to two solutions for the alpha-function.

The standard deviations determined for all five situations are normalized as $\sigma_{\varepsilon,x}/\varepsilon_N$ and equally weighted. The maximum of the five values $\max[\sigma_{\varepsilon,x}/\varepsilon_N]$ is shown in Fig. B.2 (left). The same procedure is applied in analogy for the y plane, with the results presented in Fig. B.2 (right).

The objective of the optimization is to find a pair of $(\Delta\mu_{x,\text{cell}}, \Delta\mu_{y,\text{cell}})$, at which the minimum of $\max[\sigma_{\varepsilon,x}/\varepsilon_N]$ and $\max[\sigma_{\varepsilon,y}/\varepsilon_N]$ are obtained at the same time. It can be seen that the choice of the phase advances has larger influence on the emittance measurement in the x plane than the y plane: $\max[\sigma_{\varepsilon,x}/\varepsilon_N]$ varies between 7% – 21%, while $\max[\sigma_{\varepsilon,y}/\varepsilon_N]$ between 5% – 10%. The combination of $\Delta\mu_{x,\text{cell}} = 90°$ and $\Delta\mu_{y,\text{cell}} = 76°$, which leads to $\max[\sigma_{\varepsilon,x}/\varepsilon_N] = 7\%$ and $\max[\sigma_{\varepsilon,y}/\varepsilon_N] = 5\%$, is adopted for simultaneous projected emittance measurement in the x and y planes.

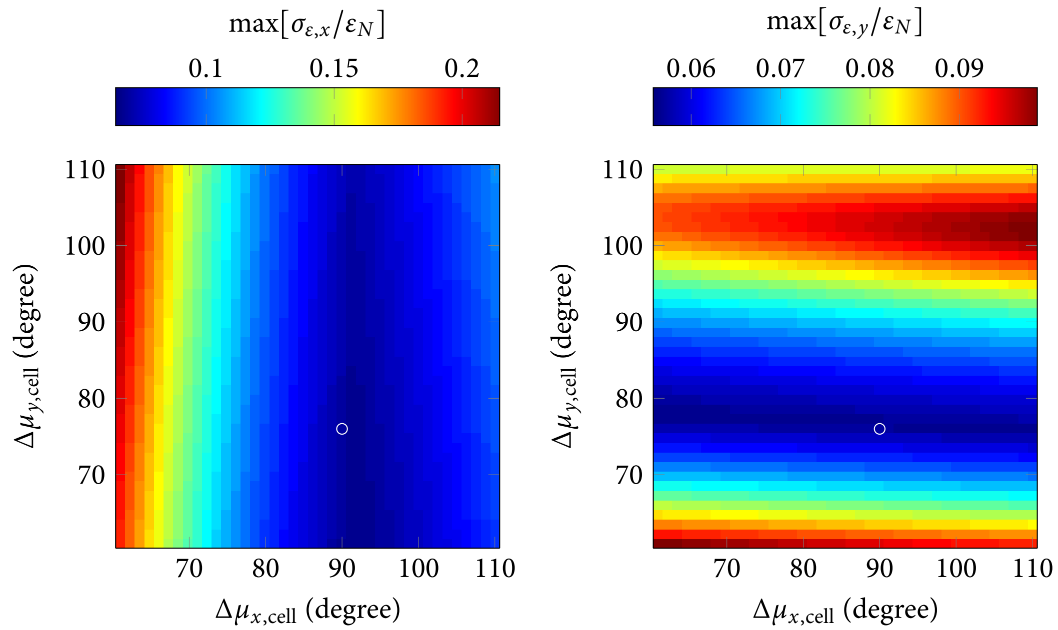

Figure B.2: Maximum standard deviation of the reconstructed emittance due to statistical errors in the x plane (left) and the y plane (right) for different combinations of phase advances per cell. The white dots at $\Delta\mu_{x,\text{cell}} = 90°$ and $\Delta\mu_{y,\text{cell}} = 76°$ indicate the adopted design for projected emittance measurement.

B.2 Slice emittance measurements

Slice emittance measurement has to be performed in the same beamline section that is used for projected emittance measurement. Optimization procedure presented in Section B.1 has indicated that a phase advance of $\Delta\mu_{y,\text{cell}} = 76°$ in the y plane is particularly suitable for emittance measurement because of the small relative standard deviation of ~ 5% in the reconstructed emittance. Therefore a phase advance of 76° is adopted for the y plane of the FODO cell, which is the plane for measuring the slice emittance. The phase advance in the x plane is closely related to the streaking effect of TDS. According to Eq. 2.21, the longitudinal resolution R_z scales inversely with $\sin(\Delta\mu_{x,TDS\rightarrow screen})$ and is optimized at a phase advance of 90°. Unfortunately the optimized phase advance of 90° cannot be obtained at all four screens at the same time. In the optimization procedure, the phase advance in the x plane from the centre of the TDS to the middle position between the second and third screen is assumed to have a fixed value of 90°. Figure B.3 shows the arrangement of the beamline section and the corresponding preconditions for slice emittance measurement. The degree of freedom in the optimization is reduced to the phase advance $\Delta\mu_{x,\text{cell}}$ in the x plane only.

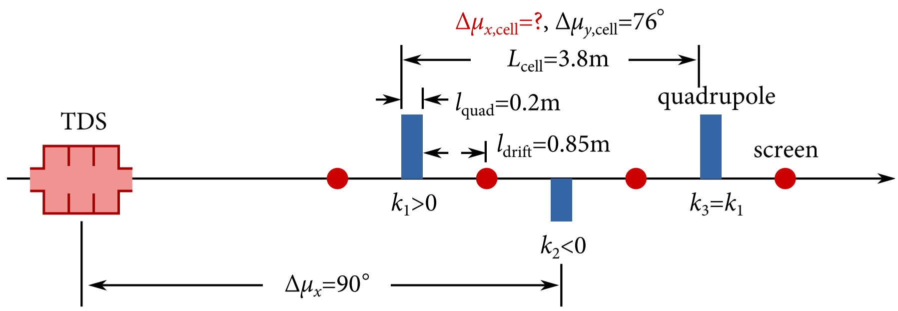

Figure B.3: Arrangement of the beamline components for the optimization of slice emittance measurement in the BC1 section of the European XFEL. The positions of the quadrupoles (blue bars) and screens (red dots) are the same as those used for projected emittance measurement (see Fig. B.1). The streaking plane and emittance measurement plane are in x and y, respectively. The horizontal phase advance from the TDS, located upstream of the first screen, to the centre of the 1.5-cell FODO structure (i.e. the centre of the second quadrupole) is assumed to be 90°. The phase advance of one FODO cell is fixed to $\Delta\mu_{y,\text{cell}} = 76°$ in the emittance measurement plane. With these preconditions, the phase advance $\Delta\mu_{x,\text{cell}}$ per cell in the streaking plane remains as the only degree of freedom.

The phase advance $\Delta\mu_{x,\text{cell}}$ determines uniquely the accelerator optics inside the 1.5-cell FODO. For each value of $\Delta\mu_{x,\text{cell}}$, the following parameters and aspects are considered:

- **The minimum of $\sin(\Delta\mu_{x,\text{TDS}\to\text{screen}})$ amongst the values obtained for the four screens: $\min[\sin(\Delta\mu_{x,\text{TDS}\to\text{screen}})]$**. A large value of this parameter is desired, since it means (i) good longitudinal resolution at the four screens, and (ii) small variation of the longitudinal resolutions at the four screens.

- **The horizontal beta-function $\beta_{x,\text{screen}}$ at the four screens**[3]. The streaking effect of TDS scales linearly with $\sqrt{\beta_{x,\text{screen}}}$ (see Eq. 2.18), and determines the beam size of the streaked bunch. Therefore $\beta_{x,\text{screen}}$ should be chosen in accordance with the screen dimensions and the design of the imaging system.

- **The vertical beta-function $\beta_{y,\text{screen}}$ at the four screens**. The beam size in the y plane for slice emittance measurement is given as $\sim \sqrt{\varepsilon_y \beta_{y,\text{screen}}}$, with ε_y the emittance in the y plane. In order to obtain accurate beam size measurements, $\beta_{y,\text{screen}}$ should be chosen with consideration of the spatial resolution of the imaging system.

- **The maximum standard deviation of the reconstructed emittance estimated for five different initial Twiss parameters: $\max[\sigma_{\varepsilon,y}/\varepsilon_N]$**. The procedure of the error analysis and the

[3]The beta-functions at the four screens have identical values, when the optics are matched to the periodic solutions of the FODO cell.

choices of the Twiss parameters are the same as described in Section B.1.

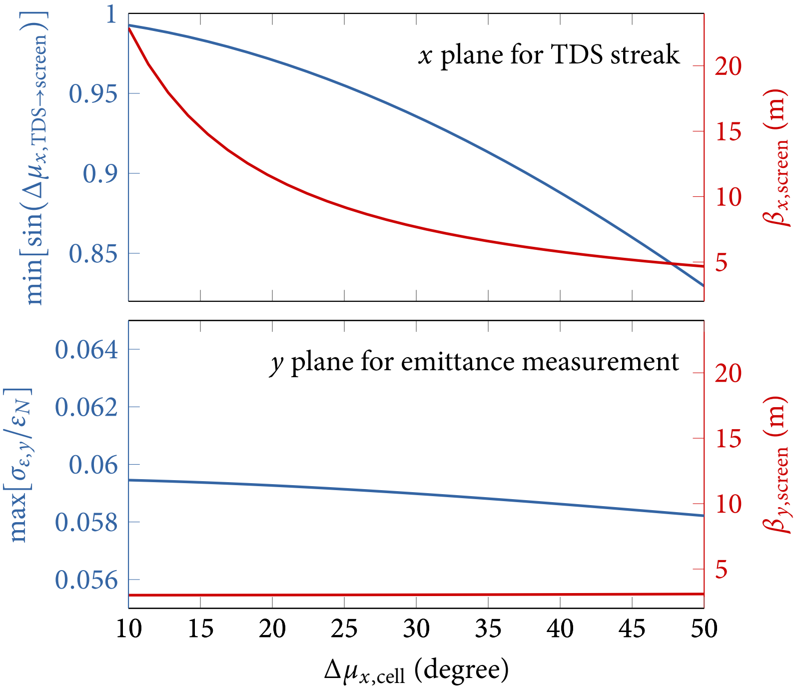

Figure B.4: Variation of various parameters with respect to the horizontal phase advance $\Delta\mu_{x,\text{cell}}$ in (top) the streaking plane and (bottom) emittance measurement plane.

Figure B.4 shows the four parameters calculated for phase advances $\Delta\mu_{x,\text{cell}}$ in the range from 10° to 50°. In the streaking plane x (Fig. B.4 top), the parameter $\min[\sin(\Delta\mu_{x,\text{TDS}\rightarrow\text{screen}})]$ reduces from 0.99 to 0.83 with increasing $\Delta\mu_{x,\text{cell}}$. It implies that small values for the phase advance $\Delta\mu_{x,\text{cell}}$ are preferred due to the better longitudinal resolution yielded. However, the beta-function $\beta_{x,\text{screen}}$ at the screens is too large at small $\Delta\mu_{x,\text{cell}}$, for example, $\beta_{x,\text{screen}} = 23$ m at $\Delta\mu_{x,\text{cell}} = 10°$. As a result of having large $\beta_{x,\text{screen}}$ and $\sin(\Delta\mu_{x,\text{TDS}\rightarrow\text{screen}})$ at the same time, the beam size of the streaked bunch can be prohibitively large for the imaging of the bunch at the screens. In the emittance measurement plane y (Fig. B.4 bottom), the influences of the phase advance $\Delta\mu_{x,\text{cell}}$ are negligible on both $\max[\sigma_{\varepsilon,y}/\varepsilon_N]$ and $\beta_{y,\text{screen}}$. For a change of $\Delta\mu_{x,\text{cell}}$ from 10° to 50°, the maximum of the relative standard deviations $\max[\sigma_{\varepsilon,y}/\varepsilon_N]$ reduces by a factor of 2% and the beta-function at the screens $\beta_{y,\text{screen}}$ increases by a factor of 3%. Taking into account the performance in both planes, a horizontal phase advance of $\Delta\mu_{x,\text{cell}} = 30°$ is chosen. In summary, the 1.5-cell FODO for slice emittance measurement is designed with phase advances of 30° and 76° per cell respectively in the streaking plane and the emittance measurement plane.

C Generalized formalism of transition radiation

When a charged relativistic particle passes through the intersection between two media with different dielectric constants, transition radiation (TR) is emitted. The Ginzburg-Frank formula [GF35] describes the TR process in an ideal case: a single relativistic electron travels from vacuum through an infinite metallic half plane. The radiated energy per angular frequency ω and solid angle Ω is given as

$$\frac{d^2U_{GF}}{d\omega d\Omega} = \frac{e^2}{4\pi^3\varepsilon_0 c}\cdot\frac{\beta^2\sin^2\theta}{(1-\beta^2\cos^2\theta)^2}, \tag{C.1}$$

where $\beta = v/c$ describes the relative velocity of the electron in comparison to the speed of light c, θ the angle with respect to the specular reflection axis of the incident electron, $-e$ the charge of an electron and ε_0 the vacuum permittivity. With the substitution of $\cos^2\theta = 1 - \sin^2\theta$, Eq. C.1 can be written as

$$\frac{d^2U_{GF}}{d\omega d\Omega} = \frac{e^2}{4\pi^3\varepsilon_0 c}\cdot\frac{\beta^2}{\left(\frac{1-\beta^2}{\sin\theta}+\beta^2\sin\theta\right)^2}. \tag{C.2}$$

It can be then easily derived that the maximum radiated energy is obtained at an angle

$$\theta_{max} = \arcsin\left(\sqrt{\frac{1-\beta^2}{\beta}}\right) \approx \frac{1}{\gamma}, \tag{C.3}$$

with $\gamma = 1/\sqrt{1-\beta^2}$ being the Lorentz-factor of the electron and $\gamma \gg 1$ used for relativistic electron .

Now we consider a realistic case using the coordinations illustrated in Fig. C.1: the radiation source has a round shape with a finite radius, and the radiated energy at a observation point within certain distance is considered. An expression for such generalized Ginzburg-Frank formula is derived and given in Eq.25 in Ref. [CSS05] as:

$$\frac{d^2U_{generalized}}{d\omega d\Omega} \propto \left|\int_0^a J_1(k\rho\sin\theta)K_1\left(\frac{k\rho}{\beta\gamma}\right)\exp\left(ik\frac{\rho^2}{2R}\right)\rho \mathrm{d}\rho\right|^2, \tag{C.4}$$

where J_1 and K_1 are the Bessel function of the first and second kind, and $k = \omega/c$ the corresponding wavenumber. If the far-field condition

$$a \geq \gamma\lambda = \gamma\frac{2\pi}{k} \tag{C.5}$$

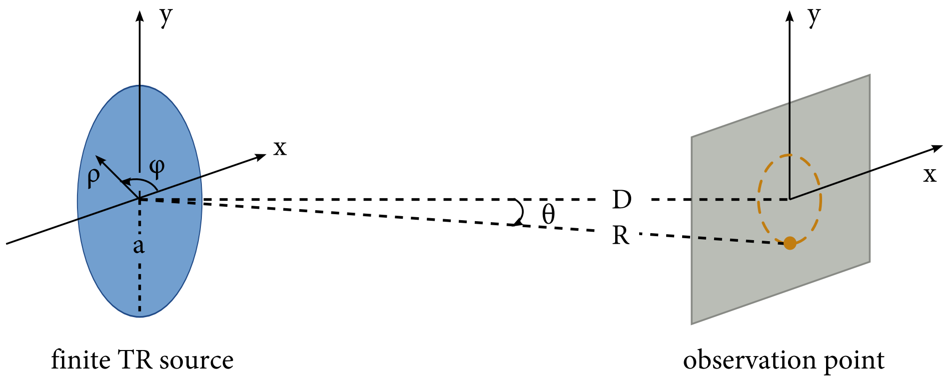

Figure C.1: Coordinate system used for describing the generalized Ginzburg-Frank formular. The radiation source has a round shape with a finite radius of a. Radiated TR energy is calculated for an observation point (yellow dot) at a distance of $R = D/\cos\theta$ to the centre of the source.

and the effective-source condition

$$D \geq \gamma^2 \lambda \tag{C.6}$$

are fulfilled, Eq. C.4 reduces to the Ginzburg-Frank formular as given in Eq. C.1.

The integration in the generalized Ginzburg-Frank formular in Eq. C.4 cannot be solved analytically. Numerical computation is possible, and applied to generate Fig. 4.7.

D Algorithm for image processing

Each raw image of the beam recorded with a camera is processed before it is used for evaluating the beam parameters. The algorithm of image processing is explained with an example image obtained at the dispersive section of FLASH (see Section 5.2).

Firstly, the background image is determined. The background is defined as the signal recorded with the camera when the electron beam is switched off. The background signals originate mainly from dark current, i.e. undesired release of electrons inside the beam pipe of the accelerating structures due to field emission [Frö07]. Another source of background signals is the noise in the CCD sensor. Multiple background images are taken for statistical reasons, and the mean value of the background images is subtracted from the raw beam image. The raw image and the image after the subtraction of background are shown in Fig. D.1 (a) and (b), respectively. It should be noted that some pixels may have negative values after the subtraction.

Then the intensity of the noise signal in the image with the background subtracted is estimated. As illustrated in Fig. D.1 (c), the frequencies of the pixel intensities are counted and plotted in a histogram. The intensities with dominant appearances are attributed to the noise signal. A split Gaussian fit[1] is applied to the intensity histogram. The mean value determined from the Gaussian fit is termed the mean noise intensity μ_{noise}, and the larger one of the two variances as the variance of the noise intensity σ^2_{noise}. The mean noise intensity μ_{noise} is then subtracted from each pixel of the image (b), and the image corrected with noise is shown in (d).

Image (d) could contain areas not belonging to the beam, but with intensities comparable to the actual beam, for example due to dirts and defects on the screen. Image (d) is then convoluted with a 7×7 Gaussian matrix. As a result, the image is blurred and appears smoother, as can be seen in (e). The parameters μ_{noise} and σ_{noise} of image (e) are determined with the procedure described for image (c). All pixels in image (e) with values smaller than the threshold of $\mu_{noise} + 2 \cdot \sigma_{noise}$ are set to zero. The remaining pixels are highlighted in image (f). The one isolated area in the middle of the image is selected and defined as the region of interest (ROI), as shown in image (g). All pixels outside the ROI are again set to zero, and all pixels inside the ROI are restored to their original values after background subtraction, i.e. the values in image (b). The final processed image is shown in (h). This method has successfully identified and isolated the beam in an arbitrary shape.

[1] $f(x) = A \exp(-\frac{(x-\mu)^2}{2\sigma_1^2})$, if $x < \mu$; $f(x) = A \exp(-\frac{(x-\mu)^2}{2\sigma_2^2})$, otherwise.

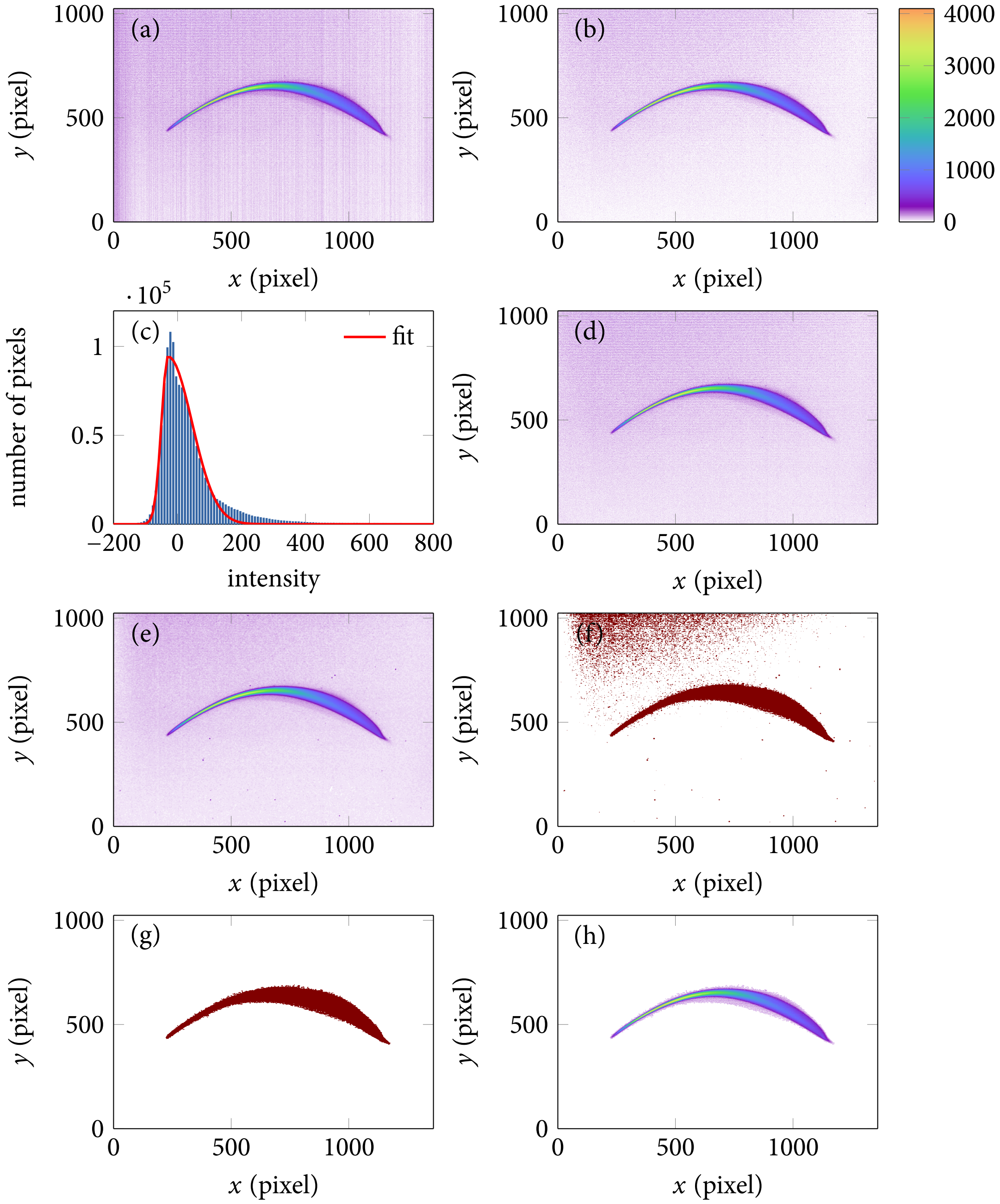

Figure D.1: Procedures of image processing: (a) raw image, (b) image after background subtraction, (c) histogram of pixel intensities for image (b), (d) image corrected with noise, (e) smoothed image, (f) pixels with intensities larger than the threshold, (g) the region of interest, (h) final processed image. It should be noted that the images (b), (d), (e) and (h) may contain pixels with negative intensities, which are displayed with the same colour code as for pixels with intensities of 0.

Bibliography

[AAD+08] A. Agababyan, et al., *Multi-Processor based Fast Data Acquisition for a Free Electron Laser and Experiments*, IEEE Transactions on Nuclear Science, vol. 55, 2008, p. 256.

[ALL64] O. H. Altenmueller, R. R. Larsen, and G. A. Loew, *Investigations of Travelling-Wave Separators for the Stanford Two-Mile Linear Accelerator*, Review of Scientific Instruments **35** (1964), 438.

[APS] Advanced Photon Source, `http://aps.anl.gov/`.

[AVT] Allied Vision Technologies, *Prosilica GC1380 camera specifications*, `http://www.alliedvisiontec.com/us/products/cameras/gigabit-ethernet/prosilica-gc/gc1380.html`.

[B+08] U. Bergmann, et al., *Science and Technology of Future Light Sources: A White Paper*, 2008, ANL-08/39, BNL-81895-2008, LBNL-1090E-2009, SLAC-R-917.

[Ban90] K. L. Bane, *Simulating longitudinal phase space in the SLC, from the damping rings to the final focus*, SLAC-AP-80, 1990.

[Bas] Basler AG, *Basler avA2300-25gm Camera Specification using the EMVA Standard 1288*, Version 01.

[Bas07] Basler AG, *Basler A311f Camera Specification*, October 2007.

[BBC+10] W. Barletta, et al., *Free electron lasers: Present status and future challenges*, Nuclear Instruments and Methods in Physics Research Section A: Accelerators, Spectrometers, Detectors and Associated Equipment **618** (2010), 69 – 96.

[BCE+02] M. Borland, et al., *Start-to-end simulation of self-amplified spontaneous emission free electron lasers from the gun through the undulator*, Nuclear Instruments and Methods in Physics Research Section A: Accelerators, Spectrometers, Detectors and Associated Equipment **483** (2002), 268 – 272.

[BDD+14] C. Behrens, et al., *Few-femtosecond time-resolved measurements of X-ray free-electron lasers*, Nature Communications **5** (2014), 3762.

[BDG14] Beam Dynamics Group at DESY, *Start-to-end simulations: the European XFEL*, `http://www.desy.de/fel-beam/s2e/xfel.html`, October 2014.

[Beh12] C. Behrens, *Characterization and control of femtosecond electron and X-ray beams at free-electron lasers*, Ph.D. thesis, Universität Hamburg, 2012.

[BGG+12] C. Behrens, N. Gerasimova, C. Gerth, B. Schmidt, E. A. Schneidmiller, S. Serkez, S. Wesch, and M. V. Yurkov, *Constraints on photon pulse duration from longitudinal electron beam diagnostics at a soft x-ray free-electron laser*, Phys. Rev. ST Accel. Beams **15** (2012), 030707.

[BGK+12] C. Behrens, C. Gerth, G. Kube, B. Schmidt, S. Wesch, and M. Yan, *Electron beam profile imaging in the presence of coherent optical radiation effects*, Phys. Rev. ST Accel. Beams **15** (2012), 062801.

[Bor00] M. Borland, *elegant: A Flexible SDDS-Compliant Code for Accelerator Simulation*, Advanced Photon Source LS-287, September 2000.

[BPN84] R. Bonifacio, C. Pellegrini, and L. Narducci, *Collective instabilities and high-gain regime in a free electron laser*, Optics Communications **50** (1984), 373 – 378.

[C+11] H. N. Chapman, et al., *Femtosecond X-ray protein nanocrystallography*, Nature **470** (2011), 73–77.

[Cha93] A. W. Chao, *Physics of Collective Beam Instabilities in High Energy Accelerators*, John Wiley, New York, 1993.

[CIL+13] P. Craievich, R. Ischebeck, F. Loehl, G. Orlandi, and E. Prat, *Transverse deflecting structures for bunch length and slice emittance measurements on SwissFEL*, Proceedings of FEL2013, New York, NY, USA, 2013, TUPSO14.

[Cry] Crytur Ltd., `http://www.crytur.cz/`.

[CS58] E. D. Courant, and H. S. Snyder, *Theory of the Alternating-Gradient Synchrotron*, Annals of Physics **3** (1958), 1–48.

[CSS05] S. Casalbouni, B. Schmidt, and P. Schmüser, *Far-Infrared Transition and Diffraction Radiation Part I*, TESLA Reports, 2005, TESLA 2005-15.

[DBD+09] Y. Ding, et al., *Measurements and Simulations of Ultralow Emittance and Ultrashort Electron Beams in the Linac Coherent Light Source*, Phys. Rev. Lett. **102** (2009), 254801.

[DOO] Distributed Object Oriented Control System DOOCS, `http://doocs.desy.de`.

[DL13] W. Decking, and T. Limberg, *European XFEL Post-TDR Description*, February 2013, XFEL.EU TN-2013-004-01.

[DRAS+14] S. Düsterer, et al., *Development of experimental techniques for the characterization of ultrashort photon pulses of extreme ultraviolet free-electron lasers*, Phys. Rev. ST Accel. Beams **17** (2014), 120702.

[EAA+10] P. Emma, et al., *First lasing and operation of an angstrom-wavelength free-electron laser*, Nature Photonics **4** (2010), 641–647.

[EFK00] P. Emma, J. Frisch, and P. Krejcik, *A transverse RF deflecting structure for bunch length and phase space diagnostics*, LCLS Technical Notes, 2000, LCLS-TN-00-12.

[EXF] European X-Ray Free-Electron Laser Facility GmbH (European XFEL GmbH), `http://www.xfel.eu`.

[FHL+06] L. Fröhlich, et al., *First operation of the FLASH machine protection system with long bunch trains*, Proceedings of LINAC2006, Knoxville, Tennessee USA, 2006, TUP099.

[FLA] Free-electron Laser in Hamburg, `http://flash.desy.de/`.

[FMS+14] A. Fognini, et al., *Ultrafast reduction of the total magnetization in iron*, Applied Physics Letters **104** (2014), no. 3.

[Frö07] L. Fröhlich, *Dark current transport in the FLASH linac*, Proceedings of PAC2007, Albuquerque, USA, 2007, TUPMN018.

[G+12] R. Ganter, et al., *SwissFEL Conceptual Design Report*, PSI Report, 2012, No. 10-04.

[GC07] K. J. Gaffney, and H. N. Chapman, *Imaging Atomic Structure and Dynamics with Ultrafast X-ray Scattering*, Science **316** (2007), no. 5830, 1444–1448.

[GF35] V. Ginzburg, and I. Frank, *Radiation of a uniformly moving electron due to its transition from one medium into another*, Journal of Physics USSR **9** (1935), 353.

[GHM+11] T. Gorniak, et al., *X-ray holographic microscopy with zone plates applied to biological samples in the water window using 3rd harmonic radiation from the free-electron laser FLASH*, Opt. Express **19** (2011), 11059–11070.

[GHM12] J. E. Gentle, W. K. Härdle, and Y. Mori, *Handbook of Computational Statistics: Concepts and Methods*, Springer, 2012.

[Göt04] P. Göttlicher, *Fast Pulse Masker User Manual*, `https://wof-cluster.desy.de/sites/site_fe/content/feb/documents/`, November 2004.

[GS06] O. Grimm, and P. Schmüser, *Principles of longitudinal beam diagnostics with coherent radiation*, TESLA FEL Reports, 2006, TESLA-FEL 2006-03.

[HBC+08] U. Hahn, N. Bargen, P. Castro, O. Hensler, S. Karstensen, M. Sachwitz, and H. Thom, *Wire scanner system for FLASH at DESY*, Nuclear Instruments and Methods in Physics Research Section A: Accelerators, Spectrometers, Detectors and Associated Equipment **592** (2008), 189 – 196.

[HBD+10] Z. Huang, et al., *Measurements of the linac coherent light source laser heater and its impact on the x-ray free-electron laser performance*, Phys. Rev. ST Accel. Beams **13** (2010), 020703.

[HBE+04] Z. Huang, M. Borland, P. Emma, J. Wu, C. Limborg, G. Stupakov, and J. Welch, *Suppression of microbunching instability in the linac coherent light source*, Phys. Rev. ST Accel. Beams **7** (2004), 074401.

[HBF+03] K. Honkavaara, et al., *Design of OTR beam profile monitors for the TESLA Test Facility, Phase 2 (TTF2)*, Proceedings of PAC2003, Portland, USA, 2003, WPPB028.

[HBS+10] S. Hellmann, et al., *Ultrafast Melting of a Charge-Density Wave in the Mott Insulator $1T$-TaS$_2$*, Phys. Rev. Lett. **105** (2010), 187401.

[HEBK03] Z. Huang, P. Emma, M. Borland, and K.-J. Kim, *Effectis of Linac Wakefield on CSR Microbunching in the Linac Coherent Light Source*, 2003, SLAC-PUB-9818.

[HLN+07] A. Hamdi, M. Luong, J. Novo, F. Ballester, L. Frölich, M. Görler, M. Werner, S. Magnus, and M. Staack, *Toroid protection system for FLASH*, Proceedings of DIPAC2007, Venice, Italy, 2007.

[HTT12] T. Hara, K. Togawa, and H. Tanaka, *Progess in SACLA Operation*, Proceedings of FEL2012, Nara, Japan, 2012, MOOB03.

[Hua13] Z. Huang, *Brightness and Coherence of Synchrotron Radiation and FELs*, 2013, SLAC-PUB-15449.

[IBO+10] R. Ischebeck, B. Beutner, G. L. Orlandi, M. Pedrozzi, T. Schietinger, V. Schlott, and V. Thominet, *Profile monitors for the SwissFEL Injector Test Facility*, Proceedings of LINAC2010, Tsukuba, Japan, 2010, TUP103.

[IBSS09] R. Ischebeck, B. Beutner, B. Steffen, and V. Schlott, *Screen monitor design for the SwissFEL*, Proceedings of DIPAC2009, Basel, Switzerland, 2009, TUPD45.

[IKL+14] R. Ischebeck, P. Krejcik, H. Loos, E. Prat, V. Schlott, V. Thominet, and M. Yan, *Transverse profile monitors for SwissFEL*, Proceedings of IBIC2014, 2014, TUCYB3.

[INR11] Institute for Nuclear Research of Russian Academy of Sciences, *Transverse deflecting structures and high power RF systems for the XFEL TDS systems conceptual design report*, March 2011, Revision 2.

[IOS00] International Organization for Standardization, *Photography – Electronic still picture imaging – Resolution and spatial frequency responses*, 2000, ISO 12233.

[Isc] R. Ischebeck, private communication.

[IT14] R. Ischebeck, and V. Thominet, European Patent Application, 2014, EP2700979A1.

[KBG+12] G. Kube, C. Behrens, C. Gerth, B. Schmidt, M. Yan, and W. Lauth, *Inorganic scintillators for particle beam profile diagnostics of highly brilliant and highly energetic electron beams*, Proceedings of IPAC2012, New Orleans, Lousiana, USA, 2012, WEOAA02.

[KBL10] G. Kube, C. Behrens, and W. Lauth, *Resolution Studies of Inorganic Scintillation Screens for High Energy and High Brilliance Electron Beams*, Proceedings of IPAC2010, Kyoto, Japan, 2010, MOPD088.

[KDD+13] P. Krejcik, et al., *Commissioning the new LCLS X-band transverse deflecting cavity with femtosecond resolution*, Proceedings of IBIC2013, Oxford, UK, 2013, TUAL2.

[Kim86] K.-J. Kim, *Three-Dimensional Analysis of Coherent Amplification and Self-Amplified Spontaneous Emission in Free-Electron Lasers*, Physical Review Letters **57** (1986), 15.

[KMW+12] M. Krikunova, T. Maltezopoulos, P. Wessels, M. Schlie, A. Azima, T. Gaumnitz, T. Gebert, M. Wieland, and M. Drescher, *Strong-field ionization of molecular iodine traced with XUV pulses from a free-electron laser*, Phys. Rev. A **86** (2012), 043430.

[KS80] A. M. Kondratenko, and E. L. Saldin, *Generation of coherent radiation by a relativistic electron beam in an ondulator*, Particle Accelerators **10** (1980), 207–216.

[KS13] R. Kammering, and C. Schmidt, *Feedbacks and automation at the free electron laser in Hamburg (FLASH)*, Proceedings of ICALEPCS2013, San Francisco, CA, USA, 2013, THPPC121.

[Kub99] K. Kubo, *How to calculate "intrinsic" emittances from 4-dimensional beam matrix*, ATF internal report, February 1999, ATF-99-02.

[Kub08] G. Kube, *Imaging with Optical Transition Radiation, Transverse Beam Diagnostics for the XFEL*, TESLA FEL Reports, 2008, TESLA-FEL 2008-01.

[LABD08] H. Loos, R. Akre, A. Brachmann, and F.-J. Decker, *Observation of coherent optical transition radiation in the LCLS linac*, Proceedings of FEL2008, Gyeongju, Korea, 2008, THBAU01.

[LAG+06] P. Lecoq, A. Annenkov, A. Gektin, M. Korzhik, and C. Pedrini, *Inorganic Scintillators for Detector Systems*, Springer, 2006.

[LBEU09] A. Lehmann, A. Britting, W. Eyrich, and F. Uhlig, *Studies of MCP properties*, Journal of Instrumentation **4** (2009), 11024.

[Löh05] F. Löhl, *Measurements of the Transverse Emittance at the VUV-FEL*, diploma thesis, Universität Hamburg, August 2005.

[Loo] H. Loos, *Reconstruction of a filamentary phase space from two projections*, private communication.

[LS97] R. Lai, and A. Sievers, *On using the coherent far IR radiation produced by a charged-particle bunch to determine its shape: I Analysis*, Nuclear Instruments and Methods in Physics Research Section A: Accelerators, Spectrometers, Detectors and Associated Equipment **397** (1997), 221 – 231.

[LSB+09] A. H. Lumpkin, N. S. Sereno, W. J. Berg, M. Borland, Y. Li, and S. J. Pasky, *Characterization and mitigation of coherent-optical-transition-radiation signals from a compressed electron beam*, Phys. Rev. ST Accel. Beams **12** (2009), 080702.

[Mad71] J. M. J. Madey, *Stimulated Emission of Bremsstrahlung in a periodic magnetic field*, Journal of Applied Physics **42** (1906 (1971)).

[MBD+13] T. J. Maxwell, C. Behrens, Y. Ding, A. S. Fisher, J. Frisch, Z. Huang, and H. Loos, *Coherent-Radiation Spectroscopy of Few-Femtosecond Electron Bunches Using a Middle-Infrared Prism Spectrometer*, Phys. Rev. Lett. **111** (2013), 184801.

[MEK+12] H. Maesaka, H. Ego, C. Kondo, T. Ohshima, H. Tomizawa, Y. Otake, S. Matsubara, T. Matsumoto, and K. Yanagida, *Electron beam diagnostic system for the japanese XFEL, SACLA*, Proceedings of IBIC2012, Tsukuba, Japan, 2012, MOIC02.

[MJR+00] A. Murokh, E. Johnson, J. Rosenzweig, X. J. Wang, and V. Yakimenko, *Limitations on the resolution of YAG:CE beam profile monitor for high brightness electron beam*, 2nd ICFA Advanced Accelerator Workshop on the Physics of High Brightness Beams, 2000.

[MMIO12] S. Matsubara, H. Maesaka, S. Inoue, and Y. Otake, *Improvement of screen monitor with suppression of coherent-OTR effect for SACLA*, Proceedings of IBIC2012, Tsukuba, Japan, 2012, MOCC04.

[MZ03] M. Minty, and F. Zimmermann, *Measurement and Control of Charged Particle Beams*, Springer-Verlag Berlin Heidelberg New York, 2003.

[Nik] Nikon Corporation, `http://www.nikon.com`.

[NWvdS+00] R. Neutze, R. Wouts, D. van der Spoel, E. Weckert, and J. Hajdu, *Potential for biomolecular imaging with femtosecond X-ray pulses*, Nature **406** (2000), 752–757.

[P+10] M. Pedrozzi, et al., *250 MeV Injector Conceptual Design Report*, PSI Report, 2010, PSI-10-05.

[PA14] E. Prat, and M. Aiba, *Four-dimensional transverse beam matrix measurement using the multiple-quadrupole scan technique*, Phys. Rev. ST Accel. Beams **17** (2014), 052801.

[PAB+14] E. Prat, M. Aiba, S. Bettoni, B. Beutner, S. Reiche, and T. Schietinger, *Emittance measurements and minimization at the SwissFEL Injector Test Facility*, Phys. Rev. ST Accel. Beams **17** (2014), 104401.

[PCO] PCO AG, *Dicam Pro camera date sheet*, `http://www.pco.de/fileadmin/user_upload/db/products/datasheet/dicam_pro_20110531.pdf`.

[Phi61] P. R. Phillips, *Microwave separator for high energy particle beams*, Review of Scientific Instruments **32** (1961), 13.

[Pra14] E. Prat, *Symmetric single-quadrupole-magnet scan method to measure the 2D transverse beam parameters*, Nuclear Instruments and Methods in Physics Research Section A: Accelerators, Spectrometers, Detectors and Associated Equipment **743** (2014), 103 – 108.

[PW56] W. K. H. Panovsky, and W. A. Wenzel, *Some considerations concerning the transverse deflection of charged particles in radiofrequency fields*, Review of Scientific Instruments **27** (1956), 967.

[Rau00] T. O. Raubenheimer, *Estimates of emittance dilution and stability in high-energy linear accelerators*, Phys. Rev. ST Accel. Beams **3** (2000), 121002.

[RBH+92] M. C. Ross, E. Bong, L. Hendrickson, D. McCormick, and M. Zolotorev, *Experience with wire scanners at SLC*, December 1992, SLAC-PUB-6014.

[RGS+09] M. Röhrs, C. Gerth, H. Schlarb, B. Schmidt, and P. Schmüser, *Time-resolved electron beam phase space tomography at a soft x-ray free-electron laser*, Phys. Rev. ST Accel. Beams **12** (2009), 050704.

[Röh08] M. Röhrs, *Investigation of the Phase Space Distribution of Electron Bunches at the FLASH-Linac Using a Transverse Deflecting Structure*, Ph.D. thesis, Universität Hamburg, 2008.

[RS93] J. Rossbach, and P. Schmüser, *Basic course on accelerator optics*, DESY internal report, 1993, M-93-02.

[RST+01] F. Richard, J. R. Schneider, D. Trines, A. Wagner, R. Brinkmann, K. Flöttmann, and J. Rossbach, *TESLA Technical Design Report*, TESLA Reports, 2001, TESLA 2001-23.

[San91] M. Sands, *A beta mismatch parameter*, SLAC internal report, April 1991, SLAC-AP-85.

[Sch04] T. Scheimpflug, *Method of distorting plane images by means of lenses or mirrors*, Patent US751347, 1904.

[SDR08] P. Schmüser, M. Dohlus, and J. Rossbach, *Ultraviolet and Soft X-Ray Free-Electron Lasers*, Springer, 2008.

[SF14] S. Schreiber, and B. Faatz, *First lasing at FLASH2*, Proceedings of FEL2014, Basel, Switzerland, 2014, MOA03.

[SFF+10] S. Schreiber, B. Faatz, J. Feldhaus, K. Honkavaara, R. Treusch, M. Vogt, and J. Rossbach, *FLASH upgrade and first results*, Proceedings of FEL2010, Malmö, Sweden, 2010, TUOB12.

[Sha15] Shareholders of the European XFEL GmbH, `http://www.xfel.eu/organization/company/shareholders/`, April 2015.

[SLA] SLAC national accelerator laboratory, `https://www6.slac.stanford.edu/`.

[SSK+13] K. Schnorr, et al., *Time-Resolved Measurement of Interatomic Coulombic Decay in* Ne_2, Phys. Rev. Lett. **111** (2013), 093402.

[SSK+14] K. Schnorr, et al., *Electron Rearrangement Dynamics in Dissociating* I_2^{n+} *Molecules Accessed by Extreme Ultraviolet Pump-Probe Experiments*, Phys. Rev. Lett. **113** (2014), 073001.

[SSY98] E. Saldin, E. Schneidmiller, and M. Yurkov, *Statistical properties of radiation from VUV and X-ray free electron laser*, Optics Communications **148** (1998), 383 – 403.

[SSY00] E. L. Saldin, E. A. Schneidmiller, and M. V. Yurkov, *The Physics of Free Electron Lasers*, Springer, Berlin, 2000.

[SSY02a] E. L. Saldin, E. A. Schneidmiller, and M. V. Yurkov, *An analytical description of longitudinal phase space distortions in magnetic bunch compressors*, Nuclear Instruments and Methods in Physics Research Section A: Accelerators, Spectrometers, Detectors and Associated Equipment **483** (2002), 516 – 520.

[SSY02b] E. L. Saldin, E. A. Schneidmiller, and M. V. Yurkov, *Klystron instability of a relativistic electron beam in a bunch compressor*, Nuclear Instruments and Methods in Physics Research Section A: Accelerators, Spectrometers, Detectors and Associated Equipment **490** (2002), 1 – 8.

[SSY04] E. Saldin, E. Schneidmiller, and M. Yurkov, *Longitudinal space charge-driven microbunching instability in the TESLA Test Facility linac*, Nuclear Instruments and Methods in Physics Research Section A: Accelerators, Spectrometers, Detectors and Associated Equipment **528** (2004), 355 – 359.

[Ste07] B. Steffen, *Electro-Optic Methods for Longitudinal Bunch Diagnostics at FLASH*, Ph.D. thesis, Universität Hamburg, 2007.

[UNI] UNIQ VISION, INC., `http://www.uniqvision.com/`.

[WBSS09] S. Wesch, C. Behrens, B. Schmidt, and P. Schmüser, *Observation of coherent optical transition radiation and evidence for microbunching in magnetic chicanes*, Proceedings of FEL2009, Liverpool, UK, 2009, WEPC50.

[Wes12] S. Wesch, *Echtzeitbestimmung longitudinaler Elektronenstrahlparameter mittels absoluter Intensitäts- und Spektralmessung einzelner kohärenter THz Strahlungspulse*, Ph.D. thesis, Universität Hamburg, 2012.

[WHK+13] C. Wiebers, M. Holz, G. Kube, D. Nölle, G. Priebe, and H.-C. Schröder, *Scintillating screen monitors for transverse electron beam profile diagnostics at the European XFEL*, Proceedings of IBIC2013, Oxford, UK, 2013, WEPF03.

[Wie93] H. Wiedemann, *Particle Accelerator Physics*, Springer, 1993.

[WSB+11] S. Wesch, B. Schmidt, C. Behrens, H. Delsim-Hashemi, and P. Schmüser, *A multichannel THz and infrared spectrometer for femtosecond electron bunch diagnostics by single-shot spectroscopy of coherent radiation*, Nuclear Instruments and Methods in Physics Research Section A: Accelerators, Spectrometers, Detectors and Associated Equipment **665** (2011), 40 – 47.

[Wyc] J. Wychowaniak, Ph.D. thesis in progress.

[Yan12] M. Yan, *Suppression of COTR in electron beam imaging diagnosis at FLASH*, diploma thesis, Universität Hamburg, 2012.

[YBG+13] M. Yan, C. Behrens, C. Gerth, R. Kammering, A. Langner, F. Obier, and J. Wychowaniak, *First realization and performance study of a single-shot longitudinal bunch profile monitor utilizing a transverse deflecting structure*, Proceedings of IBIC2013, Oxford, UK, 2013, TUPC36.

[YMG+00] X. Yan, A. M. MacLeod, W. A. Gillespie, G. M. H. Knippels, D. Oepts, A. F. G. van der Meer, and W. Seidel, *Subpicosecond Electro-optic Measurement of Relativistic Electron Pulses*, Phys. Rev. Lett. **85** (2000), 3404–3407.

[ZD11] I. Zagorodnov, and M. Dohlus, *Semianalytical modeling of multistage bunch compression with collective effects*, Phys. Rev. ST Accel. Beams **14** (2011), 014403.

Acknowledgements

My sincere acknowledgements go to:

Dr. Christopher Gerth

Dr. Winfried Decking

Dr. Christopher Behrens

Dr. Rasmus Ischebeck

Dr. Eduard Prat

Dr. Bolko Beutner

Eugen Hass

Prof. Dr. Jörg Roßbach

all my colleagues at DESY, PSI and SLAC

my boyfriend Yunlong

and my family.

Eidesstattliche Versicherung

Hiermit erkläre ich an Eides statt, dass ich die vorliegende Dissertationsschrift selbständig verfasst und – einschließlich beigefügter Abbildungen und Diagramme – keine anderen als die im Literaturverzeichnis angegebenen Quellen und Hilfsmittel benutzt habe.

Minjie Yan – Hamburg, 18.5.2015